

VOL.107 NO.ST9. SEPT. 1981

# **JOURNAL OF THE STRUCTURAL DIVISION**

PROCEEDINGS OF  
THE AMERICAN SOCIETY  
OF CIVIL ENGINEERS







VOL.107 NO.ST9. SEPT. 1981

# JOURNAL OF THE STRUCTURAL DIVISION

PROCEEDINGS OF  
THE AMERICAN SOCIETY  
OF CIVIL ENGINEERS



Copyright© 1981 by  
American Society  
of Civil Engineers  
All Rights Reserved  
ISSN 0044-8001

**John E. Bower, Editor**  
**U.S. Steel Corporation**

## AMERICAN SOCIETY OF CIVIL ENGINEERS

### BOARD OF DIRECTION

#### *President*

Irvan F. Mendenhall

#### *Past President*

Joseph S. Ward

#### *President Elect*

James R. Sims

#### *Vice Presidents*

Robert D. Bay  
Francis J. Connell

Lyman R. Gillis  
Albert A. Grant

#### *Directors*

Martin G. Abegg	Paul R. Munger
Floyd A. Bishop	William R. Neuman
L. Gary Byrd	Leonard S. Oberman
Larry J. Feaser	John D. Parkhurst
John A. Focht, Jr.	Celestino R. Pennoni
Sergio Gonzalez-Karg	Robert B. Rhode
James E. Humphrey, Jr.	S. Russell Stearns
Richard W. Karn	William H. Taylor
Leon D. Luck	Stafford E. Thornton
Arthur R. McDaniel	Robert E. Whiteside
Richard S. Woodruff	

### EXECUTIVE OFFICERS

Eugene Zwoyer, *Executive Director*  
Julie E. Gibouleau, *Assistant to the Executive Director*  
Louis L. Meier, *Washington Counsel/Assistant Secretary*  
William H. Wisely, *Executive Director Emeritus*  
Michael N. Salgo, *Treasurer*  
Elmer B. Isaak, *Assistant Treasurer*

### STAFF DIRECTORS

Donald A. Buzzell, *Managing Director for Education and Professional Affairs*  
Robert A. Crist, Jr., *Managing Director for Publications and Technical Affairs*  
Alexandra Bellow, *Director, Human Resources*  
David Dresia, *Director, Publications Production and Marketing*  
Barker D. Herr, *Director, Membership*  
Richard A. Jeffers, *Controller*  
Carl E. Nelson, *Director, Field Services*  
Don P. Reynolds, *Director, Policy, Planning and Public Affairs*  
Bruce Rickerson, *Director, Legislative Services*

Albert W. Turchick, *Director, Technical Services*

George K. Wadlin, *Director, Education Services*

R. Lawrence Whipple, *Director, Engineering Management Services*

### COMMITTEE ON PUBLICATIONS

Stafford E. Thornton, *Chairman*

Martin G. Abegg

Richard W. Karn

John A. Focht, Jr.

Paul R. Munger

William R. Neuman

### STRUCTURAL DIVISION

#### *Executive Committee*

John E. Bower, *Chairman*

Ronald G. Damer, *Vice Chairman*

Peter B. Cooper

Roland L. Sharpe

Donald McDonald, *Secretary*

Frederick H. Sterbenz, *Management Group B Contact Member*

Joseph H. Appleton, *Management Group B Contact Member*

#### *Publications Committee*

John E. Bower, *Chairman, Editor and Exec.*

#### *Comm. Contact Member*

Mihran S. Agbabian

Bruce E. Lyons

Marvin E. Criswell

Walter Podolny

John T. DeWolf

Emil Simiu

Douglas Foutch

John F. Stolz

Ovadia E. Lev

C. K. Wang

Le-Wu Lu

James T. P. Yao

### PUBLICATIONS SERVICES DEPARTMENT

David Dresia, *Director, Publications Production and Marketing*

#### *Technical and Professional Publications*

Richard R. Torrens, *Manager*

Chuck Wahrhaftig, *Chief Copy Editor*

Corinne Bernstein, *Copy Editor*

Linda Ellington, *Copy Editor*

Walter Friedman, *Copy Editor*

Shiela Menaker, *Production Co-ordinator*

Richard C. Scheblein, *Draftsman*

#### *Information Services*

Elan Garonzik, *Editor*

## PERMISSION TO PHOTOCOPY JOURNAL PAPERS

Permission to photocopy for personal or internal reference beyond the limits in Sections 107 and 108 of the U.S. Copyright Law is granted by the American Society of Civil Engineers for libraries and other users registered with the Copyright Clearance Center, 21 Congress Street, Salem, Mass. 01970, provided the appropriate fee is paid to the CCC for all articles bearing the CCC code. Requests for special permission or bulk copying should be addressed to the Manager of Technical and Professional Publications, American Society of Civil Engineers.

## CONTENTS

### Shear Lag in Box Girders

*by Bogdan O. Kuzmanović and H. James Graham . . . . .* 1701

### Seismic Damage in Reinforced Concrete Frames

*by Hooshang Banon, John M. Biggs, and H. Max Irvine . . . . .* 1713

### Collapse by Ponding of Air-Supported Spherical Caps

*by David J. Malcolm and Peter G. Glockner . . . . .* 1731

### Optimization Procedure for Pulse-Simulated Response

*by Sami F. Masri and Frederick B. Safford . . . . .* 1743

### Approximate Design by Geometric Series

*by Bogdan O. Kuzmanović and Nicholas Willems . . . . .* 1763

### An Evaluation of Inelastic Seismic Design Spectra

*by Stephen A. Mahin and Vitelmo Bertero . . . . .* 1777

### Cellular and Voided Slab Bridges

*by Baidar Bakht, Leslie G. Jaeger, and Mo S. Cheung . . . . .* 1797

The Journal of the Structural Division (ISSN 0044-8001) is published monthly by the American Society of Civil Engineers. Publications office is at 345 East 47th Street, New York, N.Y. 10017. Address all ASCE correspondence to the Editorial and General Offices at 345 East 47th Street, New York, N.Y. 10017. Allow six weeks for change of address to become effective. Subscription price to members is \$22.50. Nonmember subscriptions available; prices obtainable on request. Second-class postage paid at New York, N.Y. and at additional mailing offices. ST.

POSTMASTER: Send address changes to American Society of Civil Engineers, 345 East 47th Street, New York, NY 10017.

The Society is not responsible for any statement made or opinion expressed in its publications.

<b>Static Behavior of Beam-to-Column Moment Connections</b> by <i>W. F. Chen and K. V. Patel</i> . . . . .	1815
<b>Limit Design of Slabs for Concentrated Loads</b> by <i>Hans Gesund</i> . . . . .	1839
<b>Steel Struts under Severe Cyclic Loadings</b> by <i>Egor P. Popov and R. Gary Black</i> . . . . .	1857

---

## DISCUSSION

Proc. Paper 16481

---

<b>Stability of Flexibility Connected Plate Systems</b> , by Milija Pavlovic, Donald S. Mansell, and Leonard K. Stevens (Oct., 1980). <i>errata</i> . . . . .	1885
<b>Research Needs in Stability of Metal Structures</b> ,* by Reidar Bjorhovde (Dec., 1980). by <i>Charles E. Massonnet and Rene Maquoi</i> . . . . . by <i>Roman Wolchuk</i> . . . . .	1885 1889
<b>Membrane Reinforcement in Shells</b> ,* by Ajaya K. Gupta (Jan., 1981). by <i>Morris N. Fialkow</i> . . . . .	1890

## INFORMATION RETRIEVAL

The key words, abstract, and reference "cards" for each article in this Journal represent part of the ASCE participation in the EJC information retrieval plan. The retrieval data are placed herein so that each can be cut out, placed on a 3 × 5 card and given an accession number for the user's file. The accession number is then entered on key word cards so that the user can subsequently match key words to choose the articles he wishes. Details of this program were given in an August, 1962 article in CIVIL ENGINEERING, reprints of which are available on request to ASCE headquarters.

---

\*Discussion period closed for this paper. Any other discussion received during this discussion period will be published in subsequent Journals.

## 16514 SHEAR LAG IN BOX GIRDERS

**KEY WORDS:** Bending; **Box girders;** Concrete (reinforced); **Load distribution;** Loads (forces); **Reinforced concretes;** **Shear lag;** Slabs

**ABSTRACT:** An initial approximate method is presented to evaluate the shear lag phenomenon in reinforced concrete single-box girder bridges. Assuming an ideal cross-section and considering a symmetrical deformation of the top and bottom slabs, but preserving continuity conditions at the web-slab intersection points, a fourth order non-homogeneous differential equation with constant coefficients was obtained. Making further simplifications, quick results are obtained for uniformly distributed loads. In spite of all the simplifications these results were in good agreement with the German specifications for shear lag provided that midspan reduction factors are desired. The factors are the most important anyway, because they are valid practically almost for the whole span length.

**REFERENCE:** Kuzmanovic, Bogdan O. (Prof., Dept. of Civ. Engrg., Univ. of Kansas, Lawrence, Kans.), and Graham, H. James, "Shear Lag in Box Girders," *Journal of the Structural Division*, ASCE, Vol. 107, No. ST9, **Proc. Paper 16514**, September, 1981, pp. 1701-1712

## 16496 SEISMIC DAMAGE IN REINFORCED CONCRETE FRAMES

**KEY WORDS:** Analytical techniques; Cyclic loads; **Damage estimation;** Ductility; Earthquake resistant structures; Inelastic action; **Reinforced concretes;** Seismic design; **Structural deformation analysis;** **Structural dynamics**

**ABSTRACT:** Seismic damage in reinforced concrete frames is predicted by analytical methods. Analytical models are developed which can reproduce the behavior of reinforced concrete members under cyclic loads. Accuracy of the analytical models is checked by considering a set of quasi-static cyclic load tests, and the models are found to be sufficiently accurate. Several damage indicators such as ductility, flexural damage ratio, dissipated energy, and cumulative plastic rotation are investigated for each experiment. Based on the test results and physical grounds, flexural damage ratio and dissipated energy are chosen as damage state parameters. The results of the present study are later used to develop a probabilistic model of member failure in reinforced concrete structures.

**REFERENCE:** Banon, Hooshang (Structural Mechanics Associates Newport Beach, Calif.), Biggs, John M., and Irvine, H. Max, "Seismic Damage in Reinforced Concrete Frames," *Journal of the Structural Division*, ASCE, Vol. 107, No. ST9, **Proc. Paper 16496**, September, 1981, pp. 1713-1729

## 16520 COLLAPSE OF AIR-SUPPORTED SPHERICAL CAPS

**KEY WORDS:** Air supported structures; Collapse; Laboratory tests; Ponding; **Ponding tests;** **Structural behavior;** **Structural design;** **Structural models;** Weight limits; **Weight (mass)**

**ABSTRACT:** A theory is presented to predict the critical central weight which, in the presence of a ponding medium, will lead to collapse of an inextensible air supported spherical membrane. Results are developed for a range of radii, pressures and ponding medium densities. Also explored is the manner in which these results will be effected by meridional action only, such as would be caused by a system of cables converging at the apex. A description is given of a series of tests carried out on two laboratory models to confirm the theoretical results. The experimental results indicate that the theory may lead to under design and that this instability is particularly sensitive to surface irregularities near the apex.

**REFERENCE:** Malcolm, David J. (Sr. Engr., DAF Indal Ltd., 3570 Hawkstone Road, Mississauga, Ontario, L5C 2V8 Canada), and Glockner, Peter G., "Collapse by Ponding of Air-Supported Spherical Caps," *Journal of the Structural Division*, ASCE, Vol. 107, No. ST9, **Proc. Paper 16520**, September, 1981, pp. 1731-1742

## 16521 PROCEDURE FOR PULSE-SIMULATED RESPONSE

**KEY WORDS:** Algorithms; **Dynamic response;** Earthquake simulation models; Impulses; Pulse frequency; **Pulses;** **Structural dynamics;** Structural stability; Vibration response

**ABSTRACT:** A computationally efficient technique is presented for optimizing the selection of pulse train characteristics, to be used for simulating the response of general types of structural systems to arbitrary dynamic environments. The optimization procedure uses an adaptive random search algorithm that incorporates a periodic exploratory search for the optimal step-size variance, which significantly improves the convergence characteristics. Pulse trains (to induce specified or criterion structural motion) are not unique and are largely dependent upon constraints. The method is demonstrated for a 25-story building and a steel one-bay structure.

**REFERENCE:** Masri, Sami F. (Prof., Civ. Engrg. Dept., of Southern California, Los Angeles, Calif. 90007), and Safford, Frederick B., "Optimization Procedure for Pulse-Simulated Response," *Journal of the Structural Division, ASCE*, Vol. 107, No. ST9, **Proc. Paper 16521**, September, 1981, pp. 1743-1761

## 16486 APPROPRIATE DESIGN BY GEOMETRIC SERIES

**KEY WORDS:** Approximation method; Frame design; **Frames;** **Moment distribution;** **Optimization;** Rectangles; Series (mathematics); **Structural design;** Two-dimensional

**ABSTRACT:** An approximate optimization method is presented that is applicable to rectangular, two-dimensional multistory frames. Using special moment distribution techniques, the optimization of linearized frame "weight" is achieved for an infinite number of iterations. A closed-form exact formula makes it possible to avoid these iterations. Thus, when this program is used, a minicomputer with 4K memory can handle a four-story, four-bay frame subject to asymmetrical loading. The method is programmed in BASIC.

**REFERENCE:** Kuzmanovic, Bogdan O. (Prof. of Civ. Engrg., Univ. of Kansas, Lawrence, Kans. 66045), and Willems, Nicholas, "Appropriate Design by Geometric Series," *Journal of the Structural Division, ASCE*, Vol. 107, No. ST9, **Proc. Paper 16486**, September, 1981, pp. 1763-1775

## 16501 SEISMIC DESIGN SPECTRA

**KEY WORDS:** Ductility; **Dynamic loads;** Earthquakes; **Plastic analysis;** Reliability; **Seismic design;** Seismic stability; Structural analysis; **Structural design**

**ABSTRACT:** After reviewing general methods available for determining seismic design forces for structures which can tolerate limited amounts of inelastic deformations, the reliability of two representative procedures is evaluated. In the methods evaluated, inelastic design response spectra are obtained by modifying a linear elastic design response spectrum in terms of a specified ductility factor as suggested by Newmark and Hall and the Applied Technology council. The effect of different accelerograms, as well as of different system damping and hysteretic characteristics, on the inelastic response of single degree-of-freedom systems designed using these methods is thoroughly investigated, considering maximum displacement ductilities, maximum and permanent drifts, number of yield events, and hysteretic energy dissipation. Application of these design methods to multistory buildings is also briefly considered. Results obtained for ideal inelastic systems indicate that these methods do not reliably limit displacement ductilities to specified values.

**REFERENCE:** Mahin, Stephen A. (Asst. Prof. of Civ. Engrg., Univ. of California, Berkeley, Calif. 94720), and Bertero, Vitelmo V., "An Evaluation of Inelastic Seismic Design Spectra," *Journal of the Structural Division, ASCE*, Vol. 107, No. ST9, **Proc. Paper 16501**, September, 1981, pp. 1777-1795

## 16495 CELLULAR AND VOIDED SLAB BRIDGES

**KEY WORDS:** Bridges (structures); Cellular structures; Characteristics; Distortion (structural); Longitudinal force; Longitudinal stability; Orthotropic plate; Slabs; Structural analysis; Structural dynamics

**ABSTRACT:** Bridges of the cellular and voided slab type are explored. These types of bridges have either rectangular or circular holes running in the direction of the bridge span. In these structures the transverse distortion of the cross section may significantly affect the load distribution properties of a bridge to the extent that it can no longer be analyzed by conventional orthotropic plate theory. A simplified method is developed which can account for the increases in longitudinal moment and shear intensities which result from distortion of the cross section. Existing simplified methods, which are applicable only when transverse cell-distortion is absent, may be used in conjunction with certain modifying factors even when such effects are present.

**REFERENCE:** Bakht, Baidar (Sr. Research Officer, Policy Planning and Research Div., Ontario Ministry of Transportation and Communications, Downsview, Ontario, Canada), Jaeger, Leslie G., and Cheung, Mo S., "Cellular and Voided Slab Bridges," *Journal of the Structural Division, ASCE*, Vol. 107, No. ST9, **Proc. Paper 16495**, September, 1981, pp. 1797-1813

## 16512 BEAM-TO-COLUMN CONNECTIONS

**KEY WORDS:** Beams (structural); Connections (joints); Fabrication; Flanges; High strength bolts; Stiffeners; Structural design; Structural steel; Tests; Welds

**ABSTRACT:** A review is presented of tests on beam-to-column moment flange connections. The main objective of these tests was to study the behavior and to develop the design method for flange moment connections. A test program of flange connections consisted of 12 full-size beam-to-column connections. This test series included specimens representing connections for the lower stories, middle stories, and upper stories of a multi-story frame. Primary attention is focused on strength, deformation capacity and overall stiffness of the connection. The load-deflection plot of each connection is compared with its control test behavior, in the adequacy of AISC specifications is studied.

**REFERENCE:** Chen, W. F. (Prof. of Struc. Engrg., School of Civ. Engrg., Purdue Univ., West Lafayette, Ind. 47907), and Patel, K. V., "Static Behavior of Beam-to-Column Moment Connections," *Journal of the Structural Division, ASCE*, Vol. 107, No. ST9, **Proc. Paper 16512**, September, 1981, pp. 1815-1838

## 16504 LIMIT DESIGN OF SLABS FOR CONCENTRATED LOADS

**KEY WORDS:** Design; Limit design; Loads (forces); Orthotropism; Plasticity; Plates (structural members); Reinforced concretes; Reinforcement (structures); Slabs; Strength

**ABSTRACT:** Yield Line Theory is used to derive expressions for the flexural limit loads of reinforced concrete slabs subjected to simultaneously acting concentrated and distributed loads. The "concentrated" loads are assumed to have a rectangular footprint of any reasonable size and aspect ratio. The slab reinforcement can be orthotropic, different over each supported boundary, and the positive and negative moment reinforcements can also be different. The slab boundaries may be rigidly supported or consist of beams whose bending and torsional strengths, and weight, can be incorporated into the analysis. One of the boundaries can also be unsupported. The geometrically admissible collapse mechanisms for the combined loadings are studied and results obtained by their use are compared with some presented in the literature for individual loadings.

**REFERENCE:** Gesund, Hans (Prof. of Struct. Engrg., Univ. of Kentucky Lexington, Ky. 40506), "Limit Design of Slabs for Concentrated Loads," *Journal of the Structural Division, ASCE*, Vol. 107, No. ST9, **Proc. Paper 16504**, September, 1981, pp. 1839-1856

## 16497 STEEL STRUTS UNDER SEVERE CYCLIC LOADINGS

**KEY WORDS:** Buckling; Buildings; Columns; Cyclic loads; Earthquakes; Engineering mechanics; Plastic properties; Steels; Stretching; Structural analysis; Structural dynamics; Struts

**ABSTRACT:** An experimental study is presented of the inelastic behavior of axially loaded steel members subjected to repeated buckling and stretching. Tests on 24 commercially available steel struts commonly used as bracing members are reported. A large variety of shapes were tested including wide flanges, structural tees, double-angles, a double-channel, and thick and thin-walled square and round tubes. The boundary conditions were of two types, pinned-pinned and fixed-pinned, while the effective slenderness ratios were either 40, 80, or 120. The effects were investigated of loading patterns, end conditions, cross-sectional shapes, and slenderness ratios on the hysteresis response of members. An explanation is given regarding the fundamental mechanisms responsible for the observed degradation in the buckling load capacity during inelastic cycling.

**REFERENCE:** Popov, Egor P. (Prof., Dept. of Civ. Engrg., Univ. of California, Berkeley, Calif. 94720), and Black, R. Gary, "Steel Struts under Severe Cyclic Loadings," *Journal of the Structural Division*, ASCE, Vol. 107, No. ST9, **Proc. Paper 16497**, September, 1981, pp. 1857-1881



## SHEAR LAG IN BOX GIRDERS

By Bogdan O. Kuzmanović,<sup>1</sup> F. ASCE and H. James Graham,<sup>2</sup> F. ASCE

### INTRODUCTION

Shear lag phenomena, or the nonuniform distribution of bending stresses across wide flanges of a beam cross section, have long been recognized (3,5,6,12). First studies were mainly concerned with steel beams of *I* or *T* shape without composite action (1,3,5,6) while later investigations dealt with composite action (2,4,9). When box girders made their comeback in bridge construction, most of the studies either considered only steel box sections (7,16,18,19) or sections with a wide concrete slab acting compositely with the steel part of the box section (23). Reinforced concrete *T*-beams were also studied (10,14,15,20), but reinforced concrete box sections of the dimensions usually encountered in highway bridges were discussed very rarely (13,17). The American Association of State Highway and Transportation Officials, AASHTO, specifications (3) draw attention to the shear-lag problem, but do not give any guidance on how to proceed. The German Industrial Standards, DIN, issued in August, 1973 (8), give the effective width of reinforced concrete box sections for uniform load and various support conditions. These widths for uniform loads are in agreement with test results (21), and they are on the conservative side. Presently, most studies on shear lag have been performed using computerized finite element or folded plate analysis (16,17,18,23). A quick evaluation of the possible shear lag effect is of importance to a practicing engineer at the early stage of the design of a box girder bridge. A computer run at this stage is neither feasible nor economical as even the cross section itself might be changed in further studies. Therefore, there is a real need for an approximate but quick method of reasonable accuracy entailing a limited amount of numerical work.

In this paper, the writers develop a simplified method for bridge sections of the type shown in Fig. 1(a) using the principle of minimum potential energy and adapting the method originally proposed by E. Reissner (19) for the cross section in Fig. 2.

The effective width is a function of geometrical factors, such as slab width, effective span, and the type of stress distribution. Boundary conditions at bridge

<sup>1</sup>Prof., Dept. of Civ. Engrg., Univ. of Kansas, Lawrence, Kans.

<sup>2</sup>Assoc., Beiswenger, Hoch, and Associates, North Miami Beach, Fla.

Note.—Discussion open until February 1, 1982. To extend the closing date one month, a written request must be filed with the Manager of Technical and Professional Publications, ASCE. Manuscript was submitted for review for possible publication on October 8, 1980. This paper is part of the Journal of the Structural Division, Proceedings of the American Society of Civil Engineers, ©ASCE, Vol. 107, No. ST9, September, 1981. ISSN 0044-8001/81/0009-1701/\$01.00.

supports and the type of loading, e.g., point load, uniform load, and prestressing are also affecting this width. A few codes that do consider shear lag do not take into account the load parameters. Similarly, the mutual dependence between the effective width and the distribution of moments along the bridge axis in practical bridge design is either completely disregarded, or the total effect of moment changes is included, e.g., as a fixed percentage reduction or increase

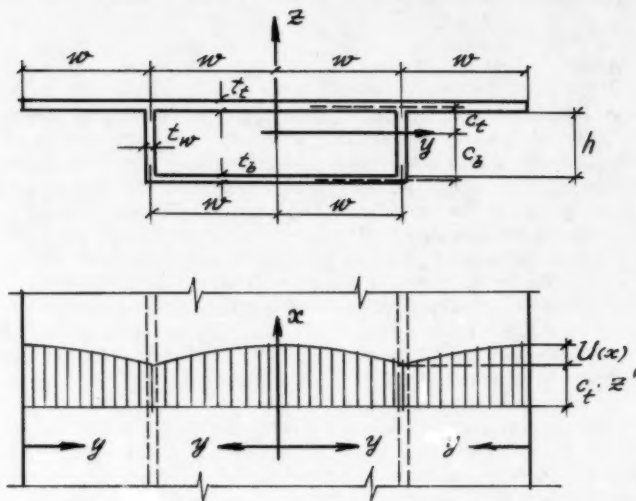


FIG. 1.—(a) Ideal Box Section; (b) Assumed Displacement Function  $U(x)$

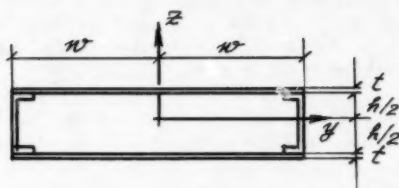


FIG. 2.—Rectangular Doubly Symmetrical Box Section of Ref. 19

of moments, or both. Again, the reason lies in the considerable amount of numerical work in solving this complex problem.

#### METHOD OF ANALYSIS

To reduce the amount of numerical work in developing the method an ideal box section, shown in Fig. 1a, is considered, although later on the method

will be applied to an actual bridge section, Fig. 3. The top slab has a width of  $4w$  and a uniform thickness  $t_t$ . The bottom slab is  $2w$  in width and has a thickness  $t_b$ . The web has a thickness  $t_w$  and depth  $h$ . A symmetrical load distribution  $q(x)$  is specified along the span  $l$ , and it acts symmetrically on the webs, normal to the slab plane. This load causes a known distribution of bending moments along the length of the span,  $M(x)$ , neglecting any influence of the effective widths. Both slabs are assumed to be in a two-dimensional stress state, usually identified as a plane stress state. The model is further simplified by assuming the slab rigidity in the chordwise ( $y$ -axis) direction to be large while the spanwise ( $x$ -axis) slab displacement  $u(x, y)$  is assumed to be completely symmetrical for all four segments of  $w$  as shown in Fig. 1(b):

$$\text{top slab } u_t(x, y) = c_t \left[ z'(x) + \left( 1 - \frac{y^2}{w^2} \right) U(x) \right] \dots \dots \dots (1)$$

$$\text{bottom slab } u_b(x, y) = c_b \left[ z'(x) + \left( 1 - \frac{y^2}{w^2} \right) U(x) \right] \dots \dots \dots (2)$$

The variation of  $u(x, y)$  of course for a cantilever slab is different from that for a slab between webs. However, this assumed symmetry cuts down numerical

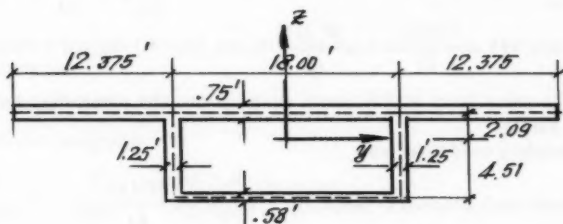


FIG. 3.—Example

work considerably and, as the worked examples demonstrate, is still acceptable.

The continuity of displacements at the intersection between web and slab (in which  $y = w$ ) is preserved in Eqs. 1 and 2. At points where  $y = 0$ , the spanwise displacement  $u(x, 0)$  is expressed in terms of an unknown function  $U(x)$ . This function is a measure of the magnitude of the shear lag effect. For the points between  $y = 0$  and  $y = w$  a parabolic variation of  $u(x, y)$  is assumed. By applying variational calculus to the total potential energy, two differential equations are obtained from which the unknown function  $U(x)$  and its derivatives can be eliminated. Therefore, the final differential equation is in terms of derivatives of the deflection  $z$  only. Although its solution follows closely Reissner's procedure (19) with some changes, the complete solution is given in the Appendix I for a better understanding by users of the proposed method.

**Solution.**—The total potential energy  $\Pi$  of the load system, slabs and webs equals

$$\Pi = \int_0^l \left\{ \frac{EI}{2} [z''(x)]^2 + M(x) z''(x) \right\} dx + \int_0^l \frac{EI_s}{2} \left\{ \frac{8}{15} [U'(x)]^2 + \frac{4}{3} z''(x) U'(x) + \frac{G}{E} \cdot \frac{4}{3w^2} [U(x)]^2 \right\} dx \quad (3)$$

where  $I = I_w + I_s$  is the moment of inertia of the whole cross section, i.e.,

$$I = 2 \left[ \frac{t_w h^3}{12} + t_w h \left( \frac{h}{2} - c_t \right)^2 \right] + 4wt_t c_t^2 + 2wt_b c_b^2 \quad (4)$$

From the minimizing condition,  $\delta\Pi = 0$ , three differential equations are obtained which enable the elimination of the unknown function  $U(x)$ , its derivatives, and the satisfying of its boundary and continuity conditions.

Using Reissner's two parameters  $k$  and  $n$ , in which

$$k = \frac{1}{w} \sqrt{\frac{5n}{2} \cdot \frac{G}{E}} \quad \text{and} \quad n = \frac{1}{1 - \frac{5}{6} \cdot \frac{I_s}{I}} \quad (5)$$

the final form of the differential equation for the vertical displacement  $z(x)$  is

$$z^{IV}(x) - k^2 z''(x) = \frac{k^2 M(x)}{EI} - n \frac{M''(x)}{EI} \quad (6)$$

This is the same form of Reissner's equation but the parameters have now different values.

The boundary conditions are

$$\text{for fixed end (slab attached to support)} \quad z'''(x) = -n \frac{M'(x)}{EI} \quad (7)$$

$$\text{for slabs not attached to supports} \quad z''(x) = -n \frac{M(x)}{EI} \quad (8)$$

By expressing the stress in the slab at the intersection with the webs in the form  $\sigma_w = E\epsilon_x$ , and noticing that  $\epsilon_x = cz''$ , where  $c$  is the distance of the point under consideration from the  $y$ -axis, the stress including shear lag effect

$$\sigma_{w,t,b} = \pm Ec_{t,b} \cdot z''(x) \quad (9)$$

The use of the method is illustrated in the following example.

**Example.**—The shear lag of the first and second span of a three-span continuous bridge 106' + 188' + 106' (32.3 + 57.3 + 32.3 m) is considered. Only uniform load is applied. The bridge somewhat idealized cross-section is given in Fig. 3 with the following characteristic data  $I_s = 352 \text{ ft}^4$  (3.038 m<sup>4</sup>);  $I_w = 84 \text{ ft}^4$  (0.725 m<sup>4</sup>);  $I = 436 \text{ ft}^4$  (3.763 m<sup>4</sup>);  $I_s/I = 0.8073$ ;  $5/6 \times I_s/I = 0.6728$ ;  $n = 3.0560$ ;  $k = 0.1983$ ;  $kl/2 = 10.511$ ;  $G/E = 0.417$ .

**First Span.**—To reduce further the numerical work, the actual moment distribution (already simplified by disregarding the shear lag effect) is replaced by that for a propped cantilever (Fig. 4). In the beam on elastic foundation analogy method used for the design of box-girders (22), the solution is approximated by a mean value between the solution for free and fixed supports. Here

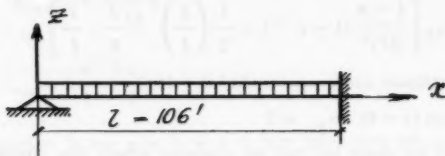


FIG. 4.—First Span Treated as Propped Cantilever

for uniform load and not too unbalanced spans, the assumption of a rigid interior support is close enough. The bending moment at any  $x$  is

$$M(x) = \frac{3}{8} qlx - \frac{qx^2}{2} \quad \dots \dots \dots (10)$$

The differential equation is Eq. 6

$$z^{iv} - k^2 z'' = \frac{k^2 M}{EI} - n \frac{M''}{EI} \quad \dots \dots \dots (11)$$

The solution is straight-forward, and only the results are given. The complementary function is

$$z_h = C_1 + C_2 e^{kx} + C_3 e^{-kx} \quad \dots \dots \dots (12)$$

The particular integral is

$$z_p = \frac{q}{24EI} x^4 - \frac{ql}{16EI} x^3 + \frac{q(1-n)}{2k^2 EI} x^2 \quad \dots \dots \dots (13)$$

The boundary conditions are

$$\text{at } x = 0; \quad z = 0; \quad \text{and} \quad z'' = 0 \quad \dots \dots \dots (14)$$

$$\text{at } x = l; \quad z = 0; \quad z' = 0; \quad \text{and} \quad z''' = -\frac{nM'}{EI} \quad \dots \dots \dots (15)$$

The constants of integration are

$$C_1 = -C_3 = \frac{q(1-n)}{k^4 EI}; \quad C_2 = 0 \quad \dots \dots \dots (16)$$

When the values from Eqs. 16 are substituted into Eq. 12 and Eq. 13 and added together, the following expressions for  $z$  and  $z''$  are obtained:

$$z = \frac{q(1-n)}{k^4 EI} - \frac{q(1-n)}{k^4 EI} \cdot e^{-kx} + \frac{q}{24EI} x^4 - \frac{ql}{16EI} x^3 + \frac{q(1-n)}{2k^2 EI} x^2 \quad \dots \quad (17)$$

$$z'' = + \frac{q^{(1-n)}}{k^2 EI} (1 - e^{-kx}) + \frac{q}{2EI} x^2 - \frac{3}{8} \cdot \frac{ql}{EI} x \dots \dots \dots (18)$$

Substituting the value for  $z''$  from Eq. 18 into Eq. 9, the stress in the mid-slab at the web locations is

$$\sigma_{w_{t,b}} = \pm \frac{ql^2}{I} \cdot c_{t,b} \left[ \frac{1-n}{(kl)^2} (1 - e^{-kx}) + \frac{1}{2} \left( \frac{x}{l} \right)^2 - \frac{3}{8} \cdot \frac{x}{l} \right] \dots \dots \dots (19)$$

Therefore, the stresses are

$$\text{at the left support } (x = 0) \quad \sigma_{w_{t,b}} = 0 \dots \dots \dots (20)$$

This means that no shear lag can be assessed where this stress is zero. This is the deficiency of this method.

At midspan ( $x = l/2$ ) because  $e^{-kx} = e^{-10.511} = 2.724 \times 10^{-5} \approx 0$  and  $M_{l/2} = ql^2/16$  we have

$$\sigma_{w_{t,b}} = \frac{ql^2}{16} \cdot \frac{c_{w_{t,b}}}{I} \left[ 1 + \frac{16(n-1)}{(kl)^2} \right] \dots \dots \dots (21)$$

or, using the values from Eq. 5

$$\sigma_{w_{t,b}} = \frac{M}{I} c_{w_{t,b}} (1 + 0.074) \dots \dots \dots (22)$$

The width reduction factor in this case is

$$\beta = \frac{1}{1.074} = 0.931 \dots \dots \dots (23)$$

DIN 1075 (8) gives for a top interior slab a value of 0.920, a value that is slightly more conservative. The width reduction factor at the first interior support will be obtained from consideration of the second span.

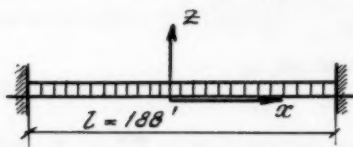


FIG. 5.—Second Span Treated as Fixed-end Beam

**Second Span.**—Again, in order to minimize the amount of numerical work, this span is taken as fixed at both ends (Fig. 5)

Proceeding in the same way as for the first span, the expression for the second derivative  $z''$  is obtained ( $x$  is now measured from the midspan).

$$z'' = - \frac{ql^2}{2EI} \left[ \left( \frac{x}{l} \right)^2 - \frac{1}{12} + \frac{n-1}{kl} \left( \frac{\cosh kx}{\sinh k \frac{l}{2}} - \frac{1}{k \frac{l}{2}} \right) \right] \dots \dots \dots (24)$$

The stresses are

At the left support  $\left(x = \frac{-l}{2}\right)$

the moment is  $M_{x=l/2} = -\frac{ql^2}{12}$

The stress is  $\sigma_{w_{t,b}} = \pm \frac{ql^2}{12} \frac{c_{w_{t,b}}}{I} (1 + 0.313) \dots \dots \dots (25)$

The width reduction factor now is  $\gamma = 0.762$ ; DIN 1075 (9) gives a value of  $0.740 < 0.762$

At midspan  $(x = 0)$

Moment is  $M_{x=0} = \frac{ql^2}{24}$

The stress is

$\sigma_{w_{t,b}} = \mp \frac{M}{I} \cdot c_{w_{t,b}} (1 + 0.036)$

The reduction factor is  $\beta = 0.966$ ; the DIN 1075 (8) value is 0.963, which is very close.

## CONCLUSIONS

1. The proposed approximate method developed for an idealized cross-section yields initial values about expected shear lag in a box girder design.

2. The minimum potential energy principle provides a suitable approach to evaluate the shear lag in box girders.

3. In case of uniform loading and using several simplifications, it appears that manual calculation is still practical, yielding width reduction factors close to those given by DIN 1075, although less conservative.

4. The same method can be applied for other types of loading, by integrating within several domains where  $M(x)$  is a continuous function. The calculations, now, however, are much longer due to added continuity conditions between the integration regions.

## ACKNOWLEDGMENT

The results of this paper were obtained as part of work done by the Bridge Section of the firm Beiswenger, Hoch, and Associates, Consulting Engineers, North Miami Beach, Florida. For permission to publish this paper the authors are indebted to Mr. F. A. Noroña.

## APPENDIX I.—SOLUTION

The potential energy of the load system,  $\Pi_l$ , is

$$\Pi_l = \int_0^l M(x) z''(x) dx \quad (26)$$

The strain energy of the sidewebs,  $\Pi_w$  is

$$\Pi_w = \frac{1}{2} \int_0^l EI_w (z'')^2 dx \quad (27)$$

in which the moment of inertia of both webs is

$$I_w = 2 \left[ \frac{t_w h^3}{12} + t_w h \left( \frac{h}{2} - c_t \right)^2 \right] \quad (28)$$

The strain energy of both slabs,  $\Pi_s$ , is

$$\begin{aligned} \Pi_s = & \frac{1}{2} \int_0^l \int_0^w 4t_t (E \epsilon_{x_t}^2 + G \gamma_t^2) dx dy \\ & + \frac{1}{2} \int_0^l \int_0^w 2t_b (E \epsilon_{x_b}^2 + G \gamma_b^2) dx dy \quad (29) \end{aligned}$$

in which linear strains and shearing strains are, respectively,

$$\begin{aligned} \epsilon_{x_t} = \frac{\partial u_t}{\partial x} = c_t \left[ z'' + \left( 1 - \frac{y^2}{w^2} \right) U'(x) \right]; \\ \epsilon_{x_b} = \frac{\partial u_b}{\partial x} = c_b \left[ z'' + \left( 1 - \frac{y^2}{w^2} \right) U'(x) \right] \quad (30) \end{aligned}$$

$$\gamma_t = \frac{\partial u_t}{\partial y} = -\frac{2c_t}{w} \cdot \frac{y}{w} U(x); \quad \gamma_b = \frac{\partial u_b}{\partial y} = -\frac{2c_b}{w} \cdot \frac{y}{w} U(x) \quad (31)$$

$E$  and  $G$  are the elastic and shear modulus, respectively.

By substituting Eqs. 30 and 31 into Eq. 29, and after integration with respect to  $y$ , the following expression is obtained.

$$\begin{aligned} \Pi_s = & \frac{1}{2} \int_0^l EI_s \left\{ [z''(x)]^2 + \frac{8}{15} [U'(x)]^2 + \frac{4}{3} z''(x) U'(x) \right. \\ & \left. + \frac{G}{E} \cdot \frac{4}{3w^2} [U(x)]^2 \right\} dx \quad (32) \end{aligned}$$

in which  $I_s = 4wt_t c_t^2 + 2wt_b c_b^2$ , moment of inertia of both slabs. By summing Eqs. 26, 27, and 32, the total potential energy  $\Pi$  is

$$\Pi = \int_0^l \left\{ \frac{EI}{2} [z''(x)]^2 + M(x) z''(x) \right\} dx + \int_0^l \frac{EI_s}{2} \left\{ \frac{8}{15} [U'(x)]^2 \right.$$



$$+ \frac{4}{3} z''(x) U'(x) + \frac{G}{E} \cdot \frac{4}{3w^2} [U(x)]^2 \Big\} dx \dots \dots \dots (33)$$

in which  $I = I_w + I_s$ , moment of inertia of the whole cross section.

If we denote by  $x_1$  and  $x_2$ , the ends of the interval of integration and apply the minimum condition

$$\delta \Pi = 0 \dots \dots \dots (34)$$

to Eq. 33, the first variation is

$$\begin{aligned} \delta \Pi = & \int_0^l \left\{ \left[ EI z''(x) + M(x) + \frac{2}{3} EI_s U'(x) \right] \delta z'' \right. \\ & + EI_s \left[ -\frac{8}{15} U''(x) - \frac{2}{3} z'''(x) + \frac{G}{E} \cdot \frac{4}{3w^2} U(x) \right] \delta U \Big\} dx \\ & + \left\{ EI_s \left[ \frac{8}{15} U'(x) + \frac{2}{3} z''(x) \right] \delta U \right\} \Big|_{x_2}^{x_1} = 0 \dots \dots \dots (35) \end{aligned}$$

To satisfy Eq. 34 for any arbitrary values of  $\delta z''$  and  $\delta U$  (positive or negative), both terms under the integral must vanish. This condition produces the following two differential equations

$$z''(x) + \frac{2}{3} \cdot \frac{I_s}{I} U'(x) + \frac{M(x)}{EI} = 0 \dots \dots \dots (36)$$

$$EI_s \left[ U''(x) - \frac{5}{2} \cdot \frac{G}{E} \cdot \frac{U(x)}{w^2} + \frac{5}{4} z'''(x) \right] = 0 \dots \dots \dots (37)$$

It is also easily seen that the last term in Eq. 35 must again vanish, thus:

$$EI_s \left[ U'(x) + \frac{5}{4} z''(x) \right] \delta U = 0 \dots \dots \dots (38)$$

This equation defines the boundary and continuity conditions of  $U(x)$  for adjacent segments of different stiffnesses. At a section where the slab is fixed to the supports  $\delta U = 0$  and

$$U(x) = 0 \dots \dots \dots (39)$$

$\delta U$  is arbitrary at a section where the slab is not fixed, therefore the bracketed value in Eq. 38, must vanish

$$EI_s \left[ U'(x) + \frac{5}{4} z''(x) \right] = 0 \dots \dots \dots (40)$$

The transition conditions require continuity of the function  $U(x)$  and of the expression between brackets in Eq. 40.

These conditions, as in Eqs. 39 and 40 and the continuity conditions, are in addition to those imposed on  $z(x)$  and  $M(x)$  by the simple technical bending theory.

By elimination of  $U(x)$  and its derivatives from Eqs. 36 and 37, a differential equation involving only the derivative of the vertical displacement of  $z$  as an unknown is obtained:

$$z''(x) + \frac{M(x)}{EI} - w^2 \frac{E}{G} \left\{ \frac{2}{5} \left[ z''(x) + \frac{M(x)}{EI} \right]'' - \frac{I_s}{3I} z^{iv} \right\} = 0 \dots \dots \dots (41)$$

The last bracketed term in Eq. 41 represents the shear lag effect. If shear deformability were zero, i.e.,  $G = \infty$ , this equation would reduce to the known equation of simple bending.

Eq. 41 has the same form as obtained by E. Reissner (8) in which he developed for a rectangular doubly symmetrical box section (Fig. 2). Only  $I_s$  and  $I$  have now different values. As suggested by Reissner, this equation can be written in a different form as:

$$z''(x) - \frac{2}{5} \frac{E}{G} \left( 1 - \frac{5}{6} \cdot \frac{I_s}{I} \right) w^2 z^{iv}(x) = -\frac{M(x)}{EI} + \frac{2}{5} \frac{E}{G} \cdot w^2 \frac{M''(x)}{EI} \dots \dots (42)$$

By introducing the following two parameters,  $k$  and  $n$ , where

$$k = \frac{1}{w} \sqrt{\frac{5n}{2} \cdot \frac{G}{E}} \dots \dots \dots (43)$$

$$\text{and } n = \frac{1}{1 - \frac{5}{6} \cdot \frac{I_s}{I}} \dots \dots \dots (44)$$

Eq. 42 can be written in its final form as

$$z''(x) - \frac{1}{k^2} \cdot z^{iv}(x) = -\frac{M(x)}{EI} + \frac{n}{k^2} \cdot \frac{M''(x)}{EI} \dots \dots \dots (45)$$

This is a linear non-homogeneous differential equation of the fourth order with constant coefficients. Using the same parameters  $n$  and  $k$ , the boundary conditions may be written as follows:

$$\text{for fixed end (slab attached to support)} \quad z'''(x) = -n \frac{M'(x)}{EI} \dots \dots \dots (46)$$

$$\text{for slabs not attached to supports} \quad z''(x) = -n \frac{M(x)}{EI} \dots \dots \dots (47)$$

## APPENDIX II.—REFERENCES

1. Abdel Sayed, G., "Effective Width of Steel-deck-plate in Bridges," *Journal of the Structural Division*, ASCE, Vol. 95, No. ST7, July, 1969, pp. 1459-1474.
2. Adekola, A. O., "Effective Widths of Composite Beams of Steel and Concrete," *The Structural Engineer*, Vol. 46, No. 9, Sept., 1968, pp. 285-289.
3. Bertsch, R., *Bauingenieur*, Vol. 2, 1921, p. 662.
4. Chapman, J. C., and Teraszkiewicz, J. S., "Research on Composite Construction at Imperial College," *Proc. of the British Construction Steelwork Assoc.*, Conference on Steel Bridges, London, 1968, p. 49.

5. Chwalla, E., "Die Formeln der "voll-mitragenden Breite" dünner Gurt-und R'open-platten," *Der Stahlbau*, Vol. 9, No. 10, May, 1936, pp. 73-78.
6. Eggenschwyler, A., *Eisenbau*, Vol. 8, 1917, p. 228.
7. Flint, A. R., and Horne, M. R., "Conclusions of research programme and summary of parametric studies," *Proc. of the International Conference on Steel Box Girder Bridges*, London, 1973, p. 173.
8. German Standards, Richtlinien für die Bemessung und Ausführung Massiver Brücken, August, 1973, substitute for DIN 1075, Dec., 1955.
9. Heins, C. P., "Effective Composite Beam Width at Ultimate Load," *Journal of the Structural Division*, ASCE, Vol. 102, No. ST11, November, 1976, pp. 2163-2180.
10. Homberg, H., "Beitrag zur Berechnung von Zweistegigen Plattenbalken-Brücken," *Der Bauingenieur*, Vol. 48, No. 12, 1973, pp. 444-450.
11. *Interim Specifications, Bridges*, American Association of State Highway and Transportation Officials, 1979, p. 136A, Section 1.6.25 (A).
12. v. Kármán, Th., "Beitrag zur Technischen Mechanik und Technischen Physik," *A. Föppl-Festschrift*, 1924, pp. 114-127.
13. Knittel, G., "The Analysis of Thin-Walled Box Girders of Constant Symmetrical Cross-Section (in German)," *Beton-und Stahlbetonbau*, Sept., 1964, p. 205.
14. Koepcke, W., and Denecke, G., "Die Mitwirkende Breite der Gurte Breiter Plattenbalken," *Veröffentlichungen des Deutschen Ausschusses für Stahlbeton*, No. 192, 1967.
15. Lee, J., "Effective Width of T-beams," *The Structural Engineer*, Vol. 40, No. 1, Jan., 1962, London, pp. 21-27.
16. Malcolm, D. J., and Redwood, R. G., "Shear Lag in Stiffened Box Girders," *Journal of the Structural Division*, ASCE, Vol. 96, No. ST7, Proc. Paper 7409, July, 1970, pp. 1403-1419.
17. Maisel, B. I., Rowe, R. E. and Swann, R. A., "Concrete Box-girder Bridges," *The Structural Engineer*, Vol. 51, No. 10, Oct. 1973, pp. 363-376.
18. Moffatt, K. R., and Dowling, P. J., "Shear Lag in Steel Box Girder Bridges," *The Structural Engineer*, Vol. 53, No. 10, 1975, pp. 439-448.
19. Reissner, E., "Analysis of Shear Lag in Box Beams by the Principle of Minimum Potential Energy," *Quarterly of Applied Mathematics*, Vol. IV, No. 3, Oct., 1946, pp. 268-278.
20. Reissner, E., "Beitrag zur Theorie der Plattenbalken," *Det Kongelige Norske Videnskabers Selskab*, Vol. VIII, No. 4, pp. 13-16.
21. Roik, K., "Effective Breadth and Shear Lag in Plate-girder Bridges with Elastic and Elastoplastic Material Behavior, Paper 7, pp. 169-182.
22. Steinle, A., "Praktische Berechnung eines Durch Verkehrslasten Unsymmetrisch Belasteten Kastenträgers an Beispiel der Henschbachtalbrücke," *Beton-und Stahlbetonbau*, No. 10, 1970, pp. 249-253.
23. Van Dalen, K., and Narasimham, S. V., "Shear Lag in Shallow Wide-flanged Box Girders," *Journal of the Structural Division*, ASCE, Vol. 102, No. ST10, Proc. Paper 12449, Oct., 1976, pp. 1969-1979.

### APPENDIX III.—NOTATION

*The following symbols are used in this paper:*

- $c_t, c_b$  = distance of neutral axis from top and bottom of cross sections, respectively;  
 $h$  = web depth;  
 $E, G$  = Young's and shear modulus, respectively;  
 $I, I_s, I_w$  = moment of inertia of whole section, of slabs and web, respectively;  
 $k, n$  = parameters;  
 $l$  = span length;  
 $M(x)$  = bending moments;

- $t_t, t_b, t_w$  = thickness of top and bottom slab, and web, respectively;  
 $x, y, z$  = coordinates;  
 $u(x, y), U(x)$  = spanwise displacement, measure of shear lag, respectively;  
 $\epsilon_{x_t}, \epsilon_{x_b}$  = linear strain in span direction of top and bottom slab, respectively;  
 $\beta, \gamma$  = reduction factors;  
 $\gamma_t, \gamma_b$  = shear strain of top and bottom slab, respectively;  
 $\sigma_{w_{b,t}}$  = stress in slab at the contact with web at bottom and top; and  
 $\Pi, \Pi_1, \Pi_s, \Pi_w$  = total potential energy, potential energy of the load system, of the slabs and webs, respectively.

## SEISMIC DAMAGE IN REINFORCED CONCRETE FRAMES

By Hooshang Banon,<sup>1</sup> John M. Biggs,<sup>2</sup> M. ASCE and H. Max Irvine<sup>3</sup>

### INTRODUCTION

Damage prediction for reinforced concrete (RC) frames is usually measured in terms of ductility demands for beams and columns. In order to develop a more rigorous model of member damage in RC frames, other damage parameters are introduced, and their effectiveness in prediction of damage is tested. Laboratory tests of RC members and subassemblages are used to check the accuracy of both mechanical models and damage parameters.

Reinforced concrete members, when subjected to cyclic inelastic deformations, exhibit both stiffness and strength degradation. Development and testing of mechanical models with satisfactorily reproduce the behavior of RC members under cyclic loads is an important step in the prediction of damage by calculation. Once the accuracy of the model is tested, damage indicators such as damage ratio, ductility, energy, and cumulative plastic rotation may be used in a model of damage. In the present work, attention is restricted to the mechanical model and the choice of damage parameters. A probabilistic model of failure for RC elements employing the results of the present study is developed elsewhere (2, and will be published elsewhere).

### MECHANICAL MODELS

When a reinforced concrete frame is subjected to severe earthquakes, some of the beams and columns are expected to undergo substantial inelastic actions. A mechanical model used to analyze RC frames should be able to reproduce inelastic cyclic deformations of the structure under inelastic cyclic loads. The choice of a mechanical model depends on factors such as expected accuracy of results and cost of the analysis. Since the goal of the present study is to

<sup>1</sup>Struct. Mechanics Associates, Newport Beach, California; formerly Grad. Research Asst., Dept. of Civ. Engrg., Massachusetts Institute of Technology, Cambridge, Mass. 08139.

<sup>2</sup>Prof., Dept. of Civ. Engrg., Rm 1-238, Massachusetts Institute of Technology, Cambridge, Mass. 08139.

<sup>3</sup>Edgerton Assoc. Prof., Dept. of Civ. Engrg., Rm 1-232, Massachusetts Institute of Technology, Cambridge, Mass. 08139.

Note.—Discussion open until February 1, 1982. To extend the closing date one month, a written request must be filed with the Manager of Technical and Professional Publications, ASCE. Manuscript was submitted for review for possible publication on October 8, 1981. This paper is part of the Journal of the Structural Division, Proceedings of the American Society of Civil Engineers, ©ASCE, Vol. 107, No. ST9, September, 1981. ISSN 0044-8001/81/0009-1713/\$01.00.

be able to predict damage via a set of calculated response parameters, special care has been taken in choosing a mechanical model. The following is a list of some of the more popular models which are available but were *not* employed in this study.

In a *dual component model*, each member is replaced by an elastic element and an elasto-plastic element in parallel (4). It is also possible to extend the dual component model into a *multicomponent model* by assuming several members in parallel. Since the end rotations of both components in a dual component model are the same, the element stiffness matrix may be easily formulated. One advantage of the dual component model is that the yield condition at one end of the member depends on end rotations at both ends. On the other hand, since the dual component model can reproduce only bilinear behavior and not any stiffness degradation, it is not suitable for analyzing reinforced concrete members (7).

In a *fiber model*, each section is divided into many layers or fibers (8,13), and the moment-curvature relationship for the section is determined from steel and concrete constitutive laws. Member stiffness may then be determined by integrating along the member length. Since setting up the stiffness matrix of each member requires many computations at each time step, the fiber model becomes very expensive. Finally, various *finite element* models have been used to analyze RC structures, but they are also uneconomical for inelastic dynamic analysis.

In this study, a *single component model* (6) is employed to analyze inelastic behavior of RC frames. In this model, each member is represented by an elastic beam element with inelastic springs (hinges) at its two ends [Fig. 1(a)]. These two inelastic springs represent inelastic flexural deformations within the length of a member, i.e., inelastic flexural deformations are lumped at the two ends. In order to find the characteristics of the two hinges, it is assumed that the member deforms in antisymmetric bending [Fig. 1(b)]. Since the point of contraflexure is in the middle, each half of the member may be viewed as a cantilever. By setting the tip displacements of the half-length cantilever and the model equal [Fig. 1(c)], stiffness characteristics of each hinge is found. In reality, plastic rotation at one end of the member depends on rotation at the other end. Therefore, if the antisymmetric bending condition changes, stiffness characteristics of the two hinges become dependent. The antisymmetric bending assumption is fairly accurate for girders if the effect of dead load is negligible, and it is also accurate for columns in low-rise buildings.

Flexural deformations of each hinge are assumed to follow the Takeda model (19). A modified version of the Takeda model (10) is employed in the present study. Fig. 2 depicts the moment-rotation hysteresis curve for the modified Takeda model. The basic modifications to the original Takeda model are as follows: (1) The hysteresis curve has a bilinear (instead of a trilinear envelope); and (2) stiffness degradation is built into the model. A complete description of the Takeda model and the present modifications may be found elsewhere (2,10,19).

There are two other sources of deformations, other than flexural deformations, in a reinforced concrete member subjected to high flexural, shear, and axial loads. These two sources are inelastic shear deformations and slippage of main longitudinal reinforcement. High shear loads in a reinforced concrete member

cause propagation of inclined cracks at the ends of the member. On the other hand, slippage of the main longitudinal reinforcement causes a crack opening at the joint interface; i.e., the member starts to rotate at the joint interface. The main effect of the aforementioned two inelastic deformations is a pinching of hysteresis loops which is often observed in laboratory experiments (18). If the effects of shear and slippage are minimized in the laboratory test of a specimen, the Takeda model can accurately reproduce the hysteretic behavior of the specimen. On the other hand, it is important to take shear and slippage deformations into account when they are present. In the present study, a further pair of inelastic springs is added at each end of the member for this purpose. The characteristics of these springs may be found by considering the mechanics of opening and closing of cracks due to shear and slippage deformations (2). Since the mechanism is the same for shear and slippage, both deformations are found to have the same effect on the hysteretic behavior of a member (15). The proposed hysteresis model for shear and slippage is shown in Fig.

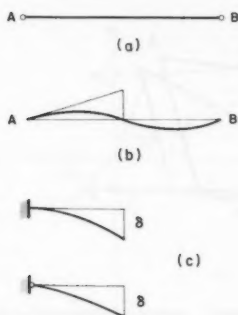


FIG. 1.—Single Component Model

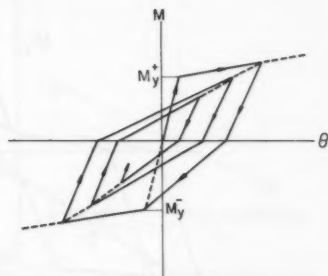


FIG. 2.—Takeda Model

3. This model is completely defined by a set of seven rules, which are shown in Fig. 3 and briefly summarized below.

1. Moment-rotation relationship is elastic up to the yield point.
2. Once the yield point is exceeded, loading proceeds on the second slope of the bilinear envelope.
3. Unloading from rule 2 is parallel to the elastic stiffness.
4. Once the unloading from 3 has ended, there is a marked reduction in stiffness; i.e., little load may be applied in the opposite direction until the crack is closed. In the present study, the stiffness of this part is assumed to be 50% of the second slope of the bilinear envelope [a result in conformity with experiments (3,17)].
- 5,6. If the direction of loading changes while closing the crack, loading or unloading will be parallel to the elastic stiffness.
7. Once the crack is closed, loading will be towards the previous maximum rotation point (Point A in Fig. 3). However, a strength-degrading feature has

also been built into the model. Thus, a new point of maximum is defined as follows:

$$\theta_{\max}^* = \frac{\theta_{\max}}{\alpha}$$

A value of  $\alpha = 0.8$  is suggested in this study.

8. If the direction of moment changes while unloading (rule 3), loading is also parallel to the elastic stiffness until the previous intermediate point (Point B in Fig. 3) is reached, and rule 7 applies thereafter.

It may be noted that the inelastic springs at the end of a member act independently; therefore there is no interaction between flexural, shear, and slippage deformations. In reality, both shear and flexural deformations in a

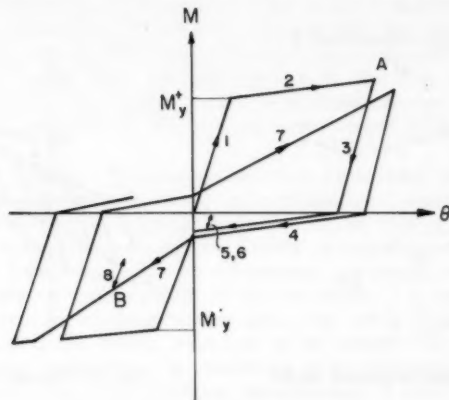


FIG. 3.—Moment-Rotation Hysteresis Model for Shear and Slippage

member are primarily concentrated near the joint; thus there is interaction between these two inelastic deformations. Slippage of the main longitudinal reinforcement would make the picture even more complicated. Although the simplifying assumption of independent springs is not quite correct, it is both convenient and (it is believed) sufficiently accurate. Other studies (9, 14), which have employed such a procedure, have also found the method to be satisfactory.

In practice, most RC beam sections are designed to have different amounts of steel at the top and bottom. This means that most sections have different stiffnesses and yield moments in the positive and negative directions (Fig. 4). A simple method of analyzing such sections is to use an average stiffness in both directions, which would result in an overestimate of stiffness in the positive directions and an underestimate in the negative direction. Instead, a modification to the single component model is made to take into account this effect. Fig. 5 shows a member which is acted upon by two moments of opposite sign.



The point of contraflexure divides the member into two cantilevers, where each cantilever has different stiffness properties. Let us assume again that, as with the single component model, all the inelastic rotation is lumped at the two end hinges, and the properties of these hinges which follow the Takeda model are set a priori. The difference is that the elastic element in this case is made up of two segments with different stiffness properties. The stiffness matrix of the elastic element is constructed by static condensation of degrees of freedom at their connecting point (Point C in Fig. 5). A more consistent model is the connected two-cantilever model suggested by Otani (14), where the Takeda model is applied to the load deflection of each cantilever. Unfortunately, the connected two-cantilever model results in a nonsymmetric element stiffness matrix. Although the present model fixes the point of contraflexure in the middle to find the hinge properties and then later takes the location of the point of contraflexure into consideration to construct the member stiffness, it has the advantage over the connected two-cantilever model of producing a symmetric stiffness matrix. It may also be noted that since the length of each segment (Fig. 5) changes

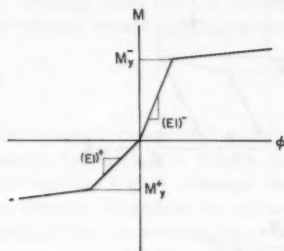


FIG. 4.—Moment-Curvature Relation for Nonsymmetric Section

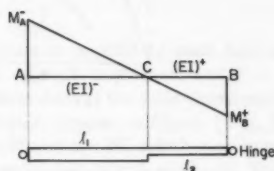


FIG. 5.—(a) Moment Distribution; and (b) Stiffness Properties for Nonsymmetric Section

at each time step, the element stiffness matrix has to be set up at each time step. Therefore, this element is not attractive for dynamic analysis of RC frames on a routine basis.

#### DAMAGE INDICATORS

Prediction of damage in reinforced concrete structures is usually made in terms of ductility demands for individual members. Although much effort has been spent on the computation of ductility in RC frames, there is little research available which correlates ductility demand with actual observed damage in laboratory experiments. One major problem is that ductility alone may not be a good indicator of damage in RC members. Low-cycle fatigue-type damage, which is caused by a number of inelastic cycles, is also important in failing a reinforced concrete member. Therefore, a combination of sudden high deformations (e.g., denoted by ductility demand) and cumulative fatigue damage may cause the member to fail. The present work concentrates on alternative methods

of prediction of damage in RC frames through the use of *damage indicators* which are computed from analytical models. It is felt that any mechanical model which is sufficiently accurate in reproducing the member behavior may be used for this purpose. The emphasis here is mainly on computing the damage indicators and their applicability in prediction of damage in RC members. A brief description of various damage indicators for reinforced concrete members is given in the following section.

The most widely used indicator of damage is *rotation ductility*, which is the ratio of maximum rotation at the end of a member to the yield rotation [Fig. 6(a)].

$$\mu_\theta = \frac{\theta_{\max}}{\theta_y} = 1 + \frac{\theta_o}{\theta_y} \quad \dots \dots \dots (1)$$

in which  $\theta$  in Fig. 6(a) represents total deformation at the end of a member.

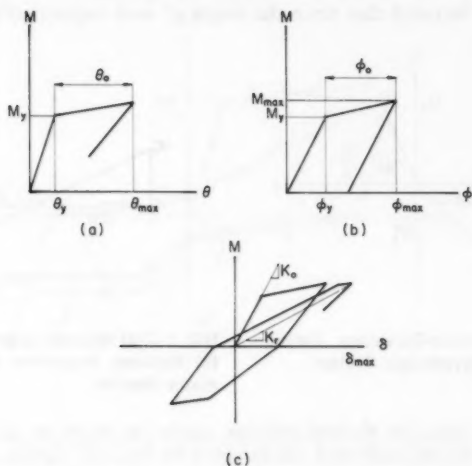


FIG. 6.—Definitions of: (a) Rotation Ductility; (b) Curvature Ductility; and (c) Damage Ratio

In a single component model, plastic rotations ( $\theta_o$ ) occur at the end hinges. In order to estimate  $\theta_y$ , it is assumed that the member yields in antisymmetric bending:

$$\mu_\theta = 1 + \frac{\theta_o}{\frac{M_y L}{6EI}} \quad \dots \dots \dots (2)$$

in which  $L$  = the member length; and  $EI$  = the member stiffness. The same definition of ductility may also be applied to the moment-curvature relationship of a section. *Curvature ductility* is simply [see Fig. 6(b)]:

$$\mu_\phi = \frac{\phi_{\max}}{\phi_y} = 1 + \frac{\phi_o}{\phi_y} \dots \dots \dots (3)$$

Assuming a bilinear moment-curvature relationship, curvature ductility may be written as [see Fig. 6(b)]:

$$\mu_\phi = 1 + \frac{M_{\max} - M_y}{pM_y} \dots \dots \dots (4)$$

in which  $p$  = the ratio of the second slope to initial elastic stiffness and  $M_{\max}$  = the maximum moment. This definition of ductility is intended to eliminate the need for assuming antisymmetric bending of an element. On the other hand, curvature ductility applies only to the most damaged section along a member, and it does not reflect the overall state of damage for a member. This definition is even less reliable for the single component model because it does not take into account any stiffness or strength degradation.

Another interesting idea for prediction of damage was first proposed by Sozen (11). Damage ratio (DR) is defined to be the ratio of initial tangent stiffness to a reduced secant stiffness at maximum displacement [Fig. 6(c)]:

$$DR = \frac{K_o}{K_r} \dots \dots \dots (5)$$

For a single component model, the definition is applied to each half of a member, in which  $\delta$  = the tip displacement of each cantilever; and  $P$  = the shear load (see Fig. 1). Although the DR is independent of the yield displacement, it is directly dependent on estimating the initial tangent stiffness ( $K_o$ ). It is usually difficult to compute the post cracking stiffness of a RC member accurately, because shear and slippage deformations greatly reduce the stiffness. This is examined in more detail later when comparing experimental and analytical results. A modified version of damage ratio is suggested in this study. Since flexural stiffness of a cracked member may be computed separately,  $K_o$  is replaced by this quantity. The Flexural Damage Ratio (FDR) is defined as

$$FDR = \frac{K_f}{K_r} \dots \dots \dots (6)$$

For a member which is in antisymmetric bending,  $K_f = 24EI/L^3$ . The damage ratio in general is expected to be a better predictor of damage than ductility, because the reduced secant stiffness also reflects strength degradation.

All the damage parameters introduced up to this point lack one important feature: they do not reflect the cumulative damage effect on failure of a member. It must be realized that low-cycle fatigue-type damage is possible under earthquake excitation. Two other damage parameters are introduced for this purpose. *Normalized cumulative rotation* (NCR) is defined as the ratio of the sum of all plastic rotations in inelastic springs, except for unloading parts, to yield rotation:

$$NCR = \frac{\Sigma|\theta_o|}{\theta_y} = \frac{\Sigma|\theta_o|}{\frac{M_y L}{6EI}} \dots \dots \dots (7)$$

*Normalized dissipated energy* at each time is defined as the ratio of energy that is dissipated in inelastic springs up to that time to the maximum elastic energy that would be stored in a member if it is subjected to antisymmetric bending:

$$E_n(t) = \frac{\int_0^t M(\tau)\theta(d\tau)}{\frac{M_y\theta_y}{2}} = \frac{\int_0^t M(\tau)\theta(d\tau)}{\frac{M_y^2 L}{12EI}} \dots \dots \dots (8)$$

in which  $t$  = time elapsed since the beginning of loading; and  $\theta(d,)$  is the rotation increment at one end of the member during the time interval from  $\tau - \tau + d\tau$ . For the present model, hinge moments are the same as the member end moment, and the summation of hinge rotations plus the rotation of the elastic element make up the member end rotation ( $\theta$ ).

From the foregoing review on damage parameters it may be noted that they belong to two general categories. Rotation ductility, curvature ductility, and damage ratio are indicators of damage which is inflicted upon a member because of large inelastic displacements. On the other hand, cumulative plastic rotation and dissipated energy reflect cumulative fatigue-type damage which is due to a significant number of inelastic cycles. Any method of predicting damage in RC members should include one parameter from each category. The choice of damage indicators would then depend on whether one is more informative than another, and on the accuracy of the computed damage indicators from analytical models.

**Choice of Experimental Specimens.**—In order to test the accuracy of mechanical models and determine the effectiveness of damage indicators in predicting damage, it was decided to analyze a sample of laboratory tests of RC frames. Although the results of many dynamic (shaking table) tests of specimens have become available in recent years, they do not directly provide the type of information which would lead to a model of damage in reinforced concrete members. Therefore, for the purpose of this study, it is found appropriate to limit our attention to available static test results in the literature. Changes in stiffness and strength properties of a specimen may be directly observed in a quasi-static cyclic load test. Once some kind of damage (or failure) criteria is established, it is also possible to identify the time of failure in a static cyclic load test. Another advantage is that loading in a static cyclic test may be closely monitored.

The sample in this study includes laboratory tests on 32 specimens from eight different sets of experiments (1,3,5,7,12,13,17,20). All of these tests are on large-scale members or subassemblages. Special care was taken in choosing the experiments to ensure that they represent in a reasonably realistic manner the behavior of RC buildings under earthquake excitations. It should be kept in mind that inertia and damping forces are absent in quasi-static tests, and the rate of loading is also different from a real seismic loading. Since there is no conclusive evidence on the effect of rate of loading on the failure of a member, the results are expected to apply to dynamic cases as well.

There are three main objectives in comparing analytical and experimental results of the sample of cyclic load experiments. First, it is determined whether the mechanical model, which is the single component model in this case, is

sufficiently accurate. Second, by monitoring the computed damage indicators from the analytical model, a relationship to damage may be established. At this point, it is also possible to compare the computed values of damage indicators with those measured in the test. Third, by choosing a criteria for the failure of a member, experimental failure points are determined. The failure point marks the end of the analysis, at which point all of the damage indicators at failure are computed.

**Definition of Damage.**—Many difficulties arise when one tries to define a quantitative measure of damage in buildings. There are schemes for quantifying post earthquake damage into different categories (21), but these schemes do not apply in this case. Instead, it is decided to define only the point of *excessive damage* or *failure* for each specimen. Therefore, the objective is to predict failure of each member (local damage) in a frame, given that it has undergone certain inelastic deformations.

Failure of a member in the present study is assumed to be an instantaneous phenomenon. This is also true of many laboratory tests of specimens that are considered in this study, i.e., the load-carrying capacity of some members starts to drop off very fast. In such instances, it is fairly easy to define the point of failure. In other cases, failure of the member is gradual, e.g., the member can go through a few more cycles of loading although the capacity of the member to sustain loads drops off with each additional cycle. For members with gradual failure, load-carrying capacity is used as the failure criteria. If there is more than 20% difference between analytical and experimental load at maximum displacement in a cycle, the member is assumed to have failed. It is assumed here that the analytical model can reproduce the behavior of a member until an event, such as buckling of main longitudinal reinforcement, causes failure of the member—at which point the model becomes ineffective. In practice, although the member may be able to carry some load beyond its theoretical failure point, it is best to assume that the member has failed.

Accumulation of damage in RC members may be modeled through the use of damage indicators. Values of damage indicators are monitored throughout the test for all the specimens considered in this study. The failure point for a member, as defined previously, is considered the terminal point of a test, and the objective is to predict the failure point via the knowledge of damage indicators. One may note that any other logical definition of failure could also be used for this purpose. However, it is felt that other definitions of failure will not change the final values of damage indicators appreciably.

**Comparison of Theory and Experiments.**—The sample of laboratory experiments which is gathered in the present study covers a wide variety of loading conditions on RC members. As mentioned before, the sample consists of 32 experiments from eight different sets of tests. Although the sample size is rather small, it is felt that general conclusions and recommendations would not be affected by including more data in the sample. On the other hand, for a model of damage in RC frames, a large sample size would result in a more accurate and reliable model. The following is a comparison of the experimental and analytical results for some individual cases and the sample as a whole.

Fig. 7 is a comparison of the hysteretic behavior of specimen 8 (A8) tested by Atalay and Penzien (1). These sets of tests were designed to study the behavior of reinforced concrete columns under high axial and flexural loads.

The test set-up for the experiment is also shown in Fig. 7. The tests specimen represents two columns of a high-rise building between their inflection points, which are assumed to be at their midheights. It is seen from Fig. 7 that the test set-up does not simulate double curvature in columns; however, this type of test set-up is used for simplicity. The test procedure consisted of putting an axial load on the specimen, and then applying predetermined cyclic displacements on the joint. All specimens in this set of tests had cross sections of 12 in.  $\times$  12 in. and a length of 11 ft, and for specimen 8 in Fig. 7 the axial load was 120 kips. Fig. 7(a) and 7(b) are the experimental and analytical

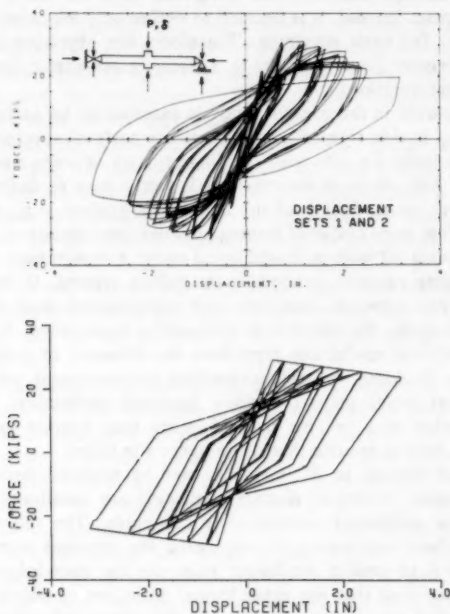


FIG. 7.—(a) Experimental; and (b) Analytical Load-Deflection Curves for Specimen A8 Tested by Atalay and Penzien

load-deflection curves for the specimen. The latter was computed using the model described previously. The secondary effect of axial load is clearly seen in these two figures, e.g., the load starts decreasing as the displacements increase. Hysteresis loops for this specimen are very stable up to the failure point. Failure for this specimen is a rather sudden phenomenon, so the analysis is also terminated at the experimental failure point.

There are two aspects of the inelastic cyclic behavior which are important in this type of test, namely, peak loads and the energy dissipation. A visual inspection of Fig. 7(a) and 7(b) reveals that the model is fairly accurate in predicting both loads and the dissipated energy for this experiment. Accurate

prediction of load also implies that the secant stiffness in DR and FDR is accurately computed. On the other hand, it is observed that the analytical yield displacement is much lower than the yield displacement observed in the experiment. In fact, the displacement ductility, which is the same as rotation ductility in this case, is measured to be 5.4 and 3.6 from the analytical model and the experiment respectively. On the other hand, since the experiment is carried out well beyond the yield displacement, overestimating the initial tangent stiffness of the member has little effect on the overall inelastic behavior of the specimen. It may also be noted that the analytical model is fairly accurate in this case, because shear and slippage deformations are not present in this set of experiments. In fact, the main longitudinal bars were welded to steel plates inside the joint to minimize the effect of slippage, and due to rather long span-to-depth ratio, shear effects are not important for these specimens. It is observed throughout this study that the single component model employing the Takeda model is accurate in predicting the inelastic behavior of RC members under flexure.

Analytical and experimental load-deflection curves for specimen 6 (S6) in the experiments by Scribner and Wight (17) are shown in Fig. 8. The test set-up

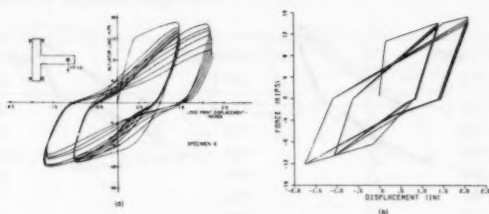


FIG. 8.—(a) Experimental; and (b) Analytical Load-Deflection Curves for Specimen S6 Tested by Scribner and Wight

for the specimen is also depicted on the same figure. The specimen represents an exterior joint, with two columns and a beam in between their inflection points. This specimen is a half-scale model of a joint in a tall building. After application of axial load to the columns, predetermined displacements were applied at the tip of the beam, and the necessary loads were measured. The loading scheme consisted of six cycles of displacement ductility six in the positive direction and ductility four in the negative direction. If the specimen survived these cycles, more cycles of higher ductilities were also applied. Since the inelastic action is intended to be confined to the beam, all columns were designed to stay elastic.

Pinching of hysteresis loops due to the effects of shear and slippage is clearly seen in Fig. 8. Although the computed yield displacement is much lower than the actual yield displacement, the overall match between the experiment and theory is very good, e.g., normalized dissipated energy is computed to be 441 up to the theoretical failure point, which compares well with 490 listed in the experiment. A gradual failure is observed for this specimen. Strength degradation during cycles of equal ductility may be attributed to the presence of shear and slippage deformations in this specimen. It may also be noted that, using

load-carrying capacity of the member as the failure criteria, the theoretical failure point is reached one-and-a-half cycles before the experiment is terminated. The definition of failure is expected to affect dissipated energy and normalized cumulative rotation at failure, but in most cases it has little effect on computed ductilities and damage ratios.

Fig. 9 shows the load-deflection curves for specimen 10 (S10) in the same set of experiments (18). The difference in the two specimens is only in their size and steel reinforcement; specimen 10 is a full-scale model. Pinching of hysteresis loops is also present for this specimen. On the other hand, a comparison of Figs. 9(a) and 9(b) reveals that the computed loads at peak displacements of each cycle are generally lower than the actual loads measured in the test. This has caused the analytical normalized dissipated energy (197) to be roughly 30% lower than the energy measured in the experiment (294). Specimen 10 exhibits a sudden drop in its load-carrying capacity beyond the seventh cycle of loading. The analytical failure point is defined to be at zero displacement before the last half cycle, i.e., for practical purposes the member may be assumed to have failed at this point.

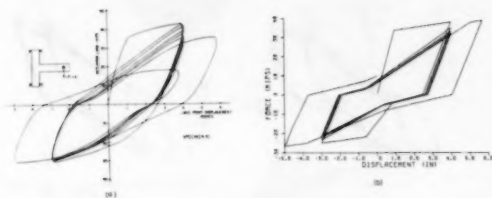


FIG. 9.—(a) Experimental; and (b) Analytical Load-Deflection Curves for Specimen S10 Tested by Scribner and Wight

Table 1 lists analytical and experimental dissipated energies for the ten specimens in the tests by Scribner and Wight which are included in this study. Specimens 4–8 are half-scale models, whereas specimens 9–12 are full-scale models; all represent an exterior joint in a tall building. Dissipated energies listed in Table 1 all represent values up to the theoretical failure points. Dissipated energies compare well for the first six specimens, but much lower dissipated energies are computed from the model for the last four specimens. The difference, as in the case of specimen 10, is due to underestimation of the yield load by the analytical model. Unfortunately, dissipated energy is rarely measured quasi-static cyclic load tests. For other specimens in the sample where energies were measured in experiments, analytical and experimental results compared well [e.g., see Banon (2)].

Based on the study of analytical and experimental hysteretic behavior of the sample of RC specimens, the following conclusions are reached:

1. The single component model is sufficiently accurate in predicting the behavior of RC members (see Figs. 7, 8, 9). There is especially good agreement between the model and experiments when the flexural mode of deformation



is dominant and shear and slippage deformations are minimized. This proves that the Takeda model can accurately reproduce deformations of RC members under cyclic loads.

2. Rotation ductility, which is a popular measure of member damage in RC frames, is generally computed to be higher than actual experimental ductilities. This is due to the fact that the elastic stiffness of a RC member is reduced by shear and slippage effects; therefore, the yield rotation is underestimated. It is also found that the overall inelastic behavior of RC members is insensitive to the initial elastic stiffness, i.e., hysteretic behavior and stiffness degradation beyond the yield level are little affected by the elastic stiffness of the member.

3. Curvature ductility in a single component model can be computed only by assuming a bilinear moment-curvature relationship (Eq. 4). On the other hand, using stiffness-degrading hinge characteristics is obviously in conflict with the above assumption. Therefore, employing the present analytical model, it is doubtful that curvature ductility has any meaning in prediction of damage in RC members.

TABLE 1.—Comparison of Experimental and Analytical Normalized Dissipated Energy ( $E_n$ ) for the Tests by Scribner-Wight (18)

Specimen (1)	Experimental (2)	Analytical (3)
S3	179	158
S4	381	325
S5	456	415
S6	490	441
S7	285	240
S8	260	245
S9	290	197
S10	294	197
S11	210	146
S12	215	140

4. Flexural damage ratio (FDR) may be a better substitute for ductility in predicting damage. Since there was good agreement between analytical and experimental loads at peak displacements of each cycle, flexural damage ratios computed for the sample are expected to be accurate. The only other source of uncertainty in FDR (Eq. 6) comes from flexural stiffness ( $K_f$ ), but flexural stiffness in a RC member may be accurately determined by considering the cracked member.

5. Dissipated energy ( $E_n$ ) and normalized cumulative rotation (NCR) reflect cumulative fatigue-type damage in RC members. For experiments where energies were listed, generally good agreement was found between analytical and experimental results.

Table 2 lists the five damage indicators, computed at failure from the analytical model, for all of the members in the sample. Unfortunately, all of the computed damage indicators show large variability which is in part due to intrinsic differences

in member resistances. If one of the computed damage indicators at failure, such as  $\mu_o$ , were stable, it would be very easy to predict the failure of RC

TABLE 2.—Damage Indicators for Specimens Tested in Laboratory

Specimen specification (1)	$\mu_o$ (2)	$\mu_o$ (3)	FDR (4)	$E_o$ (5)	NCR (6)
R1	8.2	11.4	6.8	116.	117.
R2	8.9	10.5	7.8	107.	113.
R3	10.3	17.1	8.5	199.	193.
R4	13.9	24.0	10.6	98.	70.
R5	14.2	12.1	11.0	220.	240.
R6	8.9	9.7	7.4	182.	187.
T1	10.4	21.8	9.0	169.	162.
T2	14.6	31.2	11.4	63.	36.
T3	11.3	15.0	8.5	249.	242.
A4	7.8	9.0	8.7	257.	282.
A7	5.4	4.2	7.3	180.	205.
A8	5.4	4.2	7.3	145.	168.
A11	3.6	2.4	5.1	60.	64.
A12	3.0	2.1	4.0	54.	60.
H7 <sup>c</sup>	6.5	13.3	5.6	24.	25.
H9	10.5	26.9	8.3	78.	84.
W33 <sup>d</sup>	12.9	23.4	10.0	269.	272.
W35I	16.8	35.4	11.7	457.	417.
VBC3	8.1	23.4	8.2	84.	96.
F1 <sup>e</sup>	8.0	3.7	7.2	64.	72.
F4	11.7	8.0	9.4	182.	162.
P43 <sup>f</sup>	14.4	21.9	11.0	227.	225.
S3 <sup>g</sup>	13.0	11.1	10.4	158.	142.
S4	16.8	12.9	13.1	325.	307.
S5	22.0	15.2	14.6	415.	356.
S5	18.8	13.4	14.1	441.	394.
S7	15.1	9.2	13.1	240.	249.
S8	15.6	10.2	12.2	245.	237.
S9	15.3	11.8	14.1	197.	245.
S10	16.1	20.0	14.4	197.	243.
S11	14.2	12.7	11.4	146.	157.
S12	13.9	17.0	11.3	140.	153.

<sup>a</sup>R1-T3 = Ma, et al. (12).

<sup>b</sup>A4-A12 = Atalay, Penzien (1).

<sup>c</sup>H7-H9 = Hanson, Conner (7).

<sup>d</sup>W33-VBC3 = Bertero, et al (3).

<sup>e</sup>F1-F4 = Fenwick, Irvine (5).

<sup>f</sup>P43 = Popov, et al. (16).

<sup>g</sup>S3-S12 = Scribner, Wight (17).

members. Consequently, failure of RC members has to be predicted via a probabilistic model. In order to construct a damage model for RC members,

one would like to use as few and as informative damage indicators as possible. As mentioned before, the set of damage indicators presented in this study represent two different types of damage in RC members. Ductility and damage ratios indicate a suddenly inflicted damage due to large deformations, whereas energy and cumulative rotation represent cumulative fatigue-type damage. A high degree of correlation (0.95) is found between rotation ductility ( $\mu_\theta$ ) and FDR for the sample. From the foregoing review, FDR seems to be superior to  $\mu_\theta$  because it also takes into account strength degradation in a member. Also, a high degree of correlation (0.98) is found between normalized dissipated energy ( $E_n$ ) and normalized cumulative rotation (NCR), which is to a large extent a direct result of the hysteretic behavior in the analytical model. Quite arbitrarily, it is decided to retain  $E_n$  for a model of damage.

Using  $E_n$  and FDR as damage state parameters, one may set up a probabilistic model of failure in RC members (2). Damage may be thought of as a cumulative process which causes deterioration of a RC member until conditions are reached for the failure to occur. The analytical model gives information on  $E_n$  and FDR as a function of time. One is interested in the probability of failure of a member at any time, given the knowledge of load history on the FDR- $E_n$  plane. The probability may be computed if one has a knowledge of the so-called "hazard" or "risk" function on the  $E_n$ -FDR plane. For a one-dimensional control parameter  $T$  (e.g.,  $E_n$  or FDR), with  $f(t)$  being the probability density function of  $T$  to failure and  $F(t) = \int_0^t f(\tau) d\tau$ , the hazard (risk) function,  $\lambda(t)$ , is defined as

$$\lambda(t) = \frac{f(t)}{1 - F(t)} = -\frac{F'(t)}{1 - F(t)} \quad \dots \dots \dots (9)$$

in which the prime denotes differentiation. Conversely

$$F(t) = 1 - \exp \left[ - \int_0^t \lambda(\tau) d\tau \right] \quad \dots \dots \dots (10)$$

Clearly,  $\lambda(\tau)d\tau$  is the probability of failure before  $\tau + d\tau$ , given survival at time  $\tau$ , and  $F(t)$  is the probability that failure occurs at or before  $t$ . The present case is more complicated, because the notion of the hazard function has to be extended to two dimensions. Such an approach has been used in Ref. 2. Results of the laboratory experiments are then used to estimate parameters of the probabilistic model. It should be noted that any probabilistic model of failure in RC members will incorporate both the uncertainty in member resistance and structural properties, and also modeling errors in calculation of damage parameters.

## CONCLUSIONS

A single component model, with modifications to take into account shear deformations and slippage of longitudinal reinforcement, has been used to analyze a set of quasi-static cyclic load tests. Rotation ductility, curvature ductility, flexural damage ratio, dissipated energy, and cumulative rotation are computed from the analytical model for each one of the specimens. It is found that the single component model is sufficiently accurate in reproducing the inelastic

cyclic behavior of RC members. The match between experimental and analytical results is especially good when flexural deformations are dominant. Based on accuracy of results and physical grounds, flexural damage ratio (FDR) and dissipated energy ( $E_n$ ) are chosen as damage state parameters for a probabilistic model of member resistance. The FDR and  $E_n$  represent damage due to large deformations and cumulative fatigue-type damage respectively. On this basis, it is believed that damage can be predicted from analytical results with some confidence.

#### ACKNOWLEDGMENT

This paper is based on part of the first writer's Sc.D. thesis done under the supervision of the other two. The support of the National Science Foundation under Grant ENV 77-14174 is gratefully acknowledged.

#### APPENDIX I.—REFERENCES

1. Atalay, M. B., and Penzien, J., "The Seismic Behavior of Critical Regions of Reinforced Concrete Components as Influenced by Moment, Shear, and Axial Force," Earthquake Engineering Research Council, University of California, Berkeley, Calif., Dec., 1975.
2. Banon, H., "Prediction of Seismic Damage in Reinforced Concrete Frames," Publication R80-16, Department of Civil Engineering, M.I.T., Cambridge, Mass., May, 1980.
3. Bertero, V. V., Popov, E. P., and Wang, T. T., "Hysteretic Behavior of Reinforced Concrete Flexural Members with Special Web Reinforcement," Earthquake Engineering Research Council, University of California, Berkeley, Calif., Aug., 1974.
4. Clough, R. W., Benuska, K. L., and Wilson, E. L., "Inelastic Earthquake Response of Tall Buildings," *Proceedings of the Third World Conference on Earthquake Engineering*, Vol. II, 1965.
5. Fenwick, R. C., and Irvine, H. M., "Reinforced Concrete Beam-Column Joints for Seismic Loading," *Bulletin of the New Zealand National Society for Earthquake Engineering*, 1977, Pt. I, 10, 3, 121-128; Pt. II, 10, 4, 174-185.
6. Giberson, M. F., "Two Nonlinear Beams with Definitions of Ductility," *Journal of the Structural Division*, ASCE, Vol. 95, No. ST2, Proc. Paper 6377, Feb., 1969, pp. 137-157.
7. Hanson, N. W., and Conner, H. W., "Tests of Reinforced Concrete Beam-Column Joints under Simulated Seismic Loading," *Research and Development Bulletin RDD12*, Portland Cement Association, Portland, Oreg., 1972.
8. Kent, D. C., and Park, R., "Flexural Members with Confined Concrete," *Journal of the Structural Division*, ASCE, Vol. 97, No. ST7, Proc. Paper 8243, July, 1971, pp. 1969-1990.
9. Küstü, C., and Bouwkamp, J. G., "Behavior of Reinforced Concrete Deep Beam-Column Subassemblages under Cyclic Loads," Earthquake Engineering Research Council, University of California, Berkeley, Calif., May, 1975.
10. Litton, R. W., "A Contribution to the Analysis of Concrete Structures under Cyclic Loading," thesis presented to the University of California, at Berkeley, Calif., 1975, in partial fulfillment of the requirements for the degree of Doctor of Philosophy.
11. Lybas, J. M., and Sozen, M. A., "Effect of Beam Strength and Stiffness on Dynamic Behavior of Reinforced Concrete Coupled Walls," Department of Civil Engineering, University of Illinois at Urbana-Champaign, Ill., July, 1977.
12. Ma, S. H., Bertero, V. V., and Popov, E. P., "Experimental and Analytical Studies on the Hysteretic Behavior of Reinforced Concrete Rectangular and T-Beams," Earthquake Engineering Research Council, University of California, Berkeley, Calif., May, 1976.
13. Mark, K. M. S., "Nonlinear Dynamic Response of Reinforced Concrete Frames," thesis presented to the Massachusetts Institute of Technology, at Cambridge, Mass., in 1976, in partial fulfillment of the requirements for the degree of Doctor of Philosophy.

14. Otani, S., and Sozen, M. A., "Behavior of Multistory Reinforced Concrete Frames During Earthquakes," Department of Civil Engineering, University of Illinois at Urbana-Champaign, Ill., Nov., 1972.
15. Otani, S., "Nonlinear Dynamic Analysis of 2-D Reinforced Concrete Building Structures," *Proceedings of the Third Canadian Conference on Earthquake Engineering*, Vol. 2, June, 1979.
16. Popov, E. P., Bertero, V. V., and Krawinkler, H., "Cyclic Behavior of Three R.C. Flexural Members with High Shear," Earthquake Engineering Research Council, University of California, Berkeley, Calif., Oct., 1972.
17. Scribner, C. F., and Wight, J. K., "Delaying Shear Strength Decay in Reinforced Concrete Flexural Members Under Large Load Reversals," Department of Civil Engineering, the University of Michigan, Ann Arbor, Mich., May, 1978.
18. Takayanagi, T., and Schnobrich, W. C., "Nonlinear Analysis of Coupled Wall Systems," *Earthquake Engineering and Structural Dynamics*, Jan., 1979.
19. Takeda, T., Sozen, M. A., and Nielson, N. N., "Reinforced Concrete Response to Simulated Earthquakes," *Journal of the Structural Division*, ASCE, Vol. 96, No. ST12, Proc. Paper 7759, Dec., 1970, pp. 2557-2573.
20. Viwathanatepa, S., Popov, E. P., and Bertero, V. V., "Seismic Behavior of Reinforced Concrete Interior Beam-Column Subassemblages," Earthquake Engineering Research Council, University of California, Berkeley, Calif., June, 1979.
21. Whitaman, R. V., Reed, J. W., and Hong, S. T., "Earthquake Damage Probability Matrices," *Proceedings of the 5th World Conference on Earthquake Engineering*, Paper No. 321, 1973.

## APPENDIX II.—NOTATION

*The following symbols are used in this paper:*

- $E_n$  = normalized energy;  
 $EI$  = cracked member stiffness;  
 $f(t)$  = probability density function at  $t$ ;  
 $F(t)$  = cumulative density function at  $t$ ;  
 $K_f$  = flexural stiffness;  
 $K_o$  = tangent stiffness;  
 $K_r$  = reduced secant stiffness;  
 $L$  = member length;  
 $M_{max}$  = maximum moment;  
 $M(\tau)$  = moment at time,  $\tau$ ;  
 $NCR$  = normalized cumulative rotation;  
 $p$  = ratio of second slope to initial slope;  
 $\alpha$  = parameter of shear or slippage hysteresis model;  
 $\lambda(t)$  = hazard function at  $t$ ;  
 $\mu_\phi$  = curvature ductility;  
 $\mu_\theta$  = rotation ductility;  
 $\phi_{max}$  = maximum curvature;  
 $\phi_o$  = plastic curvature;  
 $\phi_y$  = yield curvature;  
 $\theta(d\tau)$  = rotation increment during time interval  $\tau$  to  $\tau + d\tau$ ;  
 $\theta_y$  = yield rotation; and  
 $\theta_o$  = plastic rotation.

The first part of the paper is devoted to the study of the properties of the function  $f(x)$  defined by the equation  $f(x) = \int_0^x f(t) dt$ . It is shown that  $f(x)$  is a constant function, and the value of this constant is determined by the initial condition  $f(0) = 1$ . The second part of the paper is devoted to the study of the properties of the function  $g(x)$  defined by the equation  $g(x) = \int_0^x g(t) dt$ . It is shown that  $g(x)$  is a constant function, and the value of this constant is determined by the initial condition  $g(0) = 1$ .

The third part of the paper is devoted to the study of the properties of the function  $h(x)$  defined by the equation  $h(x) = \int_0^x h(t) dt$ . It is shown that  $h(x)$  is a constant function, and the value of this constant is determined by the initial condition  $h(0) = 1$ . The fourth part of the paper is devoted to the study of the properties of the function  $k(x)$  defined by the equation  $k(x) = \int_0^x k(t) dt$ . It is shown that  $k(x)$  is a constant function, and the value of this constant is determined by the initial condition  $k(0) = 1$ .

The fifth part of the paper is devoted to the study of the properties of the function  $l(x)$  defined by the equation  $l(x) = \int_0^x l(t) dt$ . It is shown that  $l(x)$  is a constant function, and the value of this constant is determined by the initial condition  $l(0) = 1$ . The sixth part of the paper is devoted to the study of the properties of the function  $m(x)$  defined by the equation  $m(x) = \int_0^x m(t) dt$ . It is shown that  $m(x)$  is a constant function, and the value of this constant is determined by the initial condition  $m(0) = 1$ .

The seventh part of the paper is devoted to the study of the properties of the function  $n(x)$  defined by the equation  $n(x) = \int_0^x n(t) dt$ . It is shown that  $n(x)$  is a constant function, and the value of this constant is determined by the initial condition  $n(0) = 1$ . The eighth part of the paper is devoted to the study of the properties of the function  $o(x)$  defined by the equation  $o(x) = \int_0^x o(t) dt$ . It is shown that  $o(x)$  is a constant function, and the value of this constant is determined by the initial condition  $o(0) = 1$ .

The ninth part of the paper is devoted to the study of the properties of the function  $p(x)$  defined by the equation  $p(x) = \int_0^x p(t) dt$ . It is shown that  $p(x)$  is a constant function, and the value of this constant is determined by the initial condition  $p(0) = 1$ .

## COLLAPSE BY PONDING OF AIR-SUPPORTED SPHERICAL CAPS

By David J. Malcolm,<sup>1</sup> A. M. ASCE and Peter G. Glockner,<sup>2</sup> M. ASCE

### INTRODUCTION

Air-supported enclosures have been in use only since World War II but they are now a common sight in most cities, where they cover, e.g., tennis courts, offices, exhibitions, and greenhouses. However, the building codes for these membrane structures are, in most western countries, not yet completed partly due to the lack of documented case histories, and partly due to the continuing research into the structural behavior of these forms.

One structural aspect that has been given only limited attention is the possibility of collapse through accumulation of rain, ice or snow. Failure in this mode has not been widely recognized (3)\* but it has been a contributing factor in several failures known to the writers and is a possibility of which designers should be aware.

Previous work in this field has been limited to part-cylindrical inflatables (1), this being the most common geometry and the one that lends itself to the simplest analysis. Experimental models have indicated the basic correctness of the predictions of the theory for cylindrical structures (2). The next most common inflated form is the part-sphere and is the simplest shape having double curvature. Interesting investigations into the axisymmetric deformation and wrinkling of such a shape have been presented (4) but the present paper is, to the writers' knowledge, the first to present theoretical and experimental results on the ponding stability of these domes.

The following section outlines the assumptions and theoretical development of the governing equations for both the uniform membrane and for a system of one-way acting cables. It also shows how the influence of an irregularity in the form of an axisymmetric bubble may be considered. The section entitled "Numerical Solution" gives a brief description of the solution algorithm and computer program together with some relevant numerical results. In the section

<sup>1</sup>Sr. Engr., DAF Indal Ltd., 3570 Hawkstone Road, Mississauga, Ontario, L5C 2V8.

<sup>2</sup>Prof. and Head, Dept. of Mechanical Engrg., The Univ. of Calgary, Calgary, Alberta, T2N 1N4.

Note.—Discussion open until February 1, 1982. To extend the closing date one month, a written request must be filed with the Manager of Technical and Professional Publications, ASCE. Manuscript was submitted for review for possible publication on October 8, 1980. This paper is part of the Journal of the Structural Division, Proceedings of the American Society of Civil Engineers, ©ASCE, Vol. 107, No. ST9, September, 1981. ISSN 0044-8001/81/0009-1731/\$01.00.

on experimental models, the experimental tests are described and results from these tests are compared with those from the theoretical model.

### THEORETICAL DEVELOPMENT

**Spherical Membrane.**—The development is based on the assumptions that the initial geometry is a perfect sphere of radius  $R$ , the material is inextensible and weightless, and that the deformations are axisymmetric. Fig. 1 is a cross section through the central axis showing the initial and deformed outlines. In the deformed state the central portions of the cap are deflected downwards and result in circumferential wrinkling due to the assumed inextensibility. This wrinkled zone, in which the membrane acts in the meridional direction only, and in which the radial tension per radian subtended must remain constant, extends as far as the "transition level." The location of this level depends on the parameters of the particular problem.

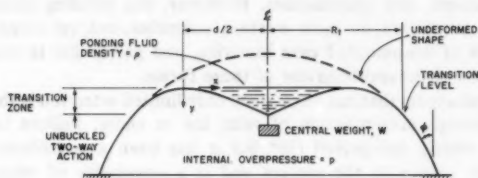


FIG. 1.—Cross Section through Spherical Cap with Central Pond

Noting that at the edge of the pond the membrane is horizontal, the overall vertical equilibrium of the cap within the transition zone is described by

$$\pi \left( r^2 - \frac{d^2}{4} \right) p = 2\pi T \cos \phi \quad \dots \dots \dots (1)$$

in which  $r$  = radius;  $d$  = diameter of the pond;  $p$  = internal over-pressure;  $T$  = radial tension per radian subtended; and  $\phi$  = angle of membrane with the vertical. For continuity of slope at the transition level,  $\cos \phi = R_t/R$ , and Eq. 1 may be used to solve for the transition level radius,  $R_t$ , as

$$R_t = \frac{T}{pR} + \sqrt{\left( \frac{T}{pR} \right)^2 + \frac{d^2}{4}} \quad \dots \dots \dots (2)$$

At any other point within the transition zone, defined by a radius  $r$ , Eq. 1 may be used to write the angle of inclination as

$$\cos \phi = \frac{p \left( r^2 - \frac{d^2}{4} \right)}{2T} \quad \dots \dots \dots (3)$$

Writing an element of membrane length as  $ds = dr/\sin \phi$ , Eq. 3 may be used to describe the total length of membrane in the transition zone as



$$S_2 = \int_{r=d/2}^{R_1} \left\{ 1 - \left[ \frac{p \left( r^2 - \frac{d^2}{4} \right)}{2T} \right]^2 \right\}^{-1/2} dr \dots \dots \dots (4)$$

The differential equation of equilibrium normal to the membrane within the ponding region is

$$T \frac{d\phi}{ds} = (p - \rho y) \left( \frac{d}{2} - x \right) \dots \dots \dots (5)$$

in which  $\rho$  = density of ponding medium; and  $x$  and  $y$  = coordinates originating at the edge of the pond (see Fig. 1). This equation may be written in terms of derivatives of  $y$  as

$$\frac{d^2 y}{dx^2} = \left[ 1 + \left( \frac{dy}{dx} \right)^2 \right]^{3/2} (p - \rho y) \frac{\left( \frac{d}{2} - x \right)}{T} \dots \dots \dots (6)$$

which may be numerically integrated to enable the (half) length of membrane beneath the pond to be obtained from

$$S_1 = \int_0^{d/2} \sqrt{1 + \left( \frac{dy}{dx} \right)^2} dx \dots \dots \dots (7)$$

Due to the assumed inextensibility the total meridional length is unchanged and

$$S_1 + S_2 = R \sin^{-1} \frac{R_1}{R} \dots \dots \dots (8)$$

In addition there is an equilibrium condition to be satisfied at the center of the cap where a concentrated vertical load,  $W$ , exists in equilibrium with the radial tension,  $T$ , per radian. At this point therefore

$$W = 2\pi T \frac{dy}{dx} \left[ 1 + \left( \frac{dy}{dx} \right)^2 \right]^{-1/2} \dots \dots \dots (9)$$

**Irregularities in Sphere.**—Only axisymmetric irregularities can be admitted if the surface is still to be considered as a shell of revolution about the central axis; however, such irregularities are often encountered when fabrication is designed as axisymmetric.

In this development the irregularity is regarded as a part spherical cap of radius,  $R'$ , which is less than the radius,  $R$ , of the remaining cap and has a span,  $2l'$ , at its junction with the remaining cap (see Fig. 10). When a central vertical load is first applied, the deformation is that defined by a cap of radius  $R'$  but as the deformation and pond diameter increase to engulf the smaller cap the problem reverts to the original one with the single exception of the (inextensible) length between the transition level and the centre now being slightly longer. Eq. 8 must now be adjusted to read

$$S_1 + S_2 = R \left( \sin^{-1} \frac{r}{R} - \sin^{-1} \frac{l'}{R} \right) + R' \sin^{-1} \frac{l'}{R} \dots \dots \dots (10)$$

Alternatively the total length ( $S_1 + S_2$ ) may be increased by a chosen percentage to correspond to the possibility of a series of axisymmetric irregularities.

**One-Way Action.**—If the membrane is made up of a number of meridional cables between which the membrane spans, then a description of the ponding deformation of such a structure follows very similar steps to that described above. However, there is now no transition between one-way, meridional, and

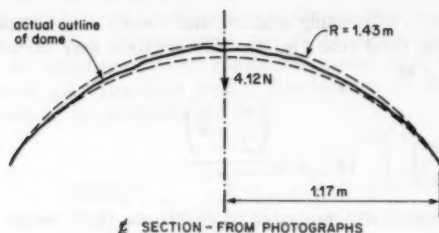


FIG. 2.—Outline of 1.43 m Radius Dome

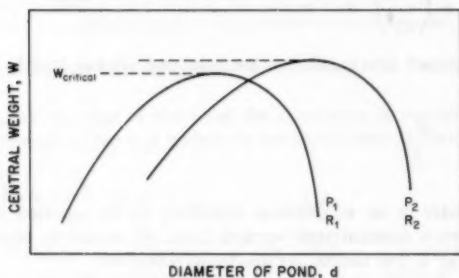


FIG. 3.—Typical Results of Central Weight Versus Pond Diameter

two-way action of the membrane, and the unknown,  $R_1$ , may be replaced by the known (half) span,  $l$ , of the spherical cap. Eq. 4 therefore becomes

$$S_2 = \int_{d/2}^l \left\{ 1 - \left[ \frac{P \left( r^2 - \frac{d^2}{4} \right)}{2T} \right]^2 \right\}^{-1/2} dr \dots \dots \dots (11)$$

while Eqs. 5–9 remain unaltered.

#### NUMERICAL SOLUTION

It is required to determine the maximum value of the central weight,  $W$ ,

that can be supported under given values of  $R$ ,  $\rho$ , and  $p$ . (It is assumed that the collapse is slow and that the internal overpressure will remain constant.)

To use Eq. 9 to calculate  $W$  the value of the meridional tension,  $T$ , must be known. For a chosen value of pond diameter,  $d$ ,  $T$  may be obtained by an iterative scheme (such as Newton-Raphson) which attempts to satisfy the condition of constant meridional length represented by Eq. 8 or modified as in Eq. 10 to account for irregularities.

The membrane length within the pond,  $S_1$ , is obtained by a numerical integration scheme after the values of  $dy/dx$  have been determined by solution of the differential equation, Eq. 6, using a Runge-Kutta fourth order algorithm. The length of the membrane within the transition zone was obtained by numerical integration (using a Romberg integration algorithm) of Eq. 4 and in the case of the one-way acting membrane the limit of integration was extended to include the entire cap.

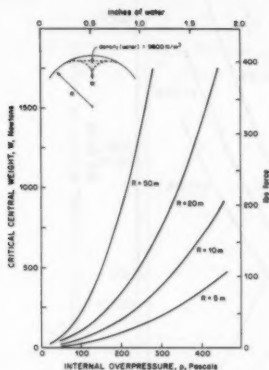


FIG. 4.—Effect of Pressure and Radius on Critical Central Weight

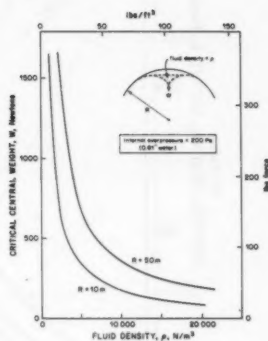


FIG. 5.—Effect of Fluid Density on Critical Central Weight

The typical form of the numerical results obtained is shown in Fig. 3, which demonstrates that a limiting value of the central weight does exist and that if the pond diameter is increased further then the central weight must be decreased.

Fig. 4 shows the effect of the internal pressure and radius (with fluid density that of water) on the critical central weights, and indicates the greater susceptibility (in theory) of structures with small radii of curvature. Fig. 5 plots the influence of fluid density and radius on the critical central weight when the internal overpressure is kept constant at 200 Pa (0.81 in. of water). It is not surprising to learn that fluids with higher densities pose the more serious hazard.

The influence of irregularities in the initially spherical dome is demonstrated in Fig. 6. The extent of the axisymmetric irregularities is not given in the form of radius and span of a central bubble but instead is described as a percentage increase (over the perfect sphere) in the total membrane length within the ponding and transition zones. This would correspond to a series of axisymmetric ripples in the initial membrane. Fig. 6 shows that an increase in the meridional length

of as little as 0.1% can cause an appreciable decrease in the critical central weight. The structure may therefore be described as imperfection sensitive in this mode of failure.

Fig. 7 gives results for the dome having one-way meridional action only and shows the influence of pressure and span on the critical central weight. It is important to note that such a structure is not initially a sphere but is flattened at the apex and, strictly, should not be included under the title of this report. However, it is relevant to observe the possible effect of imposing a one-way

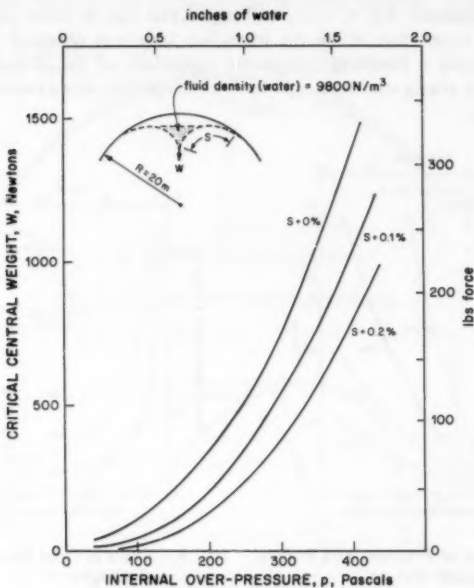


FIG. 6.—Effect of Irregularities on Critical Central Weight

system of cables onto a spherical cap and to realize that the meridional tensions are now functions of the span as well as initial radius.

#### EXPERIMENTAL MODELS

**Fabrication.**—Tests were carried out on two air-supported spherical caps, both made from axisymmetric segments of a polyester fibre reinforced PVC membrane (approx  $6.8 \text{ N/m}^2$ , or  $0.14 \text{ lb/ft}^2$ ). The first was already available, having been initially used for other purposes and had a radius of 1.43 m (4.69 ft) with a total span of 2.34 m (7.68 ft); the second model was fabricated as a complete hemisphere with a radius of 0.80 m (2.62 ft).

The first model was made from 36 segments whereas the second dome comprised 12 only. The smaller number was considered to approximate a sphere accurately enough and to offer less opportunity for error in fabrication. A template for the segments for the second model was made from hardboard and a 1/2-in. (12-mm) overlap was allowed for bonding. This bonding was achieved using prior treatment of surfaces with a solvent containing equal volumes of isopropyl alcohol and tolenol, followed by A4924 adhesive and clamping for a minimum of 20 h. A specially made mold was used to carry out this clamping [see Fig. 8(a)].

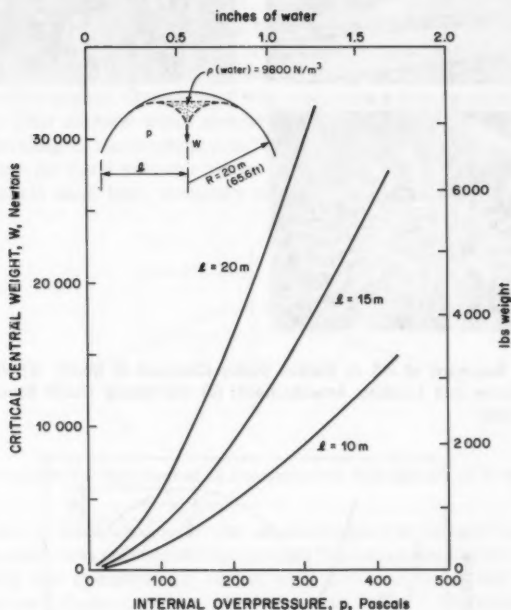


FIG. 7.—Effect of Pressure and Span on Critical Central Weight—One-Way Action Only

Both models included an air-tight floor and were secured around their perimeter to a 3/4 inch plywood base. The central load was applied through a 1/4 in. diameter steel plunger (weighing 4.12 N, 0.93 lbs), which was contained by a guide located in the center of a steel member spanning above the dome. The plunger rod supported a platform at its upper end to which additional weights could be added and a pointer was attached so that the central deflection could be read off a scale connected to the cross beam. Some of these details are visible in Fig. 8(b).

Both short and long-term tensile loading tests were carried out on material samples as well as on test joints.

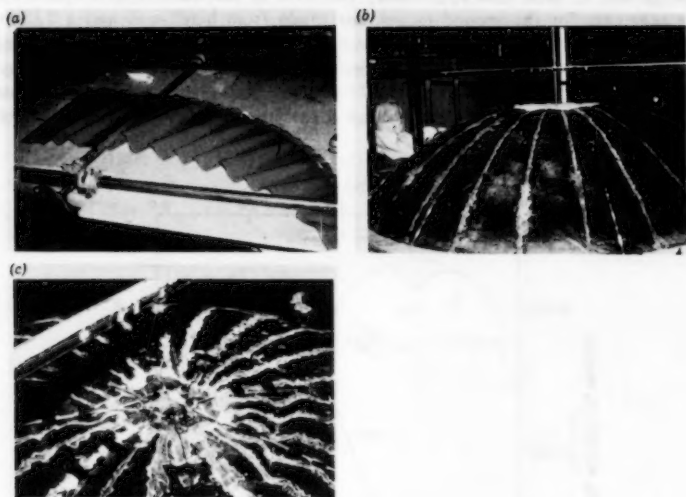


FIG. 8.—(a) Segment of 0.8 m Radius Dome Clamped in Mold; (b) View of 1.43 m Radius Dome and Loading Arrangement; (c) Meridional Cable System on 1.43 m Radius Dome

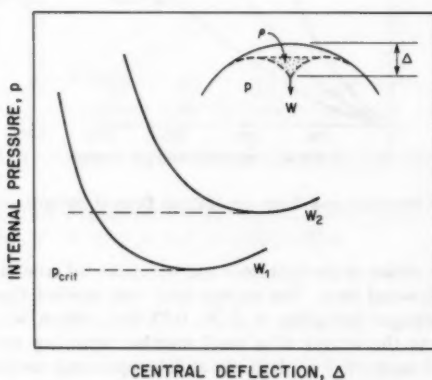


FIG. 9.—Typical Test Results of Pressure Versus Central Deflection

**Cable System.**—In order to simulate one-way meridional action, a set of eight steel cables, joined at the apex by a 80-mm (3.1-in.) diam ring, was placed over the first (1.43 m radius) dome. Each cable was secured to the plywood base and could be tightened by means of a series of turn-buckles. In the region of the apex the cables were loosely connected to the membrane by a number of bonded strips to ensure that the membrane and cable system deflected together. Details of the cable system are shown in Fig. 8(c).

**Testing Procedure.**—The domes were inflated by means of an electrically driven portable compressor and the overpressure was measured by a manometer accurate to 0.01 in. of water.

Although the most common ponding medium available to full-size structures is water, it was not possible to contain such a fluid without considerable spillage, due in part to the irregular furrows that the deformation caused in the membrane. Therefore a fine quality, Ottawa sand was used, with a density of  $14,300 \text{ N/m}^3$  ( $91 \text{ lb/ft}^3$ ). This allowed exact measurement of the ponding medium to be made and levelling of the medium could be carried out at lesiure.

To simulate the pond diameter versus central weight relationships shown in Fig. 3, it would have been necessary to maintain a constant pressure. Since

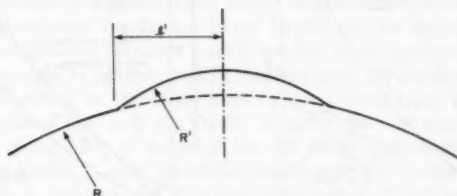


FIG. 10.—Irregularity Represented as Axisymmetric Part-Sphere of Radius  $R' < R$

this could not be done accurately, the central weight was instead kept constant while the pressure was reduced and the ponding fluid maintained at the appropriate level. During this operation the central deflection was noted and a graph of pressure versus deflection was obtained as depicted in Fig. 9. The critical pressure for each value of the central weight was obtained by noting the minimum pressure value attained.

The main difficulties encountered during the testing were: (1) Due to imperfections in the shape of the domes the pond formed was not circular; (2) imperfections in the membrane shape resulted in difficulty in judging the correct level of ponding medium; and (3) small air leaks in the first (1.43 m radius) dome limited the pressures under which that dome could be tested. Nevertheless all results obtained were reproducible. At values of the central weight lower than the self-weight of the plunger (4.12 N), small dead weights were placed at the apex of the dome.

The initial shape of each dome was examined photographically to obtain an estimate of the irregularities in the spherical shape. Fig. 10 shows a tracing of the outline of the first (1.43 m radius) dome and comparison with a circular outline. It is difficult, however, to quantify the extent of irregularities.

Results from the testing of the 1.43 m radius dome are shown in Fig. 11 and results from the 0.8 m radius dome are given in Fig. 12. Both are compared to theoretical predictions for exact spheres and for spheres with a 2% increase in meridional length in the displaced zones. Fig. (11) also shows theoretical and experimental results for the one-way action on a sphere of initial radius 1.43 m. The eight radial cables placed on this dome were tightened by means of turn-buckles until further tightening made no difference to the experimental results. (These cables are visible in Fig. 8(b) and (c).) However, as may be noted from Fig. 11, the presence of these cables made little difference to the experimental results.

A system of meridional cables was also imposed on the second, 0.8 m, dome. This time the strips which loosely secured the cables to the membrane were omitted and the result was that the weight of the ponding medium depressed

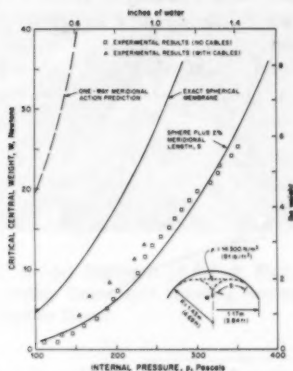


FIG. 11.—Experimental Results from 1.43 m Radius Dome

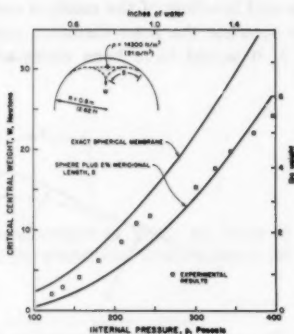


FIG. 12.—Experimental Results from 0.80 m Radius Dome

the membrane, separating it from the cables at the center, and causing very early collapse.

## CONCLUSIONS

The experimental results differ considerably from the theoretically predicted values for perfect spheres and suggest that failure may occur at values of central load far less than expected. The only satisfactory way of explaining this apparent discrepancy is to suppose that the sphere is not perfect since, indeed, the predictions are extremely sensitive to small increases in the meridional length available to form the pond. This small increase in length may be interpreted as an equivalent decrease in radius, which may be shown by calculation to be appreciable.

No adjustment has been made for the self-weight of the membrane which was measured as  $8 \text{ N/m}^2$ . However, near the apex where the membrane overlapped considerably, the self-weight may have averaged about  $14 \text{ N/m}^2$ . The experimental results should, therefore, especially at lower pressures and



smaller pond sizes, be corrected accordingly. This has the effect of producing somewhat better agreement with predicted values.

The membranes were assumed inextensible and material tests carried out supported this assumption within the range of membrane loads involved in these experiments. However, it is expected that a theory which includes the elastic deformation of the membrane will require higher central loads to cause failure at a given pressure.

The experimental results obtained using a cable system on the 1.43 m dome give critical weights far lower than expected. The reasons for this are firstly that the wide spacing of cables (only eight were used) did not prevent considerable circumferential stresses from remaining; secondly, the flattening of the surface in the region of the apex, caused by the one-way action of the cables, also produced considerable wrinkling of the membrane and these wrinkles collected the ponding sand and hence increased the deflection due to ponding. Indeed this wrinkling also occurred to some extent on the domes without cables and no doubt contributed in the same way to the increased displacement and premature collapse in those experiments. The experience with the cable system on the 0.8 m dome, in which the membrane was free to separate inwards away from the cables, suggest that this is the most dangerous situation of all despite the theoretical prediction of added stability due to increased meridional tensions.

Indeed the theoretical results are based largely on the meridional tension that can be developed and therefore predict that low profile pneumatic structures will have greater stability against ponding than will more curved shapes. However the theory also points to the importance of the concentrated central weight in initiating ponding and it is the flatter surfaces that are less able to shed external loads in the form of lumps of ice and snow. Unfortunately this type of concentrated loading, unlike an internal load applied to a cable intersection, e.g., is difficult to estimate and it is only observation of full scale structures in poor weather and under low pressure that will indicate the magnitude of these external point loads.

Although the lack of full scale experiments and the uncertainties in explaining the discrepancy between theoretical and experimental models prevent any firm design rules from being formulated, the following recommendations are made:

1. It is possible that the danger of collapse by ponding is even greater than theory predicts for surfaces of double curvature.
2. These structures are extremely sensitive to surface irregularities near the apex.
3. Further model tests should be made in which exact control or measurement of the surface geometry is included.
4. Observations should be made of full scale inflatables (of either single or double curvature) to determine the likely accumulation of snow and ice which could initiate ponding collapse.
5. The exact interaction between cables and membrane under ponding conditions should be investigated.

#### ACKNOWLEDGMENTS

The financial assistance from the Natural Science and Engineering Research

Council of Canada in the form of Operating Grant Nos. A-4174 and A-2736 and Strategic Grant No. G-0106, is gratefully acknowledged as is also the support from the Department of Computer Services at The University of Calgary. Special thanks are owed to L. Druhall for carrying out the laboratory experiments and to the technical support staff in the Department of Mechanical Engineering.

#### APPENDIX I.—REFERENCES

1. Malcolm, D. J., and Glockner, P. G., "Collapse by Ponding of Air-Supported Membranes," *Proceedings*, ASCE, Vol. 104, No. ST9, Proc. Paper 14002, Sept., 1978, pp. 1525-1532.
2. Malcolm, D. J., "Ponding Instability of Air-Supported Cylinders—Some Experimental Results," *Report No. 137*, Department of Mechanical Engineering, University of Calgary, Calgary, Canada, Dec., 1978.
3. Srivastava, N. K., Handa, V. K., and Critchley, S., "Failures of Air-Supported Structures," presented at the June, 1977, CIB/IASS International Symposium on Air-Supported Structures, held at Venice, Austria.
4. Yoko, Y., Matsunaga, H., and Yokoyama, Y., "On the Behaviour of Wrinkled Regions of Pneumatic Membranes in the Form of a Surface of Revolution Under Symmetric Loading," *Proceedings IASS Pacific Symposium (Pt. II), Tension Structures and Space Frames*, 1971, pp. 449-460.

#### APPENDIX II.—NOTATION

*The following symbols are used in this paper:*

- $d$  = diameter of ponding medium;
- $l$  = span of part-sphere;
- $p$  = internal over-pressure within inflatable;
- $r$  = radial distance from central axis of symmetry;
- $R$  = initial radius of sphere;
- $R_t$  = radial distance to transition level;
- $s$  = meridional distance along deformed membrane;
- $T$  = meridional tension per radian subtended;
- $W$  = central point weight;
- $x$  = horizontal coordinate from edge of pond;
- $y$  = vertical coordinate from edge of pond;
- $\phi$  = angle between meridian and vertical; and
- $\rho$  = density of ponding medium.

## OPTIMIZATION PROCEDURE FOR PULSE-SIMULATED RESPONSE<sup>a</sup>

By Sami F. Masri<sup>1</sup> and Frederick B. Safford<sup>2</sup>

### INTRODUCTION

The capability for simulating the response of structures, in-place and as-built, to transient dynamic loadings (such as earthquakes and blast loads), is useful for testing structural adequacy, for improving mathematical models, and for investigating the response of equipment in a structure (9). In addition to various types of vibration generators that are appropriate for certain classes of structural systems, large testing facilities (which have limited availability) and ground-explosion approaches (which are economically and practically limited) can be used for dynamic tests on equipment and structural systems (3,10).

The concept of using pulse techniques to simulate dynamic environments acting on structural systems has been investigated both analytically and experimentally. Housner demonstrated the feasibility of using a sequence of discrete pulses with random amplitude to represent the effects of earthquakes on dynamic systems (8). Scruton and Harding used a crude explosive charge to excite a tall chimney in order to determine its damping characteristics (20).

A simple mechanical pulse-generating device of fairly recent development is capable of producing short duration forces of large magnitudes over a wide frequency range that can be controlled to satisfy multimode system response (16). Such force pulse generators have been successfully used to simulate the in-place motions of up to 500 Hz in equipment weighing up to 200,000 lb and to measure system impedance functions (17,22).

The procedure for developing a suitable pulse train to simulate the effects of arbitrary dynamic environments on a structure is shown in Fig. 1. A recent study demonstrated the ability of force pulse excitation to simulate structural

<sup>a</sup>Presented at the October 27-31, 1980, ASCE Annual Convention, held at Hollywood, Fla.

<sup>1</sup>Prof., Civ. Engrg. Dept., Univ. of Southern California, Los Angeles, Calif. 90007.

<sup>2</sup>Assoc., Agbabian Associates, 250 N. Nash Street, El Segundo, Calif. 90245.

Note.—Discussion open until February 1, 1982. To extend the closing date one month, a written request must be filed with the Manager of Technical and Professional Publications, ASCE. Manuscript was submitted for review for possible publication on November 26, 1980. This paper is part of the Journal of the Structural Division, Proceedings of the American Society of Civil Engineers, ©ASCE, Vol. 107, No. ST9, September, 1981. ISSN 0044-8001/81/0009-1743/\$01.00.

vibrations produced by continuous forcing functions such as those occurring during earthquakes (11). During the course of this study, an optimization program was developed to obtain the pulse parameters that yielded the best possible fit to the criteria response data.

The computationally efficient optimization scheme of Ref. 11 has been shown to yield good results when applied to a variety of multidegree-of-freedom (MDOF) systems. However, this computational efficiency was achieved at the expense of the pulse characteristics: all of the pulse trains at different locations within the structure were assumed to be scalar multiples of a nominal pulse train. This constraint restricted the individual pulses within trains at different locations from selecting the optimum pulse initiation time as well as pulse duration for each individual location.

While the limitations previously mentioned may not be very restrictive for low-order systems, their effects become more pronounced for high-order dynamic systems with large spatial distribution (e.g., tall multistory buildings). In addition, as the size of the structure to be tested increases, the energy requirements become more demanding. The lessening of the constraints on the pulse trains

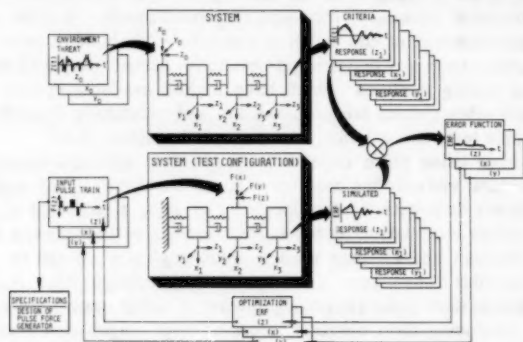


FIG. 1.—Optimum Response Simulation of Multidegree Systems by Pulse Excitation

will permit more efficient utilization of the energy content of pulse excitation, thereby leading to a more optimum selection of pulse train parameters.

The present study is concerned with the development of an efficient optimization algorithm for selecting the characteristics (initiation time, amplitude, duration) of the pulse trains acting on a distributed system whose structural dynamic response to some arbitrary continuous criterion excitation is to be simulated by the pulse trains. The structure does not necessarily have to be linear, and the pulse trains may be spatially distributed in the structure.

The following section presents the optimization algorithm. The validity of this procedure is demonstrated in the section headed "Applications," by applying it to two systems: (1) A hypothetical 25 DOF system that is representative of typical modern tall buildings; and (2) an actual three-story frame structure that has been subjected to exhaustive analytical and experimental studies at the University of California, Berkeley (UCB).

## OPTIMIZATION ALGORITHM

**Statement of Problem.**—Consider a linear MDOF system (continuous or with lumped parameters) subject to several pulse trains applied at locations  $j = 1, 2, \dots$ , NFRLOC. Assume that the response of the system,  $X_i(t)$ , at locations,  $i = 1, 2, \dots$ , NRESP is desired (see Fig. 2). Let the impulsive response at location  $i$  due to an impulse at location  $j$ , be denoted by  $h_i^{(j)}(t)$ .

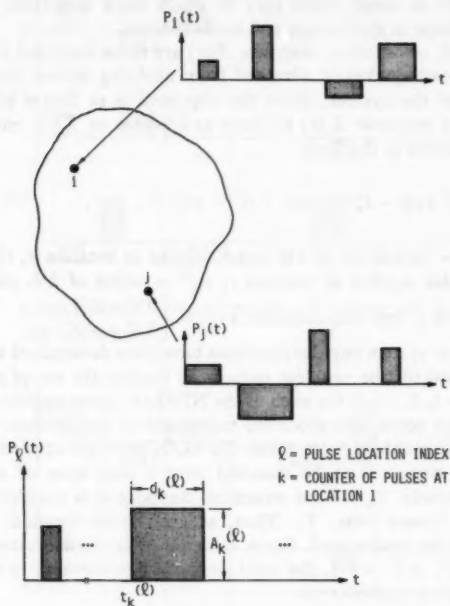


FIG. 2.—Typical Pulse Trains

Due to the linearity of the system, the total response at location  $i$  can be found by superposing the contribution of different pulse trains from different locations:

$$X_i(t) = \sum_{j=1}^{\text{NFRLOC}} X_i^{(j)}(t) \dots \dots \dots (1)$$

$$\text{in which } X_i^{(j)}(t) = \int_0^t h_i^{(j)}(t - \tau) F_j(\tau) d\tau \dots \dots \dots (2)$$

$$F_j(t) = \text{Excitation at location } j \text{ and time } t \dots \dots \dots (3)$$

Assume now that desired response at some points of interest in the structure is specified and denoted by  $\hat{X}_i(t)$ ,  $i = 1, 2, \dots$ , NRESP. The "goodness of

fit" between the system response  $X_i(t)$  to pulse trains and the specified response,  $\hat{X}_i(t)$ , can be measured by the nonnegative error criterion

$$\epsilon = \int_0^t \sum_{i=1}^{NRESP} \{ [X_i(t) - \hat{X}_i(t)] e_i \}^2 dt \dots \dots \dots (4)$$

in which the constants  $e_i$  = weighting factors that can be adjusted to emphasize or de-emphasize the significance of the fit at different points in a structure, since a good fit at some points may be much more important for simulating certain phenomena (e.g., damage and malfunctions).

The specified, or criterion, response  $\hat{X}_i(t)$  are those recorded in the structure (as during an earthquake) or obtained from applying known excitation forces to the model of the system. Since the objective is to find a pulse excitation that produces a response  $X_i(t)$  as close as possible to  $\hat{X}_i(t)$ , each component of  $F(t)$  is restricted to the form

$$F_j(t) = \sum_{k=1}^N A_k^{(j)} [u(t - t_k^{(j)}) - u(t - t_k^{(j)} - w_k^{(j)})] \dots \dots \dots (5)$$

in which  $A_k^{(j)}$  = amplitude of  $k$ th pulse applied at location  $j$ ;  $t_k^{(j)}$  = initiation time of  $k$ th pulse applied at location  $j$ ;  $w_k^{(j)}$  = width of  $k$ th pulse applied at location  $j$ ; and  $u$  = unit step function;  $u(a) = \begin{cases} 0 & \text{if } a \leq 0 \\ 1 & \text{if } a > 0 \end{cases}$ .

Once the linear system impulse functions have been determined and the criteria response established, the problem reduces to finding the set of numbers  $\{t_k^{(j)}, A_k^{(j)}, w_k^{(j)}\}$ ,  $k = 1, 2, \dots, N$  for each of the NFRLOC pulse application locations.

In order to get some idea about the magnitude of the solution task, consider a typical case where three pulse trains (NFRLOC = 3) are applied to a structure whose criteria motion is to be matched over a time span of about  $N = 20$  fundamental periods,  $T_1$ , of the structure. Suppose it is decided to use about one pulse per system time,  $T_1$ . Thus, at each pulse location, 20 individual pulses need to be determined. Since each pulse is characterized by a triplet of numbers  $\{t_k^{(j)}, A_k^{(j)}, w_k^{(j)}\}$ , the total number of parameters to be determined in this optimization procedure is

$$(NFRLOC) \times (N) \times \text{Triplet} = 3 \times 20 \times 3 = 180 \text{ parameters} \dots \dots \dots (6)$$

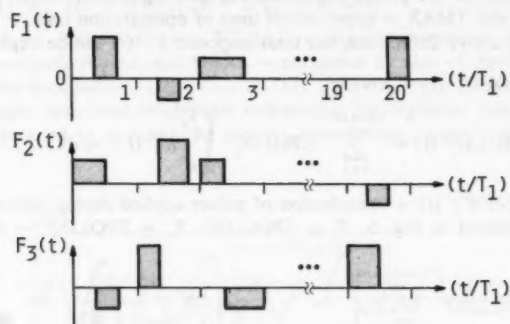
Although a large number of optimization procedures are available (7), none of them can realistically tackle a problem of such magnitude. The next section describes the procedure for formulating the identification problem in a way that is feasible for implementation with efficient optimization techniques.

**Development of Optimization Algorithm.**—The basic idea behind the present optimization procedure is shown in Fig. 3. In Fig. (a) of this figure, the solution of pulse train parameters for a system with three pulse application locations and 20 pulses each in a train is posed as a single optimization problem involving the simultaneous optimization of 180 distinct parameters that characterize the pulse trains. Fig. 3(b) shows how the size of the problem can be reduced to a manageable level by sequentially solving 20 optimization problems, each with nine distinct parameters.

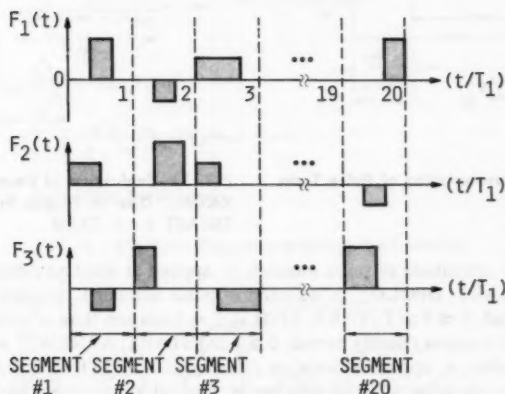
By using the procedure depicted in Fig. 3, an optimization problem of size  $(NFRLOC) \times (N) \times (\text{Triplet})$  can be handled as  $N$  sequential problems, each

involving (Triplet  $\times$  NFRLOC) parameters. This drastic reduction in the order of the problem (from an impractical size to a large size) allows the application of modern optimization techniques to select the "best" pulse train parameters.

**Transient Response of Linear System to Pulse Excitation.**—The response of a location  $i$  in the system at a given time,  $t$ , due to the excitation applied



(a) Simultaneous optimization: 1 operation with 180 parameters



(b) Sequential optimization: 20 operations with 9 parameters

FIG. 3.—Segmentation of Optimization Period for System with 3 Pulse Locations

at location  $j$  can be expressed as  $X_j^{(i)}(t)$ . Assume now that the input at  $j$  is separated into two time periods: from  $t = 0$  to  $t = \text{TSTART}$ , and from  $t = \text{TSTART}$  to  $t = \text{TEND}$  as shown in Fig. 4.

Suppose that the excitation at location  $j$  during the period,  $t = 0$  to  $t =$

TSTART, has been determined and will not be altered. The number of these pulses that have already been determined is NPOLD<sup>(j)</sup>. The problem now is to optimally select a total of NPNEW<sup>(j)</sup> pulses to be applied at location *j* during the period,  $t = \text{TSTART}$  to  $t = \text{TEND} \leq \text{TMAX}$ , in which TSTART = starting time to the present optimization time segment; ( $0 \leq \text{TSTART} \leq \text{TMAX}$ ); TEND = ending time of the present optimization time segment; ( $\text{TSTART} \leq \text{TEND} \leq \text{TMAX}$ ); and TMAX = upper cutoff limit of optimization time.

Using the above definitions, the total response  $X_i^{(j)}(t)$  can be expressed as

$$X_i^{(j)}(t) = \text{XOLD}_i^{(j)}(t) + \text{XNEW}_i^{(j)}(t) \quad (7)$$

$$\text{in which } \text{XOLD}_i^{(j)}(t) = \sum_{k=1}^{\text{NPOLD}^{(j)}} \text{APOLD}_k^{(j)} \int_{T_i}^{T_u} h_i^{(j)}(t - \tau) d\tau \quad (8)$$

in which XNEW<sup>(j)</sup><sub>*i*</sub>(*t*) = contribution of pulses applied during period TSTART  $\leq t$  as explained in Fig. 5;  $T_i = \text{TPOLD}_k^{(j)}$ ;  $T_u = \text{TPOLD}_k^{(j)} + \text{DPOLD}_k^{(j)}$ ;

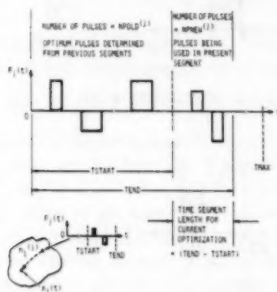


FIG. 4.—Representation of Pulse Train at Location *j*

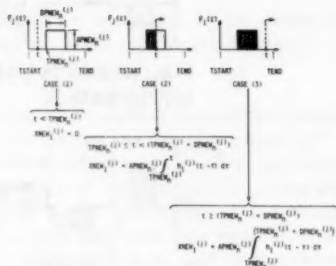


FIG. 5.—Evaluation of Response Term XNEW<sub>*i*</sub><sup>(j)</sup> Due to Single Pulse During TSTART  $\leq t < \text{TEND}$

APOLD<sub>*k*</sub><sup>(j)</sup> = amplitude of pulse number, *k*, applied at location *j* during period,  $0 \leq t \leq \text{TSTART}$ ; DPOLD<sub>*k*</sub><sup>(j)</sup> = duration of pulse number *k*, applied at location *j* during period,  $0 \leq t \leq \text{TSTART}$ ; TPOLD<sub>*k*</sub><sup>(j)</sup> = initiation time of pulse number, *k*, applied; at location *j* during period,  $0 \leq t \leq \text{TSTART}$ ; APNEW<sub>*n*</sub><sup>(j)</sup> = amplitude of pulse number, *n*, applied at location *j* during period,  $\text{TSTART} < t \leq \text{TEND}$ ; DPNEW<sub>*n*</sub><sup>(j)</sup> = duration of pulse number, *n*, applied at location *j* during period,  $\text{TSTART} < t \leq \text{TEND}$ ; and TPNEW<sub>*n*</sub><sup>(j)</sup> = initiation time of pulse number, *n*, applied at location *j* during period,  $\text{TSTART} < t \leq \text{TEND}$ .

Once  $X_i^{(j)}(t)$ , the contribution of the *j*th pulse train to the response at location *i*, is computed from Eqs. 7 and 8, the total response at *i* can be found successively by superposition from each pulse location:

$$X_i(t) = \sum_{j=1}^{\text{NFRLOC}} X_i^{(j)}(t) \quad (9)$$

Assuming that the impulse functions and the response are digitized at the



rate of  $\Delta t_s$ , which is small compared to the shortest system characteristic time (see Fig. 6), then

$$\text{DSP}(I, NT) = X_i[(NT - 1)\Delta t_s], NT = 1, 2, \dots, NTMAX \quad (10)$$

$$\text{DSPHAT}(I, NT) = \hat{X}_i[(NT - 1)\Delta t_s], NT = 1, 2, \dots, NTMAX \quad (11)$$

$$\text{PHI}(I, J, L) = h_i^{(j)}[(L - 1)\Delta t_s], L = 1, 2, \dots, MAXL \quad (12)$$

in which  $\Delta t_s$  = digitization rate;  $NTMAX$  = maximum number of digitized points in the criteria record; and  $MAXL$  = maximum number of digitized points in the impulse functions.

Using simple numerical integration techniques, the digitized values of Eqs. 10-12 can be used to evaluate the various convolution integrals appearing in Eq. 8.

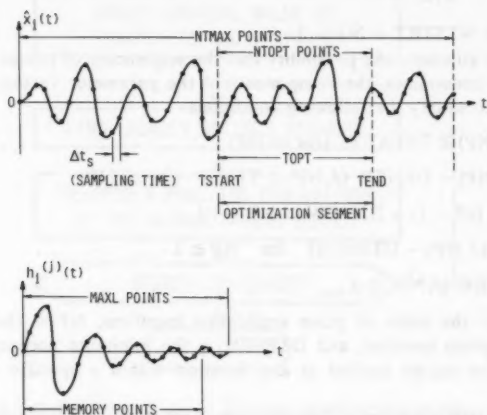


FIG. 6.—Digitized Response and Impulse Function

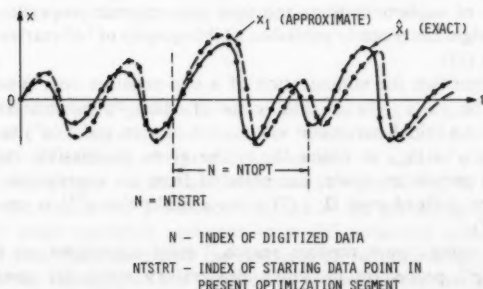


FIG. 7.—Evaluation of Cost Function

**Evaluation of Cost Function.**—Consider the portion of the response shown in Fig. 7. Let  $n$  = index of digitized data points,  $n = (t/\Delta t_s) + 1$ ; NTSTRT = index of starting data point in present optimization segment; and NTOPT = total number of data points in present optimization segment.

The cost function,  $J$ , is set equal to the root mean square deviation error between the criterion response,  $\hat{X}_i$ , and the pulse response,  $X_i$ , summed and weighted over all response locations and for all data points starting from NTSTRT to (NTSTRT + NTOPT):

$$J = \sqrt{\frac{1}{\text{NTOPT}} \sum_{i=1}^{\text{NRESP}} (\text{WF}_i)^2 S_i} \dots \dots \dots (13)$$

$$\text{in which } S_i = \sum_{n=\text{NTSTRT}}^{\text{NTOPT}} [X_i(n \Delta t_s) - \hat{X}_i(n \Delta t_s)]^2 \dots \dots \dots (14)$$

in which  $n = \text{NTSTRT} + \text{NT} - 1$ .

In order to eliminate the possibility that the sequencing of pulses does violate the physical constraints, the components of the parameter vector,  $\mathbf{P}$ , must be constrained to satisfy the following conditions:

$$\text{TPNEW}(J, \text{NP}) \geq \text{TSTART} \quad (\text{for all NP}) \dots \dots \dots (15)$$

$$\text{TPNEW}(J, \text{NP}) + \text{DPNEW}(J, \text{NP}) \leq \text{TEND} \quad (\text{for all NP}) \dots \dots \dots (16)$$

$$[\text{TPNEW}(J, \text{NP} - 1) + \text{DPNEW}(J, \text{NP} - 1)] \\ \leq [\text{TPNEW}(J, \text{NP}) - \text{DTPMIN}] \quad \text{for } \text{NP} \geq 2 \dots \dots \dots (17)$$

$$A_{\min} \leq \text{APNEW}(J, \text{NP}) \leq A_{\max} \dots \dots \dots (18)$$

in which  $J$  = the index of pulse application locations; NP = the counter of pulses at a given location; and DTPMIN = the minimum acceptable spacing of consecutive pulses applied at any location within a specific optimization segment.

**Random Search Algorithm.**—Random search optimization algorithms have been widely explored and utilized for more than 20 yr. Brooks described a random search optimization method in 1958 (4). Analog computer implementations of random optimization schemes were published as early as 1959 (6,13). Since then, a variety of implementations and their convergence properties have been explored. Rastrigin has recently published a bibliography of 760 entries concerning random search (15).

The basic algorithm for minimization of a non-negative cost function,  $J(\alpha)$ , in which  $\alpha = (\alpha_1, \alpha_2, \dots, \alpha_M)^T$  is a vector of unknown parameters, proceeds as follows: (1) An initial parameter value  $\alpha^0$  is chosen and  $J(\alpha^0)$  is evaluated; (2) trial points  $\alpha^i \in \Omega_\alpha$ , in which  $\Omega_\alpha$  = the given permissible region in the  $M$ -dimensional parameter space, are selected from an appropriate probability density function defined over  $\Omega_\alpha$ ; (3) a successful point  $\alpha^{i+1}$  is one for which  $J(\alpha^{i+1}) < J(\alpha^i)$ .

Rather than using "pure random search," most algorithms are based on a "random creep" procedure in which exploratory steps are confined to a hypersphere centered about the latest successful point  $\alpha^i$ . However, convergence by such procedures may be extremely slow, since no allowance is made for

variations in the nature of the cost function surface as the search progresses toward a minimum (1,14,19).

The algorithm (12) employed in this study is another approach to the determination of the locally optimal step size. Rather than using a fixed-length step, steps used are random in both length and direction. The adaptation is based on the selection of the optimal variance of the step-size distribution as the search progresses. Large variances  $\sigma^2$  are desirable in the early, exploratory portions of a search. However, in the vicinity of an optimum, a smaller value of  $\sigma^2$  will decrease the probability of overshoot.

A second and equally important aspect of the algorithm is that the periodic (wide variance range) exploration, which is used to find the locally optimum step size variance, also locates new areas of improvement and decreases the

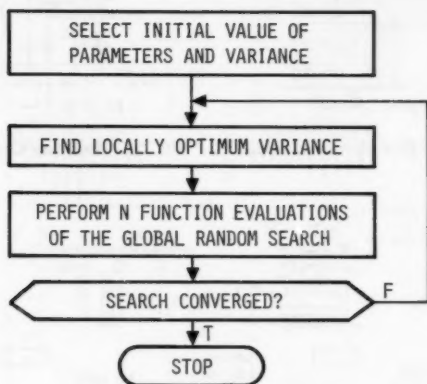


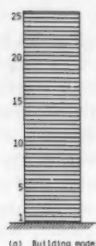
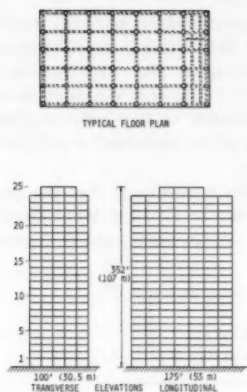
FIG. 8.—Overall Flow Chart of Adaptive Random Search Algorithm

probability that the search will stop at a local minimum. Thus, the algorithm tends toward the *global* optimum. The overall flow chart of the adaptive random search algorithm used in this study is given in Fig. 8.

#### APPLICATIONS

The system shown in Fig. 9 is a 25-story office building designed in accordance with applicable building code provisions for recommended lateral force requirements (2). Modal analysis of this building, treated as a linear elastic structure, yields the mode shapes and natural frequencies shown in Fig. 10.

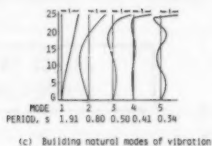
To show the simulation procedure outlined in the preceding, it was decided to use four pulse-excitation locations at modal antinodes (Floors 8, 13, 18, and 23) and to attempt to match the response of two locations (Floors 13 and 23). Due to the linearity of the system, its transient response to pulse trains could be determined by using the convolution integral approach. The necessary displacement impulse response functions were determined and are shown in



(a) Building model

Floor	Mass $10^3 \text{ lb-mass}^2$	Damping Coefficient $10^3 \text{ lb-sec/in.}$
25	1.27	6.3
24	1.57	6.4
23	10.79	9.7
22	7.68	7.2
21	7.68	7.9
20	7.68	6.7
19	6.19	10.1
18	6.19	10.1
17	6.31	11.5
16	6.42	14.1
15	6.42	14.1
14	6.52	16.7
13	6.60	19.5
12	6.68	19.5
11	6.85	21.0
10	6.93	21.0
9	5.03	14.0
8	5.19	15.2
7	5.87	11.8
6	5.87	11.5
5	5.96	13.4
4	10.19	20.8
3	10.19	20.5
2	11.29	42.4
1	11.06	20.1

(b) Building parameters



(c) Building natural modes of vibration

FIG. 9.—Plan and Elevation of Example Building (2)

FIG. 10.—Building Characteristics

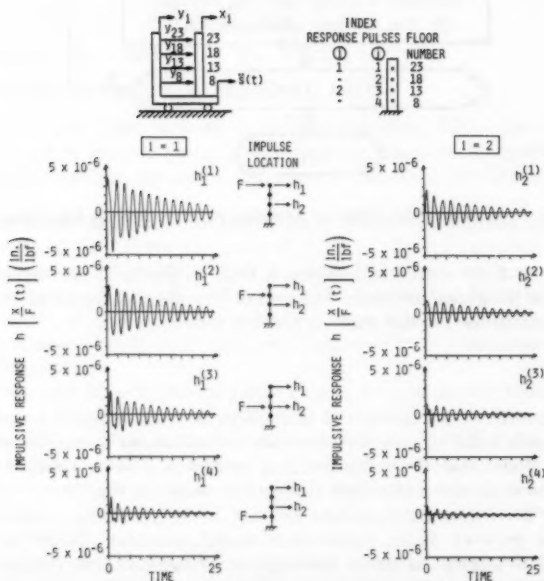


FIG. 11.—Impulsive Displacement Response of 25 DOF System

Fig. 11 in which  $h_i^{(j)}(t)$  denotes the response of Location,  $i$ , due to a unit impulse applied at Location  $j$  with units in inches per pound-force (in meters per Newton).

The El Centro 1940 earthquake ground motion was used as specified base input, and it resulted in the criteria response for both displacement-time histories and shock spectra shown in Fig. 12 as solid lines. The earthquake criteria response was simulated by four suitable pulse trains using the optimization algorithm outlined above. The simulated response is superposed (dotted lines) on top of the criteria response in Fig. 12, and the time histories of the four required pulse trains are shown in Fig. 13.

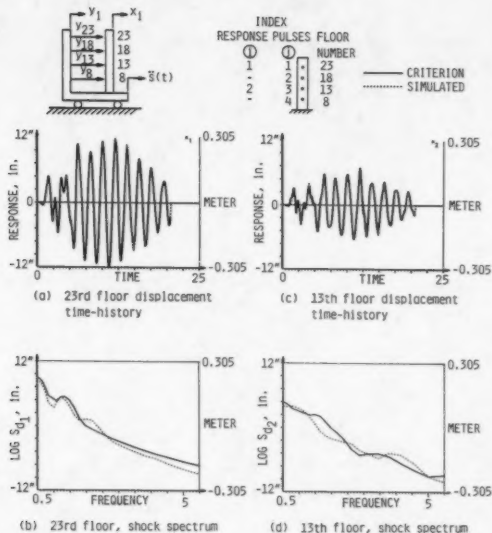


FIG. 12.—Comparison of Criterion and Simulated Response of 25 DOF System at 23rd and 13th Floors to El Centro 1940

It is clear from the comparison shown in Fig. 12 that a good match is obtained between the criterion and simulated response. Note that this simulation of the motion over a period of  $\approx 20$  sec required  $\approx 13$  pulses in each of the four pulse trains.

Referring to Fig. 13 and noting that pulse trains  $F_1(t)$  and  $F_2(t)$  correspond to the simulation forces acting on response Locations 1 and 2 (story Number 23 and 13), it is seen that more simulation force is needed at  $m_{13}$  than at  $m_{23}$ . In the present example, the error weighting functions,  $e_i$ , appearing in Eq. 4 were all equal; consequently the optimization algorithm tends to achieve an equally good fit for the response of both locations.

By the nature of Eq. 4, only the displacement response is being matched, with no attempt being made to optimize the velocity and acceleration response.

TABLE 1.—Summary of Pulse Train Requirements to Excite 25-Story Office Building

Floor (1)	Number of pulses (2)	Pulse Width			Pulse
		Average, in seconds (3)	Maximum, in seconds (4)	Minimum, in seconds (5)	Average, in pound-force (6)
23	13	0.46	0.65	0.25	296,850
18	13	0.42	0.60	0.08	496,600
13	13	0.47	0.57	0.35	443,150
8	13	0.27	0.45	0.10	641,530
Summary and average	52	0.41	0.65	0.10	470,000 ( $2.09 \times 10^6$ N)

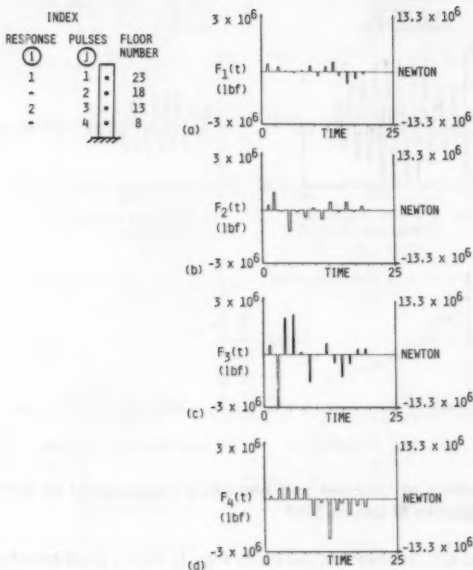


FIG. 13.—Optimum Pulse Trains for 25 DOF Structure

If one is interested in matching other response measures, the expression for the cost function can be modified to become

$$\epsilon = \int_0^t \sum_{i=1}^n \{ [x_i(t) - \hat{x}_i(t)]^2 e_{1i}^2 + [\dot{x}_i(t) - \hat{\dot{x}}_i(t)]^2 e_{2i}^2 + [\ddot{x}_i(t) - \hat{\ddot{x}}_i(t)]^2 e_{3i}^2 \} dt \dots \dots \dots (19)$$

to El Centro 1940 Earthquake (Pulsers Located at 23rd, 18th, 13th, and 8th floors)

Force		Impulse	
Maximum, in pound-force (7)	Minimum, in pound-force (8)	Average, in pounds per second (9)	Total, in pounds per second (10)
577,000	100,000	137,600	1,788,900
1,000,000	100,000	180,490	2,346,300
1,000,000	15,000	204,930	2,664,050
1,000,000	80,000	157,650	2,049,500
1,000,000	15,000	170,000	8,848,750
$(4.48 \times 10^6 \text{ N})$	$(66,720 \text{ N})$	$(756,160 \text{ N-sec})$	$(39.4 \times 10^6 \text{ N-sec})$

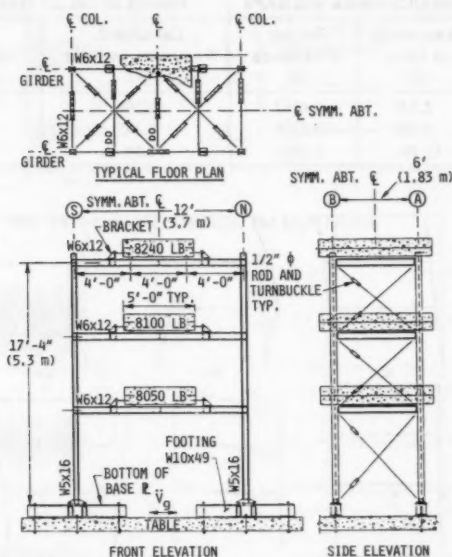


FIG. 14.—Plan and Elevations of UCB Test Structure (21)

in which  $e_1$ ,  $e_2$ , and  $e_3$  = weighting factors associated with the displacement, velocity, and acceleration response. This approach normally implies a larger number of pulses of shorter duration. Thus, the 13 pulses used in this application for displacement matching could change to 25 pulses with a significant reduction in average pulse force required.

Pulse trains to induce criteria motions are not unique, as indicated previously. Constraints for number of pulses, number of pulse units, maximum and minimum force, pulse duration, initiation time, and location can be stipulated a priori

to accommodate pulse generator performance capabilities. An algorithm to optimize for the foregoing variables (constraints) is currently under development. No effort was made to optimize the pulse train requirements as given in Fig. 13, which is summarized in Table 1. Force requirements given in the table indicate 6 pulse generators will be required for the 23rd floor and 10 units for the 18th, 13th, and 8th floors for each direction, for a total of 72 units. Performance studies indicate that pulse units of 100,000 lb (444,800 N) force capacity provide adequate flexibility for mobility in field tests and particularly in turn-on/turn-off timing.

TABLE 2.—Comparison of Lowest Three Natural Frequencies

Mode number (1)	Results of Present Study with UCB Frame and SAP6		Results of Ref. 21 (Table 4-4, p. 99)	
	Frequency, in hertz (2)	Period, in seconds (3)	Calculated frequency in hertz (4)	Measured frequency in hertz (5)
1	2.279	0.4387	2.295	2.240
2	7.950	0.1258	8.345	7.941
3	15.80	0.0633	17.54	16.79

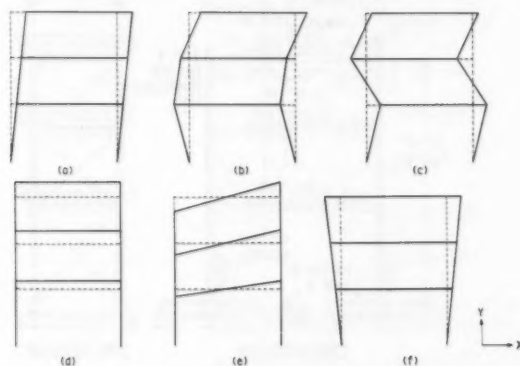


FIG. 15.—Mode Shapes of UCB Frame Determined by SAP6

**UCB Structure.**—A three-story steel frame structure consisting of two identical, single-bay, moment-resistant frames has been extensively tested by means of the earthquake simulation facility at the University of California, Berkeley (UCB). Detailed experimental and analytical studies regarding the subject frame are given in Refs. 5 and 21. The plan and elevations of the test structure are shown in Fig. 14.

In the present study, a general purpose finite element computer program SAP6 (18) was used to analyze a linear model (henceforth referred to as the



UCB frame) of one of the two identical frames shown in Fig. 14. The characteristics of the mathematical model of the UCB frame were developed from information given in Ref. 21. The frequencies and mode shapes of the UCB frame and the corresponding measured and calculated frequencies given in Ref. 21 are shown in Fig. 15 and Table 2.

Pulse trains were to be applied at the three floor locations. The needed impulsive response functions were analytically determined and are shown in Fig. 16. The criteria response to the El Centro 1940 earthquake was likewise analytically determined by using SAP6, and the results are shown as solid lines in response

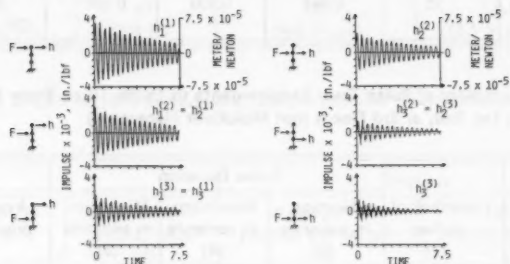


FIG. 16.—Impulse Functions for UCB Frame

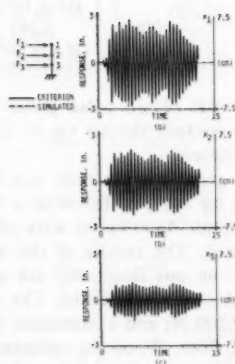


FIG. 17.—Comparison of Criterion and Simulated Response of UCB Frame

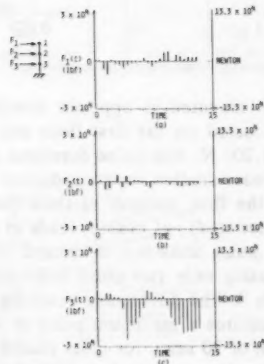


FIG. 18.—Optimum Pulse Trains for UCB Frame

time history of Fig. 17. The adaptive random research optimization procedure was again used to determine the required pulse trains. The resulting simulated motion and the three required pulse trains for each floor location are shown in Figs. 17 and 18.

A summary of the pulse generator performance requirements is shown in Table 3. This table shows that two pulse generators are required for each floor

TABLE 3.—Summary of Pulse Train Requirements to Excite Three-Story UCB Test

Floor (1)	Number of pulses (2)	Pulse Duration			Pulse
		Average, in seconds (3)	Maximum, in seconds (4)	Minimum, in seconds (5)	Average, in pound-force (6)
3	25	0.046	0.100	0.039	2,430
2	25	0.072	0.100	0.053	1,726
1	25	0.026	0.100	0.009	9,365
Average and summary	75	0.048	0.100	0.009	4,507 ( $20 \times 10^3$ N)

TABLE 4.—Summary of Pulse Train Requirements to Excite Three-Story UCB Test used Only on 1st, 2nd, or 3rd Floors (not Multifloor Placement)

Floor (1)	Number of pulses (2)	Pulse Duration			Pulse
		Average, in seconds (3)	Maximum, in seconds (4)	Minimum, in seconds (5)	Average, in pound-force (6)
3	23	0.100	0.103	0.090	1,882 ( $8.4 \times 10^3$ N)
2	23	0.083	0.103	0.026	4,076 ( $18 \times 10^3$ N)
1	24	0.077	0.103	0.006	6,387 ( $28.4 \times 10^3$ N)

and are mounted in opposite directions, for a total of six pulse generators. Units located on the first floor are required to produce thrusts up to 25,000 lbf (111,200 N) with pulse durations as short as 9 msec.

Alternate studies were conducted using pulse generators on only one floor (either the first, second, or third floor) and also on any two floors at a time. The latter study, of course, leads to six combinations. Restrictions were placed on the pulse units not to exceed 10,000 lbf thrust. The results of the study for locating only two pulse units (in opposition) on one floor only are given in Table 4. The differences resulting from the tables are substantial. The third floor requires a maximum pulse of 4,322 lbf (19,200 N) and a minimum pulse duration of 90 msec for units placed on the third floor. When the optimization algorithm is complete for pulser locations and impulse minimization, further improvement is expected.

The programmable gas pulse generator shown in Fig. 19 is currently under construction. Initial use provides for cold gas but the system is adaptable for both steam and chemically generated hot gas. Thrust amplitudes are controlled in the on-state by positioning the metering plug for flow control. Off-state for the pulse occurs by signaling the hydraulic actuator to move the metering plug to seal off gas flow at the nozzle. This device will be used for earthquake and antearthquake investigations on the UCB structure shown in Fig. 14. In these tests, response motions of the structure will be compared when: (1) The

## Structure to El Centro 1940 Earthquake. Pulse Units Located on all Three Floors

Force		Impulse	
Maximum, in pound-force (7)	Minimum, in pound-force (8)	Average, in pounds per second (9)	Total, in pounds per second (10)
8,190	176	108	2,701
4,643	47	121	3,019
25,470	495	153	3,825
25,470	47	127	9,545
( $113 \times 10^3$ N)	(209 N)	(564 N-sec)	( $42.5 \times 10^3$ N-sec)

## Structure to El Centro 1940 Earthquake. Compares Pulse Requirements if Units are

Force		Impulse	
Maximum, in pound-force (7)	Minimum, in pound-force (8)	Average, in pounds per second (9)	Total, in pounds per second (10)
4,322	123	189	4,324
( $19 \times 10^3$ N)	(547 N)	(841 N-sec)	( $19 \times 10^3$ N-sec)
10,000	165	302	6,906
( $45 \times 10^3$ N)	(734 N)	(1,343 N-sec)	( $30.7 \times 10^3$ N-sec)
10,000	253	446	10,704
( $45 \times 10^3$ N)	(1,125 N)	(1,984 N-sec)	( $47.6 \times 10^3$ N-sec)

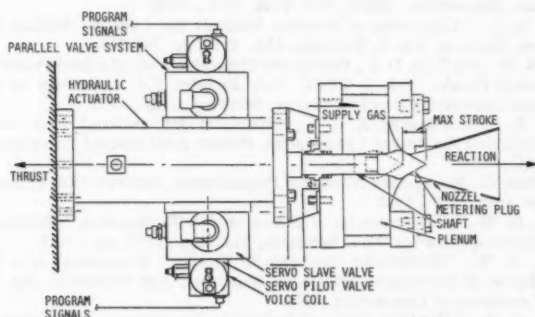


FIG. 19.—Programmable Gas Pulse Generator Cold Gas System

structure is vibrated by the shake table as base motion; and (2) the structure is vibrated with pulsers attached to the frame and with the shaker table blocked. Additionally, the structure will be vibrated by the shake table for several earthquake motions and the pulse units will be counter-fired to suppress the structural response.

## SUMMARY AND CONCLUSIONS

A computationally efficient technique for optimizing the selection of pulse train characteristics to be used for simulating the response for general types of structural systems to arbitrary dynamic environments is presented. The optimization procedure uses an adaptive random search algorithm that incorporates a periodic exploratory search for the optimal step-size variance, which significantly improves the convergence characteristics.

The method is applied to two example structures: (1) A hypothetical 25-story building; and (2) a moment-resisting frame that has been extensively investigated both analytically and experimentally by others. It is shown that pulse-excitation techniques offer a viable alternative to large testing facilities and ground-explosion approaches in simulating earthquake effects on structures.

## ACKNOWLEDGMENT

This study was supported in part by the National Science Foundation under Grant No. PFR77-15010.

## APPENDIX.—REFERENCES

1. Bekey, G. A., and Ung, M. T., "A Comparative Evaluation of Two Global Search Algorithms," *IEEE Transactions on Systems, Man and Cybernetics*, Vol. SMC-4, No. 1, 1974, pp. 112-116.
2. Blume, J. A., Newmark, N. M., and Corning, L. H., *Design of Multistory Reinforced Concrete Buildings for Earthquake Motions*, Portland Cement Association, Skokie, Ill., 1961.
3. Bouwkamp, J. G., "Dynamics of Full-Scale Structures," *Applied Mechanics in Earthquake Engineering*, ASME, New York, N.Y., 1974.
4. Brooks, S. F., "Discussion of Random Methods for Locating Surface Maxima," *Operations Research*, Vol. 6, Bethesda, Md., 1958, pp. 244-251.
5. Clough, R. W., and Tang, D. T., *Earthquake Simulator Study of a Steel Frame Structure, Experimental Results*, Vol. 1, EERC 75-6, Berkeley, CA, University of California Earthquake Engineering Research Center, Berkeley, Calif., 1975.
6. Favreau, R. R., and Franks, R. G. E., "Statistical Optimization," *Proc. 2nd International Conference for Analog Computation*, Presses Academiques Europeennes, 1959, pp. 437-443.
7. Himmelblau, D. M., *Applied Nonlinear Programming*, McGraw-Hill, Publishing Co., Inc., New York, N.Y., 1972.
8. Housner, G. W., "Characteristics of Strong-Motion Earthquakes," *Bulletin, Seismological Society of America*, 37:1, Baltimore, Md., Jan., 1947, pp. 19-27.
9. Housner, G. W., "Earthquake Environment Testing," *Proceedings of a Workshop on Simulation of Earthquake Effects on Structures*, San Francisco, Sep 7-9, 1973, National Academy of Engineering, 1974.
10. Hudson, D. E., "Dynamic Tests of Full-Scale Structures," *Proceedings Dynamic Responses of Structures, Instrumentation, Testing Methods, and System Identification*, University of California, at Los Angeles, Mar. 30-31, 1976.
11. Masri, S. F., Bekey, G. A., and Safford, F. B., "Optimum Response Simulation of Multidegree Systems by Pulse Excitation," *Journal of Dynamic Systems Measurement and Control*, Trans. ASME, Series G, Vol. 97, No. 1, Mar., 1975, p. 46.
12. Masri, S. F., Bekey, G. A., and Safford, F. B., "An Adaptive Random Search Method for Identification of Large-Scale Nonlinear Systems," presented at the September, 1976, *4th Symp. for Identification and System Parameter Estimation*, International Federation of Automatic Control, held at Tbilisi, USSR.

13. Munso, J. K., and Rubin, A. I., "Optimization by Random Search on the Analog Computer," *IRE Transactions on Electronic Computer*, Vol. EC-8, No. 2, 1959, pp. 200-203.
14. Rastrigin, L. A., "The Convergence of the Random Search Method in the Extremal Control of a Many Parameter System," *Automation and Remote Control*, Vol. 24, No. 11, 1963, pp. 1337-1342.
15. Rastrigin, L. A., "Random Search," (A Bibliography in Russian), Riga, 1973; Supplement 1977.
16. Safford, F. B., and Masri, S. F., "Analytical and Experimental Studies of a Mechanical Pulse Generator," *Journal of Engineering for Industry*, ASME, Series B, 96:2, May, 1974, pp. 459-470.
17. Safford, F. B., et al., "Air-Blast and Ground-Shock Simulation Testing of Massive Equipment by Pulse Techniques," presented at the May 23-26, 1977, 5th International Symposium on Military Application of Blast Simulation, Fortifikationsforvaltningen, held at Stockholm, Sweden.
18. SAP6 Computer Program Manual, Civil Engineering Department, University of Southern California, Los Angeles, Calif., 1978.
19. Schumer, M. A., and Steiglitz, K., "Adaptive Step Size Random Search," *IEEE Transactions on Automatic Control*, Vol. AC-13, No. 3, 1968, pp. 170-276.
20. Scruton, C., and Harding, D. A., *Measurement of the Structural Damping of a Reinforced Concrete Chimney Stack at Ferrybridge "B" Power Station*, NPL/Aero/323, Wallingford, England, 1957.
21. Tang, D. T., *Earthquake Simulator Study of a Steel Frame Structure. Analytical Results*, Vol. 2, EERC 75-36, Univ. of Calif. Earthquake Engineering Research Center, Berkeley, Calif., 1975.
22. Yates, D. G., and Safford, F. B., "Measurement of Dynamic Structural Characteristics of Massive Buildings by High-Level Multiple Techniques," *Shock & Vibration Bulletin*, 50, SVIC, Naval Research Lab., Washington, D.C., 1980.

*[The page contains extremely faint, illegible text, likely bleed-through from the reverse side.]*

## APPROXIMATE DESIGN BY GEOMETRIC SERIES

By Bogdan O. Kuzmanović,<sup>1</sup> F. ASCE and Nicholas Willems,<sup>2</sup> M. ASCE

### INTRODUCTION

Often a designer has to minimize the structural weight of a given frame configuration for a given loading. The most natural and rigorous way of dealing with such problems is to make use of mathematical programming methods. It is also well known that strict application of available constrained minimization techniques invariably has failed to produce fully satisfactory results and that this has led to design procedures based on approximation concepts (5). By constructing a high quality approximation of the minimizing process, a practical and meaningful design is generally obtained. In practice, the results of a structural weight optimization normally serve only as a first approximation of the final design because of various practical design and construction considerations. Therefore, it is important for a practicing engineer to have access to a sufficiently accurate optimal design method which uses an algorithm and can be executed fairly simply on a desk calculator that can be programmed. It is further desirable that the input data be basic, i.e., contain only geometrical and load data. As input, neither the starting values of member cross sections nor their mutual ratios should be required. Such an algorithm will be much easier, quicker, and cheaper to use than more exact methods which make use of mathematical programming (1, 4, and 8). The weight of each frame member depends upon the maximum bending moment acting on that member. The algorithm, therefore, has to represent an automatic successive reduction of characteristic moments, without violation of equilibrium, resulting in the successive creation of plastic hinges and a corresponding collapse mechanism.

It was previously shown (6) that the plastic moment distribution can be used for automatic optimization by using an iteration procedure. Later (7), it was also shown that correction and carry-over moments can be made to form terms of infinite convergent geometrical series with known exact sums. If this is the case, iteration loops can be eliminated and substituted by closed-form formulas representing the sums of an infinite number of iterations. This drastically reduces the required size of core memory and the operational time. This way it is

<sup>1</sup>Prof. of Civ. Engrg., Univ. of Kansas, Lawrence, Kans. 66045.

<sup>2</sup>Prof. of Civ. Engrg., Univ. of Kansas, Lawrence, Kans. 66045.

Note.—Discussion open until February 1, 1982. To extend the closing date one month, a written request must be filed with the Manager of Technical and Professional Publications, ASCE. Manuscript was submitted for review for possible publication on June 13, 1980. This paper is part of the *Journal of the Structural Division*, Proceedings of the American Society of Civil Engineers, ©ASCE, Vol. 107, No. ST9, September, 1981. ISSN 0044-8001/81/0009-1763/\$01.00.

possible to solve an optimization problem of an unsymmetrically loaded four-story, four-bay rectangular plane frame using a minicomputer with only a 4K direct read-write memory. Use is also made of partitioning of multistory frames (2). Starting with the top story and moving downward, each story is optimized separately. This procedure is equivalent to the assumption that in each column of every story a plastic hinge will develop just above the beams of the story below it. Therefore, this assumption is also the first condition of reaching a global optimum. Often, this assumption proves to be correct, and the optimization procedure, in that case, could result in a global optimum. The second condition in reaching a global optimum requires that the true collapse mechanism of the frame be the one obtained by combination of beam and sway mechanisms. This requires two successive hinges in each beam, two hinges in the last column, and one hinge at the bottom of all the other columns of that story. If any of these assumptions are violated, the obtained result represents only an approximate value, but with small error. Comparative analysis has shown such an error to be less than 4%. The explanation why this error is so small is given elsewhere (3,7).

For the sake of simplicity, the method is restricted to plane rectangular frames composed of prismatic members subjected to static loads. Vertical loads are always applied at the beam midpoints, and horizontal loads, which are assumed to act from left to right, are applied at the floor levels.

Use is also made of the simplified plastic theory with its usual approximations and limitations, i.e., no work-hardening of steel, no occurrence of frame instability, and small deformations at collapse.

A further limitation is that the first admissible moment configuration must be such that bending moments at the beam centers due to gravity or combined loading are larger than the moments at both beam ends. For normal loading conditions under existing building codes and frame configurations, this is always true.

#### PROPOSED METHOD

The linearized objective function, the weight of the frame, is approximated by the sum of the products of the length and the required full plastic moment capacity for each frame member. Therefore, reducing plastic moments obviously will reduce the overall weight. At collapse, a true plastic moment diagram must satisfy equilibrium and have a sufficient number of plastic hinges for the formation of a collapse mechanism. If all three characteristic beam moments are successively corrected so as to equalize two out of three beam moments, i.e., create two adjacent beam hinges, and if the largest of the three beam moments is constantly being reduced by this equalization, the total weight of the frame will also be decreasing. If this procedure is repeated an infinite number of times, the possibility exists of reaching a global optimum provided the two conditions, mentioned before, are satisfied. If this is not the case, however, a local one will be reached but of sufficient accuracy. The frame weight will be reduced by iteration cycle, and a collapse mechanism will also be created.

For each frame story, the first maximum beam moment reduction and the creation of two beam hinges is performed in the first bay,  $j = 1$ , when a suitable correction moment,  $D(1,1)$ , is first applied to the right-hand beam



end-moment and then, for the sake of equilibrium, carried over with a carry-over factor ( $CO$ ) of  $-1/2$  to the midbeam moment. Once two moments are equalized, they will remain equal because, as will be seen, they will be changed in each future cycle by exactly the same amounts. To satisfy equilibrium of the common beam joint between the first and second bay, this first correction,  $D(1, 1)$ , has to be subtracted from the left beam end-moment of the second bay. Now, to satisfy beam equilibrium of the second bay, a part of this correction,  $-D(1, 1)$ , will be carried over to midspan, with  $CO + 1/2$ , and the remainder to the right-hand beam end-moment (with a  $CO = +1$ ). If two-thirds of  $-D(1, 1)$  are carried to the midspan and only one-third to the right-hand beam end, both moments at the midspan and the right end will be reduced by the same amount of  $-1/3D(1, 1)$ . This correction from the second bay will effect the third bay in the same manner and will be carried over to the midspan and right-hand beam end, after another reduction by  $1/3$ . This value, so reduced, will now pass on to the next bay, and so on. The first correction,  $D(1, 1)$ , and its reduced values will thus flow along all beams from left to right, through the last column from top to bottom as one and the same correction, back to the first column, and finally to the left end beam moment of the first bay as a correction of  $(-1)^n \times (D(1, 1))/3^{n-1}$ , in which  $n$  = number of bays. This is the end of the first cycle of equalization of moments in the first bay. If this same process is now repeated, an infinite number of times, all the corrections at any one and the same section will form an infinite decreasing geometric series due to the equalization of two moments in the first bay. The sum of all the terms of this series can easily be obtained. Next, two beam moments, at midspan and right-hand beam end, in the second bay are equalized and corrections flow around the frame an infinite number of times. Their sums for each section are obtained. This same process is now repeated for all  $n$  bays of a particular story, resulting in  $n$  sums of  $n$  infinite decreasing series for each characteristic section. As will be shown later, these sums at any one particular section luckily form elements of a matrix that can be generated easily. Therefore, there is no need to generate infinite series and find their sums. All that is needed is to generate two such matrices—one for midspan beam moments and another for right-hand beam end-moments. Each row  $j$  of the matrix elements represents the correction sums for the corresponding bay  $j$ .

The whole method can be presented by the general flow chart (Fig. 1). This method will be first applied to a single story multibay frame and then to a multistory frame. As an illustration of the method a completely worked out example is also given.

Moments are taken as positive if they act clockwise at member ends and at beam midspan if they are sagging moments. Bending moment diagrams are always drawn on the tension side of each member.

**Single Story.**—Let us first consider a multibay single-story frame (Fig. 2). The bays are numbered  $j = 1, 2 \dots n$ . Each bay has seven potential critical sections where plastic hinges might develop. The moments at these locations are called  $M(j, 1), M(j, 2) \dots M(j, 7)$ .

**First Admissible Moments.**—These are obtained in two steps. First, by considering the simple beam and sway (panel collapse) mechanisms an initial set of bending moments is obtained. The necessary correction moments to establish joint equilibrium are carried back from corrected joints to all midbeam moments

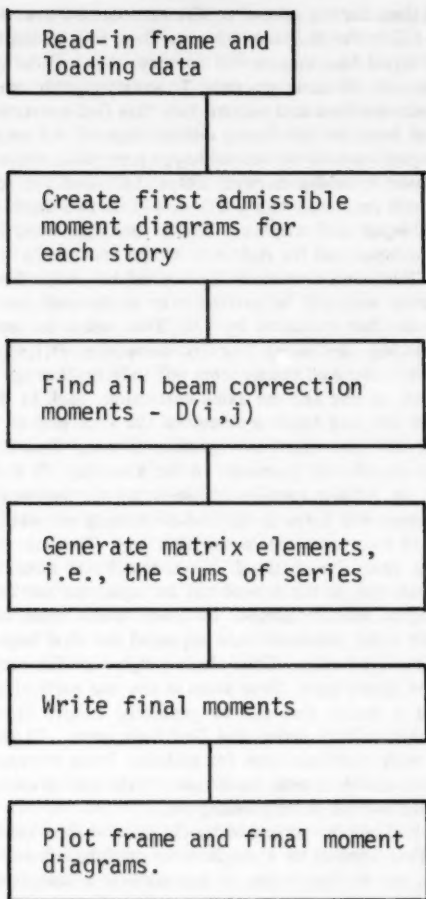


FIG. 1.—General Flow Chart

except in the first bay, where both end moments are corrected by the same amount. Therefore, the corrected first admissible moments are

Sway Moments  $M(1,1) = M(1,2) = M(j,6) = M(j,7)$

$$= -\frac{W(1) \times H(1)}{2(n+1)} = -C(1) \dots \dots \dots (1)$$

in which  $j = 1, 2, \dots, n$ . Each column carries an equal portion of the total sway moment,  $-C(1)$ .

$$\text{Beam Moments } M(1,4) = \frac{P(1,1) \times L(1)}{4}$$

$$M(j,4) = \frac{P(1,j) \times L(j)}{4} - \frac{1}{2} C(1) \dots \dots \dots (2)$$

in which  $j = 2, 3 \dots n$  at midspan.

$$\text{Beam Moments } M(j,5) = C(1) = \frac{W(1) \times H(1)}{2(n+1)} \dots \dots \dots (3)$$

in which  $j = 1, 2 \dots n$  at right-hand beam end.

$$\text{Beam Moments } M(1,3) = C(1)$$

$$M(j,3) = 0 \dots \dots \dots (4)$$

in which  $j = 2, 3 \dots n$  at left-hand beam end. Instead of assigning equal portions of the total sway moment to each column, it is also possible to assign  $-W(1) \times H(1)$  completely to the first column.

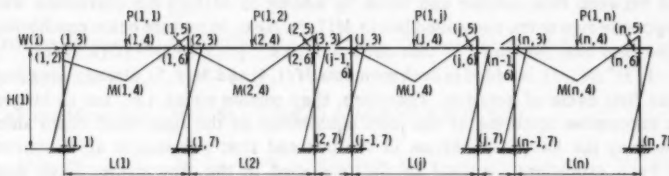


FIG. 2.—First Admissible Moments

**Optimization.**—To start the optimization procedure, the beam moments in the first bay ( $j = 1$ ) at locations 4 and 5 (Fig. 2) are equalized by applying a correction moment:

$$D(1,1) = \frac{2}{3} [M(1,4) - M(1,5)] \dots \dots \dots (5)$$

This correction,  $D(1,1)$ , is added to the right-hand end beam moment,  $M(1,5)$ , and, for beam equilibrium, carried back to the midbeam moment,  $M(1,4)$ , with a  $-1/2$  carry-over factor, i.e., two plastic hinges in the first bay are formed and the midspan moment is reduced. Actually, this means that half of this correction  $D(1,1)$  is subtracted from  $M(1,4)$  and the whole amount added to  $M(1,5)$ . The disturbance of equilibrium of the joint at the right-hand end of the first beam is therefore  $D(1,1)$ . To restore equilibrium of that joint,  $-D(1,1)$  is added to the beam moment in the next bay,  $M(2,3)$ . Next, to restore beam equilibrium in the second bay,  $-2/3 D(1,1)$  is carried over (with a carry-over factor  $CO = +1/2$  to  $M(2,4)$  and  $-1/3 D(1,1)$  (with  $CO = +1$ ) to  $M(2,5)$ . This means that the midbeam and right-hand end-beam moments of the second bay are reduced by the same amount of  $1/3 D(1,1)$ . To restore joint equilibrium now at the right-hand end of the beam of the second bay,  $+1/3 D(1,1)$  is added to  $M(3,3)$  of the next bay. To establish equilibrium of the beam, here

in the third bay, this correction,  $1/3 D(1,1)$  is again divided into two-thirds and one-third, as was done previously in the second bay. Half of it, i.e.,  $[1/(-3)^2] D(1,1)$  is added to  $M(3,4)$  and the same amount to  $M(3,5)$ .

This process is again repeated for the next bay, and so on, until the last bay is reached with the correction  $[D(1,1)/(-3)^{n-1}]$  added to  $M(n,4)$  and  $M(n,5)$ . When the equilibrium of the last joint at the right-hand beam end of the last,  $n$ th, bay is restored by adding to  $M(n,6)$   $(-1)^n \cdot [D(1,1)/(3)^{n-1}]$  to the top of last column, the sway equilibrium of the whole frame has been violated and needs to be restored. The sway equilibrium condition requires that the sum of all corrections added to any of the column moments be zero. To achieve this and also to achieve a "minimum column design," the same correction applied at section  $(n,6)$  is added to  $(n,7)$ , and with opposite sign to sections  $(1,1)$  and  $(1,2)$  of the first column. These corrections affect, therefore, all beams from left to right, then the last column, and finally the first one. In this way, the original minimum sway moments remain intact in all columns except the first and the last ones. This represents "minimum stanchion design."

This completes the first iteration cycle by arriving at the top section of the first column. The second cycle starts with reestablishing equilibrium of that joint between first column and beam by adding to  $M(1,3)$  the correction with an opposite sign to the one added last to  $M(1,2)$ . Next, to restore beam equilibrium of the first bay, one-third of that correction, i.e.,  $[1/3](-1)^n \cdot [D(1,1)/(3)^{n-1}] = (-1/3)^n D(1,1)$ , is added to both moments  $M(1,4)$  and  $M(1,5)$ , already equalized in the first cycle of iteration. Therefore, they remain equal, i.e., act as hinges. The successive restoring of the joint equilibrium at the right-hand beam sides as well as the sway equilibrium in the last and first columns is again carried out by a procedure identical to the one used in the first cycle. Each next cycle is performed exactly in the same manner. This is done an infinite number of times. In this way, due to the equalization of two moments in the first bay, all the corrections at any frame section form terms of an identical decreasing geometric series, which has a known sum for an infinite number of terms. For example, for a two-bay frame ( $n = 2$ )

$$\begin{aligned}\bar{M}(1,3) &= C(1) + \frac{1}{3} D(1,1) \left( 1 + \frac{1}{3^2} + \frac{1}{3^4} + \frac{1}{3^6} + \dots \right) \\ &= C(1) + D(1,1) \frac{1}{3} \times \frac{1}{1 - \frac{1}{3^2}} = C(1) + \frac{3}{3^2 - 1} \times D(1,1) \dots \dots \dots (6)\end{aligned}$$

The same procedure is now applied to the second bay by equalizing  $M(2,4)$  and  $M(2,5)$  with a new correction factor of the same form as Eq. 5. The correction factor for the second bay is calculated as

$$D(1,2) = \frac{2}{3} [M(2,4) - M(2,5)] \dots \dots \dots (7)$$

$M(2,4)$  and  $M(2,5)$  are the first admissible moments, given in Eqs. 2 and 3 due to the fact that both moments were previously changed by the same amount during the infinite correction cycling process with  $D(1,1)$ . The same operation is repeated as before with  $D(1,1)$ . This is then done for all bays until the

last correction,  $D(1, n)$ , is also applied by going an infinite number of times around the frame as before. There are now  $n$  infinite geometric series at each characteristic frame section. Knowing the sums of all  $n$  correction series at each critical section, it is possible to write expressions for the final moments at every critical section in closed form. In case of beam moments,  $M(j, 4)$  and  $M(j, 5)$ , these sums are grouped as elements  $(j, k)$  of a  $(n \times n)$  matrix  $[A]$  and  $[B]$ , respectively. For any bay  $j$ , instead of sums the corresponding whole row  $j$  of matrix elements is used. Any element in that particular row,  $j$ ,  $a_{jk}$ , represents the sum of the infinite number of cycling corrections started with equalization of two beam moments in the bay corresponding to column number  $k$ .

Therefore, like  $j$ ,  $k = 1-n$ . Different formulas to form these matrices and write final moments apply for an odd and an even total number of bays,  $n$ .

**Final Moments.**—If  $n$  is odd, the final moments  $\bar{M}(j, 1), \dots, \bar{M}(j, 7)$  are

Column Moments —  $\bar{M}(1, 1) = \bar{M}(1, 2) = M(1, 1) + \Delta M(1, 1)$

$$= M(1, 1) + \frac{1}{3^n + 1} \sum_{j=1}^n [(-1)^{j+1} \times 3^j \times D(1, j)] \dots \dots \dots (8)$$

Column Moments  $\bar{M}(j, 6) = \bar{M}(j, 7) = M(j, 6) = -C(1) = \text{const.} \dots \dots \dots (9)$

in which  $j = 1, 2, \dots, (n-1)$ .

Column Moments  $\bar{M}(n, 6) = \bar{M}(n, 7) = M(n, 6) + \Delta M(n, 6)$

$$= M(n, 6) - \frac{1}{3^n + 1} \sum_{j=1}^n [(-1)^{j+1} \times 3^j \times D(1, j)] \dots \dots \dots (10)$$

Beam Moments at the left-end,  $\bar{M}(1, 3) = -\bar{M}(1, 2) \dots \dots \dots (11)$

Beam Moments  $\bar{M}(j, 3) = -\bar{M}(j-1, 5)$  (see Eq. 19)  $\dots \dots \dots (12)$

in which  $j = 2, 3, \dots, n$ .

Beam Moments at mid-span  $\bar{M}(j, 4) = M(j, 4) + \Delta M(j, 4) \dots \dots \dots (13)$

in which  $j$  goes from 1 to  $n$ .

$$\text{Beam Moments } \bar{M}(j, 4) = M(j, 4) - \frac{1}{2} D(1, j) + \frac{1}{3^n + 1} \sum_{k=1}^n a_{j,k} D(1, k) \quad (14)$$

in which the coefficients  $a_{j,k}$  are elements of a square  $n \times n$  matrix. This coefficient matrix  $A$  has the property

$$a_{j,k} = a_{j-1,k-1} \dots \dots \dots (15)$$

Therefore, it is sufficient to form the first row and first column of this matrix. The first row elements are

$$a_{1,k} = (-1)^k \times 3^{k-1} \dots \dots \dots (16)$$

in which  $k = 1, 2 \dots, n$ . The first column elements are

$$a_{j,1} = (-1)^{j+1} \times 3^{n-j+1} \dots \dots \dots (17)$$

in which  $j = 2, 3 \dots, n$ . As mentioned earlier, the rows have the subscript

$j$  and the columns the subscript  $k$ . For example, for a seven-bay frame ( $n = 7$ ) the coefficient matrix for  $\bar{M}(j, 4)$  is

$$[A] = \begin{bmatrix} -3^0 & 3^1 & -3^2 & 3^3 & -3^4 & 3^5 & -3^6 \\ -3^6 & -3^0 & 3^1 & -3^2 & 3^3 & -3^4 & 3^5 \\ 3^5 & -3^6 & -3^0 & 3^1 & -3^2 & 3^3 & -3^4 \\ \hline -3^4 & 3^5 & -3^6 & -3^0 & 3^1 & -3^2 & 3^3 \\ \hline 3^3 & -3^4 & 3^5 & -3^6 & -3^0 & 3^1 & -3^2 \\ -3^2 & 3^3 & -3^4 & 3^5 & -3^6 & -3^0 & 3^1 \\ 3^1 & -3^2 & 3^3 & -3^4 & 3^5 & -3^6 & -3^0 \end{bmatrix}$$

in which rows  $j$  and columns  $k$  go from 1-7. For each bay  $j$ , the corresponding row  $j$  has to be used in Eq. 14. For instance, taking matrix elements between intermittent lines

$$\bar{M}(4, 4) = M(4, 4) - \frac{1}{2} D(1, 4) + \frac{1}{3^7 + 1} [-3^4 D(1, 1) + 3^5 D(1, 2) - 3^6 D(1, 3) - D(1, 4) + 3 D(1, 5) - 3^2 D(1, 6) + 3^3 D(1, 7)] \quad (18)$$

$$\bar{M}(j, 5) = M(j, 5) + \Delta M(j, 5) = M(j, 5) + \frac{1}{3^n + 1} \sum_{k=1}^n [b_{j,k} D(1, k)] \quad (19)$$

at the right-end.

The coefficients  $b_{j,k}$  are elements of another square matrix  $[B]$ , with the same property expressed in Eq. 15. The difference between these two matrices is in the elements of the principal diagonal. All the elements on the principal diagonal of matrix  $[B]$  are equal to

$$b_{j,k} = 3^n \quad (20)$$

in which  $j$  and  $k = 1, 2, \dots, n$ . All the other elements of this matrix are exactly the same as in the matrix for  $\bar{M}(j, 4)$ , described previously.

For  $n = \text{even}$ , the final moments  $\bar{M}(j, 1) \dots M(j, 7)$  are

$$\begin{aligned} \text{Column Moments } \bar{M}(1, 1) &= \bar{M}(1, 2) = M(1, 1) + \Delta M(1, 1) \\ &= M(1, 1) + \frac{1}{3^n - 1} \sum_{j=1}^n [(-1)^j \times (3)^j \times D(1, j)] \quad (21) \end{aligned}$$

$$\text{Column Moments } \bar{M}(j, 6) = \bar{M}(j, 7) \quad (22)$$

for  $j = 1, 2, \dots, (n - 1)$  as given in Eq. 9.

$$\begin{aligned} \text{Column Moments } \bar{M}(n, 6) &= \bar{M}(n, 7) = M(n, 6) + \Delta M(n, 6) = M(n, 6) \\ &- \frac{1}{3^n - 1} \sum_{j=1}^n [(-1)^j \times (3)^j \times D(1, j)] \quad (23) \end{aligned}$$

It is easily noticed that the only difference between Eqs. 21-23 and the corresponding Eqs. 8 and 10 is that each term under the summation sign has an opposite sign, and the denominator is changed from  $(3^n + 1)$  to  $(3^n - 1)$ .

Beam Moments  $\bar{M}(1,3) = -\bar{M}(1,2)$  given in Eq. 18

$$\bar{M}(j,3) = -\Delta M(j-1,5) \quad (\text{See Eq. 28}) \quad (24)$$

in which  $j = 2, 3, \dots, n$

$$\bar{M}(j,4) = M(j,4) - \frac{1}{2} D(1,j) + \frac{1}{3^n - 1} \sum_{k=1}^n [a_{j,k} D(1,k)] \quad (25)$$

The coefficients  $a_{j,k}$  are elements of a matrix similar to  $[A]$  for  $n = \text{odd}$  except for opposite signs. Therefore, the first row elements are

$$a_{1,k} = (-1)^{k+1} \times (3)^{k-1} \quad (26)$$

in which  $k = 1, 2, \dots, n$ . The first column elements are

$$a_{j,1} = (-1)^{j-1} \times 3^{n-j+1} \quad (27)$$

in which  $j = 2, 3, \dots, n$ .

$$\bar{M}(j,5) = M(j,5) + \Delta M(j,5) = M(j,5) + \frac{1}{3^{n-1}} \sum_{k=1}^n [b_{j,k} D(1,k)] \quad (28)$$

The  $b_{j,k}$  are elements of a matrix similar to the previous matrix  $[B]$ , in which  $n$  was an odd number. Eq. 20 does not apply for the elements are the same as those given in Eqs. 26 and 27 for matrix  $[A]$ .

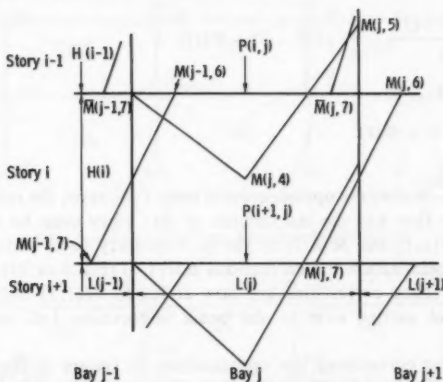


FIG. 3.— $j$  Bay of Any Story,  $i$

### Multi-story Frames

**Top Story ( $i = 1$ ).—**Whatever was said so far for a single-story frame again applies to the top story with respect to first admissible moments, optimization and final moments.

### Any Other Story ( $i = 2, 3, \dots, m$ )

**First Admissible Moments.**—Again, in the formation of the sway and beam moments two steps are utilized.

**Sway Moments.**—The sway moments of any  $i$ th story are obtained from the sway moments of the story just above it, story  $i - 1$ , (Fig. 3) plus an additional

correction coming from the  $i$ th story. Therefore, we have

$$C(i) = C(i-1) + \frac{H(i)}{2(n+1)} \sum_{i=1}^i W(i) \dots \dots \dots (29)$$

and all the column moments equal

$$M(1,1) = M(1,2) = M(j,6) = M(j,7) = -C(i) \dots \dots \dots (30)$$

in which  $j = 1, 2 \dots n$ .

**Beam Moments.**—The corrections to the beam moments due to the restoration of joint equilibrium now are larger than those in the top story because the column moments of the story above  $i$  and of the  $i$ th story itself need to be compensated for in the second step of the procedure to obtain first admissible moments. Thus, we have

$$M(1,3) = C(i-1) + C(i) \\ M(j,3) = 0 \dots \dots \dots (31)$$

in which  $j = 2, 3 \dots n$ .

$$M(1,4) = \frac{P(i,1) L(1)}{4} \\ M(j,4) = \frac{P(i,j) L(j)}{4} - \frac{1}{2} [C(i-1) + C(i)] \dots \dots \dots (32)$$

in which  $j = 2, 3 \dots n$ .

$$M(j,5) = C(i-1) + C(i) \dots \dots \dots (33)$$

in which  $j = 1, 2 \dots n$ .

**Optimization.**—Before the optimization of story  $i$  can start, the joint equilibrium at the top of the first and the last column of that story must be reestablished. The moments  $\bar{M}(1,1)$  and  $\bar{M}(n,7)$  of the  $(i-1)$  story have undergone during  $(i-1)$ th story optimization the corrections  $\Delta M(1,1)$  (Eq. 8 or 21) and  $\Delta M(n,7)$  (Eq. 10 or 23). These corrections are now added to  $M(1,3)$  and  $M(n,5)$  with opposite sign and carried over to the beam midsection, i.e., to  $M(1,4)$  and  $M(n,4)$ .

After these two corrections the optimization procedure is the same as for a single story as explained earlier. Occasionally, it will happen that in the last bay ( $j = n$ ) the moment  $M(n,4) < M(n,5)$ . In that case, the correction  $D(i,n)$  would be negative:

$$D(i,n) = \frac{2}{3} [M(n,4) - M(n,5)] \dots \dots \dots (34)$$

and, therefore, this correction is taken as zero. When the last two moments at the end of the optimization process are equalized and equilibrium at the top of the last column is reestablished, to satisfy sway equilibrium the negative of the same amount is added to  $\bar{M}(n,7)$ .

Eqs. 8-28 are valid for the final moments of the  $i$ th story. Only  $C(1)$  has everywhere to be replaced by  $C(i)$ .



Coefficient matrices developed for any previous story are the same for any other story provided the number of bays,  $n$ , for these two stories is the same. If  $n(i) \neq n(i-1)$ , new matrices must be generated using the same formulas.

#### COMPUTER PROGRAMS

A computer program was written by authors in BASIC language for an HP9830A programmable desk calculator with 4K R-W memory. This program can handle

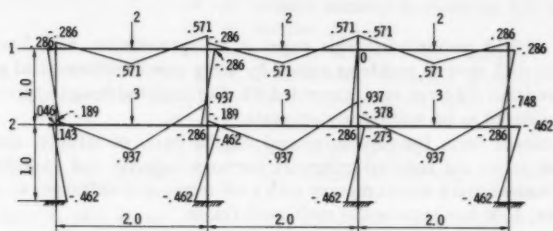


FIG. 4.—Example. Loading and Final Moments (10)

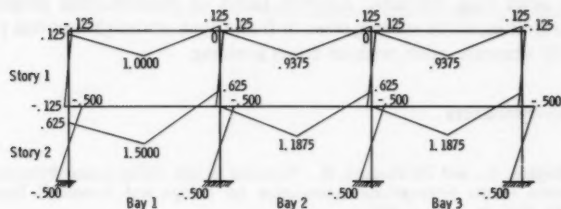


FIG. 5.—Example. First Admissible Moments

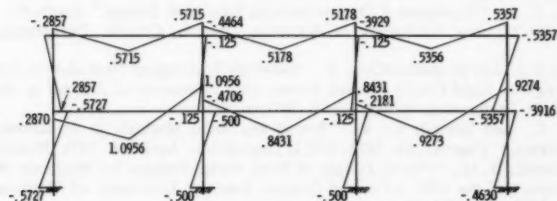


FIG. 6.—Example. Final Optimized Moments

up to a four-story, four-bay unsymmetrically loaded frame and up to 15 bays for a single-story frame.

**Example.**—To illustrate the application of the method and check its accuracy an example was taken from Professor John Munro, of Imperial College in London, England (10). In Fig. 4, the two-story, three-bay frame, its loading and its

final optimized bending moments are shown. The "weight" obtained by Munro was 12.040. The writers achieved a weight of 12.054, an error of 0.12%. Professor Munro first used a so-called "mesh unsafe" program followed by "nodal unsafe" program. In each case, the kinematic variables were evaluated directly and the static variables were obtained as the simplex multipliers at optimality (Figs. 5 and 6).

## CONCLUSIONS

1. The method presented in this paper is an approximate one; however, a comparison with several problems solved by using exact mathematical programming showed that the error never exceeded 4%. For an initial design approximation this is considered to be sufficiently accurate.

2. The closed form formula developed on the basis of infinite, decreasing geometrical series cut reduced computer memory capacity and execution time to such an extent that a minicomputer with a 4K memory is sufficient to optimize a four-story, four-bay rectangular multistory frame.

3. Although the described cycling process might look complicated, the use of equations to determine the final moments is simple. For this reason the development of a program for any available desk calculator is easy.

4. Any other long computer program based on mathematical programming that requires as input the starting sizes of frame elements might use this program to get fairly accurate input, without much guessing.

## APPENDIX I.—REFERENCES

1. Anderheggen, E., and Thürlimann, B., "Optimal Design Using Linear Programming," Publication of the International Association for Bridge and Structural Engineering (IABSE), Vol. 26, 1966, p. 555.
2. Boulton, N. S., written discussion of the paper "Plastic Design of Steel-Framed Structures," by J. Heyman, Final Report 4th Congress IABSE, Cambridge, England, 1953, pp. 113-118.
3. Cornell, C. A., "Examples of Optimization in Structural Design," *Study No. 1, Solid Mechanics Division*, University of Waterloo, Ontario, Canada, 2nd printing, 1970, p. 149.
4. Fenves, S. J., and Gonzalez-Caro, A., "Network Topological Formulation of Analysis and Design of Rigid-Plastic Framed Structures," *International Journal of Numerical Methods in Engineering*, Vol. 3, No. 3, 1971, p. 425.
5. Fleury, C., and Schmit, L. A., "Primal and Dual Methods in Structural Weight Minimization," *Preprint No. 3473*, ASCE Convention, April 2-6, 1979, Boston, Mass.
6. Kuzmanović, B. O., "Plastic Design of Steel Portal Frames for Minimum Weight," *Final Report of the NSF Advanced Science Seminar*, University of Houston, June-August, 1968, pp. A9.1-18.
7. Kuzmanović, B. O., and Willems, N., "Automatic Optimum Plastic Frame Design," Publication of IABSE, Vol. 33-II, 1973, pp. 131-147.
8. Kuzmanović, B. O., and Willems, N., "Optimum Plastic Design of Steel Frames," *Journal of the Structural Division*, ASCE, Paper No. 9154, Vol. 98, No. ST8, Aug., 1972, pp. 1697-1724.
9. Livesley, R. K., "The Automatic Design of Structural Frames," *Quarterly Journal of Mechanics and Applied Mathematics*, Vol. 9, Pt. 3, 1956, pp. 257-278.
10. Munro, J., "Optimal Plastic Design," *Proceedings of NATO-ASI Institute*, University of Waterloo, August 2-12, 1977, Pergamon Press, New York, N.Y., 1978.

## APPENDIX II.—NOTATION

*The following symbols are used in this paper:*

$a_{j,k}$	=	elements of matrix, [A];
$b_{j,k}$	=	elements of matrix, [B];
$i$	=	story number;
$j$	=	bay number;
$k$	=	column number in matrices, [A] and [B];
$m$	=	number of stories;
$n$	=	number of bays in any story $i$ ;
$C(i)$	=	column wind moments in story $i$ ;
$D(i, j)$	=	basic correction moment;
$H(i)$	=	height of story $i$ ;
$L(j)$	=	span length of a bay $j$ ;
$M(1, 1), M(1, 2), M(j, 6), M(j, 7)$	=	first admissible column moments, in which $j = 1, 2, \dots, n$ ;
$M(j, 3), M(j, 4), M(j, 5)$	=	first admissible beam moments, in which $j = 1, 2, \dots, n$ ;
$\bar{M}(1, 1), \bar{M}(1, 2), \bar{M}(j, 6), \bar{M}(j, 7)$	=	optimized column moments;
$\bar{M}(j, 3), \bar{M}(j, 4), \bar{M}(j, 5)$	=	optimized beam moments; and
$\Delta M$	=	total moment change due to optimization.



## AN EVALUATION OF INELASTIC SEISMIC DESIGN SPECTRA<sup>a</sup>

By Stephen A. Mahin,<sup>1</sup> M. ASCE and Vitelmo V. Bertero,<sup>2</sup> F. ASCE

### INTRODUCTION

Because of economic considerations, structures are usually designed so that some of the energy input during severe earthquake ground motions is dissipated by means of inelastic deformations. These deformations, however, must be controlled in order to prevent collapse due to exhaustion of the structure's energy dissipation capacity or due to excessive lateral displacements. Moreover, any economic savings made possible by allowing inelastic response should be reconciled with potential costs of damage to the building's structural system, nonstructural elements, and contents. Proper selection of seismic design forces, accounting for the expected intensity of ground shaking and the acceptable severity of inelastic response, is a complex task, and current building code recommendations (38) offer only qualitative guidelines. A number of other design methods, which explicitly account for these and other parameters, have been recently proposed. However, because of the variety of such methods available and the many simplifying assumptions generally involved in their development, it is not clear how much confidence a designer can place in them.

The purpose of this paper is to review general methods available for specifying seismic design forces for structures that can be allowed to suffer limited amounts of inelastic deformations during severe earthquake ground motions and to examine some of the problems that exist in their specification. Following a brief review of available procedures, these problems are illustrated by evaluating the reliability of two representative methods. This evaluation focuses, in turn, on three interrelated problem areas: (1) The ability of the methods to limit peak inelastic deformations to specified values is examined for a wide variety of ground motion records; (2) the sensitivity of computed inelastic response to uncertainties in structural damping and hysteretic characteristics is investigated; and (3) the adequacy of the maximum displacement ductility factor, i.e., the ratio of maximum

<sup>a</sup>Presented at the April 24-28, 1978, ASCE Spring Convention and Exhibition, Pittsburgh, Pa. (Preprint 3278).

<sup>1</sup>Asst. Prof. of Civ. Engrg., Univ. of California, Berkeley, Calif. 94720.

<sup>2</sup>Prof. of Civ. Engrg., Univ. of California, Berkeley, Calif. 94720.

Note.—Discussion open until February 1, 1982. To extend the closing date one month, a written request must be filed with the Manager of Technical and Professional Publications, ASCE. Manuscript was submitted for review for possible publication on July 9, 1980. This paper is part of the Journal of the Structural Division, Proceedings of the American Society of Civil Engineers, ©ASCE, Vol. 107, No. ST9, September, 1981. ISSN 0044-8001/81/0009-1777/\$01.00.

to yield displacements, as the primary design criterion is assessed in view of information obtained on other key response parameters, such as maximum and permanent displacements, maximum cyclic inelastic deformations, numbers of yield excursions and reversals, and energy dissipation demands. To simplify this presentation, emphasis will be placed on single degree-of-freedom (SDOF) systems.

#### REVIEW OF METHODS FOR OBTAINING INELASTIC DESIGN RESPONSE SPECTRA

Preliminary design forces can be derived from inelastic design response spectra (IDRS) which usually plot, as a function of period, the yielding seismic resistance coefficient or pseudo-acceleration required for a specified level of inelastic response. A number of methods exist for constructing such IDRS.

**Time History Analysis Methods.**—Nonlinear time history response analyses provide the most reliable means for constructing an IDRS for a given ground motion. For SDOF systems, the equations of motion may be conveniently nondimensionalized in terms of the fundamental period,  $T$ ; the viscous damping ratio,  $\xi$ ; and a parameter,  $\eta$ , equal to the system's yield resistance,  $F_y$ , divided by the product of its mass,  $M$ , and the peak ground acceleration,  $A$  (9, 20, 24, 27, and 33). Results of parametric studies based on such formulations can be used to estimate the strength required to limit the maximum displacement ductility demand, or another suitable response parameter, to a specified value for the earthquake record considered (7-9, 18, 19, 22, 28, and 39-41). Statistical or probabilistic analysis of these estimates for an ensemble of recorded or artificial (13) accelerograms with characteristics appropriate for a site can be used to develop IDRS corresponding to the specified maximum inelastic response (8, 20, 24, 27, and 33). While IDRS constructed in this manner are powerful tools for preliminary design, the efforts needed to obtain the appropriate ensemble of accelerograms and to construct the corresponding IDRS are usually excessive for most design projects.

**Random Vibration Analysis Methods.**—Random vibration theory can be used to estimate inelastic response in probabilistic terms. While an exact solution for nonlinear systems has not yet been derived, a number of approximate solutions exist (5, 14, 20, and 33).

**Methods Based on Linear Elastic Response Spectra.**—Because of the technical and practical difficulties involved with the preceding methods, it is more common in practice to use approximate methods that modify a smoothed linear elastic design response spectrum (LEDRS) developed for a site. One approach to this problem is to replace the inelastic system by an equivalent linear elastic system and use the LEDRS directly (16, 17, 33, and 34). The effective stiffness and viscous damping coefficients for the linearized system can be derived on the basis of a steady-state hysteretic loop corresponding to a specified displacement ductility factor (33,34). However, since seismic response is not steady state, nonlinear time history analyses using appropriately selected ensembles of ground motions are still required to determine the effective stiffness and damping of the linearized system (17).

In other methods, the LEDRS is modified to obtain an IDRS using factors that depend on the acceptable level of inelastic response. The simplest method for doing this is to reduce the design forces obtained using the LEDRS by

a factor that is independent of structural period. The tentative design recommendations of the Applied Technology Council (ATC) are representative of this approach (36) and are used as the basis of some of the following examples. The ATC suggests that, at the point of first significant yielding, a structure should be able to resist a total lateral seismic force equal to its total gravity load (weight of all reactive masses), times a seismic design coefficient,  $C_s$ , which is given by

$$C_s = \frac{1.2 A_v S}{RT^{2/3}} \dots \dots \dots (1)$$

which need not exceed  $2.5 A_a R^{-1}$  for rock or firm soil conditions and in which  $A_a$  represents the effective peak acceleration;  $A_v$  represents the effective peak velocity-related acceleration,  $R$  is an empirical seismic response modification coefficient intended to account for the damping as well as the inelastic deformation capacity of the structure; and  $S$  = a seismic coefficient accounting for the soil profile characteristics at the site. The ATC also indicates that the maximum

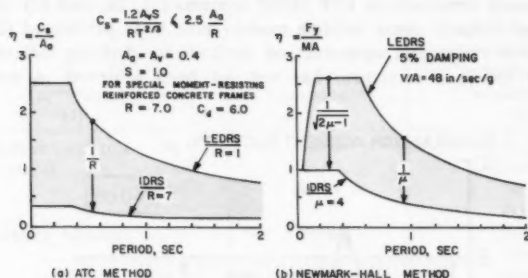


FIG. 1.—Comparison of Methods for Constructing IDRS from LEDRS: (a) ATC Method; (b) Newmark-Hall Method

first-order lateral displacements of such structures can be estimated as the product of a factor,  $C_d$ , times the displacement when first significant yielding occurs, i.e., the nominal displacement ductility factor equals  $C_d$ . In some of the subsequent examples, these variables were specified to correspond to reinforced concrete, special (ductile) moment-resisting frames located on stiff soil in a region of severe seismic exposure ( $A_a = 0.4$ ,  $A_v = 0.4$ ,  $C_d = 6$ ,  $R = 7$ , and  $S = 1$ ). The resulting IDRS is shown in Fig. 1(a).

In other methods for obtaining IDRS from LEDRS, modification factors have been analytically derived by evaluating the response of elasto-perfectly plastic (EPP) SDOF systems, and are usually expressed as a function of period as well as of the maximum specified displacement ductility,  $\mu$  (2, 20, 25–29, 33, 40, and 41). Since these types of reduction factors are based on results obtained for idealized structural models subjected to limited numbers of ground motion records, designers have usually been cautioned against applying them to structures that exhibit substantially different hysteretic or damping characteristics or experience significantly different types of ground motion records.

Based on analytical studies, Newmark and Hall (28) concluded that: (1) For short period structures, any significant reduction in design forces required for elastic response would result in unacceptably large ductilities; (2) for moderate period structures, the energy absorbed by an inelastic structure at its maximum displacement approximates that absorbed by an elastic system resulting in a strength modification factor of  $(2\mu - 1)^{-1/2}$ ; and (3) for relatively long period structures, the maximum displacements of elastic and inelastic systems were nearly equal, so a strength modification factor of  $\mu^{-1}$  would be appropriate. This well-known method (28) is representative of this general approach for obtaining IDRS from LEDRS, and is used to establish the strength of structures considered in some of the subsequent examples. In most of the examples considered, a maximum displacement ductility factor of 4 is specified, and the LEDRS is developed, (28) assuming a ratio of peak ground velocity,  $V$ , to acceleration,  $A$ , of 48 in./sec/g (1,220 mm/s/g) and 5% viscous damping. The IDRS corresponding to these values is shown in Fig. 1.

**Application to Multiple Degree-of-Freedom Systems.**—Most IDRS are not strictly applicable to conventional multistory buildings since it is usually very difficult to idealize such structures as EPP SDOF systems (21, 28, and 30). A number of studies of inelastic shear building models have been performed (2, 20, 23, and 42); however, general agreement on methods for deriving inelastic design story shear for such structures has not yet been achieved. A number of

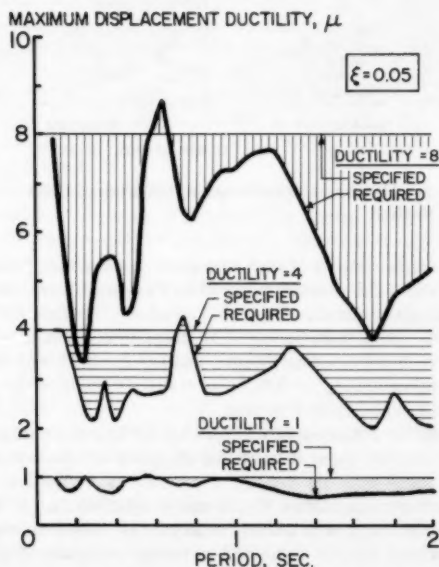


FIG. 2.—Comparison of Required and Specified Ductilities for EPP SDOF Systems Subjected to 1940 El Centro Record (S00W)—Newmark-Hall IDRS



investigators have either proposed or derived approximate seismic design forces for multistory building structures based on elastic root-mean-squared modal superposition techniques using the initial dynamic characteristics of the structure and an IDRS obtained for an SDOF system (3, 4, 15, 27, 30, 35, and 43). Although convenient for preliminary design, such approximate methods have been found to have a number of defects (3, 7, and 15). Additional information regarding problems in applying IDRS to multiple degree-of-freedom systems is presented in Bertero, et al. (7).

#### DISPLACEMENT DUCTILITY DEMANDS FOR VARIOUS GROUND MOTIONS

Since most IDRS use the displacement ductility factor as the primary index of structural response, it is desirable to assess the reliability with which they

TABLE 1.—Standard-Type Ground Motion Records Considered

Earthquake (1)	Component (2)	$V/A$ , in inches (millimeters) per second per gravitational acceleration (3)
1934, Lower California (El Centro)	S00W	51.39 (1,305.3)
	S90W	24.95 (633.7)
1935, Helena, Montana	S90W	36.14 (917.0)
	S00W	19.77 (502.2)
1940, Imperial Valley (El Centro)	S00W	42.80 (1,087.1)
	S90W	67.89 (1,724.4)
1949, Western Washington (Olympia)	S86E	24.04 (610.6)
	S04W	51.16 (1,299.5)
1952, Kern County (Taft)	N21E	39.78 (1,010.4)
	S69E	38.90 (988.1)

limit inelastic deformations to specified values. In this section, displacement ductility demands are presented for ideal EPP SDOF systems, ranging in period from 0.1 sec–2.0 sec, designed using IDRS suggested by Newmark and Hall (28) and by the ATC (36). Comparison of ductility demands obtained for a variety of ground motions with the specified ductility values gives an indication of the reliability of these representative types of IDRS. For these analyses,

the ground motion records were normalized to have the same peak acceleration as used in developing the IDRS.

**Newmark-Hall Type IDRS.**—Computed ductility demands corresponding to the basic Newmark-Hall IDRS with specified ductilities of 1, 4, and 8 are shown in Fig. 2 for the S00W component of the 1940 El Centro record. Ductility demands vary considerably with period and can differ significantly from the specified value. For this record, ductility demands are usually conservatively less than the specified values; the maximum discrepancy increases with increasing values of specified ductility so that, for a specified ductility of 8, the actual ductility demands are as low as 43% of this value.

**TABLE 2.—Average Ductilities (and Coefficients\* of Variation given between) for SDOF Systems with Periods between 0.1 and 2.0 Seconds, Subjected to Standard Ground Motions**

Type of ductility factor (1)	NEWMARK-HALL IDRS				ATC IDRS	
	$V/A = 48$ inches per second per gravitational acceleration, (1,220 millimeters per second per gravitational acceleration) $\mu = 4$		$V/A = 39.68$ inches per second per gravitational acceleration, (1,010 millimeters per second per gravitational acceleration) $\mu = 4$	$V/A = 48$ inches per second per gravitational acceleration, (1,220 millimeters per second per gravitational acceleration) $\mu = 8$	$R = 7; C_d = 6$	
	EPP model (2)	Stiffness degrading model (3)	EPP model (4)	EPP model (5)	EPP model (6)	Stiffness degrading model (7)
Maximum displacement	2.85 (54)	2.59 (46)	3.44 (57)	6.25 (59)	9.54 (59)	9.02 (53)
Cyclic displacement	3.26 (56)	3.17 (50)	4.11 (61)	8.11 (69)	12.65 (71)	13.37 (63)
Permanent displacement	1.21 (103)	0.55 (83)	1.53 (104)	2.92 (99)	4.19 (105)	2.01 (81)
Hysteretic energy	7.13 (70)	8.90 (62)	10.08 (70)	26.59 (66)	52.37 (66)	47.51 (47)

\*Coefficient of variation given as a percentage.

**Results for Standard Ground Motion Records.**—Ductility demands were also computed for 10 standard accelerograms representative of severe ground motions recorded on firm ground at moderate epicentral distances (Table 1). The results are plotted in Fig. 3 and summarized in Table 2. For a specified ductility of 4 the average maximum displacement ductilities computed for these records [Fig. 3(a)] are generally smaller (29%) than the specified value. The computed displacement ductilities are very sensitive to the ground motion record as well as to the period; values as high as 8 and as low as 0.5 were obtained in some

cases. This large variation is indicated by the coefficients of variation plotted in Fig. 3(a), which average 54% over the entire period range (Table 2). For a specified ductility of 8, the same general trends are observed, as can be seen in Fig. 3(c) and Table 2. In this case, the ductility demands average 22% less than the specified value, indicating that the basic Newmark-Hall type IDRS is somewhat less conservative for higher ductility values, as has been noted (20, and 29). Moreover, ductility demands in excess of 27 were computed in some cases. Such high ductilities may be difficult to develop in practice.

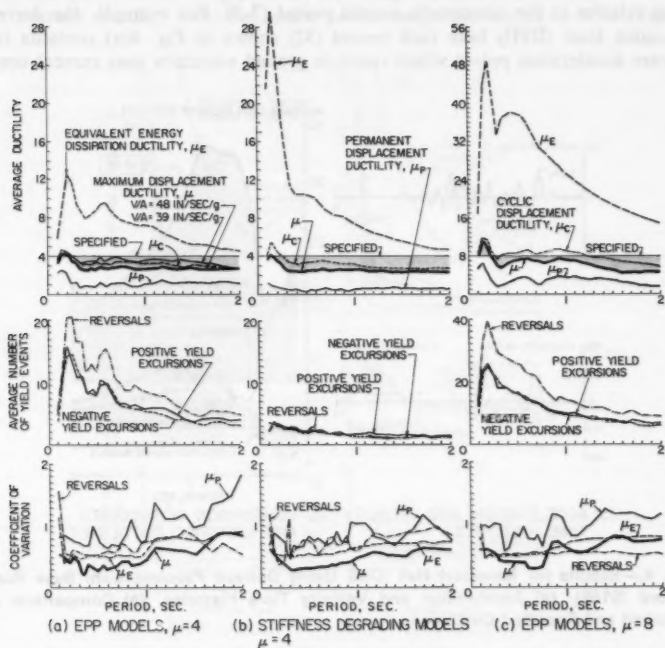


FIG. 3.—Response of SDOF Systems Design Using Newmark-Hall IDRS with  $\xi = 0.05$  and  $V/A = 48$  in./sec/g (1,219 mm/s/g) Subjected to Standard Records: (a) EPP Models with  $\mu = 4$ ; (b) Stiffness Degrading Models with  $\mu = 4$ ; (c) EPP Models with  $\mu = 8$

One possible reason for the relatively large difference between the specified and average ductility demands in the intermediate period range is that the LEDRS used is based on a  $V/A$  ratio of 48 in./sec/g (1,220 mm/s/g) as commonly recommended for firm soil sites (28). The average  $V/A$  ratio for the standard ground motions considered in Table 1, however, is only 39.68 in./sec/g (1,010 mm/s/g), indicating that design forces could be reduced for these records in this period range. When the correct average  $V/A$  ratios used to derive

the IDRS the ductility demands, shown in Fig. 3(a) and Table 2, average only 14% less than the specified value.

**Results for Near-Fault Ground Motion Records.**—The importance of proper estimation of the LEDRS is also illustrated by the response of systems to records containing severe, long-duration acceleration pulses. Recently obtained accelerograms and theoretical studies (10, 11, and 37) indicate that such ground motions may occur near the fault rupture, as well as at some other locations. While such excitations are not critical for most elastic systems, unusually large ductility demands can develop in yielding systems when the duration of the pulse is long relative to the structure's natural period (7-9). For example, the derived Pacoima Dam (DPD) base rock record (32) shown in Fig. 4(a) contains two severe acceleration pulses which result in ground velocities near current upper

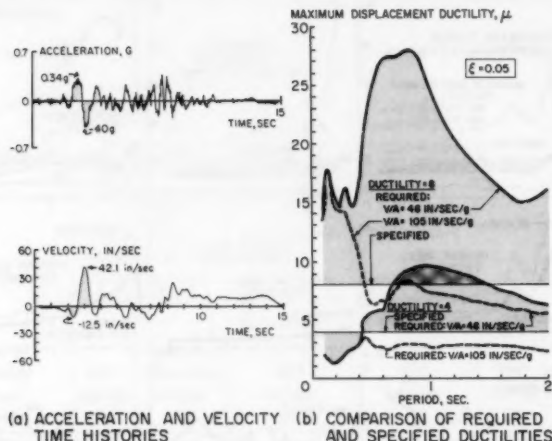


FIG. 4.—Results for Newmark-Hall IDRS Using Derived Pacoima Dam Base Rock Record (S16E): (a) Acceleration and Velocity Time Histories; (b) Comparison of Required and Specified Ductilities

bound estimates (1, 12, and 28). For a specified ductility of 4, the basic Newmark-Hall IDRS is unconservative, especially for periods greater than 0.4 sec, [Fig. 4(b)]. For a specified ductility of 8, ductility demands of nearly 30 were required in some period ranges. If the EPP SDOF systems considered were designed using a modified Newmark-Hall IDRS based on a V/A ratio of 105 in./sec/g (2,670 mm/s/g), which corresponds to the actual accelerogram values, displacement ductilities are always significantly smaller than specified when the specified ductility is 4. However, when the specified displacement ductility is 8, use of increased design forces corresponding to a realistic V/A ratio does not achieve conservative results in the short period range.

**ATC Type IDRS.**—The tentative ATC design recommendations utilize a constant reduction factor over the entire period range, whereas the reduction factors for the Newmark-Hall type method vary (Fig. 1). For comparable LEDRS

this usually results in substantially lower design forces for the ATC method in the short period range. The effect of this difference is examined below.

**Results for Standard Ground Motion Records.**—The ground motion records listed in Table 1 were used to compute the inelastic response of EPP SDOF systems designed according to the ATC IDRS shown in Fig. 1. In these analyses, viscous damping was assumed to be 5% of critical. As indicated in Fig. 5, the average displacement ductility values are slightly less than the specified value of 6 for periods in excess of 1.5 sec. However, ductility demands increase significantly with decreasing periods, especially for periods less than 0.4 sec. The average ductility over the entire period range considered is 9.54 (Table

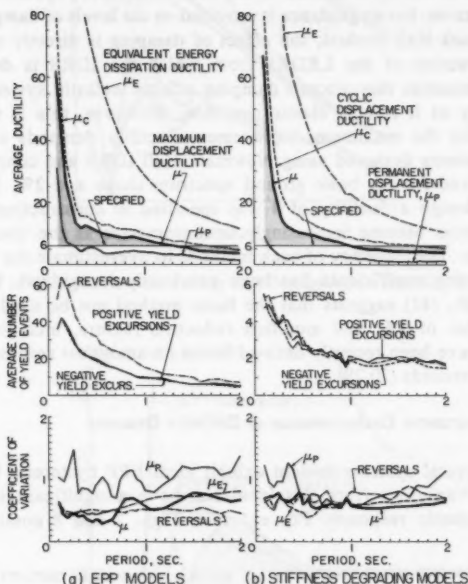


FIG. 5.—Response of SDOF Systems Designed Using ATC IDRS with  $R = 7$  and  $C_d = 6$  Subjected to Standard Records,  $\xi = 0.05$ : (a) EPP Models; (b) Stiffness Degrading Models

2), and at a period of 0.1 sec an average ductility in excess of 60 is obtained. While the coefficients of variation are only slightly larger than those obtained with the Newmark-Hall IDRS, the large average ductilities in the short and moderate period ranges result in very large variations in ductilities. For example, for a period of 0.1 sec, computed ductilities ranged from 2.8 to more than 130. While it may be possible to detail short period structures to develop such large ductilities, and a number of factors not considered in these analyses, such as the use of minimum rather than probable material strengths in design, conservatism in proportioning and detailing due to practical considerations

or code limitations on member sizes and strengths, contribution of nonstructural components; soil-structure interaction, etc., could reduce the actual ductility demands on short period structures, it is evident that a constant reduction factor, such as used in the ATC method, does not give the designer consistent control over the expected structural damage.

#### INFLUENCE OF VISCOUS DAMPING ON DUCTILITY DEMANDS

Small amounts of viscous damping can substantially reduce the response of elastic systems (7,28). The effect of damping on nonlinear systems is apparently accounted for in the ATC method in the reduction values specified for various types of structures, but no guidance is provided on the levels of damping assumed. In the Newmark-Hall method, the effect of damping is directly accounted for in the construction of the LEDRS from which the IDRS is derived. Thus, this method assumes that viscous damping affects inelastic systems in exactly the same way as it affects elastic response. However, this is not the case, as indicated by the maximum displacement ductility demands shown in Fig. 6 for EPP systems designed using Newmark-Hall IDRS and constructed using LEDRS, derived for the basic ground spectrum shape and 2%, 5%, and 10% damping. Although a ductility of 4 was specified in constructing each IDRS, the design forces become increasingly unconservative as the viscous damping ratio increases. The tendency of such methods to overestimate the effectiveness of large damping coefficients has been previously recognized. For example, Veletsos, et al., (41) suggests that the basic method not be used for damping ratios in excess of 5%, and modified reduction factors, including the effect of damping, have been recently derived based on analytical results for different ensembles of records (20,29).

#### INFLUENCE OF HYSTERETIC CHARACTERISTICS OF DUCTILITY DEMANDS

Actual structural systems seldom exhibit ideal EPP hysteretic behavior (21, 30, and 43). Variations from this ideal can have a significant effect on the structure's inelastic response. For example, Figs. 7 and 8 compare ductility

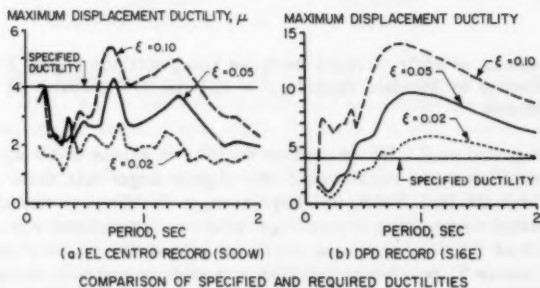


FIG. 6.—Effect of Damping on Ductility Demand—Newmark-Hall IDRS with  $\mu = 4$ : (a) El Centro (S00W) Record; (b) DPD (S16E) Record

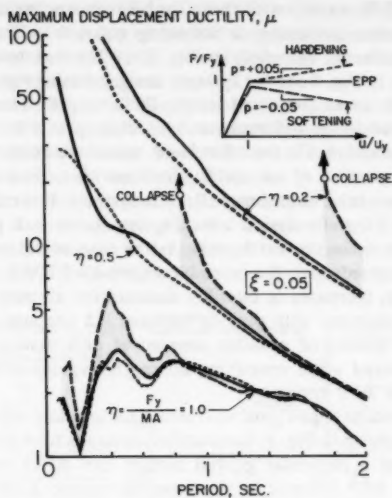


FIG. 7.—Effect of Deformation Hardening and Softening on Ductility Demands—DPD Record, S16E

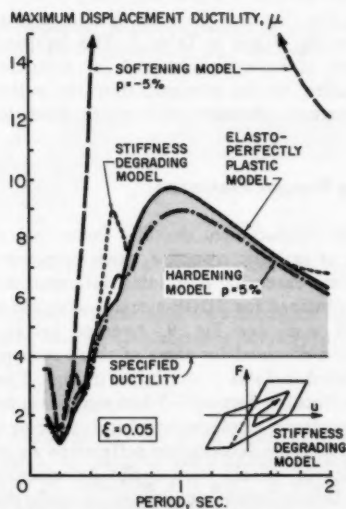


FIG. 8.—Effect of Mechanical Model on Ductility Demand of Structures Designed Using the Basic Newmark-Hall IDRS,  $\mu = 4$ —DPD Record, S16E

demands for ideal EPP models with those for bilinear mechanical models having post-yield deformation hardening or softening equal to a fraction,  $p$ , of the initial structural stiffness. The plots in Fig. 7 are for structures with constant  $\eta$  values, and those in Fig. 8 are for systems designed using the basic Newmark-Hall IDRS, in both cases subjected to the DPD record. The results indicate that the effect of moderate deformation hardening,  $p = 5\%$ , is only marginal and generally conservative. On the other hand, moderate deformation softening,  $p = -5\%$ , representative of geometric nonlinearities, tends to significantly increase deformations in all but the most flexible systems. For example, according to Fig. 7, for  $\eta = 0.5$ , deformation softening structures with periods less than 0.8 sec would collapse for this earthquake. In the case of deformation softening systems designed according to the basic Newmark-Hall IDRS, the DPD record results in significant increases in ductility demand for all periods and collapse would result for structures with periods between 0.5 sec and 1.6 sec (Fig. 8). Thus, the adverse effects of possible sources of deformation softening must be carefully considered when specifying acceptable values of ductility for use with IDRS based on EPP systems.

Structures can exhibit significant stiffness deterioration when cycled in the inelastic range. As shown in Fig. 8, the ductility demands for a stiffness degrading system subjected to a particular ground motion can differ significantly from those obtained for EPP systems in some period ranges. However, it appears that on average, for the standard earthquakes listed in Table 1, the differences are generally small. This can be seen by comparing the average ductility demands for stiffness degrading systems with corresponding values for EPP systems, for example, results for systems designed according to the Newmark-Hall IDRS,  $\mu = 4$ , are shown in Fig. 3 and in Table 2. Similar comparisons can be made for the ATC IDRS in Fig. 5 and in Table 2. The displacement ductilities and associated coefficients of variation obtained for stiffness degrading systems are both slightly smaller, on the average, over the entire period range than they are for EPP systems. Similar observations have been made by other researchers (29,31).

#### CONSIDERATION OF OTHER RESPONSE PARAMETERS

While the maximum displacement ductility factor is a common and useful index of the severity of inelastic response, other response parameters may be more meaningful in some cases. To assess this, information on various response parameters has been obtained for SDOF systems designed using the Newmark-Hall and ATC IDRS, e.g., see Fig. 9. Average values and corresponding coefficients of variation obtained for some of these response parameters using the ground motions listed in Table 1 are shown in Figs. 3 and 5 and in Table 2.

**Cyclic Displacement Ductility Factors.**—When significant inelastic displacement reversals occur, the maximum displacement ductility factor does not realistically measure the maximum inelastic deformation suffered by a system. Real structures have limited capacities to sustain such cyclic deformations (6). To quantify the magnitude of the largest inelastic excursion, a cyclic displacement ductility factor,  $\mu_c$ , can be defined (21) as indicated in Fig. 10. Values of  $\mu_c$  will usually be similar to those for  $\mu$ , except where significant displacement reversals occur. The average cyclic ductility developed by EPP systems designed using the



Newmark-Hall IDRS is 14% greater than the average maximum displacement ductility for a specified ductility of 4 and 30% greater when the specified ductility is 8 (Table 2). For the ATC IDRS, the differences are greater, especially for stiffness degrading systems.

**Displacement and Drift Limitations.**—Because of a desire to mitigate the adverse effects of geometric nonlinearities or to control damage to deformation sensitive nonstructural components, it may be necessary to limit maximum displacements or interstory drifts. The curves in Fig. 9(b) clearly indicate that the maximum displacements, here normalized by the peak ground acceleration, increase significantly with increasing period, even though the maximum displacement ductilities are nearly constant or even decrease for periods in excess of 1 sec. Consequently, specified ductilities may have to vary with period to account

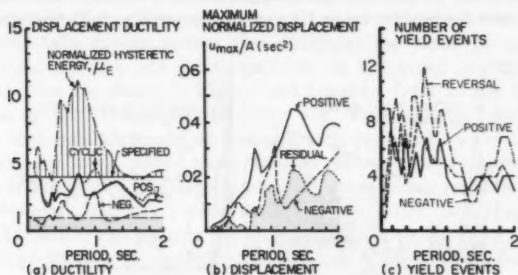


FIG. 9.—Response Envelopes for El Centro Record (S00W)—Newmark-Hall IDRS,  $\mu = 4$ ,  $\xi = 5\%$ : (a) Ductility; (b) Displacement; (c) Yield Events

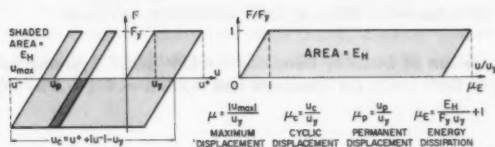


FIG. 10.—Definition of Alternate Ductility Factors

for displacement limitations. For example, for a maximum allowable displacement,  $u_{limit}$ , the corresponding limiting displacement ductility,  $\mu_{limit}$ , is

$$\mu_{limit} = \frac{u_{limit}}{u_y} = \frac{4\pi^2 M}{T^2 F_y} u_{limit} = \frac{4\pi^2}{\eta T^2 A} u_{limit} \quad (2)$$

In practice, limiting displacements are often specified in terms of an allowable average story drift index,  $\Theta$ , equal to the limiting displacement divided by the height of the structure,  $H$ . Assuming  $T = \alpha H^\beta$ , in which  $\alpha$  and  $\beta$  = empirical constants (36), Eq. 2 can be rewritten in terms of  $\Theta$ :

$$\mu_\Theta = \frac{4\pi^2 \gamma}{\eta \alpha^{1/\beta} T^{2-1/\beta} A} \quad (3)$$

in which  $\gamma$  relates the maximum displacement of a multiple degree-of-freedom system to that of an equivalent SDOF system. For a single-story structure,  $\gamma$  equals unity, whereas for multistory systems with uniformly distributed mass vibrating with a displaced shape varying linearly with height,  $\gamma$  equals 2/3. These deformation limited ductilities are plotted in Fig. 11 for the case where  $\alpha = 0.025$ ,  $\beta = 0.75$ ,  $\gamma = 0.67$ , and  $\Theta = 0.01$ . The  $\eta$  values correspond to the IDRS in Fig. 1, and  $A$  equals 40% of gravity. For these values, relatively large ductilities can be tolerated for periods less than 0.3 sec. For systems designed in accordance with the basic Newmark-Hall IDRS with a specified ductility of 4, none of the maximum displacement ductility demands computed for the standard records in Table 1 exceed this drift limitation. However, the average ductility demands for systems designed using the ATC IDRS exceed the drift limitation for periods less than 0.2 sec and demands for some records exceed the limit for periods up to 1.1 sec. Consequently, drift limitations, rather

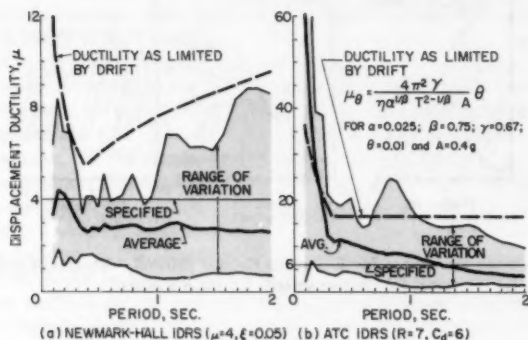


FIG. 11.—Comparison of Ductility Demands for EPP SDOF Systems with Ductility Corresponding to Drift Limit: (a) Newmark-Hall IDRS,  $\mu = 4$ ,  $\xi = 5\%$ ; (b) ATC IDRS,  $R = 7$ ,  $C_d = 6$

than the displacement ductility capacity, may control design in some cases. The values of ductility that can be accepted in design would be even smaller than indicated in Fig. 11 for higher values of  $A$  or lower values of  $\Theta$ .

**Permanent Displacements.**—Following an earthquake, inelastic systems may retain a permanent displacement. As indicated in Figs. 3 and 5 and in Table 2, these permanent displacements ( $\mu_p$ ) are generally a significant portion of the maximum displacement. For EPP systems, permanent displacements average more than 40% of the maximum displacements. Moreover, the coefficients of variation associated with these permanent displacements average about unity—nearly twice the value associated with maximum displacements. Permanent deformations are somewhat smaller for stiffness degrading systems. In some cases, large permanent displacements can make structural repair infeasible and can accumulate during severe aftershocks leading to structural instability.

**Number of Yield Excursions.**—As shown graphically in Figs. 3 and 5, all systems considered in these figures yield a large number of times. The average number

of yield events tends to increase with decreasing period, except in the very short period range. Yielding occurs about the same number of times in each direction, even though the maximum displacement is usually considerably larger in one direction than in the other. This results in a significant number of yield reversals. Especially large numbers of yield excursions and reversals are required for EPP systems when large ductilities are specified with the Newmark-Hall procedure, Fig. 3(c), or when large ductilities develop in the short period region with the ATC procedure [Fig. 5(a)].

**Energy Dissipation Demands.**—Because of the numerous cycles of reversed yielding, the total hysteretic energy dissipated by a system can be significantly larger than that inferred from its maximum displacement ductility demand or even from its maximum cyclic displacement ductility demand. A convenient comparative index of hysteretic energy dissipation is the equivalent energy dissipation ductility factor (21),  $\mu_E$ , numerically equal to the displacement ductility of a monotonically loaded system that dissipates the same energy, and has the same yield strength and initial stiffness, as the actual system (Fig. 10). Analytical results are shown in Figs. 3 and 5 and in Table 2. For the systems designed using the Newmark-Hall IDRS, Fig. 3 shows that relatively large dissipation demands are made on systems with periods between 0.2 sec and 1.0 sec. Systems in this period range develop relatively large numbers of yield excursions and reversals. The large number of yield reversals generally associated with the Newmark-Hall IDRS when the specified ductility is 8 [Fig. 3(c)] and with the ATC IDRS, especially in the short period range [Fig. 5(a)], also results in large energy dissipation demands. Stiffness degrading systems dissipate about the same amount of hysteretic energy as EPP systems, even though they do not reach their full yield capacity nearly as often, as shown in Figs. 3 and 5. Energy is dissipated hysteretically by EPP systems only when the full yield capacity is reached, whereas it is dissipated on nearly all cycles following the first yield for the stiffness degrading models considered. In view of the large energy dissipation demands that sometimes occur, caution should be exercised in selecting ductility or reduction factors for use in the design of structures with limited energy dissipation capacities.

## CONCLUSIONS

General methods for specifying preliminary seismic design forces for structures that can tolerate limited amounts of inelastic deformations have been reviewed. The reliability of approximate methods suggested by Newmark and Hall (28) and the ATC (36) for obtaining IDRS by modifying LEDRS has been evaluated in a series of analyses of idealized SDOF systems subjected to a variety of ground motions.

The results indicate that inelastic response is particularly sensitive to the actual excitation input as well as to the dynamic and mechanical characteristic of the structure. The scatter in peak response values obtained is so large that the approximate methods considered cannot be viewed as reliably limiting maximum ductility demands to specified values, even for ideal EPP SDOF systems. Nonetheless, such methods can provide very valuable guidelines for design, if their limitations and relationship to the overall design process is fully recognized. In particular, the large scatter in results reemphasizes the need

for proper selection of structural systems and materials, and for detailing to insure ductility capacities far in excess of the values specified in constructing IDRS.

Displacement ductility demands computed for EPP SDOF systems designed using the Newmark-Hall IDRS with 5% damping were on the average less than the specified values. The Newmark-Hall method became less conservative as the values of the specified ductility and viscous damping were increased. Differences between the values of  $A$  and  $V$  assumed in constructing the LEDRS and those corresponding to the actual ground motion experienced led to very large errors.

Computed displacement ductility demands for EPP SDOF systems designed using ATC recommendations also varied considerably with ground motion and structural period. The ability of the method to limit ductility demands to specified values was not uniform over the period range considered. In particular, average ductility demands substantially exceeded specified values in the short period range.

Results indicate that IDRS obtained from LEDRS tend to overestimate the effects of viscous damping on inelastic response. Stiffness deterioration and moderate amounts of deformation hardening generally appear to have small effects on ductility demands of SDOF systems. Moderate amounts of deformation softening, however, were found to increase ductility demands substantially in several cases.

For certain types of structures and occupancies, response parameters like maximum and permanent displacements, hysteretic energy dissipation demand, and number and magnitude of inelastic reversals may have to be considered in establishing seismic design forces, in addition to the maximum displacement ductility. Results indicate that drift limitations can control the design of structures, especially short period structures designed according to the ATC method. Moreover, permanent displacements averaged more than 40% of the maximum displacements for EPP SDOF systems designed by either method.

Additional studies are needed in several areas. In particular, it may be possible to reduce the scatter of response values by normalizing ground motions in terms of parameters other than peak ground acceleration, e.g., peak or incremental ground velocity, peak ground displacement, spectral intensity, Ayre's intensity, etc. (2, 16, 17, 26, and 24). More reliable methods are needed to account for variations in response associated with uncertainties in determining the initial period of a structure as well as its damping and hysteretic characteristics. Methods should also be developed to account for and mitigate the potentially adverse effects of deformation softening. The effect of severe, long duration earthquakes or intense aftershock sequences, or both, on design requirements should be investigated. The reliability of available method for establishing critical seismic design forces for multiple degree-of-freedom systems should be evaluated.

#### ACKNOWLEDGMENTS

The financial support of the National Science Foundation under Grants ENV 76-01419 and ENV 76-04262 is gratefully acknowledged. The assistance of E. Matthews and D. Ullman in preparing this paper is appreciated.

## APPENDIX I.—REFERENCES

1. Ambraseys, N. N., "Maximum Intensity of Ground Movements Caused by Faulting," *Proceedings of the Fourth World Conference on Earthquake Engineering*, Vol. 1, Santiago, Chile, 1969, pp. 154-171.
2. Anagnostopoulos, S. A., "Nonlinear Dynamic Response and Ductility Requirements of Building Structures Subjected to Earthquakes," *Publication R72-54*, Massachusetts Inst. of Tech., Cambridge, Mass., Sept., 1972.
3. Anagnostopoulos, S. A., Haviland, R. W., and Biggs, J. M., "Use of Inelastic Spectra in Aseismic Design," *Journal of the Structural Division*, ASCE, Vol. 104, No. ST1, Jan., 1978, pp. 95-109.
4. *An Evaluation of a Response Spectrum Approach to Seismic Design of Buildings*, Applied Technology Council, San Francisco, Calif., Sept., 1974.
5. Barber, T. T., and Wen, T. K., "Random Vibration of Hysteretic Degrading Systems," *Proceedings*, Third ASCE Engineering Mechanics Division Specialty Conference, Sept., 1979, pp. 51-54.
6. Bertero, V. V., Bresler, B., and Liao, H. M., "Stiffness Degradation of Reinforced Concrete Members Subjected to Cyclic Flexural Moments," *Report No. EERC 69-12*, Earthquake Engineering Research Center, Univ. of California, Berkeley, Calif., Dec., 1969.
7. Bertero, V. V., Herrera, R. A., and Mahin, S. A., "Establishment of Design Earthquakes—Evaluation of Present Methods," *Proceedings*, International Symposium on Earthquake Structural Engineering, Aug., 1976, pp. 551-580.
8. Bertero, V. V., and Mahin, S. A., "Need for a Comprehensive Approach in Establishing Design Earthquakes," *Proceedings*, Second International Conference on Microzonation for Safer Construction, Research, and Application, Nov.-Dec., 1978, pp. 1145-1156.
9. Bertero, V. V., Mahin, S. A., and Herrera, R. A., "Aseismic Design Implications of San Fernando Earthquake Records," *Journal of the International Association of Earthquake Engineering*, Vol. 6, No. 1, Jan.-Feb., 1978, pp. 31-42.
10. Boore, D. M., and Zoback, M. D., "Near-Field Motions from Kinematic Models of Propagating Faults," *Bulletin of the Seismological Society of America*, Vol. 64, No. 2, Apr., 1974, pp. 321-342.
11. Boore, D. M., and Zoback, M. D., "Two-Dimensional Kinematic Fault Modeling of the Pacoima Dam Strong-Motion Recording of the February 9, 1971, San Fernando Earthquake," *Bulletin of the Seismological Society of America*, Vol. 64, No. 3, June, 1974, pp. 555-570.
12. Brune, J. N., "Tectonic Stress and the Spectra of Seismic Shear Waves from Earthquakes," *Journal of Geophysical Research*, Vol. 75, No. 26, Sept., 1970, pp. 4997-5010.
13. Gasparini, D. A., and Vanmarke, E. H., "Simulated Earthquake Motions Compatible with Prescribed Response Spectra," *Publication R76-4*, Dept. of Civil Engineering, Massachusetts Inst. of Tech., Cambridge, Mass., Jan., 1976.
14. Grossmeyer, R. L., "A Simple Approach for Elasto-Plastic Systems Under Stationary Random Excitation," *Proceedings*, Third ASCE Engineering Mechanics Division Specialty Conference, Sept., 1979, pp. 55-59.
15. Haviland, R. W., Biggs, J. M., and Anagnostopoulos, S. A., "Inelastic Response Spectrum Design Procedures for Steel Frames," *Publication R76-40*, Dept. of Civil Engineering, Massachusetts Inst. of Tech., Cambridge, Mass., Sept., 1976.
16. Iwan, W. D., "The Response of Simple Stiffness Degrading Structures," *Proceedings*, Sixth World Conference on Earthquake Engineering, Vol. II, Jan., 1977, pp. 1094-1099.
17. Iwan, W. D., and Gates, N. C., "The Effective Period and Damping of a Class of Hysteretic Structures," *Journal of the International Association of Earthquake Engineering*, Vol. 7, No. 3, May-June, 1979, pp. 199-211.
18. Kaldjian, M. J., and Fan, W. R. S., "Earthquake Response of a Ramberg-Osgood Structure," *Journal of the Structural Division*, ASCE, Vol. 94, No. ST10, Oct., 1968, pp. 2451-2465.
19. Kalevras, V. C., "Ductility Requirements of R.C. Structures with Linear Elements," *Proceedings*, Symposium on Structural Concrete under Seismic Actions, 23 pp.
20. Lai, S. P., "On Inelastic Response Spectra for Aseismic Design," *Publication R78-18*,

- Dept. of Civil Engineering, Massachusetts Inst. of Tech., Cambridge, Mass., July, 1978.
21. Mahin, S. A., and Bertero, V. V., "Problems in Establishing and Predicting Ductility in Aseismic Design," *Proceedings, International Symposium on Earthquake Structural Engineering*, pp. 613-628.
  22. McKeivitt, W. E., et al., "Towards a Simple Energy Method for Seismic Design of Structures," *Proceedings, Second U.S. National Conference on Earthquake Engineering*, Aug., 1979, pp. 383-392.
  23. Montgomery, C. J., and Hall, W. J., "Seismic Design of Low-Rise Steel Buildings," *Journal of the Structural Division, ASCE*, Vol. 105, No. ST10, Oct., 1979, pp. 1917-1933.
  24. Murakami, M., and Penzien, J., "Nonlinear Response Spectra for Probabilistic Seismic Design of Reinforced Concrete Structures," *Proceedings of the U.S.-Japan Cooperative Research Program in Earthquake Engineering*, Assn. for Sci. Documents Information, Aug., 1976, pp. 247-273.
  25. Newmark, N. M., "Current Trends in the Seismic Analysis and Design of High Rise Structures," *Earthquake Engineering*, Wiegel, R. L., ed., Prentice-Hall, Inc., Englewood Cliffs, N.J., 1970, pp. 403-424.
  26. Newmark, N. M., "Seismic Design Criteria for Structures and Facilities of the Trans-Alaska Pipeline System," *Proceedings of the U.S. National Conference on Earthquake Engineering*, June, 1975, pp. 94-103.
  27. Newmark, N. M., "Earthquake Resistant Design and ATC Provisions," *Proceedings, Third Canadian Conference on Earthquake Engineering*, June, 1979, pp. 609-651.
  28. Newmark, N. M., and Hall, W. J., "Procedures and Criteria for Earthquake Resistant Design," *Building Practice for Disaster Mitigation, Building Science Series 45*, National Bureau of Standards, Washington, D.C., Feb., 1973, pp. 209-236.
  29. Newmark, N. M., and Riddell, R., "A Statistical Study of Inelastic Response Spectra," *Proceedings, Second U.S. National Conference on Earthquake Engineering*, Aug., 1979, pp. 495-504.
  30. Pique, J. R., "On the Use of Simple Models in Nonlinear Dynamic Analysis," *Publication 76-43*, Dept. of Civil Engineering, Massachusetts Inst. of Tech., Cambridge, Mass., Sept., 1976.
  31. Powell, G. H., and Row, D. G., "Influence of Analysis and Design Assumptions on Computed Inelastic Response of Moderately Tall Frames," *Report No. EERC 76-11*, Earthquake Engineering Research Center, Univ. of California, Berkeley, Calif., Apr., 1976.
  32. Reimer, R. B., "Deconvolution of Seismic Response for Linear Systems," *Report No. EERC 73-10*, Earthquake Engineering Research Center, Univ. of California, Berkeley, Calif., Oct., 1973.
  33. Sehayek, S., "Effect of Ductility on Response Spectra for Elasto-Plastic Systems," *Publication R76-42*, Dept. of Civ. Engrg., Massachusetts Inst. of Tech., Cambridge, Mass., Sept., 1976.
  34. Shibata, A., and Sozen, M., "Substitute-Structure Method for Seismic Design in R/C," *Journal of the Structural Division, ASCE*, Vol. 102, No. ST1, Jan., 1976, pp. 1-18.
  35. Tansirikongkol, V., and Pecknold, D. A., "Approximate Modal Analysis of Bilinear MDF Systems Subjected to Earthquake Motions," *Structural Research Series No. 449*, Dept. of Civ. Engrg., Univ. of Illinois, Urbana, Ill., Aug., 1978.
  36. "Tentative Provisions for the Development of Seismic Regulations for Buildings," *NSF Publication 78-8, NBS Special Publication 510*, Applied Technology Council, U.S. Dept. of Commerce, Washington, D.C., June, 1978.
  37. Trifunac, M. D., "A Three-Dimensional Dislocation Model for the San Fernando, California, Earthquake of February 9, 1971," *Bulletin of the Seismological Society of America*, Vol. 64, No. 1, Feb., 1974, pp. 149-172.
  38. *Uniform Building Code*, International Conference of Building Officials, Whittier, Calif., 1979.
  39. Veletsos, A. S., "Maximum Deformations of Certain Nonlinear Systems," *Proceedings, Fourth World Conference on Earthquake Engineering*, 1969, pp. 155-170.
  40. Veletsos, A. S., and Newmark, N. M., "Effect of Inelastic Behavior on the Response of Simple Systems of Earthquake Motions," *Proceedings, Second World Conference on Earthquake Engineering*, 1960, pp. 895-912.

41. Veletsos, A. S., Newmark, N. M., and Chelapati, C. V., "Deformation Spectra for Elastic and Elastoplastic Systems to Ground Shock and Earthquake Motions," *Proceedings, Third World Conference on Earthquake Engineering*, 1965, pp. 663-682.
42. Veletsos, A. S., and Vann, W. P., "Response of Ground-Excited Elasto-Plastic Systems," *Journal of the Structural Division, ASCE*, Vol. 97, No. ST4, Apr., 1971, pp. 1257-1281.
43. Zagajski, S. W., and Bertero, V. V., "Optimum Seismic-Resistant Design of R/C Frames," *Journal of the Structural Division, ASCE*, Vol. 105, No. ST5, May, 1979, pp. 829-846.

## APPENDIX II.—NOTATION

*The following symbols are used in this paper:*

- $A$  = peak ground acceleration;
- $A_a$  = effective peak ground acceleration;
- $A_v$  = effective peak velocity-related acceleration;
- $C_d$  = coefficient for estimating displacement, using Ref. 5;
- $C_s$  = seismic design coefficient, using Ref. 5;
- $F_y$  = system yield resistance;
- $H$  = height of structure;
- $M$  = system mass;
- $p$  = rate of post-yield deformation hardening or softening as fraction of initial stiffness;
- $R$  = empirical seismic response parameter accounting for damping and inelastic deformation capacity of structure, using Ref. 5;
- $S$  = seismic coefficient related to soil profile characteristics at site, using Ref. 5;
- $T$  = fundamental period of system;
- $u_{\text{limit}}$  = limiting system displacement;
- $V$  = peak ground velocity;
- $\alpha, \beta$  = empirical coefficients;
- $\gamma$  = parameter relating displacement of multi-degree-of-freedom system to that of equivalent single-degree-of-freedom system;
- $\eta$  = system strength parameter;
- $\Theta$  = story drift index;
- $\mu$  = maximum displacement ductility factor;
- $\mu_c$  = cyclic displacement ductility factor;
- $\mu_E$  = equivalent hysteretic energy dissipation ductility factor;
- $\mu_p$  = permanent displacement ductility factor;
- $\mu_{\text{limit}}$  = maximum displacement ductility factor corresponding to attainment of limiting displacement; and
- $\xi$  = system viscous damping coefficient as fraction of critical.





## CELLULAR AND VOIDED SLAB BRIDGES

By Baidar Bakht,<sup>1</sup> Leslie G. Jaeger,<sup>2</sup> and Mo S. Cheung<sup>3</sup>

### INTRODUCTION

The terms "cellular bridges" and "voided slabs" are used in this paper for the bridge types shown in Fig. 1(a) and 1(b) respectively. In spite of the apparent differences in the two types of structures, their structural behavior can be mathematically modeled by the same methods.

The main feature which distinguishes these structures from other common bridge types is the deformable nature of their cross sections. The need for a method of analysis which will take into account the deformable nature of the cross section has been stressed by many (5,10,11,14,17,20).

There is a general agreement that neglect of cell distortion can lead to serious underestimation of live load longitudinal moments and shears in cellular structures. In the case of voided slabs, however, opinions differ with regard to the influence of cell distortion. Some maintain that transverse cell distortion in voided slabs is negligible, while others contend that the analysis must take into account this distortion.

As described by Bakht, et al. (paper to be published in the *Canadian Journal of Civil Engineering*) there are several readily available rigorous methods of analysis which can take into account the effects of cell distortion. However, many bridge designers in North America, being accustomed to the simplified methods of analysis of AASHTO (American Association of State Highway and Transportation Officials) (22), and lately the Ontario Highway Bridge Design Code (16), would prefer to analyze these structures by simplified means without having to resort to computer based methods. Recognizing this, a simplified method has been developed for the analysis of cellular and voided slab bridges.

This paper presents the basis of this method and its development details. The method provides a measure of the increase in longitudinal moments and shears due to the effect of cell distortion. It can be used in conjunction with

<sup>1</sup>Sr. Research Officer, Policy Planning and Research Div., Ontario Ministry of Transportation and Communications, Downsview, Ontario, Canada.

<sup>2</sup>Prof. of Engrg. and Special Asst. to the Pres., Technical Univ. of Nova Scotia, Halifax, Nova Scotia, Canada.

<sup>3</sup>Mgr., Civ. Engrg. Development, Built Works Tech., Dept. of Public Works, Ottawa, Ontario, Canada.

Note.—Discussion open until February 1, 1982. To extend the closing date one month, a written request must be filed with the Manager of Technical and Professional Publications, ASCE. Manuscript was submitted for review for possible publication on November 7, 1980. This paper is part of the *Journal of the Structural Division*, Proceedings of the American Society of Civil Engineers, ©ASCE, Vol. 107, No. ST9, September, 1981. ISSN 0044-8001/81/0009-1797/\$01.00.

any method, be it simplified or refined, which neglects the effects of transverse cell distortion.

### CHARACTERIZING PARAMETERS

The response to load of a conventional orthotropic plate that is simply supported on two opposite edges is governed by eight parameters, namely  $D_x$ ,  $D_y$ ,  $D_{xy}$ ,  $D_{yx}$ ,  $D_1$ ,  $D_2$ ,  $L$ , and  $b$ . The development of a simplified method for such an orthotropic plate is feasible only if the parameters which characterize its behavior can be reduced to a manageably small number. Many simplified methods have been developed for determining the transverse distribution of longitudinal moments in bridges that can be idealized as conventional orthotropic plates, by reducing

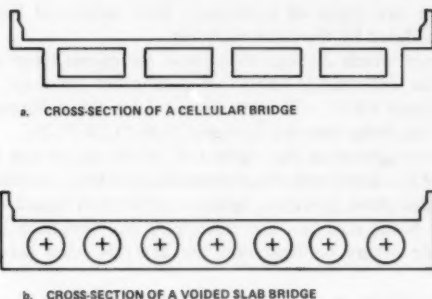


FIG. 1.—Typical Cellular and Voids Slab Bridges

the eight structural parameters to the following two dimensionless characterizing parameters (3,4,8):

$$\alpha = \frac{D_{xy} + D_{yx} + D_1 + D_2}{2(D_x D_y)^{0.5}} \dots \dots \dots (1)$$

$$\theta = \frac{b}{L} \left[ \frac{D_x}{D_y} \right]^{0.25} \dots \dots \dots (2)$$

The implication of the two characterizing parameters is illustrated in Ref. 13. This shows the transverse distribution of midspan longitudinal moments,  $M_x$ , due to a single concentrated load applied to two "different looking" bridges which, however, have the same values of  $\alpha$  and  $\theta$ . The two structures were analyzed by the orthotropic plate theory developed by Cusens and Pama (8). It is shown that the pattern of  $M_x$  distribution is the same in the two bridges in spite of the differences in the aspect ratios of their planforms.

Simplified methods based on  $\alpha$  and  $\theta$  are applicable to bridges that can be realistically idealized as orthotropic plates. If there are several transverse diaphragms in a cellular bridge, and if these are sufficient to prevent the cells from distorting in the transverse direction, the structure can be idealized as a conventional isotropic plate, as shown by Crisfield and Twemlow (7). By

contrast, the absence of transverse diaphragms causes the cells to distort, thus increasing the transverse flexibility of the structure (in other words reducing the ability of the transverse medium to distribute loads in the transverse direction). Consequently, higher concentrations of longitudinal moments and shears result than those predicted by an analysis which neglects cell distortion.

Consider a transverse slice of a cellular structure, simply supported at its extremities and subjected to a concentrated load as shown in Fig. 2. It can be readily seen that the increase in deflections caused by the flexure of flanges and webs about their own axes, is related to the transverse shear rather than transverse moments. Therefore, the representation of cell distortion by an equivalent reduction of the flexural rigidity of the transverse medium, as proposed by some research workers, e.g., Aster (1), is not realistic and is likely to lead to erroneous results.

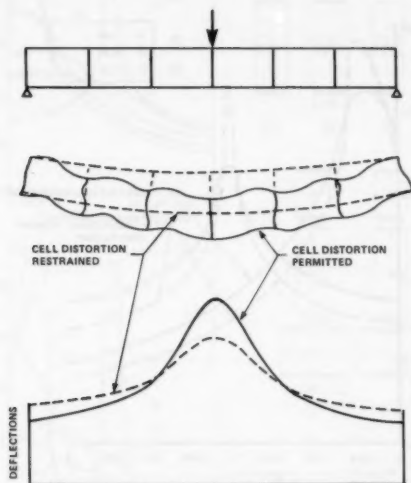


FIG. 2.—Effects of Cell Distortion

Massonnet and Gandolfi (14) proposed that the effect of cell distortion can be accounted for by an equivalent shear area in the transverse direction. This approach has since been adopted and verified by others such as Sawko (18), Hook and Richmond (12), Robertson, et al. (17) etc. Based on the premise that a cellular structure can be idealized as a shear-weak orthotropic plate, the literature contains contributions by Robertson, et al. (17) and Massonnet and Gandolfi (14).

Robertson, et al. (17) have given a harmonic analysis of shear-weak orthotropic plates, and have derived two characterizing parameters whose values depend upon the number of harmonics taken; this feature makes their proposed characterizing parameters unsuitable to be the basis of a simplified method.

Massonnet and Gandolfi (14) developed a theory for shear weak rectangular

orthotropic plates that are simply supported on two opposite edges. The behavior of these plates is characterized by three nondimensional parameters,  $\alpha$ ,  $\theta$ , and  $\delta$ . Where  $\alpha$  and  $\theta$  are defined by Eqs. 1 and 2, and  $\delta$  which reflects the influence of finite shear area in the transverse direction, is given by:

$$\delta = \frac{\pi^2 b}{L} \left[ \frac{D_x}{S_y} \right]^{0.5} \dots \dots \dots (3)$$

in which,  $S_y$ , the transverse shear rigidity = the product of shear modulus and the equivalent transverse shear area per unit length.

Massonnet and Gandolfi (14) further tried to simplify the problem by reducing the three characterizing parameters to two. This simplification was based on unrealistic assumptions, one of which was that the deflections,  $w$ , of a shear weak plate can be divided into two parts  $w_1$  and  $w_2$ , and that the ratio,  $w_1/w_2$ ,

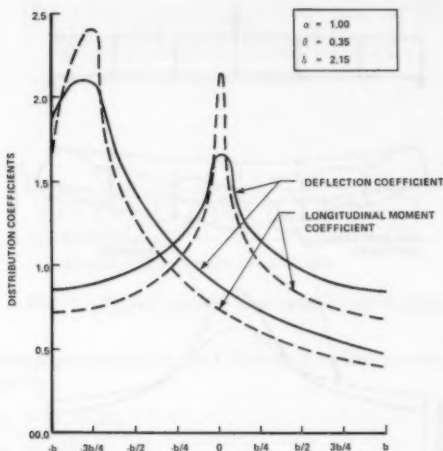


FIG. 3.—Distribution Coefficients for Deflections and Moments

remains constant at all points in the plate. The term,  $w_1$ , is the deflection of the plate with infinite shear area and  $w_2$  is the change in deflections due to the finite shear area. The fallacy of this assumption becomes obvious if the total deflections across the width of the plate are examined. The total area under the curve representing the transverse distribution of deflections must remain constant irrespective of the values of transverse shear areas and transverse flexural rigidities. When the reduction of transverse area causes an increase in deflections near a load, the deflections away from the load must decrease, a fact not borne out by the assumption of  $(w_1/w_2)$  being constant.

Despite the shortcomings of the Massonnet and Gandolfi postulate with regard to the simplification of the shear weak plate theory their derivation of the three characterizing parameters was based on sound assumptions.

**$\alpha$ - $\theta$ - $\delta$  Characterization.**—Definition: If a number of bridges which are physically

different but which all have the same values of  $\alpha$ ,  $\theta$ , and  $\delta$ , are found to display the same pattern of distribution coefficients for longitudinal moments then  $\alpha$ - $\theta$ - $\delta$  is said to characterize the distribution of longitudinal moments.

It is noted that the same three parameters may also characterize the distribution of other structural responses such as longitudinal shear and deflection. This does not imply that the pattern of deflection is the same as the pattern of longitudinal moments and shears; each response has its own pattern and this pattern is maintained for different bridges provided that the values of  $\alpha$ ,  $\theta$ , and  $\delta$  are preserved.

Fig. 3 shows the distribution coefficients for deflections and longitudinal

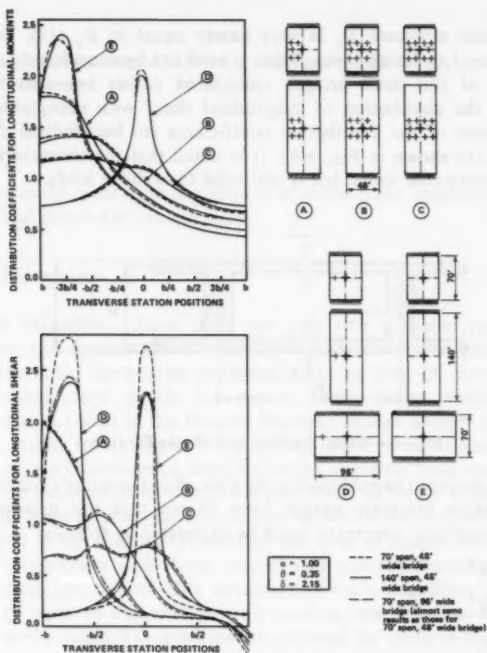


FIG. 4.—Distribution Coefficients

moments in a certain bridge. These coefficients were obtained by the already well established grillage analogy method for cellular structures (11,18,21). It is recalled that the distribution coefficient for deflections is the ratio of the actual deflection to the average deflection. From Fig. 3 it is obvious that the patterns of distribution for longitudinal moments and deflections are different. In what follows it is shown that each of these patterns is characterized by  $\alpha$ - $\theta$ - $\delta$ .

Fig. 4(a) shows distribution coefficients for longitudinal moments for single concentrated loads and for vehicle loads, in three physically different bridges,

all of which have  $\alpha = 1.00$ ;  $\theta = 0.35$ ; and  $\delta = 2.15$ . The distribution coefficients were obtained by analyzing the bridges by the grillage analogy method. The characterization of longitudinal moments by  $\alpha$ - $\theta$ - $\delta$  is convincingly demonstrated in the Figure. For the same bridges the distribution coefficients for deflections were found to be virtually indistinguishable from each other, thus demonstrating that  $\alpha$ - $\theta$ - $\delta$  also characterizes the distribution of deflections.

In conventional orthotropic plates, the distribution of longitudinal shears is characterized by  $\alpha$  and  $\gamma$  (15), in which  $\gamma$  is given by:

$$\gamma = \frac{D_y}{D_x} \dots \dots \dots (4)$$

Since in cellular structure  $D_x$  is very nearly equal to  $D_y$  (13), the value of  $\gamma$  is constant ( $= 1.0$ ) for all cases. Thus,  $\gamma$  need not be considered as a variable. The analysis of the three bridges considered earlier revealed that  $\delta$  also characterized the distribution of longitudinal shear with acceptable accuracy. The comparisons of the distribution coefficients for longitudinal shear in the three bridges are shown in Fig. 4(b). It is noted that the characterization fails for single concentrated loads, but is still valid for vehicle loads.

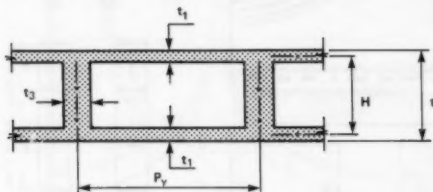


FIG. 5.—Cross Section of Cellular Structure

Bakht, et al. (paper to be published in the *Canadian Journal of Civil Engineering*) after an intensive literature search have shown that the orthotropic plate parameters for cellular structures could be calculated as follows:

$$D_x = 0.5Et_1H^2$$

$$D_y = 0.5Et_1H^2$$

$$D_1 = \nu D_x$$

$$D_2 = \nu D_y$$

$$D_{xy} = Gt_1H^2$$

$$D_{yx} = Gt_1H^2$$

$$S_y = \frac{2Et_1^3}{P_v^2 \left[ 1 + 2 \left( \frac{H}{P_v} \right) \left( \frac{t_1}{t_3} \right)^3 \right] (1 - \nu^2)} \dots \dots \dots (5)$$

in which  $E$  = the modulus of elasticity;  $G$  = the shear modulus;  $\nu$  = the Poisson's ratio and other notation is as defined in Fig. 5. For isotropic materials:

$$G = \frac{E}{2(1 + \nu)} \dots \dots \dots (6)$$

Substituting the expressions for plate parameters in Eq. 1:

$$\alpha = \frac{1 + \nu + \nu^2}{1 + \nu} \dots \dots \dots (7)$$

Since  $\nu = 0.15$  for concrete,  $\alpha$  becomes approximately equal to 1.0 for concrete cellular structures. Eq. 2 becomes:

$$\theta = \frac{b}{L} \dots \dots \dots (8)$$

Thus the conclusion is reached that for concrete cellular structures the system  $\alpha = 1.0$ ;  $\theta = b/L$ ; and

$$\delta = \frac{\pi^2 b}{L} \left[ \frac{D_x}{S_y} \right]^{0.5}$$

will characterize the transverse distribution of deflections, longitudinal moments and longitudinal shears for vehicle loads.

#### DEVELOPMENT BACKGROUND

**Concept of Magnifier.**—Since there are only two variables (namely  $\theta$  and  $\delta$ ), that affect the distribution of loads in cellular structures, the distribution of these loads could have been predicted with the help of charts developed for the practical range of the  $\theta$ - $\delta$  space. These charts would have been similar to those provided in the Ontario Highway Bridge Design Code (16) and reported by Bakht, et al. (3), for the  $\alpha$ - $\theta$  space of conventional orthotropic plates. Such charts, besides being large in number, could not have readily provided information on the extent to which cell distortion causes a cellular structure to respond differently from its counterpart in which cell distortion is absent. It was decided to develop coefficients in the form of magnifiers which could be used in conjunction with those manual and computer-based methods that neglect cell distortion effects. The advantage of such magnifiers would be that they could be used in conjunction with existing simplified methods such as those given in the AASHTO specification (22) and the Ontario Highway Bridge Design Code (16), and that they would directly reflect the influence of cell distortion.

For cellular structures the conventional orthotropic plate theory corresponds to a characterization  $\alpha = 1.0$ ,  $\theta = b/L$ , and  $\delta = 0$ . For nonzero values of  $\delta$ , a magnifier  $\lambda_m$  is introduced so that:

$$\lambda_m = \frac{\text{Maximum intensity of } M_x \text{ if cell distortion effects are present}}{\text{Maximum intensity of } M_x \text{ if cell distortion effects are absent}} \dots \dots (9)$$

The magnifiers corresponding to longitudinal shears are designated by  $\lambda_s$ .

**Effect of Number of Vehicles.**—A three-lane cellular bridge was analyzed by grillage analogy under single concentrated loads and under vehicle loads with

and without the effects of cell distortion. The bridge corresponded to  $\theta = 0.35$  and  $\delta = 2.15$ . The results, which are plotted in Fig. 6, demonstrated that the value of  $\lambda_m$  decreased with increasing eccentricity of load from the bridge center line and also with the increase in the number of lines of wheels. When the longitudinal moments under a concentrated load increases, to maintain overall statics, it is accompanied by a reduction of longitudinal moments in other transverse locations. It can be readily visualized that under the action of several

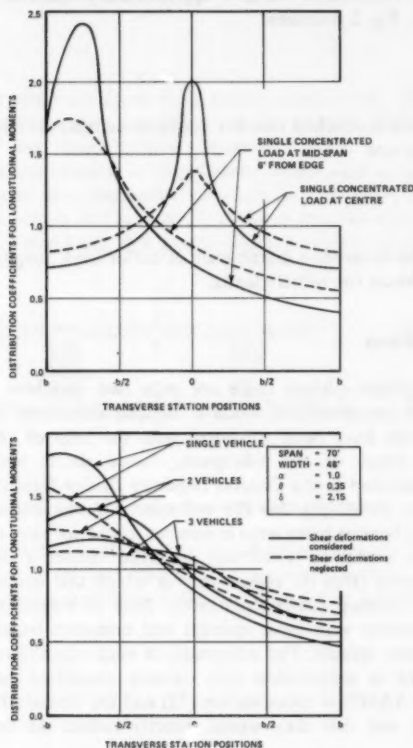


FIG. 6.—Distribution Coefficients for Longitudinal Moments

concentrated loads the effects near any one concentrated load are relatively less severe than if there was only one load on the bridge. In the extreme case of an infinite number of loads on a transverse section, i.e., a uniformly distributed load, the values of  $\lambda_m$  and  $\lambda_s$  would both be equal to 1.0. The dependence of  $\lambda_m$  and  $\lambda_s$  on the number of vehicles necessitated that values of the coefficients be developed for various loaded lane conditions.

**Ranges of  $\alpha$ ,  $\delta$ , and  $\theta$ .**—As described earlier,  $\alpha$  is effectively equal to 1.0



for all concrete cellular structures. Bridges incorporating cellular structures rarely have widths smaller than the span. Thus the maximum value of  $\theta$  was assumed to be 0.5. For the lower limit of  $\theta$  it is noted that the span will not normally exceed 10 times the width, corresponding to  $\theta = 0.05$ . A lower limit of  $\theta = 0.025$  was therefore taken in order to be sure of accommodating even truly exceptional cases of long narrow bridges. The smallest value of  $\delta$  in cellular bridges could not be less than the corresponding value for a solid slab for which:

$$V_y = Gt \dots \dots \dots (10)$$

$$\text{and } D_x = \frac{Et^3}{12} \dots \dots \dots (11)$$

Substituting the expressions for  $V_y$  and  $D_x$  in Eq. 3 and assuming that  $\nu = 0.15$ , the following expression is obtained for  $\delta$  of solid slabs:

$$\delta = 4.3 \left( \frac{b}{L} \right) \left( \frac{t}{L} \right) \dots \dots \dots (12)$$

The smallest values of  $(b/L)$  and  $(t/L)$  were assumed to be  $(1/20)$  and  $(1/40)$  respectively, thus giving the smallest value of  $\delta$  as 0.005. However, trials with realistic configurations of cellular structures showed that  $\delta$  would never be smaller than 0.1, therefore 0.1 was assumed to be the lower limit. Similarly  $\delta$  was never found to exceed 8.0. It was decided to assume 10.0 as the upper limit for  $\delta$ .

**Effect of Small Changes in Vehicle Positions.**—Although the position of loads has a significant effect on values  $\lambda_m$  and  $\lambda_s$ , the variations of vehicle positions within a lane have negligible effects on the coefficients. Analysis of a large number of bridges, effectively covering the full  $\theta$ - $\delta$  space, by the grillage analogy method, showed the effect of moving design vehicles within the design lanes to have a less than one percent effect on  $\lambda_m$ .

**Effects of Changes in Lane Width.**—The  $\alpha$ - $\theta$  method specified in the Ontario Highway Bridge Design Code (16), accounts for changes in lane widths through a correction factor. In the present study a series of four-lane bridges having lane widths of 11 ft (3.35 m) and 13 ft (3.96 m) were analyzed by grillage analogy to determine the effects of variations in lane width on  $\lambda_m$  and  $\lambda_s$ . It was found that in all cases the increase in lane width from 11 ft (3.35 m) to 13 ft (3.96 m) did not change  $\lambda_m$  and  $\lambda_s$  by more than 4.0%. Thus it was concluded that the multipliers need be developed for only one lane width, the results being applicable to bridges with other lane widths.

**Effects of Axle Spacings.**—A design vehicle represents a large variety of vehicles on the road. Therefore, any method of analysis that is applicable to the design vehicle should also be applicable to any one of the vehicles that the design vehicle is supposed to represent. If this is not the case, then either the design vehicle or the analysis is at fault. Bakht, et al. (3) are among many who have demonstrated that the simplified methods of analysis for structures that can be idealized as conventional orthotropic plate, such as those given the Ontario Highway Bridge Design Code (16), are vehicle independent. For cellular structures the effect of changes in vehicles was studied by analyzing a typical cellular

structure under different vehicle loads. It was found that the pattern of distribution of longitudinal moments under different vehicles at the same transverse position was substantially the same.

#### DEVELOPMENT DETAILS

The  $\lambda_m$  and  $\lambda_s$  values were developed first for three-lane bridges by analyzing 44 bridges by the grillage analogy method. As shown in Fig. 7, the bridges effectively covered the full  $\theta$ - $\delta$  space. All bridges had spans of 70 ft (21.34

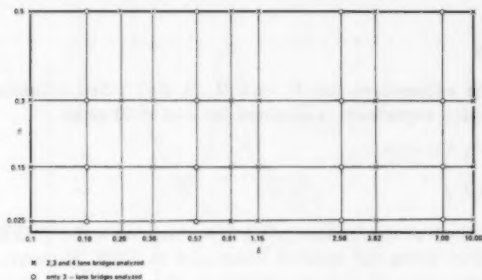


FIG. 7.—Bridges Analyzed in  $\theta$ - $\delta$  Space

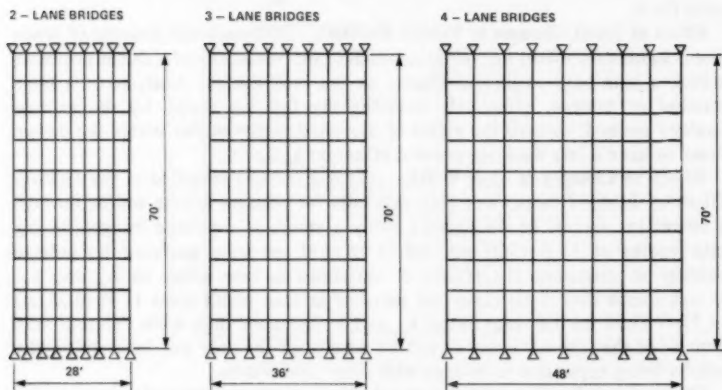


FIG. 8.—Meshes used in Analysis by Grillage Analogy

m), width of 36 ft (10.97 m), and  $\alpha$  equal to 1.0. The required values of  $\theta$  and  $\delta$  were achieved by adjusting the values of the grillage beam properties. For a given case,  $\lambda_m$  (or  $\lambda_s$ ), was calculated as the ratio of the maximum longitudinal moment (or shear) in the bridge with cell distortion and the corresponding value in the bridge in which cell distortion was neglected.

The values of  $\lambda_m$  and  $\lambda_s$  obtained from the analysis of three-lane bridges

displayed a gradual change as  $\theta$  and  $\delta$  were varied; thus eliminating the need for analyzing a large number of structures to cover effectively the full  $\theta$ - $\delta$  space. The terms,  $\lambda_m$  and  $\lambda_s$ , for two- and four-lane bridges were developed by analyzing fewer structures, as shown in Fig. 7. All structures were idealized by grillages having  $8 \times 10$  meshes as shown in Fig. 8. From the calculated

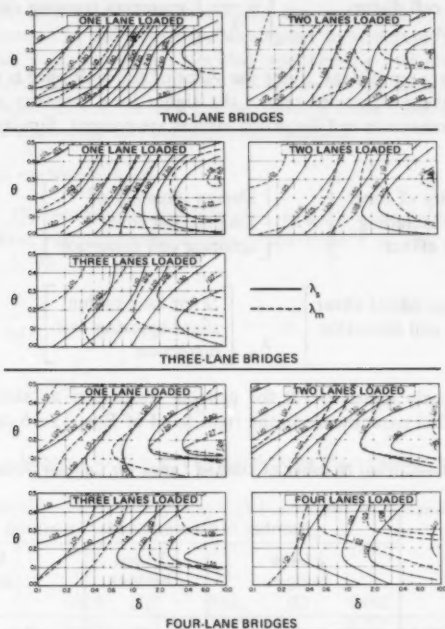


FIG. 9.—Magnifiers for Longitudinal Moments and Longitudinal Shears

values of the multipliers, charts were drawn in the form of contours of  $\lambda_m$  and  $\lambda_s$  on the  $\theta$ - $\delta$  plane. These charts are given in Fig. 9.

#### PROPOSED METHOD FOR CELLULAR STRUCTURES

The proposed method is in the form of adjustments that should be made to longitudinal moments and longitudinal shears obtained by methods that ignore the effect of cell distortion in the transverse direction. The adjustments, which depend upon the number of loaded lanes, are applicable to results obtained from both simplified and refined analyses.

The adjustments can be made either directly to the maximum responses or to the distribution factors,  $D$ , that are calculated according to some simplified methods (16,22), as follows:

$$\left[ \begin{array}{l} \text{Design intensity of longitudinal moment, including cell distortion effect} \end{array} \right] = \lambda_m \left[ \begin{array}{l} \text{Design intensity of longitudinal moment ignoring cell distortion} \end{array} \right] \dots \dots \dots (13)$$

$$\text{or } \left[ \begin{array}{l} D \text{ for longitudinal moments including cell distortion effect} \end{array} \right] = \frac{1}{\lambda_m} \left[ \begin{array}{l} D \text{ for longitudinal moments ignoring cell distortion} \end{array} \right] \dots \dots (14)$$

Eqs. 12 and 13 are equivalent. Since the value of the multiplier is always greater than 1.0, both these equations reflect the higher local intensity of longitudinal moment when transverse cell distortion effects are present. Similarly for longitudinal shear:

$$\left[ \begin{array}{l} \text{Design intensity of longitudinal shear, including cell distortion effect} \end{array} \right] = \lambda_s \left[ \begin{array}{l} \text{Design intensity of longitudinal shear ignoring cell distortion} \end{array} \right] \dots \dots \dots (15)$$

$$\text{or } \left[ \begin{array}{l} D \text{ for longitudinal shear including cell distortion effect} \end{array} \right] = \frac{1}{\lambda_s} \left[ \begin{array}{l} D \text{ for longitudinal shear ignoring cell distortion} \end{array} \right] \dots \dots \dots (16)$$

Since  $\alpha$  is nearly equal to 1.0 for cellular structures, as shown by Eq. 7, the quantity within parenthesis on the right hand of Eqs. 13-16 can be obtained

TABLE 1.—Critical Number of Loaded Lanes for Cellular Structures

Responses (1)	Number of Loaded Lanes Governing Design		
	2-Lane bridges (2)	3-Lane bridges (3)	4-Lane bridges (4)
Longitudinal moment	2	3	3 or 4 for $\theta = 0.4-0.5$ 4 for $\theta = 0.0$ -0.4
Longitudinal shear	2	2 or 3	2 or 3

by treating the structure as a solid slab. The magnifiers,  $\lambda_m$  and  $\lambda_s$ , which are functions of  $\theta$  and  $\delta$  can be read from Fig. 9 for the number of lanes in the bridge and the number of loaded lanes.

In order to apply the proposed method it is necessary to know the number of loaded lanes that govern the design moment or shear. This information is implicit in the AASHTO simplified method (22). Information about the critical number of loaded lanes can be obtained from Ref. 2, which demarcates the  $\alpha$ - $\theta$  space for conventional bridges according to the critical number of loaded lanes. These charts correspond to the multilane modification factors specified in the Ontario Highway Bridge Design Code (OHBD) (16). However, since

the OHBDC modification factors are not much different from those specified in the AASHTO specifications, the charts should also be applicable to the AASHTO loading. According to these charts the critical loading condition for 2- and 3-lane cellular bridges should be as shown in Table 1. Since the OHBD Code (16) method is vehicle independent (3), it is recommended that it be used for both the OHBDC and AASHTO loadings.

The magnifiers can be used to investigate the applicability of methods that ignore cell distortion in the transverse directions, to structure, such as voided slabs, for which it is not clearly decided whether the cell distortion can or cannot be ignored. If, for a structure, the values of the mangifiers are found to be nearly equal to 1.0 for the critical loading case, then clearly there is no need to take transverse cell distortion into account.

#### PROPOSED METHOD FOR VOIDED SLABS

Bakht, et al. (3) recommend the following equations for calculating the slab parameters. These recommendations are based upon a survey of the relevant literature (e.g., 5, 9):

$$D_x = E \frac{t^3}{12} - \frac{t_v^4}{64P_y}$$

$$D_y = \frac{Et^3}{12} \left[ 1 - 0.95 \left( \frac{t_v}{t} \right)^4 \right]$$

TABLE 2.—Values of  $F_3$  for  $S_y$  of Voids Slabs (Reproduced from Ref. 8)

$t_v/P_y$				
$t_v/t$ (1)	0.80 (2)	0.70 (3)	0.60 (4)	0.50 (5)
0.75	0.076	0.082	0.092	0.105
0.70	0.106	0.112	0.112	0.140
0.65	0.146	0.151	0.161	0.180
0.60	0.191	0.195	0.205	0.220

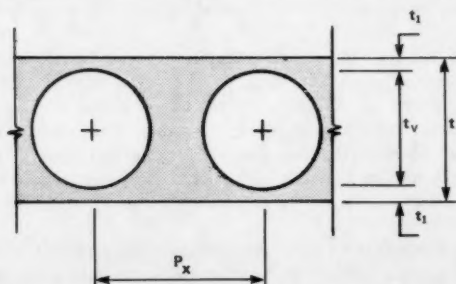


FIG. 10.—Cross Section of Voids Slab

$$D_{xy} = \frac{Gt^3}{6} \left[ 1 - 0.84 \left( \frac{t_v}{t} \right)^4 \right]$$

$$D_{yx} = D_{xy}$$

$$V_y = F_3 Gt \quad (17)$$

$F_3$  = obtained from Table 2 and other notation is as defined in Fig. 10.

Having obtained the values of the various parameters, the values of  $\theta$  and  $\delta$  can be obtained using Eqs. 2 and 3 respectively, and then the method is similar to that used for cellular structures.

The value of  $\alpha$  for most voided slab bridges ranges between 0.85 and 0.95. Although this is somewhat different from the value (1.0) for cellular structures,

TABLE 3.— $\lambda_m$  Values for Voided Slab Bridges

$t_v/t$ (1)	$t_v/P_y$ (2)	Maxi- mum $\delta$ (3)	Usual $\delta$ (4)	Number of loaded lanes (5)	3-Lane Bridges		4-Lane Bridges	
					$\lambda_m$ for maxi- mum $\delta$ (6)	$\lambda_m$ for usual $\delta$ (7)	$\lambda_m$ maxi- mum $\delta$ (8)	$\lambda_m$ for usual $\delta$ (9)
0.85	0.80	1.15	0.38	1	1.16	1.10	1.17	1.14
				2	1.07	1.04	1.08	1.05
				3	1.04	1.03	1.05	1.03
				4			1.04	1.01
0.80	0.80	1.06	0.35	1	1.12	1.10	1.14	1.14
				2	1.05	1.03	1.06	1.05
				3	1.03	1.03	1.03	1.02
				4			1.03	1.01
0.70	0.70	0.96	0.32	1	1.10	1.09	1.12	1.12
				2	1.05	1.03	1.06	1.04
				3	1.03	1.03	1.03	1.02
				4			1.03	1.01
0.65	0.70	0.77	0.26	1	1.09	1.07	1.11	1.11
				2	1.04	1.02	1.05	1.03
				3	1.02	1.02	1.02	1.01
				4			1.02	1.01

it was postulated that the values of the magnifiers would be relatively insensitive to small variations of  $\alpha$ . A few spot checks revealed that this was indeed the case. Thus  $\lambda_m$  and  $\lambda_x$ , although developed for cases with  $\alpha$  equal to 1.0, can also be used for structures in which the value of  $\alpha$  is somewhat different than 1.0. This does not mean that changes in  $\alpha$  do not affect transverse distribution of loads. It simply implies that the increases in the longitudinal responses due to transverse cell distortion (i.e., the magnifiers) remain constant if  $\alpha$  is changed by up to, say, 15%.

To investigate the effect of cell distortion in voided slabs the values of  $\lambda_m$  were obtained for slabs of various void to thickness ratios and aspect ratios of the planform. To obtain the largest, i.e., the worst, value of  $\delta$  it was assumed that  $(L/t)$  was equal to 20 and  $(L/b)$  equal to 2. For the more typical value

of  $\delta$  the value of  $(L/t)$  was taken to be the same as above but  $(L/b)$  was assumed to be equal to six. The values of  $\delta$  together with the corresponding values of  $\lambda_m$  are given in Table 3 for various bridges and different loaded lane conditions.

It can be seen from Table 3 that the parameter having the greatest effect on  $\lambda_m$  is the number of loaded lanes. When all lanes are loaded  $\lambda_m$  never exceeds 1.04 in three- and four-lane bridges, suggesting that in these bridges the neglect of cell distortion can cause the governing longitudinal moment intensity to be underestimated by at most 4%. For single-lane loaded conditions the underestimation can be as high as 17%.

## CONCLUSIONS

When a bridge cross section is subject to distortion, the pattern of transverse distribution of longitudinal moments requires three nondimensional parameters for its characterization. In the case of cellular and voided slab bridges one of these three parameters has an almost constant value. The same is true of longitudinal shears; hence the pattern of longitudinal moments and shears is characterized by the other two parameters.

This paper provides charts, plotted as functions of these two parameters, which give the contours of a "magnifier"  $\lambda$ , being the ratio of the maximum intensity of moment or shear with transverse cell distortion to that without it. It is noted that this "magnifier" or intensity multiplier, always has a value larger than unity, which depends upon the number of lanes in the bridge and the number of lanes that are loaded. In a given case it is straightforward, by referring to the appropriate chart, to ascertain whether transverse cell distortion effects are appreciable or not.

The net effect of the " $\lambda$  magnifier" method now reported is to extend the scope of the simplified methods of AASHTO (22) and OHBDC (16) to bridges having appreciable transverse cell distortion.

## APPENDIX I.—REFERENCES

1. Aster, H., "The Analysis of Rectangular Hollow RC Slabs Supported on Four Sides," thesis presented to the Technological University of Stuttgart, at Stuttgart, Germany, in partial fulfillment of the requirements for the degree of Doctor of Philosophy.
2. Bakht, B., "Use of the Simplified Methods of Analysis Specified in the OHBD Code," *Structural Research Report 79-SPR-8*. Research and Development Division, Ontario Ministry of Transportation and Communication, Downsview, Ontario, Canada, 1979.
3. Bakht, B., Cheung, M. S., and Asis, T. S., "Application of a Simplified Method of Calculating Longitudinal Moments to the Proposed Ontario Highway Bridge Design Code," *Canadian Journal of Civil Engineering*, 6(1), 1979, pp. 36-50.
4. Bares, R., and Massonnet, C., *Analysis of Beam Grids and Orthotropic Plates by the Guyon-Massonnet-Bares Method*, Crossby Lockwood and Sons Ltd., London, England, 1968.
5. Basu, A. K., Dawson, J. M., "Orthotropic Sandwich Plates," Supplement, *Proceedings Institution of Civil Engineers*, London, England, 1970, pp. 87-115.
6. Cope, R. J., Harris, G., and Sawko, F., "A Quasi-Slab Approach to the Analysis of Cellular Bridge Structures," presented at the May 11-13, 1971, Computer Aided Engineering Symposium held at University of Waterloo, Waterloo, Ontario, Canada.
7. Crisfield, M. A., and Twemlow, R. P., "The Equivalent Plate Approach for the Analysis of Cellular Structures," *Civil Engineering and Public Works Review*, Mar., 1971.

8. Cusens, A. R., and Pama, R. P., "Distribution of Concentrated Loads on Orthotropic Bridge Decks," *The Structural Engineer*, London, England, Sept., 1969.
9. Cusens, A. R., and Pama, R. P., *Bridge Deck Analysis*, John Wiley and Sons, London, England, 1975.
10. Elliott, G., discussion of "Stiffness Parameters," by Kinsey, *HECB*, Department of the Environment Conference on Computerised Bridge Design, Bristol, June, 1975.
11. Hambly, E. C., and Pennells, E., "Grillage Analysis Applied to Cellular Bridge Decks," *The Structural Engineer*, 53(7), London, England, July, 1975.
12. Hook, I. M. A., and Richmond, B., "Western Avenue Extension—Precast Concrete Box Beams in Cellular Bridge Decks," *The Structural Engineer*, London, England, 48(3), Mar., 1970.
13. Jaeger, L. G., Bakht, B., and Mufti, A. A., "The Simplified Analysis of Cellular Structures," Report submitted to the Department of Supply and Services, Ottawa, Canada, 1979.
14. Massonnet, Ch., and Gandolfi, A., "Some Exceptional Cases in the Theory of Multigrade Bridges," I.A.B.S.E. publications, 1967.
15. Merrifield, B. C., "Abutment Reactions in Right Bridge Decks," *Concrete*, Feb., 1969, pp. 67-73.
16. *Ontario Highway Bridge Design Code*, Ontario Ministry of Transportation and Communications, Downsview, Ontario, 1979.
17. Robertson, J. C., Pama, R. P., and Cusens, A. C., "Transverse Shear Deformation in Multi-Cell Box Beam Bridges," I.A.B.S.E. publication, 1970.
18. Sawko, F., "Recent Developments in The Analysis of Steel Bridges using Electronic Computers," presented at the June, 1968, BCSA Conference on Steel Bridges, held at London, England.
19. Sawko, F., discussion of "Box Improvement," by D. A. Kerensky's, *The Structural Engineer*, London, England, 46(7), July, 1968.
20. Sawko, F., Cope, R. J., "Analysis of Multicell Bridges Without Transverse Diaphragms—a Finite Element Approach," *The Structural Engineer*, London, England, 47(11), Nov., 1969.
21. Smyth, W. J. R., and Srivavasan, S., "The Analysis of Gateshead Viaduct," *The Structural Engineer*, London, England, 5(2), Feb., 1973.
22. *Standard Specifications for Highway Bridges*, American Association of State Highway and Transportation Officials, Washington, D.C., 1977.

## APPENDIX II.—NOTATION

*The following symbols are used in this paper:*

- $b$  = half width of bridge;
- $D_x$  = longitudinal flexural rigidity per unit width;
- $D_{xy}$  = longitudinal flexural rigidity per unit width;
- $D_y$  = longitudinal torsional rigidity per unit width;
- $D_{yx}$  = transverse torsional rigidity per unit length;
- $D_1$  = coupling rigidity per unit width;
- $D_2$  = coupling rigidity per unit length;
- $E$  = modulus of elasticity;
- $F_3$  = ratio of  $S_y$  for voided or cellular structure and that for corresponding solid slab;
- $G$  = shear modulus;
- $H$  = distance between flange centroids (Fig. 4);
- $L$  = span of bridge;
- $P_y$  = spacing of longitudinal webs or voids;
- $S_y$  = transverse shear rigidity per unit length;
- $t$  = overall thickness of slab;



- $t_v$  = diameter of circular void or height of rectangular void;
- $t_1$  = thickness of top flange and bottom flange of cellular structure;
- $\alpha$  = parameter defined by Eq. 1;
- $\gamma$  = parameter defined by Eq. 4;
- $\delta$  = parameter defined by Eq. 3;
- $\theta$  = parameter defined by Eq. 2;
- $\lambda_m$  = magnifier for longitudinal moments defined by Eq. 9;
- $\lambda_s$  = magnifier for longitudinal shear; and
- $\nu$  = Poisson's ratio.



## STATIC BEHAVIOR OF BEAM-TO-COLUMN MOMENT CONNECTIONS

By W. F. Chen,<sup>1</sup> M. ASCE and K. V. Patel,<sup>2</sup> A. M. ASCE

### INTRODUCTION

The cost of fabricated steel construction is controlled to a large extent by the connections. Simplicity of connection details may have a greater influence on the total economy of the structure than would a reduction in weight of the main members. Before 1950, riveting was the primary method of connecting structural steel, but, in recent years, connections using welding or high strength bolting, or both, are the most practical. Connections, which require a combination of welding and bolting, are considered economical. Previous investigations on these connections conducted at Cambridge, Cornell, and Lehigh universities were summarized and discussed in Ref. 2. Recent results conducted at the University of California at Berkeley were reported in Ref. 13. The moment connections tested at Berkeley were subjected to cyclic loading, simulating earthquake effects on a building frame.

Described herein are tests of 12 full-size welded or bolted symmetrically-loaded moment-resisting beam-to-column connections, or both, subjected to monotonically increasing static loading to failure. These connections are of importance in the design and construction of steel multi-story frames. All specimens were designed incorporating all possible limiting cases in practical connection design. This includes (1) All connections proportioned to resist a combination of high shear force and plastic moment of the beam section; (2) all specimens are made of the American Society of Testing Materials, ASTM A572 Grade 55 steel; (3) high allowable shear stresses of 30 ksi and 40 ksi are utilized for ASTM A325 and A490 bolts in bearing-type connections respectively; (4) some specimens are designed with attachments having oversize holes or slotted holes, or both; and (5) some specimens are designed using friction-type joints and others using bearing-type joints. This paper summarizes the highlights of test results of this experimental program. In addition to the behavior and the manner of failure

<sup>1</sup>Prof. and Head of Struct. Engrg., School of Civ. Engrg., Purdue University, West Lafayette, Ind. 47907.

<sup>2</sup>Asst. Prof. of Civ. Engrg., Univ. of Miami, Coral Gables, Fla; formerly, Grad. Asst., School of Civ. Engrg., Purdue University, West Lafayette, Ind. 47907.

Note.—Discussion open until February 1, 1982. To extend the closing date one month, a written request must be filed with the Manager of Technical and Professional Publications, ASCE. Manuscript was submitted for review for possible publication on March 27, 1980. This paper is part of the Journal of the Structural Division, Proceedings of the American Society of Civil Engineers, ©ASCE, Vol. 107, No. ST9, September, 1981. ISSN 0044-8001/81/0009-1815/\$01.00.

of the beams and their connections to the columns, the implications of the results on design procedures for safe, efficient, and economical beam-to-column connections receive particular attention.

In 1971, a test program was initiated at Lehigh University to study the behavior and strength and to develop the design method of moment resisting beam-to-column flange connections (7,8). These are connections in which the beams are framed into the column flanges with the beams causing bending of the column about the major axis. The test program, consisting of 12 full-size beam-to-column connections, was under the guidance of the Welding Research Council (WRC) Task Group on Beam-To-Column Connections. The investigation of the behavior of such connection is being done to aid the designer in his decisions on their use and to improve design rule. Detailed results of this experimental program may be found in Refs. 3, 8, and 15. Some of the test results together with a preliminary theoretical analysis have been reported elsewhere (6,11,16,17). A detailed elastic-plastic-fracture finite element analysis of these specimens is currently underway at Purdue University.

#### DESIGN AND FABRICATION OF SPECIMENS

The specimens were designed according to the American Institute of Steel Construction, AISC specification (10). The connections were proportioned to resist the plastic moment of the beam section. Since the loading condition resembles gravity type loading (dead load plus live load), the load factor used was 1.7. The stresses used in proportioning welds, shear plates, and top and bottom moment plates were then equal to 1.7 times those given in Sec. 1.5 of the AISC Specification. For A325 and A490 high-strength bolts in bearing-type connections the design shear stresses used were equal to 1.7 times 30 ksi and 40 ksi, respectively, instead of 22 ksi and 32 ksi suggested in the current specification. The concept of this procedure will be discussed later.

**Member Size and Beam Span.**—The connection specimens were chosen to have an appropriate combination of a beam section and a column section that represented the real interior beam-to-column connections in a multi-story frame. Three different sizes of specimens consisting of  $W14 \times 74$ ,  $W24 \times 61$ , and  $W27 \times 94$  beams connected to  $W10 \times 60$ ,  $W14 \times 136$ , and  $W14 \times 176$  columns, respectively, were used in this test program. All of the beam sections are plastic design sections that satisfy the requirements of "minimum thickness" (Width-Thickness Ratios), of the AISC Specification. Both  $W24 \times 61$  and  $W27 \times 94$  shapes are the lightest in weight in each particular group given in the AISC manual.

Another factor considered in selecting beam sizes is the way a wide-flange shape resists bending moment and shear force. It is well known that the flanges resist most of the bending moment, and the web almost entirely carries the shear force. The ratio of flange area to web area furnishes an index to the amount of moment carried by the web, which must be transferred to the flanges at the connections since the shear connections have negligible moment-resisting capacity. The ratios of one flange area to web area,  $A_f/A_w$ , for  $W14 \times 74$ ,  $W24 \times 61$ , and  $W27 \times 94$  sections are 1.39, 0.44, and 0.60, respectively. The behavior of these sections should be representative of a wide range of wide-flange sections.

It was desired to use column sections that did not need horizontal stiffeners. In each case the columns selected were the least column size based upon the AISC tension or compression flange criterion. The specimens were proportioned in such a way that at the beam-to-column juncture the plastic moment and the factored shear capacity of single shear bolts in beam web would be reached concurrently. Beam span then was simply the ratio of moment to shear values.

All test specimens were fabricated from wide-flange shapes made of ASTM A572 Gr. 55 steel. High strength steel was used because there is a narrower margin between yield and ultimate than for lower strength steels. Further, the plastic range or ductility for A572 steel is somewhat less compared to A36 steel. Thus, if the connection behavior is adequate for A572 steel, the results could be assumed to apply to lesser grade steel. A detailed report of material properties is given in Ref. 15.

**Fasteners and Holes.**—ASTM A325 and A490 bolts were used to assemble the joints. In bearing-type connections, the allowable shear stresses used in design for A325 and A490 bolts were 30 ksi and 40 ksi, respectively. The use of higher allowable shear stresses reflects the logical design criterion that would result if an adequate factor of safety were applied against the shear strength of the fasteners. This design criterion is based upon the results of a study of A7 and A440 steel lap and butt joints fastened with A325 bolts, and A440 steel joints connected with A490 bolts (5). Tests have been subsequently carried out to substantiate the suggested design criterion, especially the use of A490 bolts in A440 and A514 steel joints (9,18).

Since both oversize holes and slotted holes are desirable to facilitate erection adjustments, and slotted holes may better facilitate the assumed distribution of shear and moment at the connections, experimental justification is required for beam-to-column connections assembled with high-strength bolts with enlarged and with slotted holes. Previous research has indicated that oversize holes, sized according to bolt diameter, do not adversely affect the slip behavior of friction-type joints or cause undesirable bolt-tension losses (5). It was also observed that slotted holes did not affect the strength of bearing-type joints.

In the test program, 1 1/4 in. round holes were used in top and bottom moment plates fastened with 1 in. diameter A490 bolts and designed as a friction-type connection (Test C8 in Fig. 9). The use of 1/4 in. oversize holes is the maximum size permitted in the current Specification (14). Slotted holes were used in one-sided shear plates fastened with either A490-X bolts (C3 in Fig. 4) or A325-X bolts (C8 and C9). The remaining joints had round holes 1/16 in. larger than the nominal diameter of the bolt.

Both A325 and A490 bolts were installed by the turn-of-nut method. Washers were not used for A325 bolts. In bearing-type connections, A490 bolts had a hardened washer under the element (nut or bolt head) turned in tightening. In the friction-type connection (C8), a hardened washer was inserted under both the head and nut. Nut rotation from snug tight condition was 1/2 turn as required by the specification (14). All bolts were calibrated and installed in the Fritz Laboratory, Lehigh University.

**Welds.**—The connection specimens were welded according to the American Welding Society AWS Building Code (4). The welding process used for groove welds was the innershield procedure; the electrodes were E70TG (flux cored arc welding with no auxiliary gas shielding). The type of filler metal for beam

TABLE 1.—Test Program of C-Series

Test (1)	Beam size column size (2)	Factored Load			Beam span L (6)
		Moment (3)	Shear (4)	Stiffening (5)	
C1	W14 × 74 W10 × 60	$M_p = 6,930$ k-in. beam flange groove weld	$V = 160$ k (88.5% $V_p$ ) shear plate 3 1 in. $\phi$ A490-X in 1 1/16 in. round holes	Horizontal stiff- eners 3/4 in. × 4 in. × 8 7/8 in.	3 ft-7 in.
C2	W27 × 94 W14 × 176	$M_p = 15,290$ k-in. beam flange groove weld	$V = 374$ k (94.7% $V_p$ ) shear plate 7 1 in. $\phi$ A 490-X in 1 1/16 in. round holes	—	3 ft-5 in.
C3	W27 × 94 W14 × 176	DO	DO Shear plate has slotted holes	—	3 ft-5 in.
C4	W27 × 94 W14 × 176	DO	$V = 374$ k (94.7% $V_p$ ) two-plate welded stiff- ened seat	—	3 ft-5 in.
C5	W27 × 94 W14 × 176	To be estimated beam flange groove weld	To be estimated beam flange groove weld	—	3 ft-5 in.
C6	W14 × 74 W10 × 60	$M_p = 6,930$ k-in. moment plates 8-1 in. $\phi$ A490-X in 1 1/16 in. round holes	$V = 160$ k (88.5% $V_p$ ) stiffener plate 1 in. × 5 in. × 11 in.	Horizontal stiff- eners 1 in. × 4 in. × 8 7/8 in.	3 ft-7 in.
C7	W14 × 74 W10 × 60	DO	$V = 160$ k (88.5% $V_p$ ) shear plate 3 1 in. $\phi$ A490-X in 1 1/16 in. round holes	DO	3 ft-7 in.
C8	W24 × 61 W14 × 136	$M_p = 8,360$ k-in. moment plates 14-1 in. $\phi$ A490- F in 1 1/4 in. round holes	$V = 157.5$ k (52.5% $V_p$ ) shear plate 7 3/4 in. $\phi$ A325- X in slotted holes	—	4 ft-5 in.
C9	W24 × 61 W14 × 136	$M_p = 8,360$ k-in. moment plates 6-1 in. $\phi$ A490-X in 1 1/16 in. round holes	DO	—	4 ft-5 in.
C10	W14 × 74 W10 × 60	$M_p = 6,930$ k-in. beam flange groove weld	$V = 160$ k (88.5% $V_p$ ) beam web groove weld	Horizontal stiff- eners 3/4 in. × 4 in. × 8 7/8 in.	3 ft-7 in.

TABLE 1.—Continued

(1)	(2)	(3)	(4)	(5)	(6)
C11	W24 × 61 W14 × 136	$M_p = 8,360$ k-in. beam flange groove weld	$V = 157.5$ k (52.5% $V_p$ ) beam web groove weld	—	4 ft-5 in.
C12	W27 × 94 W14 × 176	$M_p = 15,290$ k-in. beam flange groove weld	$V = 374$ k (94.7% $V_p$ ) beam web groove weld	—	3 ft-5 in.

flange groove welds in the flat position and for moment plate groove welds in the horizontal position was NR-311; NR-202 was used for beam web groove welds in the vertical-up position. The electrodes for fillet welds were E7028. In determining the size of fillet weld, the allowable shear stress on the effective throat was 21 ksi.

Nondestructive testing methods were employed to inspect the welds before testing of the specimens. Groove welds were inspected by ultrasonic testing and fillet welds by magnetic particle. Results of weld inspection were evaluated according to the AWS Code. Those rejected were repaired and subsequently inspected prior to testing.

#### DESCRIPTION OF SPECIMENS

The test program, designated as C-series, is summarized in Table 1. Detailed descriptions of each test are given as follows.

The joint detail of Test C1 is shown in Fig. 1. Beam flanges were directly welded to the column flanges providing for plastic moment capacity. A one-sided shear plate fastened with three 1 in. diameter A490-X bolts was used to resist vertical shear. The fillet weld connecting the shear plate to the column flange was sized for vertical shear only; the moment due to the eccentricity of the applied load was neglected. Horizontal stiffeners were designed according to the AISC specification. Since the connection panel zone was under symmetrical loads, a clearance of 1/2 in. was provided between horizontal stiffeners and column web. The size of fillet welds for horizontal stiffeners was determined by computing the force taken by the stiffeners when plastic moment was attained at the beam-to-column juncture.

Fig. 2 shows Test C10, which is a fully-welded connection and was used as a control test. Beam flanges and beam web were connected to the column flanges by groove welds. An erection plate was tack welded to the column flange, and was used as the backing strip for the beam web groove weld. Test C2 is shown in Fig. 3. Its connection type is similar to Test C1, the only difference being that horizontal stiffeners are not required.

Test C3 is identical with Test C2 except that the one-sided shear plate of Test C3 (Fig. 4) has slotted holes. The dimensions of these slots conform to provisions in the current specification (14). A continuous bar 5/16 inch in thickness and having a width equal to the length of the slot was attached on the side of the slotted shear plate. (The addition of continuous bars for single shear

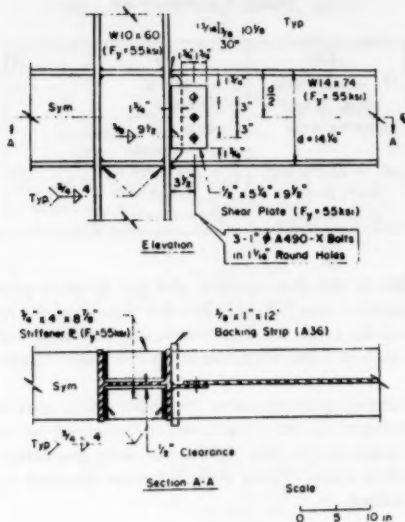


FIG. 1.—Test C1

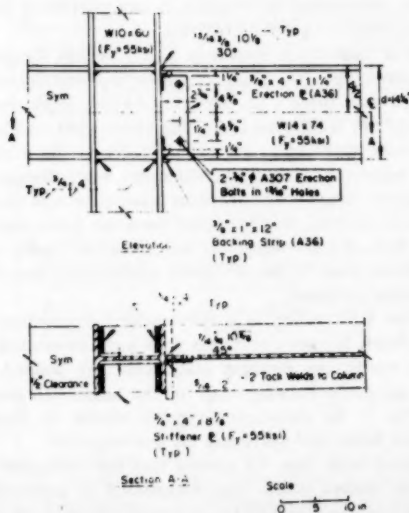


FIG. 2.—Test C10



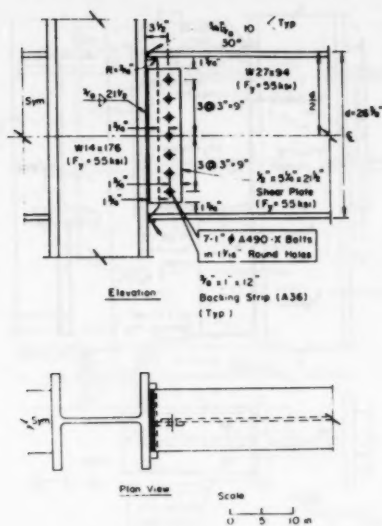


FIG. 3.—Test C2

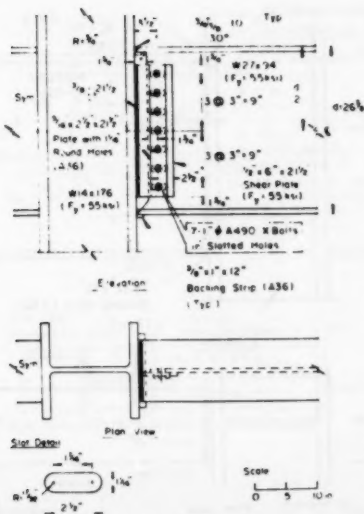


FIG. 4.—Test C3

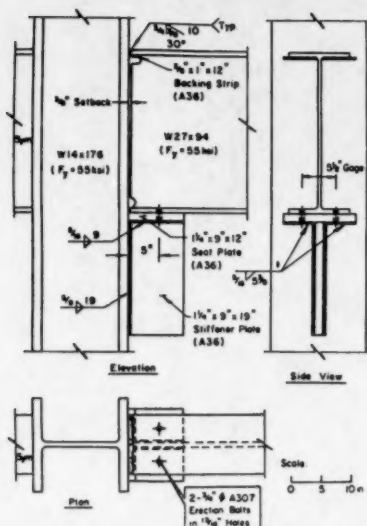


FIG. 5.—Test C4

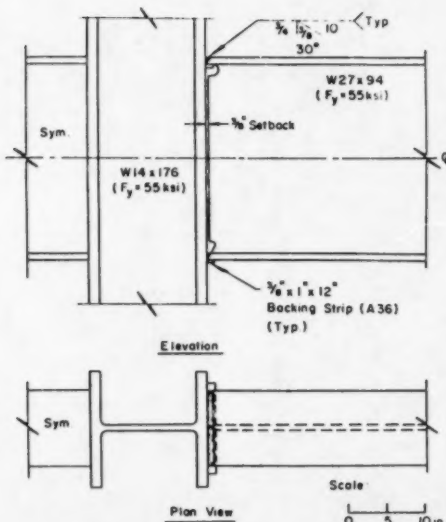
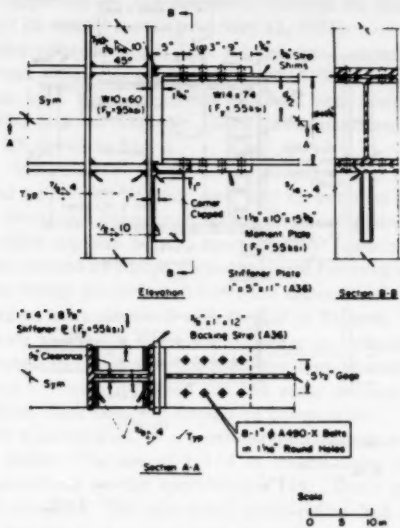
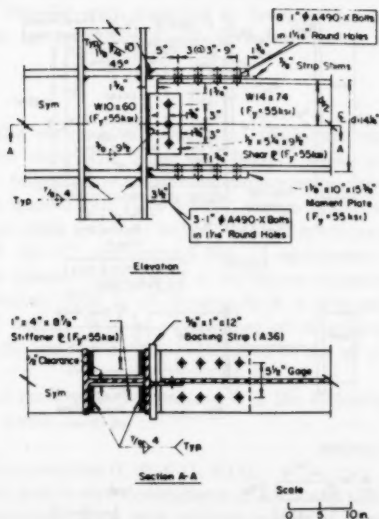


FIG. 6.—Test C5



**FIG. 7.—Test C6**



**FIG. 8.—Test C7**

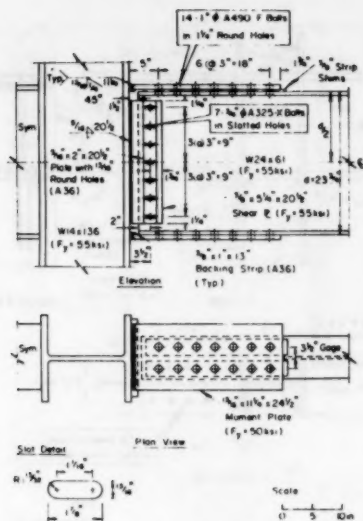


FIG. 9.—Test C8

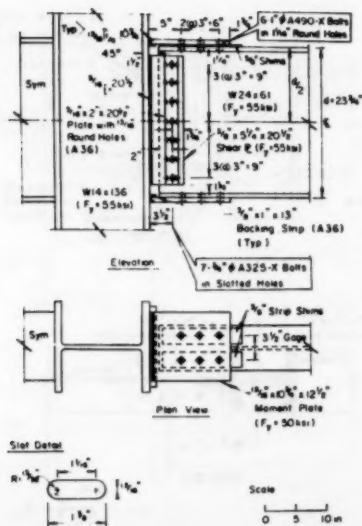


FIG. 10.—Test C9

connections was approved by the Research Council on Riveted and Bolted Structural Joints at its annual meeting on May 12, 1971).

Fig. 5 shows the joint detail of Test C4. Moment capacity was provided through direct groove welding of the beam flanges to the column flanges. Vertical shear was resisted by a two-plate welded stiffener seat designed according to Table 8 of the AISC manual. The strength of this connection should be greater than that of Test C5 shown in Fig. 6.

In the case of Test C5, the beam was connected to the column by groove welds only. It had neither an erection seat nor an erection clip. The purpose was to determine the actual capacity of the beam flange groove welds.

Fig. 7 shows bolted top and bottom moment plate connection Test C6. The plastic moment was carried by flange plates that were fastened with 1 in. diameter A490-X bolts. The design procedure follows the example of the AISC Manual. The bracket stiffeners were designed with the aid of Table 8.

Test C7 is shown in Fig. 8. The vertical shear is resisted by a one-sided shear plate connected to the beam web by three 1 in. diameter A490-X bolts. Tests C1, C6, and C7 were designed for the same amount of moment and shear, and, therefore, their behavior should be comparable.

Test C8 (Fig. 9) was designed as a friction-type connection having over-size holes in moment plates. The use of 1 1/4 in. round holes for 1 in. diameter A490-F bolts is permitted by the specification (14). There is no reduction in slip resistance of the joint. The one-sided shear plates had slotted holes and were designed as bearing-type connections. A continuous bar was also attached on the side of the shear plate (Fig. 9).

Test C9 (Fig. 10) is similar to Test C8. For the purpose of comparison, the moment plates of Test C9 were designed as bearing-type connections having round holes 1/16 in. in excess of the nominal bolt diameter.

#### TEST RESULTS

All 12 tests of the series of 12 specimens have been completed. Table 1 shows all specimens along with beam and column sizes, amount of moment and shear they are subjected to, stiffening requirements, and beam span. The type of connections studied were fully welded, flange welded with various means of carrying the shear load, and fully bolted. Table 2 contains a brief description of each failure of the 12 specimens. The 12 specimens represent typical connections for the lower stories (W27  $\times$  94 beams connected to W14  $\times$  176 column), middle stories (W24  $\times$  61 beams, W14  $\times$  136 column), and upper stories (W14  $\times$  74 beams, W10  $\times$  60 column) of a multi-story frame. Each group includes a fully groove-welded connection to act as a control specimen for comparisons.

The discussion of these tests are presented in the following. The discussion is divided into four parts

1. Fully welded connections (C10, C11, C12).
2. Flange welded, web bolted connections (C1, C2 and C3).
3. Flange welded connections with various means of carrying a shear (C4, C5).
4. Fully-bolted connections (C6, C7, C8, C9).

The overall behavior of these connections as characterized by their load-deflection curves will be discussed along with the modes of failure. The load-deflection curves reflect strength, rotational capacity, and stiffness of these connections, which must be examined to insure an adequate performance.

**Fully Welded Connections.**—The fully welded specimens serve as control specimens for evaluating the performance of several other connections of different joint design in the series. These fully welded specimens are considered the "ideal connections" because they involve the connection of metal directly to metal (beam to column) through welding.

The first specimen tested and fully analyzed was C12 (Fig. 11), a fully welded connection of the largest size considered in this study. The sections used in this connection were a W27  $\times$  94 beam and a W14  $\times$  176 column and were groove welded. The load-deflection curve of Test C12 is shown in Fig. 12 and the connection at the end of test is shown in Fig. 13. In Fig. 12,  $P_m$  is the

TABLE 2.—Description of Failure

Test (1)	Description of failure (2)
C1	Crack at the fillet weld of the tension stiffener
C2	Tearing of column web along web-to-flange juncture
C3	Fracture occurring at the heat-affected zone of the tension flange groove weld
C4	Buckling of beam web and fracture of beam web initiated at the cope hole
C5	Fracture of beam web initiated at the cope hole
C6	Eight bolts connecting the tension flange to the moment plate sheared off simultaneously
C7	Failure of five bolts in one of the tension flange
C8	Buckling of column web and test terminated
C9	Six bolts on one of the tension flange connections and one of the web bolts sheared off simultaneously
C10	Crack at the fillet weld of the tension stiffener
C11	Crack at the heat-affected zone of the tension flange groove weld
C12	Fracture at tension flange groove weld; excessive column web deformation in the compression region

maximum load of the connection under test,  $P_p$  is the theoretical plastic limit load, and  $P_w = P_p/1.7$ . The connection behaved linearly elastic until the first yield lines began forming in the compression web of the column. As the load increased, the yield spread in column web compression as well as tension regions. The testing was concluded due to a combination of excessive column web formation and fracture of weld at tension flange and along beam web (Fig. 14). From load-deflection curve, it is evident that this type of connection can be used in plastic design as the plastic limit load, sufficient rotation capacity, and adequate elastic stiffness are developed. The present AISC Specification (10) provides adequate rules in design of such welded connections. The extensive yielding in tension and compression regions of column web as well as webs of beams shows a balanced failure (Fig. 13). Detailed results and analysis of this specimen are reported in Ref. 16.

The other two fully welded connections are C10 (Fig. 2) and C11 (Fig. 15).

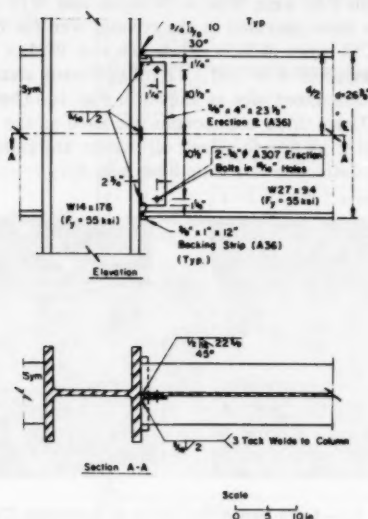


FIG. 11.—Test C11

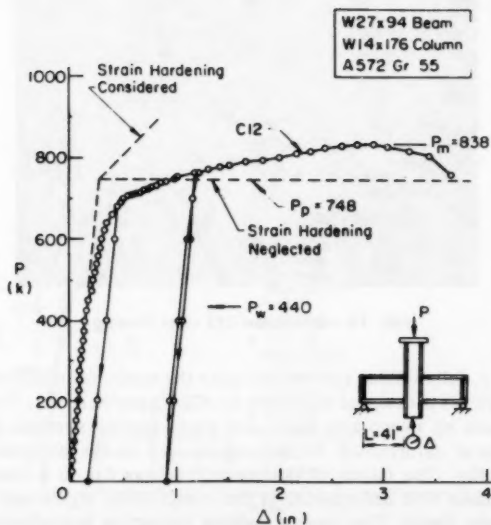


FIG. 12.—Test C12

The sections used for C10 were W14  $\times$  74 beam and W10  $\times$  60 column. The horizontal stiffeners were provided in the column web for this specimen. The sections used for C11 were W24  $\times$  61 beam and W14  $\times$  136 column. The load-deflection behavior of C10 and C11 (of different sizes) is compared to C12 on a non-dimensionalized plot as shown in Fig. 16. Their overall behavior is similar, as well. These three connections are used as the control specimens in their respective size groups to which all results are compared. In Fig. 16,  $\Delta_p$  is the theoretical deflection at plastic limit load  $P_p$ .

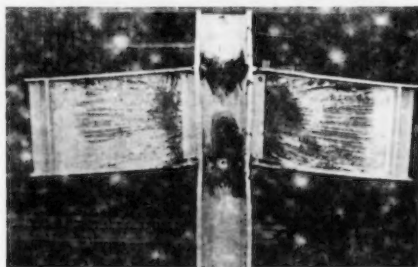


FIG. 13.—Load-Deflection Curve of Specimen C12



FIG. 14.—Specimen C12 after Testing

In summary, fully welded connections have the merits for plastically designed multi-story frames if designed according to AISC Specifications. They maintain elastic stiffness up to working load, and starts losing strength due to local yielding. Lateral deformation of the column web in the compression region causes unloading. The failure of the connection was due to a combination of excessive column web deformation in the compression region and fracture of weld at tension flange. The present welding inspection procedures are shown to be adequate as no premature welding failure occurs.

**Flange Welded-web Bolted Connections.**—The first change from the fully welded



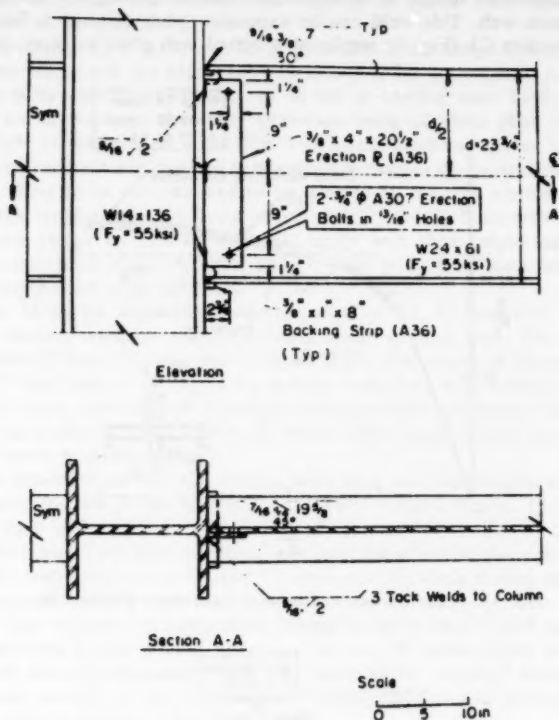


FIG. 15.—Weld Fracture at Tension Flange of C12

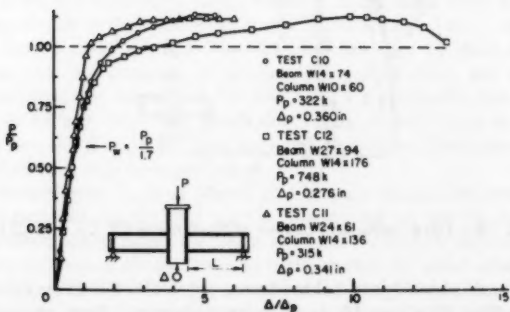


FIG. 16.—Load-Deflection Curves—Fully Welded Connections

case in connection design to be considered was eliminating the vertical weld on the beam web. This weld can be expensive when done as a field weld. The connection C1 (Fig. 1) employed a bolted web plate to carry shear, in

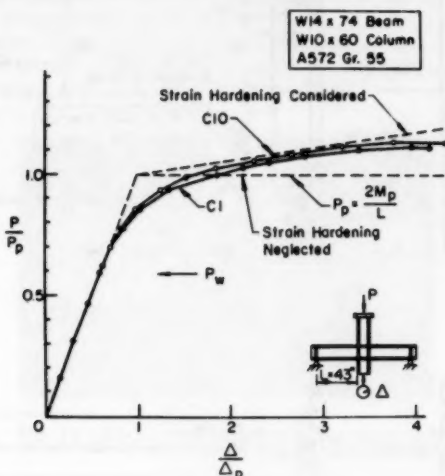


FIG. 17.—Load-Deflection Curves of Specimens C1 and C10

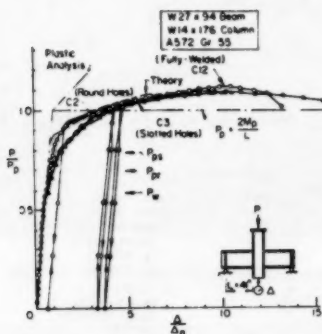


FIG. 18.—Load-Deflection Curves of Specimens C2, C3, and C12

place of the vertical weld, and behaved very much like C10 (Fig. 2), its control, as shown in Fig. 17 where  $M_P$  is full plastic moment. Both connections had horizontal stiffeners. A good correlation between predictions by simple plastic analysis (12) and experimental results is obtained. This is due to the use of

horizontal stiffeners that increase the rigidity of panel zone, meeting the assumption of the plastic analysis.

The Specimen C2 (Fig. 3) and C3 (Fig. 4) had beam flange directly welded to column flange and the beam web was bolted to the shear plate. A 490 high strength bolts with shear capacity of 40 ksi in bearing were used. Test C2 and C3 are of the same size, only difference being C2 shear plate had round holes while C3 had slotted holes (Fig. 11). At the predicted plastic limit load, the bending moment was assumed to be carried by flanges due to strain-hardening, and the shear force was assumed to be resisted by the web attachment. This assumption is examined considering the joint details used: (1) Beam web connected to column flange by groove weld; (2) beam web shear plate fastened by high-strength bolts in round holes; and (3) beam web shear plate fastened by high-strength bolts in slotted holes.

Figure 18 shows the load-deflection curves of C2, C3 and C12. Both C2 and C3 showed adequate elastic stiffness under working load. The deviation of C2 and C3 from C12 was due to slip of joints that occurred above working load. C2 failed due to tearing of the column web along web-to-flange junction while C3 failed when fracture occurred at the heat-affected zone of the groove weld at the tension flange. The bolts deformed permitting the complete redistribution of forces at maximum load.

Tests demonstrated that the flanges were able to strain harden sufficiently to transmit the full plastic moment of the beam section. In Fig. 18,  $P_p$  is the plastic limit load counting flanges only;  $P_p$  corresponds to full strength, and  $P_{ps}$  is the plastic limit load modified to include the effect of shear force. Quite evidently both connections C2 and C3 were able to strain harden sufficiently to accommodate this.

Tests also showed that connections having slotted holes (C3) and round holes (C2) exhibited similar overall behavior. The use of slotted holes is desirable to permit erection adjustments and may facilitate the assumed distribution of shear and moment at the connections. Detailed results and analysis of this part of study have been reported in Ref. 6.

In summary, the current plastic analysis is satisfactory in predicting the behavior of beam connections that are subjected to a shear force at the predicted plastic limit load of not more than 60% of  $V_p$ , where  $V_p$  is the shear force that produces full yielding of web. If the shear force is approximately equal to  $V_p$ , the proposed theory in Ref. 6 may be used. The slotted holes may be used in one-sided shear plates that are designed as bearing-type joints. Also, the column web stiffener requirements developed for A36 steel are applicable for higher yield levels (up to 55 ksi). The fillet welds connecting a shear plate to the column flange may be sized for vertical shear only and the moment due to the eccentricity of the applied load may be neglected.

**Flange Welded with Various Means of Carrying Shear.**—In this group, the connection included are C4 (Fig. 5), C5 (Fig. 6) and its control test C12 (Fig. 11). In all three connections, the beam flange is welded to the column flange. The primary difference among the three is the method by which shear is carried. The control specimen utilizes the beam web to carry shear, the C4 specimen carries shear by means of a beam seat having beam web unconnected, and the C5 carries both moment and shear in the beam flanges. This three specimens are shown in Fig. 19.

Test C4 failed prematurely with the beam web buckling (Fig. 20). This connection was then redesigned to include a beam web stiffener, labeled Test

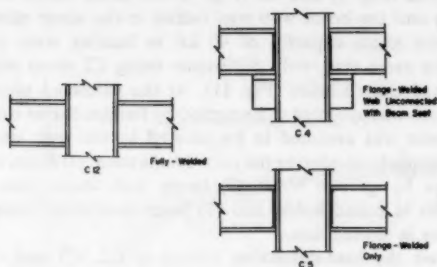


FIG. 19.—Connection Geometries C4, C5, C12

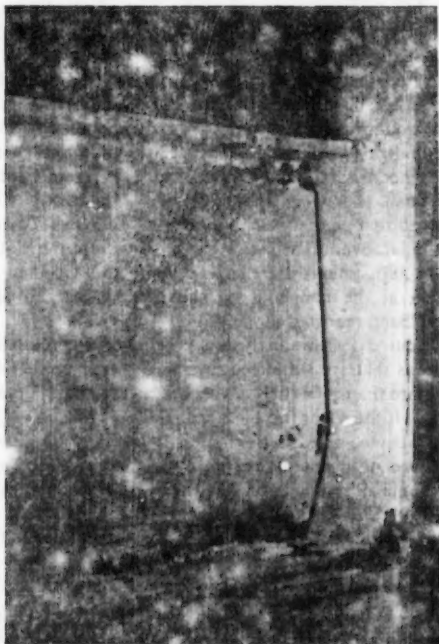


FIG. 20.—C4 at Failure

C4R. In the redesign, the web was considered to act as a column with one end hinged and one end fixed. For connection C5, the unloading started due

to a beam-web fracture, which initiated at the cope hole of beam tension flange side. Testing was terminated when the tearing of the beam web near the  $k$ -line became excessive and the beam web buckled near the beam compression flange side (Fig. 21).

The load-deflection curves of C4, C4R, C5, and C12 are compared (Fig. 22). The fully welded connection (C12), and the stiffened seated beam connection with beam web stiffeners C4R are basically identical in their general behavior of the applied loads, and may be used interchangeably. The flange-welded only connection C5 attains 51% of its predicted plastic limit load based upon the whole section, and showed sufficient initial stiffness and rotation capacity.

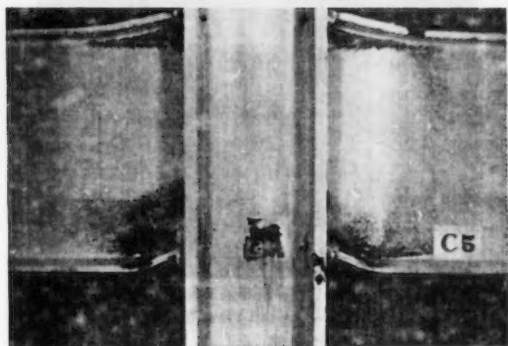


FIG. 21.—Connection C5 at End of Test

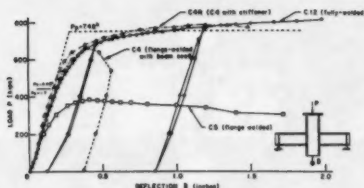


FIG. 22.—Load-Deflection Curves ( $P_p$  = Theoretical Plastic Limit Load;  $P_w$  = Working Load,  $P_w = P_p/1.7$ ) (1 in. = 25.4 mm; 1 kip = 4.45 kN)

Detailed results and analysis of this part of study have been reported in Ref. 11.

In summary, the AISC specification provides adequate rules in design for stiffened beam connection as C4 provided the possibility of the buckling of the beam web is checked and beam web stiffeners are added if necessary as C4R. Although the stiffened seated beam connection (C4) fails by excessive buckling of beam web, the specimen does exhibit sufficient stiffness under working load. The connection C5 showed substantial deformation and rotation capacity, though it attains only about half of its predicted plastic limit load.

**Fully Bolted Connections.**—Herein, the results of tests of those specimens designed with high strength bolts for resisting moment and shear force are discussed. This group includes specimens for each of the following cases: (1) Flange bearing bolted with a stiffened beam seat; (2) flange bearing bolted, web bearing bolted (both of the smallest combination considered;  $W14 \times 74$  beam section and  $W14 \times 60$  column section); (3) flange friction bolted, web bearing bolted; and (4) flange bearing bolted, web bearing bolted, (both of the intermediate size tested,  $W24 \times 61$  beam section and  $W14 \times 136$  column section). These connections are labelled as C6, C7, C8, and C9 respectively.

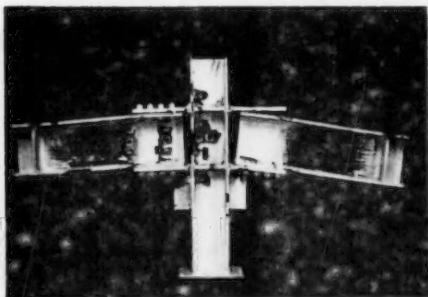


FIG. 23.—Overall View of C6

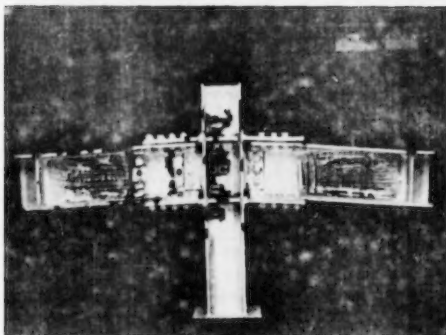


FIG. 24.—Overall View of C7

The C6 (Fig. 7) and C7 (Fig. 8) are designed to resist moment through a bearing connection using eight A490 bolts. The moment plates are groove welded to the column flange. Horizontal stiffeners are provided in the column web, and are welded to the column flanges but not the column web. Shear is carried by a stiffened beam seat fillet welded to the column flange for C6 while shear is carried by three A490 bolts in the beam web for C7. The control test for C6 and C7 is C10 (Fig. 2).

The C8 (Fig. 9) is designed to resist moment using fourteen 1 in. diameter A490 or friction type bolts having 1 1/4 in. oversized holes in the moment plate. The moment plates are groove-welded to the column flange. A bearing connection using A325 bolts in long slotted holes is used to resist shear. The C9 test (Fig. 10) is similar to C8, but for the purpose of comparison was designed as a bearing type connection for resisting moment, meaning that fewer bolts (six A490 bolts) were required in each beam flange. The control test for C8 and C9 is the fully welded test specimen C11 (Fig. 15).

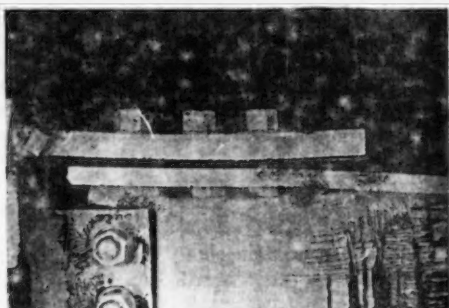


FIG. 25.—Prying Action of C7 Moment Plate

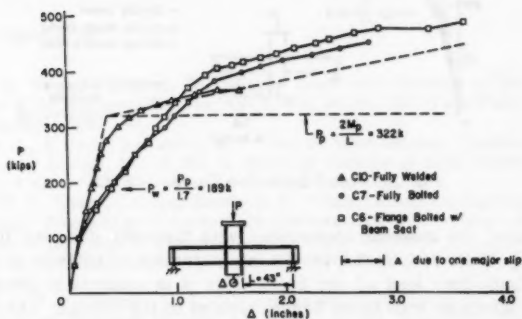


FIG. 26.—Load Deflection Curves—C6, C7

Fig. 23 shows overall view of C6 at failure. The failure of this test occurred when the eight bolts connecting the tension flange to the moment plate sheared off simultaneously. Fig. 24 shows overall view of C7 at failure. The failure was due to the failure of five bolts in one of the tension flange connections. Two bolts on the outer line of a tension beam flange failed first. The bolts appeared to fail in tension. A close look at the moment plate shows it bending and probably exerting a prying action on the outer bolts (Fig. 25). The extensive yielding of beam web up to the end of the moment plates shows that plastic

hinge, if it forms at all, will form at the end of the moment plates and not at the column face (Figs. 23 and 24).

The load-deflection curves for tests C6 and C7 along with their control test C10 are shown in Fig. 26. Test C10 closely follow the predicted stiffness, and then deviates from it in a smooth curve due to yielding. Initially, C6 and C7 follow the predicted stiffness, but at a load of approximately 150 kips, both tests abruptly display a smaller, linear stiffness. This is presumed to be due to the slipping of high strength bolts in the moment connections into bearing, and some yielding takes place.

The load deflection curves for C8, C9 and their control test C11 are shown in Fig. 27. Test C9, the bearing-type of connection, follows the prediction until it suddenly follows a smaller slope due to slips. Test C8, the friction connection, does not display the distinctive slope due to the slipping of bolts into bearing but rather follow smooth curve. The initial stiffness of C8 is slightly greater than predicted due to the longer moment plates needed for a friction connection. Detailed results and analysis for this part of study have been reported in Ref. 5.

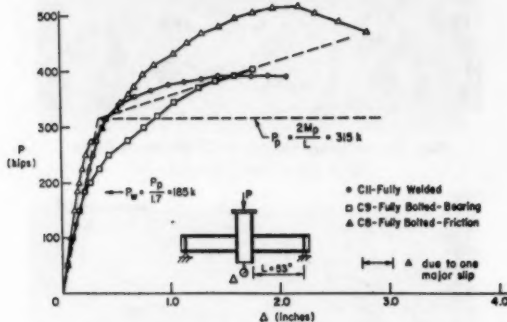


FIG. 27.—Load-Deflection Curves—C8, C9

In summary, the moment connections with fasteners designed for bearing exhibit a slip characteristic that results in a reduction of stiffness at loads less than the plastic-limit load of the beam. This is in contrast to prior tests on moment connections with beam flanges welded to the column. The deflection resulting from slip of bearing bolted moment connections may be an additional factor to be considered in the analysis of the stability of frames. The bolted moment connections tested exhibit a maximum strength that is at least equal to that of the comparable welded connection and varies up to 30% higher than the welded connection due to the strengthening effect of the moment plates. Bolted moment connections also exhibit sufficient rotation capacity when compared with welded connections. For the range of beam and column shapes tested, the results have shown the adequacy of the present stiffening requirements of the AISC Manual. When column web stiffening is required, the test data indicates that such stiffeners need not be welded to the column web for systems having equal moments of opposite sense on each side of the column.



## CONCLUSIONS AND SUMMARY

A series of 12 full-scale beam-to-column moment-resisting flange connections subjected to monotonically increasing loading to failure tested at Lehigh University are reviewed here. It shows the general behavior of moment connections and peculiar change in behavior when the connection detailings are changed from fully welded to bolted and welded and to fully bolted. This testing program along with future theoretical and analytical work will provide a thorough understanding of such connections and will lead to recommendations and guidelines for those involved in their design.

The results of these connections will provide needed information for the analytical work for the critical parts involved in these connections. By using these results, bench marks can be set and connections analyzed with numerical methods like finite element method using high speed computers. Thus these results will help to develop analytical capability needed for design of these connections.

## ACKNOWLEDGMENTS

The present paper was based on the work carried out previously at the Fritz Engineering Laboratory, Lehigh University. The authors are grateful to L. S. Beedle, J. S. Huang, and G. P. Rentschler, and J. A. Gilligan, J. E. Regec, J. Parfitt, and K. F. Standig for their valuable contributions to the research project.

## APPENDIX.—REFERENCES

1. Allan, R. N. and Fisher, J. W., "Bolted Joints with Oversize or Slotted Holes," *Journal of the Structural Division*, ASCE, Vol. 94, No. ST9, Proc. Paper 6113, Sept., 1968, pp. 2061-2080.
2. Beedle, L. S. and Christopher, R., "Test of Steel Moment Connections," *AISC Engineering Journal*, Vol. 1, No. 4, American Institute of Steel Construction, Oct., 1964, p. 116.
3. Chen, W. F., Huang, J. S., and Beedle, L. S., "Recent Results on Connection Research at Lehigh," Proceedings of the Regional Conference on Tall Buildings, Asian Institute of Technology, Bangkok, Thailand, Jan., 1974, pp. 799-813.
4. "Code for Welding in Building Construction," AWS D1.0-69, 9th ed., American Welding Society, 1969.
5. Fisher, J. W., and Beedle, L. S., "Criteria for Designing Bearing-Type Bolted Joints," *Journal of the Structural Division*, ASCE, Vol. 91, No. ST5, Proc. Paper 4511, Oct., 1965, pp. 129-154.
6. Huang, J. S., Chen, W. F., and Beedle, L. S., "Behavior and Design of Steel Beam-To-Column Moment Connections," Welding Research Council Bulletin No. 188, Oct., 1973.
7. Huang, J. S., and Chen, W. F., "Steel Beam-to-Column Moment Connections," presented at the April 9-13, 1973, ASCE National Structural Engineering Meeting, San Francisco, Calif. (Preprint 1920).
8. Huang, J. S., Chen, W. F., and Regec, J. E., "Test Program of Steel Beam-to-Column Connections," Fritz Laboratory Report 333.15, Lehigh University, Bethlehem, Pa., July, 1971.
9. Kulak, G. L., and Fisher, J. W., "A514 Steel Joints Fastened by A490 Bolts," *Journal of the Structural Division*, ASCE, Vol. 94, No. ST10, Proc. Paper 6163, Oct., 1968, pp. 2303-2323.

10. *Manual of Steel Construction, Specification for the Design, Fabrication and Erection of Structural Steel for Buildings*, 7th ed., American Institute of Steel Construction, 1970.
11. Parfitt, John and Chen, W. F., "Tests of Welded Steel Beam-to-Column Moment Connections," *Journal of the Structural Division*, ASCE, Vol. 102, No. ST1, Proc. Paper 11854, Jan., 1976, pp. 186-202.
12. *Plastic Design in Steel—A Guide and Commentary Manual No. 41*, 2nd ed., by a Joint Committee of the Welding Research Council and the American Society of Civil Engineers, ASCE, 1971.
13. Popov, E. P. and Pinkney, R. B., "Cyclic Yield Reversal in Steel Building Connections," *The Journal of the Structural Division*, ASCE, Vol. 95, No. ST3, Proc. Paper 6441, Mar., 1969, pp. 327-353.
14. "Specification for Structural Joints Using ASTM A325 or A490 Bolts," 7th ed., Research Council on Riveted and Bolted Structural Joints of the Engineering Foundation, Mar., 1970.
15. Regec, J. E., Huang, J. S. and Chen, W. F., "Mechanical Properties of C-Series Connections," *Fritz Laboratory Report 333.17*, Lehigh University, Bethlehem, Pa., Apr., 1972.
16. Regec, J. E., Huang, J. S., and Chen, W. F., "Test of a Fully-Welded Beam-to-Column Connection," *Welding Research Council Bulletin No. 188*, Oct., 1973.
17. Standig, K. F., Rentschler, G. P., and Chen, W. F., "Tests of Bolted Beam-to-Column Moment Connections," *Welding Research Council Bulletin No. 218*, Aug., 1976.
18. Sterling, G. H., and Fisher, J. W., "A440 Steel Joints Connected by A490 Bolts," *Journal of the Structural Division*, ASCE, Vol. 92, No. ST3, Proc. Paper 4845, June, 1966, pp. 101-118.

## LIMIT DESIGN OF SLABS FOR CONCENTRATED LOADS

By Hans Gesund,<sup>1</sup> F. ASCE

### INTRODUCTION

The Yield Line Theory is a well established (4,8,9,10) method for limit analysis or design of reinforced concrete slabs. Solutions are available for isotropically and orthotropically reinforced slabs, supported with a variety of boundary conditions, and subjected to either distributed or point loads (4,6,9,10). A few solutions are also given (8) for combinations of point and distributed loads acting on isotropic slabs.

Superposition in general is not valid in inelastic analysis, though it can be shown (4) that addition of the results of Yield Line analyses for individual loading cases will give a lower bound on the total upper bound load capacity of a given slab, provided none of the loading conditions causes moment reversals in any of the yield hinges. The accuracy, however, with which the collapse load can be determined in this manner depends on how nearly congruent the individual collapse mechanisms are. When concentrated loads are placed near slab boundaries, the concentrated and the distributed load mechanisms may be very different, and superposition will give poor results. An example will illustrate this later.

Reinforced concrete slabs are normally constructed with orthotropic reinforcement and different positive and negative bending moment resistances, as dictated by serviceability requirements and designer judgment. The reinforcement is also likely to be different near the boundaries and in the interior of the slab, and under some boundary conditions it may be difficult to provide sufficient embedment to make the reinforcement fully effective immediately adjacent to the boundary. Concrete slabs also tend to have considerable self weight, which will reduce the magnitude of any concentrated load a slab can carry.

True point loads do not exist. All real "concentrated" loads must actually be spread over some area. Depending on circumstances, the critical failure mode may then be either flexure, or "punching" shear. The shear problem will not be addressed here. The punching shear provisions of the American Concrete Institute (ACI) Building Code (1) appear to provide adequate guidance for safe design. The flexural problem *will* be addressed. There is also the possibility

<sup>1</sup>Prof. of Struct. Engrg., Univ. of Kentucky, Lexington, Ky. 40506.

Note.—Discussion open until February 1, 1982. To extend the closing date one month, a written request must be filed with the Manager of Technical and Professional Publications, ASCE. Manuscript was submitted for review for possible publication on July 25, 1980. This paper is part of the Journal of the Structural Division, Proceedings of the American Society of Civil Engineers, ©ASCE, Vol. 107, No. ST9, September, 1981. ISSN 0044-8001/81/0009-1839/\$01.00.

of interaction between shear and flexural failures. The ACI Code provisions deal with this only indirectly, but it seems unlikely that flexural distress will enhance shear strength. It is therefore doubly important to obtain an accurate assessment of the flexural strength.

#### ANALYSIS

In the models to be analyzed here, a "concentrated" load,  $P$ , will be assumed to be distributed over a small rectangular area of dimensions  $c$  and  $\lambda c$ , oriented and located with respect to the coordinate axes and slab boundaries as shown in Fig. 1. The entire slab, including the area beneath  $P$ , will carry a uniformly

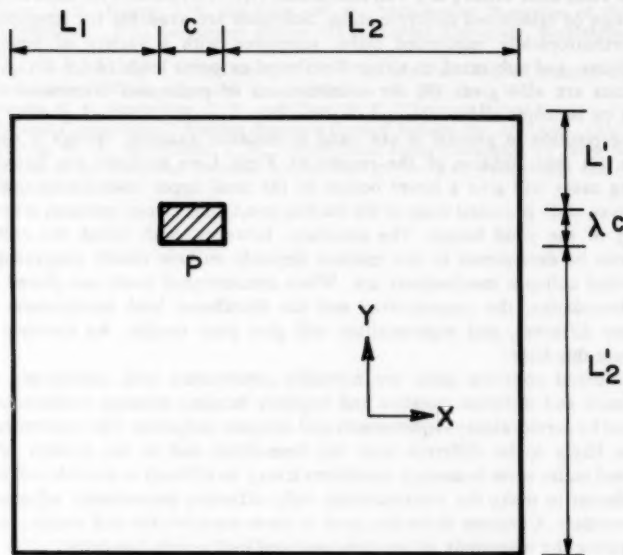


FIG. 1.—Plan View of Slab and "Concentrated" Load

distributed load of magnitude,  $w$ , per unit area, which may be self weight plus any additional likely surcharge. It will, however, be assumed that  $w\lambda c^2 \ll P$ .

Johansen's (4) stepped yield criterion, which has been validated by Lenschow and Sozen (5) and by Mills (7) among others, will be used here. The flexural strength of the slab can then be expressed as follows with reference to the coordinate axes shown in Fig. 1:  $m$  = unit yield moment per unit length;  $k_x m$  = negative yield moment per unit length provided by top tension reinforcing bars placed parallel to the  $x$ -axis;  $k'_x m$  = positive yield moment per unit length provided by bottom tension rebars placed parallel to the  $x$ -axis;  $k_y m$  = negative yield moment per unit length provided by top tension rebars placed parallel

to the  $y$ -axis; and  $k'_y m$  = positive yield moment per unit length provided by bottom tension rebars placed parallel to the  $y$ -axis. It is useful to define

$$\Sigma k = k_x + k'_x + k_y + k'_y \quad \dots \dots \dots (1)$$

leading to a total available yield moment  $m \Sigma k$ , and a coefficient of orthotropy

$$\mu = \frac{k_x + k'_x}{k_y + k'_y} \quad \dots \dots \dots (2)$$

The vector moments per unit length acting along a positive or a negative yield line making an angle  $\phi$  with the  $x$ -axis can be written as

$$m_\phi^+ = m(k'_x \sin^2 \phi + k'_y \cos^2 \phi) \quad \dots \dots \dots (3a)$$

$$m_\phi^- = m(k_x \sin^2 \phi + k_y \cos^2 \phi) \quad \dots \dots \dots (3b)$$

In what follows, extensive use will be made of virtual energy input and absorption in portions of elliptical yield fans forming in orthotropic slabs. It is convenient to present the relevant expressions here. Fig. 2 shows the geometry and notation of the elliptical fan. In polar coordinates, the equation of the ellipse is

$$R_\phi = \frac{qr}{\sqrt{q^2 \sin^2 \phi + \cos^2 \phi}} \quad \dots \dots \dots (4)$$

The angle  $\theta$ , between  $R_\phi$  and the ellipse, can be found from

$$\sin \theta = \frac{R_\phi}{\sqrt{R_\phi^2 + \left(\frac{\partial R_\phi}{\partial \phi}\right)^2}} = \frac{q^2 \sin^2 \phi + \cos^2 \phi}{\sqrt{q^4 \sin^2 \phi + \cos^2 \phi}} \quad \dots \dots \dots (5)$$

Then if point  $O$  drops a virtual distance,  $\delta$ , while the elliptical periphery remains in the original plane thus forming the fan, the virtual energy input of a uniformly distributed load,  $w$ , per unit area acting on the fan between  $\phi_i$  and  $\phi_j$  will be

$$E_{ij} = \frac{1}{2} w \frac{\delta}{3} \int_{\phi_i}^{\phi_j} \frac{R_\phi d\phi}{\sin \theta} R_\phi \sin \theta$$

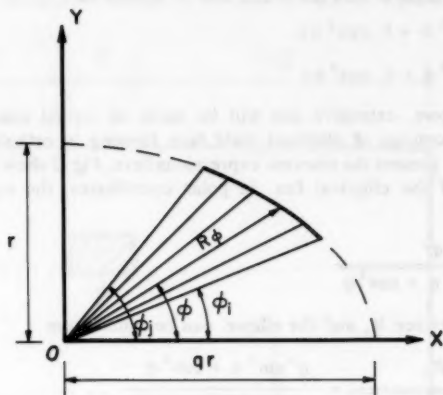
$$\text{or } E_{ij} = \frac{\delta}{6} w q r^2 [\arctan(q \tan \phi_j) - \arctan(q \tan \phi_i)] \quad \dots \dots \dots (6)$$

The virtual energy absorbed during the yield hinge rotations in the fan was given by Sawczuk and Jaeger (9). Translated into the present notation it is

$$E'_{ij} = \frac{\delta}{2} \frac{m \Sigma k}{1 + \mu} \left\{ \left( \frac{\tan \phi_j}{q^2 \tan^2 \phi_j + 1} - \frac{\tan \phi_i}{q^2 \tan^2 \phi_i + 1} \right) \left[ \frac{\mu \left( 1 - \frac{k'_x}{k_x} \right)}{1 + \frac{k'_x}{k_x}} \right] \right.$$

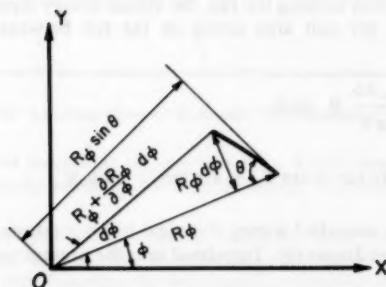
$$\left. - \frac{q^2 \left( 1 - \frac{k'_y}{k_y} \right)}{1 + \frac{k'_y}{k_y}} \right] + \left( q + \frac{\mu}{q} \right) [\text{arc tan } (q \tan \phi_i) - \text{arc tan } (q \tan \phi_j)] \} \dots (7)$$

Fig. 3 shows the collapse mechanism caused by a single concentrated load,  $P$ , acting over a rectangle  $c$  by  $\lambda c$  in the interior of an orthotropic slab of infinite extent in all directions. The slab may simultaneously be loaded with



Portion of Elliptic Yield Fan

(a)



Enlarged Portion of Yield Fan

(b)

FIG. 2.—Elliptic Yield Fan Geometry

a uniformly distributed load,  $w$  per unit area, in which  $w\lambda c^2 \ll P$ . If the uniformly distributed load were relatively large, a different mechanism, based on the uniform load and the boundary conditions, might govern and would have to be investigated. Such mechanisms are dealt with exhaustively in the literature (4,6,8,9,10).

Assuming complete symmetry in the mechanism of Fig. 3, using Eqs. 6 and 7 with  $\phi_1 = 0$  and  $\phi_2 = \pi/2$  while noting that here  $r = b$  and  $q = a/b$ , and letting  $\omega = (w\lambda c^2)/P$ ,  $\alpha = a/c$ , and  $\beta = b/c$ , the virtual energy input becomes

$$E = \delta P \left[ (1 + \omega) + \frac{\omega}{\lambda} \left( \beta + \lambda\alpha + \frac{\pi}{3} \alpha\beta \right) \right] \dots \dots \dots (8)$$

and the virtual energy absorbed will be

$$E' = \delta m \left[ \frac{2}{\beta} (k_y + k'_y) + \frac{2\lambda}{\alpha} (k_x + k'_x) + \frac{\pi \Sigma k}{1 + \mu} \left( \frac{\alpha}{\beta} + \mu \frac{\beta}{\alpha} \right) \right] \dots \dots \dots (9)$$

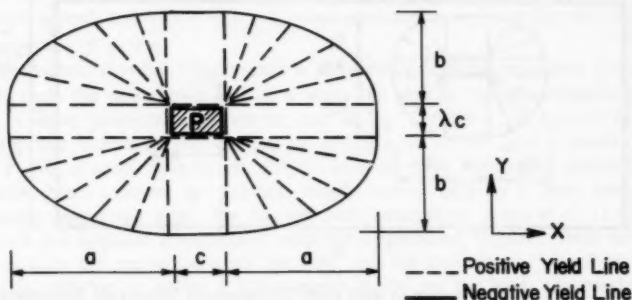


FIG. 3.—Symmetrical Interior Concentrated Load Collapse Mechanism

Equating virtual energies and noting that from Eqs. 1 and 2  $k_y + k'_y = (\Sigma k)/(1 + \mu)$  and  $k_x + k'_x = (\mu \Sigma k)/(1 + \mu)$ , it is possible to write

$$\frac{P}{m \Sigma k} = \frac{\frac{2}{\beta} + \frac{2\mu\lambda}{\alpha} + \pi \left( \frac{\alpha}{\beta} + \mu \frac{\beta}{\alpha} \right)}{(1 + \mu) \left[ 1 + \omega + \frac{\omega}{\lambda} \left( \beta + \lambda\alpha + \frac{\pi}{3} \alpha\beta \right) \right]} \dots \dots \dots (10)$$

In this unbounded mechanism symmetry dictates that the corner fans will be circular arcs if the slab is isotropic, i.e.,  $\mu = 1$ . Then from Johansen's (4) "affinity" theorem,  $q = \alpha/\beta = \sqrt{\mu}$  and Eq. 10 can be rewritten as

$$\frac{P}{m\Sigma k} = \frac{\frac{2}{\beta}(1 + \lambda\sqrt{\mu}) + 2\pi\sqrt{\mu}}{(1 + \mu) \left[ 1 + \omega + \frac{\omega\beta}{\lambda} \left( 1 + \lambda\sqrt{\mu} + \frac{\pi}{3}\beta\sqrt{\mu} \right) \right]} \dots \dots \dots (11)$$

It is obvious that the load carrying capacity of the slab will be a minimum for maximum values of  $\beta$ , i.e., that the collapse mechanism must become as large as "possible." That means the mechanism will spread until stopped by a geometrical obstacle or a reverse, i.e., positive since the peripheral yield line is negative, moment field, or both. For a slab supported along its entire periphery by strong beams or walls, such as that shown in Fig. 4, the collapse mechanism will spread until it becomes tangent to one or more of the slab boundaries. Which of the boundaries will be reached will depend on the geometry, the loading, and on the layout of the reinforcement. This is in contrast to the equation obtained if Fig. 3 is assumed to represent the collapse mechanism

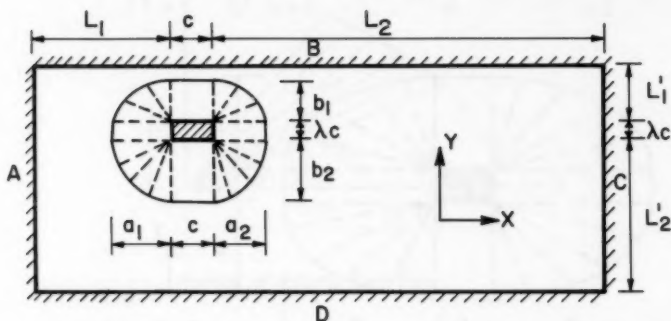


FIG. 4.—Collapse Mechanism in Slab with Continuously Supported Boundaries

of a uniformly loaded slab supported on an interior rectangular column. In that case, with  $P$  being the force in the column due to the uniformly distributed load acting on the slab

$$\frac{P}{m\Sigma k} = \frac{2 [(\pi\beta + \lambda)\sqrt{\mu} + 1]}{\beta(1 + \mu) \left\{ 1 - \frac{\omega}{\lambda} \left[ \frac{\pi}{3}\beta^2\sqrt{\mu} + (1 + \lambda\sqrt{\mu})\beta + \lambda \right] \right\}} \dots \dots \dots (12)$$

When this equation is minimized for  $P$ ,  $\beta$  is found to be self limiting, with the mechanism always having a definite size whose surface area is smaller than the area of slab required to produce  $P$ , i.e.,  $4ab + \lambda c^2 < P/w$ .

Fig. 4 represents a slab supported on rigid boundaries, which have been labelled A, B, C, and D for easy reference. To generalize the analysis, it will be assumed that the negative moment reinforcement crossing each boundary can be different, but that the positive moment reinforcement will be constant throughout the slab, though it may be orthotropic. This corresponds to frequent design practice.



Let the negative moment coefficients be:  $k_{x_1}$  over boundary A;  $k_{x_2}$  over boundary C;  $k_{y_1}$  over boundary B; and  $k_{y_2}$  over boundary D. Note that the subscripts correspond to the subscripts of the dimensions in the direction of the reinforcement. It is convenient to define  $\mu_1 = (k_{x_1} + k'_x)/(k_{y_1} + k'_y)$ ,  $\mu_2 = (k_{x_2} + k'_x)/(k_{y_2} + k'_y)$ ;  $\Sigma k_1 = k_{x_1} + k'_x + k_{y_1} + k'_y$ ,  $\Sigma k_2 = k_{x_2} + k'_x + k_{y_2} + k'_y$ ;  $\alpha_1 = a_1/c$ ,  $\alpha_2 = a_2/c$ ,  $\beta_1 = b_1/c$ ,  $\beta_2 = b_2/c$ ; and  $\lambda_1 = \bar{L}_1/c$ ,  $\lambda_2 = \bar{L}_2/c$ ,  $\lambda'_1 = \bar{L}'_1/c$ ,  $\lambda'_2 = \bar{L}'_2/c$ . The loading will be assumed as previously.

Proceeding as in the derivation of Eq. 10

$$\frac{P}{m \Sigma k_2} = \frac{\frac{1}{\beta_2} + \frac{\mu_2 \lambda}{\alpha_2} + \frac{\pi}{4} \left[ \frac{\alpha_1 + \alpha_2}{\beta_2} + \frac{\mu_2 (\beta_1 + \beta_2)}{\alpha_2} \right] + \frac{\Sigma k_1}{\Sigma k_2} \frac{1 + \mu_2}{1 + \mu_1} \left\{ \frac{1}{\beta_1} + \frac{\mu_1 \lambda}{\alpha_1} + \frac{\pi}{4} \left[ \frac{\alpha_1 + \alpha_2}{\beta_1} + \frac{\mu_1 (\beta_1 + \beta_2)}{\alpha_1} \right] \right\}}{(1 + \mu_2) \left\{ 1 + \omega + \frac{\omega}{2\lambda} \left[ \beta_1 + \beta_2 + \lambda (\alpha_1 + \alpha_2) + \frac{\pi}{6} (\alpha_1 + \alpha_2) (\beta_1 + \beta_2) \right] \right\}} \quad (13)$$

This equation must be minimized with respect to  $\alpha_1$ ,  $\alpha_2$ ,  $\beta_1$ , and  $\beta_2$  in order to obtain the lowest upper bound on  $P/(m \Sigma k_2)$ . At the same time, the geometrical constraints require that  $\alpha_1 \leq \lambda_1$ ,  $\alpha_2 \leq \lambda_2$ ,  $\beta_1 \leq \lambda'_1$ , and  $\beta_2 \leq \lambda'_2$ . The minimization is best done numerically, either iteratively on a computer or by trial and error on a programmable calculator. It will quickly be found that the mechanism will be tangent to one or more support boundaries and, depending on the magnitude of  $\omega$ , may reach all the boundaries. The larger  $\omega$ , the more the mechanism tends to spread, and  $\alpha/\beta = \sqrt{\mu}$  only when the boundaries force this relationship. In general  $\alpha/\beta \neq \sqrt{\mu}$ .

The literature (4,8,9,10) presents a different collapse mechanism for point loads from the one shown in Fig. 4 when the slab is "simply supported" on one or more boundaries. However, use of Eq. 13 with  $k_x$  or  $k_y = 0$  for the appropriate boundary and the region adjacent to it, will give a lower value for  $P$ . (As a quick illustration, for an isotropic slab with equal positive and negative yield moment  $m'$  per unit length, loaded only by a point load near a simply supported edge, the conventional mechanism gives  $P = 11.42 m'$ . Use of the elliptical formulation, with the appropriate negative yield moment set = 0 in the region between the load and the boundary, gives  $P = 10.73 m'$ .) In addition to giving a lower upper bound on the load, the mechanism of Fig. 4 is likely to fit the actual reinforcing pattern better, since designers are unlikely to provide much top reinforcement perpendicular to a simply supported slab boundary. However, if such reinforcement is provided and the so-called "simple" support can resist some torsion, then these factors can be incorporated into  $k_x$  or  $k_y$  (whichever is appropriate) and this mechanism will be all the more accurate.

The mechanism of Fig. 4 was based on the assumption that the slab boundary supports would be sufficiently strong to prevent yield hinges from forming in them. It therefore does not provide any information on the flexural strength required in the supporting beams. If required beam strengths are to be investigated or if a free slab boundary is to be considered, two additional geometrically admissible collapse mechanisms must be analyzed. They are shown in Figs. 5 and 6.

Looking first at the mechanism of figure 5, let  $W$  be the weight of the stem of the spandrel beam per unit length;  $M_1$  be its negative yield moment to the left of  $P$ ;  $M_2$  be its negative yield moment to the right of  $P$ ; and  $M'$  be its positive yield moment. The stem width of the beam will be assumed to be

negligible. The same assumptions and notation as before will be used for the slab yield moments, noting that  $k_{y1}$  should be taken equal to zero, though its value will not affect  $P$ . Then proceeding as before, the equation of virtual energy equilibrium leads to

$$\frac{P}{m \Sigma k_2} = \frac{\left( \beta_1 + \frac{\pi}{4} \beta_2 + \lambda \right) \left[ \frac{\mu_1}{\alpha_1} \left( \frac{1 + \mu_2}{1 + \mu_1} \right) \frac{\Sigma k_1}{\Sigma k_2} + \frac{\mu_2}{\alpha_2} \right] + \frac{4 + \pi(\alpha_1 + \alpha_2)}{4\beta_2} + (1 + \mu_2) \left( \frac{M_1 + M'_1}{\alpha_1 c m \Sigma k_2} + \frac{M_2 + M'_2}{\alpha_2 c m \Sigma k_2} \right)}{(1 + \mu_2) \left\{ 1 + \omega + \frac{\omega}{2\lambda} \left[ 2\beta_1 + \beta_2 + \left( \beta_1 + \lambda + \frac{\pi}{6} \beta_2 \right) (\alpha_1 + \alpha_2) \right] + \frac{Wc}{P} \left[ 1 + \frac{1}{2} (\alpha_1 + \alpha_2) \right] \right\}} \quad (14)$$

This equation, also, must be minimized with respect to the geometry, observing the limitations imposed by the boundaries. If  $\omega$  has a realistic value and the

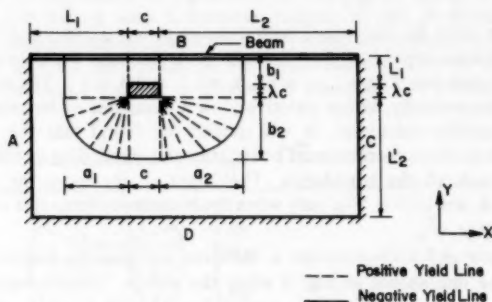


FIG. 5.—Slab with Collapsible Beam Support

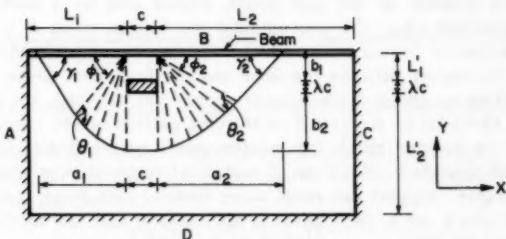


FIG. 6.—Alternate Collapsible Beam Mechanism

slab proportions are within a practical range, it is very likely that  $P$  will be a minimum when the mechanism has reached two or more of the boundaries. Thus  $\alpha_1 \leq \lambda_1$ ,  $\alpha_2 \leq \lambda_2$ , and  $\beta_2 \leq \lambda'_2$ . Of course  $\beta_1$  will equal  $\lambda'_1$ . If the beam strengths are known, it will be necessary to check  $P$  from Eq. 14 against  $P$  obtained from Eqs. 13 and 15. If the beam strengths are not known but  $P$  and the slab strengths are, Eq. 14 can be solved for the beam strengths. If  $W$ ,  $M'_1$ ,  $M_1$ , and  $M_2$  are set equal to zero, the solution for a slab with a free edge is obtained. If the slab is continuous across the beam with a mirror

loading on the other side, the two mechanisms may be combined, or else one may be solved using half the actual beam strengths and weight.

The mechanism of Fig. 6 is an alternate to that of Fig. 5. It is likely to govern if  $\lambda'_1$  is relatively small and the beam is weak or the slab edge is free. A large value of  $\mu_1$  and  $\mu_2$  will also favor its formation. In this case the equation of virtual energy equilibrium leads to

$$\frac{P}{m \Sigma k_2} = \frac{\frac{1}{2} (N_1 + N_2 + N_3 + N_4) + N_5 + N_6 + N_7 + N_8}{(1 + \mu_2) \left[ \frac{\omega}{6\lambda} (D_1 + D_2) + D_3 \right]} \dots \dots \dots (15)$$

in which  $\beta' = \beta_1 + \beta_2 + \lambda$ ;  $\gamma_1 = \theta_1 - \phi_1$ ;  $\gamma_2 = \theta_2 - \phi_2$ ; and

$$N_1 = \frac{\tan \phi_1}{q_1^2 \tan^2 \phi_1 + 1} \left[ \frac{q_1^2 \left( \frac{k_{y_2}}{k'_y} - 1 \right)}{\frac{k_{y_2}}{k'_y} + 1} - \frac{\Sigma k_1}{\Sigma k_2} \left( \frac{1 + \mu_2}{1 + \mu_1} \right) \frac{\mu_1 \left( \frac{k_{x_1}}{k'_x} - 1 \right)}{\frac{k_{x_1}}{k'_x} + 1} \right]$$

$$N_2 = \frac{\tan \phi_2}{q_2^2 \tan^2 \phi_2 + 1} \left[ \frac{q_2^2 \left( \frac{k_{y_2}}{k'_y} - 1 \right)}{\frac{k_{y_2}}{k'_y} + 1} - \frac{\mu_2 \left( \frac{k_{x_2}}{k'_x} - 1 \right)}{\frac{k_{x_2}}{k'_x} + 1} \right]$$

$$N_3 = \left[ \frac{\pi}{2} - \arctan (q_1 \tan \phi_1) \right] \left[ q_1 + \frac{\Sigma k_1}{\Sigma k_2} \left( \frac{1 + \mu_2}{1 + \mu_1} \right) \frac{\mu_1}{q_1} \right]$$

$$N_4 = \left[ \frac{\pi}{2} - \arctan (q_2 \tan \phi_2) \right] \left( q_2 + \frac{\mu_2}{q_2} \right)$$

$$N_5 = \left( \frac{\sin \phi_1}{\sin \theta_1 \sin \gamma_1} \right) \left[ \frac{\Sigma k_1}{\Sigma k_2} \left( \frac{1 + \mu_2}{1 + \mu_1} \right) \frac{\mu_1 \frac{k_{x_1}}{k'_x} \sin^2 \gamma_1}{\frac{k_{x_1}}{k'_x} + 1} + \frac{\frac{k_{y_2}}{k'_y} \cos^2 \gamma_1}{\frac{k_{y_2}}{k'_y} + 1} \right]$$

$$N_6 = \left( \frac{\sin \phi_2}{\sin \theta_2 \sin \gamma_2} \right) \left( \frac{\mu_2 \frac{k_{x_2}}{k'_x} \sin^2 \gamma_2}{\frac{k_{x_2}}{k'_x} + 1} + \frac{\frac{k_{y_2}}{k'_y} \cos^2 \gamma_2}{\frac{k_{y_2}}{k'_y} + 1} \right)$$

$$N_7 = - \left[ \frac{\mu_2 \left( \frac{\sin^2 \phi_1}{\tan \theta_1} + \frac{\sin^2 \phi_2}{\tan \theta_2} \right)}{\frac{k_{x_2}}{k'_x} + 1} + \frac{\frac{\cos^2 \phi_1}{\tan \theta_1} + \frac{\cos^2 \phi_2}{\tan \theta_2}}{\frac{k_{y_2}}{k'_y} + 1} \right]$$

$$N_8 = \frac{\frac{k_{y_2}}{k_y}}{\beta' \left( \frac{k_{y_2}}{k_y} + 1 \right)} + \left( \frac{M_1 + M'}{\alpha_1 cm \Sigma k_2} + \frac{M_2 + M'}{\alpha_2 cm \Sigma k_2} \right) (1 + \mu_2)$$

$$D_1 = \beta'^2 \left\{ q_1 \left[ \frac{\pi}{2} - \arctan(q_1 \tan \phi_1) \right] + q_2 \left[ \frac{\pi}{2} - \arctan(q_2 \tan \phi_2) \right] \right\}$$

$$D_2 = \alpha_1^2 \left( \frac{\sin \gamma_1 \sin \phi_1}{\sin \theta_1} \right) + \alpha_2^2 \left( \frac{\sin \gamma_2 \sin \phi_2}{\sin \theta_2} \right) + 3\beta'$$

$$D_3 = \frac{\beta_2 + \frac{1}{2} \lambda}{\beta'} + \frac{Wc}{P} \left( 1 + \frac{\alpha_1 + \alpha_2}{2} \right)$$

The shapes of the two elliptic arcs are given by  $q_1$  and  $q_2$ , the ratios of  $x$ -axis to  $y$ -axis lengths. The lengths of the elliptic arcs are determined by the angles  $\phi_1$  and  $\phi_2$ . The angles  $\theta_1$  and  $\theta_2$  can be obtained from the geometry of the ellipses as

$$\theta_i = \arcsin \left( \frac{q_i^2 \sin^2 \phi_i + \cos^2 \phi_i}{\sqrt{q_i^4 \sin^2 \phi_i + \cos^2 \phi_i}} \right) \dots \dots \dots (16)$$

and the spread of the mechanism in the  $y$  direction can be obtained as a function of the spread in the  $x$  direction from the geometry of the triangles as

$$\frac{\beta'}{\alpha_i} = \frac{(\sqrt{q_i^2 \sin^2 \phi_i + \cos^2 \phi_i}) \sin(\theta_i - \phi_i)}{q_i \sin \theta_i} \dots \dots \dots (17)$$

In the case of the mechanism of Fig. 6, also, even a relatively small distributed load tends to cause it to spread in all directions toward the actual slab boundaries. Thus one or more of  $\alpha_1$ ,  $\alpha_2$ , and  $\beta_2$  (and therefore also  $\beta'$ ) will be determined by the slab dimension. However, if one dimension is very different from the others, as when the concentrated load is located near boundary A or C, or if the distributed load is very small, the mechanism may not spread to all the boundaries.

It is not mathematically feasible to obtain the  $q_i$  and  $\phi_i$  directly from  $\beta'/\alpha_i$ . Fig. 7 has therefore been prepared from Eqs. 16 and 17 as a calculation aid. Eq. 15 can then be minimized for  $q_1$ ,  $q_2$ ,  $\phi_1$ , and  $\phi_2$  either iteratively or by trial and error, or a combination of the two. Setting values for  $\alpha_i$  and  $\beta'$  from the slab geometry, possible combinations of  $q$  and  $\phi$  can be obtained from Fig. 7 and tried in Eq. 15 until the lowest value of  $P$  is obtained for the given conditions. The process is not as cumbersome and time consuming as it may initially appear, i.e.,  $P$  is not very sensitive to changes in the various parameters, and a very acceptable value can usually be obtained in half a dozen or so tries on a programmable calculator or minicomputer.

If the strength of the beam along edge B is known to be small, or if its required strength is to be found, then only the mechanisms of Figs. 5 and 6 need be investigated. If the beam is known to be very strong, then only

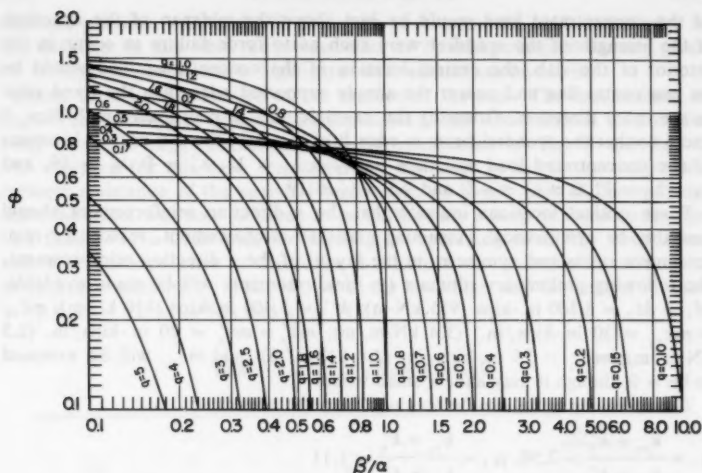


FIG. 7.—Solution of Eqs. 16 and 17

the mechanism of Fig. 4 can control. In between, all three mechanisms may have to be investigated.

If the reinforcement is arranged symmetrically and the concentrated load is movable, the worst location for it will be at  $\lambda_1 = \lambda_2$  and  $\lambda'_1 = 0$  with a weak beam, or at  $\lambda_1 = \lambda_2$  and  $\lambda'_1 \leq \lambda'_2$  for a strong beam. Symmetry of course greatly simplifies the various equations and reduces the number of iterations or trials required for minimization.

#### EXAMPLE

Consider a reinforced concrete slab, 20 ft  $\times$  25 ft (6.1 m  $\times$  7.6 m) in area and 8 in. (0.2 m) thick. The short sides and one of the long sides will be continuous over supporting girders, while the other long side is discontinuous and cast integrally with a spandrel beam which has a stem width of 12 in. (0.3 m) and stem depth below the slab of 18 in. (0.5 m). The torsional strength of the spandrel will be ignored in these calculations, but it could be taken into account if adequate torsional ductility were assured and continuity reinforcement were provided for the slab-spandrel connection.

It will be assumed that the slab may have to resist a "concentrated" service load of 40 kips (18 tons) with a footprint of 12 in.  $\times$  12 in. (0.3 m  $\times$  0.3 m), which can act at any point in the slab. The structure will also have to carry its self weight, and the effect of additional distributed load will also be investigated. Applying ACI Code (1) load factors, the load ratios to be used in the initial analysis will be, with  $w$  = self weight of the slab,  $\omega = (w\lambda c^2)/P = 0.002$  and  $(Wc)/P = 0.0045$ .

If the strength of the spandrel beam were to be critical, the worst location

of the concentrated load would be just above the midspan of the spandrel. If the strength of the spandrel were such as to force failure to occur in the interior of the slab, the critical location of the concentrated load would be on one center line and nearer the simply supported edge than the fixed edge in the other direction. Orienting the example slab in conformity with Figs. 5 and 6 so that the spandrel beam is edge B of the slab, the two critical locations of the concentrated load will then be  $\lambda_1 = \lambda_2 = 12$ ,  $\lambda'_1 = 0$ ,  $\lambda'_2 = 19$ , and  $\lambda_1 = \lambda_2 = 12$ ,  $0 \leq \lambda'_1 \leq 9.5$ , and  $9.5 \leq \lambda'_2 \leq 19$ .

These critical locations indicate that the  $x$  direction reinforcement should probably be symmetrical. Assuming grade 60 reinforcement, reasonable reinforcement ratios and symmetry in the layout of the  $x$  direction reinforcement, the following preliminary ultimate ( $\approx$  yield) moments will be made available:  $M_1 = M_2 = 8,100$  in.-kips (915 kN-m);  $M' = 5,400$  in.-kips (610 kN-m);  $mk_{x_1} = mk_{x_2} = 30$  in.-kips/in. (3.4 kN-m/m);  $mk'_x = mk'_y = 20$  in.-kips/in. (2.3 kN-m/m);  $mk_{y_2} = 25$  in.-kips/in. (2.8 kN-m/m); and  $mk_{y_1}$  will be assumed to be 0, though it may have a small value.

The following ratios can be obtained from the above:

$$\mu_1 = \frac{k_{x_1} + k'_x}{k_{y_1} + k'_y} = 2.50, \quad \mu_2 = \frac{k_{x_2} + k'_x}{k_{y_2} + k'_y} = 1.11$$

$$\frac{\Sigma k_1}{\Sigma k_2} = \frac{70}{95} = 0.74, \quad \frac{k_{x_1}}{k'_x} = \frac{k_{x_2}}{k'_x} = 1.50, \quad \frac{k_{y_2}}{k'_y} = 1.25$$

The effect of symmetry will be to make  $M_1 = M_2 = M$ ,  $k_{x_1} = k_{x_2} = k_x$ ,  $\alpha_1 = \alpha_2 = \alpha$ ,  $\phi_1 = \phi_2 = \phi$ , and  $q_1 = q_2 = q$ . These designations will be used in Table 1 to avoid duplicating information.

Table 1 presents the results of sample calculations for the problem. The top part of the table contains all the trials used in obtaining solutions for the example with each of the three possible collapse mechanisms. All calculations were carried out on a TI-58 programmable calculator to ensure that the solutions would be within the capability of any engineering office. Without the advantage of symmetry, however, Eq. 15 would require use of a TI-59 or equivalent.

Looking at the top part of Table 1 and the solution process in more detail, the first mechanism analyzed was that of Fig. 6 and Eq. 15. On the assumption that the mechanism would spread as far as possible, an initial value of  $\beta_2 = \lambda'_2 = 19$  was chosen. The first trial for  $\phi$  was  $\phi = 0$  (actually 0.0001 was used to avoid calculation difficulties) for which  $q = \alpha/\beta'$ . This led to an initial value of  $P/m\Sigma k_2 = 3.02$ . The next trial value used for  $\phi$  was 0.1, and from Fig. 7, with  $\beta'/\alpha = 20/12 = 1.67$ ,  $q \approx 0.59$ . For this trial, Eq. 15 gave  $P/m\Sigma k_2 = 3.01$ . A further trial, with  $q = 0.55$  and  $\phi = 0.24$  led to  $P/m\Sigma k_2 = 3.06$ .

Exploring the possibility that the mechanism would not spread all the way to the far boundary,  $\beta_2 = 18$  was investigated and led to almost identical results, as shown in the table. Setting  $\beta_2 = 14$  started an upward trend in the solutions. The numbers indicate that the solution surface is almost flat in the vicinity of the correct answer, making it unnecessary to perform many trials.

The process was repeated with the mechanism of Fig. 5 and Eq. 14. Again, the very flat solution surface and the tendency of the mechanism to spread made three trials sufficient. This mechanism produced a lower value of  $P/m\Sigma k_2$

than the previous one, and will therefore govern for the load at the edge in this example. In this table the lowest value of  $P/m\Sigma k_2$  obtained for any given set of physical parameters is highlighted with an asterisk beside it.

Next, the load was moved to the interior of the slab. The mechanisms of Figs. 5 and 6 will give greater load capacities as the concentrated load moves away from the edge. Therefore, only the mechanism of Fig. 4 and Eq. 13 was analyzed for this case. Parameter  $k_{y'}$  was kept = 0, but the weight and moment resistance of the spandrel beam were no longer part of the problem, since the beam was now assumed to be sufficiently strong to force an interior slab failure. Five trials with the mechanism spreading to all the boundaries, and two additional ones in which the mechanism was curtailed in size, were sufficient to establish  $P/m\Sigma k_2 = 2.16$  as the low value, and the critical location at  $\lambda_1 = \lambda_2 = 12$ ,  $\lambda'_1 = 7.5$ , and  $\lambda'_2 = 11.5$ .

TABLE 1.—Results from Example

$\frac{N_c}{F}$	$\frac{H+H'}{m\Sigma k_2}$	$\lambda$	$v_1$	$v_2$	$w$	$\alpha$	$\beta_1$	$\beta_2$	$\frac{\Sigma k_1}{\Sigma k_2}$	$\frac{k_x}{k_y}$	$\frac{k_{y'}}{k_y}$	$\phi$	$q$	$\frac{P}{m\Sigma k_2}$ for mechanisms of		
														Fig. 4	Fig. 5	Fig. 6
0.0045	11.58	1	2.5	1.11	0.002	12	0	19	0.74	1.5	1.25	0	0.60			5.02
								18				0.10	0.59			5.01
								18				0.24	0.55			5.06
								18				0	0.63			5.02
								18				0.10	0.62			5.01
								14				0.19	0.60			5.03
								10				0	0.80			5.07
								7.5				0.10	0.79			5.03
								19				0.32	0.70			5.06
								18							2.85	
								15							2.86	
								6							2.19	
								13							2.16	
								7							2.16	
								11							2.16	
								7.5							2.16	
								9							2.18	
								10							2.20	
								7.5							2.28	
								10								
0.0045	11.58				0	12	0	7	0.74	1.5	1.25	0.59	1.20			3.45
								10								3.45
								7.5								3.45
0.0045	11.58				0.004	0	19	0	0.74	1.5	1.25				2.77	2.47
								7.5								2.47
								19							1.77	2.35
								7.5								2.35
0.0045	5.49				0.002	0	0	9	0.74	1.5	1.25	0.43	1.10			2.07
								15								2.07
								7	0.74	1.5	1.25	0.59	1.20			2.30
								12								2.87
					0.004			19	0.74	1.5	1.25	0.10	0.59			1.77
								7	0.74	1.5	1.25	0.59	1.20			1.73
					0.002			7	0.74	1.5	1.25	0.59	1.20			1.26
								14								1.42
								12	0.74	1.5	1.25	0.59	1.20			1.39
					0.004			9	0.74	1.5	1.25	0.43	1.10			1.14
								16							1.20	

At this point, the preliminary design can be checked. For the slab itself, with  $P$  in the interior,  $m\Sigma k_2 = P_u/2.16 = 68/2.16 = 31.5$  in.-kips/in. (3.6 kN). The assumed  $m\Sigma k_2 = 95$  in.-kips/in. (10.7 kN-m/m), and the assumed reinforcement could therefore be reduced by a factor of about three. Alternatively, a much heavier load could be carried.

To obtain some "feel" for this type of problem, some of the physical parameters were varied. The minimum results for each mechanism are shown in the lower half of Table 1. First,  $w$ , i.e.,  $\omega$ , was set = 0, a common assumption when dealing with large concentrated loads. The result is a 28% increase in the concentrated load capacity. Doubling  $w$  on the other hand, reduced  $P$  by 22%. Interestingly, when  $\omega = 0$  the two edge load mechanisms gave the same value

for  $P$  but with two different size mechanisms, neither of which spread to the far boundary. When  $w$  was doubled, so that  $\omega = 0.004$ , the mechanisms behaved as with  $\omega = 0.002$  except that  $\beta_2 = 18$  gave somewhat larger values of  $P/m\Sigma k_2$  than  $\beta_2 = 19$  did.

Reduction in beam strength to slightly less than one half its original value caused the edge load mechanisms to become critical. For  $\omega = 0.002$  both gave the same concentrated load capacity, for  $\omega = 0$  the mechanism of Fig. 6 governed and for  $\omega = 0.004$  that of Fig. 5 gave the lowest strength. In most of these cases the mechanisms did not extend to boundary D, but did reach boundaries A and C.

Complete removal of the edge beam had similar effects. It is interesting to note, however, that the slab as originally designed could still safely carry a concentrated load approximately 1 3/4 times the assumed  $P$ , plus its self weight, with no edge beam at all.

To investigate the accuracy of the superposition method compared to the correct solution, an isotropically reinforced square slab of side length  $L =$

TABLE 2.—Comparison of Eq. 13 and Superposition (Homogeneous, Isotropic Square Plate with Clamped Edges)

$\omega$ (1)	$\alpha_1$ (2)	$\alpha_2$ (3)	$\beta_1$ (4)	$\beta_2$ (5)	$P/m\Sigma k$	
					Super- position (6)	Eq. 13 (7)
0	12	12	12	12	—	3.31
0.002	12	12	12	12	2.41	2.45
0.004	12	12	12	12	1.89	1.94
0.01	12	12	12	12	1.15	1.20
0	4	4.5	4	4.5	—	3.625
0.002	4	5	4	5	2.57	3.42
0.004	4	6	4	6	1.99	3.21
0.01	4	20	4	20	1.18	2.16

$L_1 + c + L_2 = L'_1 + \lambda_c + L'_2$ , with fixed boundaries and equal top and bottom reinforcement, can easily be analyzed. Taking corner levers into account, the uniformly distributed load carrying capacity of the slab (with  $P = 0$ ) will be (4)  $wL^2 = 11 m\Sigma k$ . When  $\lambda = 1$  and assuming  $\lambda_1 = \lambda_2 = \lambda'_1 = \lambda'_2 = 12$  and  $\omega = 0$ , Eq. 13 gives  $P = 3.31 m\Sigma k_2$ . Using superposition, the total required  $m\Sigma k = (wL^2)/11 + P/3.31$ . Rewriting in the notation used previously, and using the aforementioned dimensionless ratios, this superposition expression can be rewritten as

$$\frac{P}{m\Sigma k} = \frac{1}{56.8\omega + 0.302} \quad \dots \dots \dots (18a)$$

Results obtained by use of this equation can then be checked against those obtained by use of Eq. 13 for various magnitudes of  $\omega$ .

The upper half of Table 2 shows some results from both superposition and Eq. 13 for the centrally located concentrated load. Obviously superposition



works very well for this case, in which the collapse mechanisms tend toward congruence.

The lower half of Table 2 shows results from both superposition and Eq. 13 when the concentrated load is moved along the diagonal of the square plate to  $\lambda_1 = \lambda'_1 = 4$  and  $\lambda_2 = \lambda'_2 = 20$ . With  $\omega = 0$ , minimization of Eq. 13 gives  $P/(m\Sigma k_2) = 3.625$  and therefore the superposition equation, Eq. 18a, changes to

$$\frac{P}{m\Sigma k} = \frac{1}{56.8\omega + 0.276} \quad (18b)$$

The lower half of Table 2 shows that the mechanisms are now no longer congruent, and that for realistic values of  $\omega$  superposition will lead to a gross underestimate of the strength of the slab. It is interesting to note, also, the effect of the relative magnitude of the distributed load on the spread of the collapse mechanism as shown in Table 2 by the values of  $\alpha_2$  and  $\beta_2$  for which  $P/(m\Sigma k)$  became a minimum.

#### ADDITIONAL OBSERVATIONS

1. Other calculations which have been carried out have revealed that the solution to Eq. 15 is almost totally independent of the values of  $k_{x_1}/k'_x$  and  $k_{x_2}/k'_x$ . Multiplying or dividing these parameters by factors of three produces less than 0.1% change in results. Changing  $k_{y_2}/k'_y$  similarly produces approximately 10% changes in results. This is in agreement with previous findings for uniformly loaded slabs (3). It was also found that if edges A and C of the slab are much shorter than edges B and D, the mechanism will invariably spread to edge D, but may not reach edges A and C.

2. Reducing the size of the footprint of the concentrated load will reduce its permissible magnitude. However, this effect is also relatively small for practical cases, since the footprint must be kept sufficiently large to prevent shear punching.

3. If more than one edge of the slab is to be simply supported on collapsible beams, the mechanisms of Figs. 5 and 6 must be applied to each edge in turn. In addition, an elementary overall collapse mechanism (4) with yield lines over and between column lines must also be investigated.

4. If the collapsible beam is an interior one, with the slab continuous over it, the mechanism of Fig. 5 will be critical for the concentrated load acting on top of the beam. For calculation purposes it will then be useful to work with half the beam and half the concentrated load in conjunction with the slab on one side.

5. Sometimes the concentrated load cannot reach the edge of the slab, and  $\beta_1 = \lambda'_1 \neq 0$ . The larger  $\beta_1$ , the greater the likelihood that the mechanism of Fig. 5 will give lower carrying capacity than that of Fig. 6.

6. Only rectangular footprints have been considered here for the concentrated loads. Previous experience with the flexural strength of uniformly loaded slabs supported on columns of various shapes (2) has shown that isotropic arrangement of the reinforcement will lead to slightly lower (on the order of 1%-3%) flexural strengths for circular than for square columns. This was not necessarily true for orthotropically reinforced slabs, where appropriately oriented rectangular

columns sometimes gave slightly lower strengths. The differences were always too small, however, to be of practical significance, and for normal design purposes it will be quite satisfactory to substitute square footprints of equal area for circular ones.

7. Multiple concentrated loads acting on peripherally supported slabs, as well as single concentrated loads acting on slabs supported directly on columns (flat plates), are presently being investigated. In the multiple load case, two arrangements of the load cause little difficulty: (1) If the loads are closely spaced and approximately equal in magnitude (as the load carrying wheels of a forklift) they may conveniently be treated as a single load spread over the actual region they occupy; and (2) if one of the loads is much larger than the others, the single load mechanism may be expected to form, and a reasonable approximation to the slab strength may be obtained by smearing the smaller loads into the uniformly distributed load. In the flat plate problem, an interaction (between load and column) mechanism has been identified and analyzed for some simple cases. It leads to the lowest collapse loads for a fairly narrow range of geometries and load ratios, with overall slab collapse mechanisms or pure flexural column punching mechanisms (2) controlling more frequently.

## CONCLUSIONS

Yield Line Theory has been used to derive expressions for the flexural capacity of orthotropically reinforced concrete slabs subjected simultaneously to a concentrated and a uniformly distributed load. The weight and flexural strength of a boundary beam are included in the expressions. Example calculations have shown the effects of the location at which the concentrated load is placed, of the magnitude of the distributed load, and of the strength of the boundary beams. It was found that the collapse mechanisms have a tendency to spread until stopped by one or more boundaries, and that the tendency becomes stronger with increase in the distributed load. It was also found that the solutions are relatively insensitive to the negative to positive yield moment ratios of the slab and to the dimensions of the collapse mechanisms. An exploration of the possible use of superposition of solutions revealed that the results could be quite accurate or grossly inaccurate, depending on how nearly geometrically congruent the individual collapse mechanisms may be.

## APPENDIX I.—REFERENCES

1. "Building Code Requirements for Reinforced Concrete," ACI 318-77, American Concrete Institute Committee 318, American Concrete Institute, Detroit, Mich., 1977.
2. Gesund, H., and Goli, H. B., "Local Flexural Strength of Slabs at Interior Columns," *Journal of the Structural Division*, ASCE, Vol. 106, No. ST5, Proc. Paper 15394, May, 1980, pp. 1063-1078.
3. Goli, H. B., and Gesund, H., "Linearity in Limit Design of Orthotropic Slabs," *Journal of the Structural Division*, ASCE, Vol. 105, No. ST10, Proc. Paper 14928, Oct., 1979, pp. 1901-1915.
4. Johansen, K. W., "Yield Line Theory," Cement and Concrete Association, London, England, 1962, 181 pp.
5. Lenschow, R., and Sozen, M. A., "A Yield Criterion for Reinforced Concrete Slabs," *Proceedings*, American Concrete Institute, Vol. 64, No. 5, 1967, pp. 266-273.
6. Mansfield, E. H., "Studies in Collapse Analysis of Rigid-Plastic Plates with a Square

- Yield Diagram," *Proceedings of the Royal Society*, London, England, Series A, Vol. 241, 1957, pp. 311-338.
7. Mills, G. M., "A Partial Kinking Yield Criterion for Reinforced Concrete Slabs," *Magazine of Concrete Research*, Vol. 27, No. 90, 1975, pp. 13-22.
  8. Save, M. A., and Massonet, C. E., *Plastic Analysis and Design of Plates, Shells and Disks*, American Elsevier Publishing Company, Inc., New York, N.Y., 1972, 478 pp.
  9. Sawczuk, A., and Jaeger, T., *Grenztragfähigkeits—Theorie der Platten*, Springer Verlag, Berlin, Germany, 1963, 522 pp.
  10. Wood, R. H., *Plastic and Elastic Design of Slabs and Plates*, Ronald Press Co., New York, N.Y., 1961, 344 pp.

## APPENDIX II.—NOTATION

The following symbols are used in this paper:

- $A$  = label for one boundary of slab;  
 $a, a_1, a_2$  =  $x$  direction dimensions of collapse mechanism;  
 $B$  = label for one boundary of slab—when slab has one boundary supported on collapsible beam,  $B$  is that boundary;  
 $b, b_1, b_2$  =  $y$  direction dimensions of collapse mechanism;  
 $C$  = label for one boundary of slab;  
 $c$  =  $x$  direction dimension of area covered by concentrated load;  
 $D$  = label for one boundary of slab;  
 $D_1, D_2, D_3$  = symbols used to represent other expressions in Eq. 15;  
 $E, E_y$  = virtual energy input by loads into collapse mechanism;  
 $E', E'_y$  = virtual energy absorbed due to rotation of yield lines of collapse mechanism;  
 $i, j$  = boundaries of yield fan;  
 $k_x m, k_{x_1} m, k_{x_2} m$  = negative yield moment per unit length provided by top tension reinforcing bars placed parallel to  $x$ -axis;  
 $k'_x m$  = positive yield moment per unit length provided by bottom tension rebars placed parallel to  $x$ -axis;  
 $k_y m, k_{y_1} m, k_{y_2} m$  = negative yield moment per unit length provided by top tension rebars placed parallel to  $y$ -axis;  
 $k'_y m$  = positive yield moment per unit length provided by bottom tension rebars placed parallel to  $y$ -axis;  
 $L_1, L_2$  = slab dimensions locating position of concentrated load in  $x$  direction;  
 $L'_1, L'_2$  = slab dimensions locating position of concentrated load in  $y$  direction;  
 $M, M_1, M_2$  = negative yield moments of spandrel beam;  
 $M'$  = positive yield moment of spandrel beam;  
 $m$  = unit yield moment per unit length of slab;  
 $N_1 \rightarrow N_8$  = symbols used to represent other expressions in Eq. 15;  
 $P$  = magnitude of concentrated load;  
 $P_u$  = ultimate applied concentrated load;  
 $q, q_1, q_2$  = ratios of  $x$ -axis to  $y$ -axis length of elliptical yield fans;  
 $R_\phi$  = radius of curvature of ellipse making angle  $\phi$  with  $x$ -axis;

- $r$  =  $y$ -axis of elliptical yield fan;  
 $W$  = weight per unit length of collapsible spandrel beam;  
 $w$  = magnitude of uniformly distributed load per unit area acting on slab;  
 $x, y$  = coordinate axes;  
 $\alpha, \alpha_1, \alpha_2$  =  $a/c, a_1/c, a_2/c$ , respectively;  
 $\beta, \beta_1, \beta_2$  =  $b/c, b_1/c, b_2/c$ , respectively;  
 $\beta'$  =  $\beta_1 + \lambda + \beta_2$ ;  
 $\gamma_1, \gamma_2$  =  $\theta_1 - \phi_1, \theta_2 - \phi_2$ , respectively;  
 $\delta$  = virtual displacement of designated point in collapse mechanism;  
 $\theta, \theta_1, \theta_2$  = angles between radii and circumferences of elliptical yield fans (see Figs. 2 and 6);  
 $\lambda c$  =  $y$  direction dimension of the area covered by concentrated load;  
 $\lambda_1, \lambda_2$  =  $L_1/c, L_2/c$ , respectively;  
 $\lambda'_1, \lambda'_2$  =  $L'_1/c, L'_2/c$ , respectively;  
 $\mu, \mu_1, \mu_2$  =  $(k_x + k'_x)/(k_y + k'_y), (k_{x_1} + k'_x)/(k_{y_1} + k'_y), (k_{x_2} + k'_x)/(k_{y_2} + k'_y)$ , respectively;  
 $\theta, \theta_1, \theta_2$  = angles yield fan radii make with  $x$ -axis;  
 $\omega$  =  $(w\lambda c^2)/P$ ; and  
 $\Sigma k, \Sigma k_1, \Sigma k_2$  =  $k_x + k'_x + k_y + k'_y, k_{x_1} + k'_x + k_{y_1} + k'_y, k_{x_2} + k'_x + k_{y_2} + k'_y$ , respectively.

## STEEL STRUTS UNDER SEVERE CYCLIC LOADINGS

By Egor P. Popov,<sup>1</sup> F. ASCE and R. Gary Black<sup>2</sup>

### INTRODUCTION

Recent experience indicates that during a major earthquake stiff buildings having good ductility in the postelastic range behave better than others (11). For this reason, there is a strong renewed interest in reinforced concrete shear walls and braced steel frames for seismic design. Such structural systems are inherently stiffer than the widely used moment resisting frames and tend to reduce costly nonstructural damage during a strong earthquake. Moreover, often it is economically impractical to use moment resisting frames along a narrow width of a building.

The key element in determining the behavior of a conventionally braced steel frame in resisting seismic forces is the brace itself (6). Based on experiments with small specimens, the qualitative features of this behavior under severe cyclic loadings simulating earthquake action are now well understood (5,9,14). However, quantitative information on braces of sizes comparable to those used in practice is very limited. No attempt is made in this paper to consider other framing systems, such as eccentric bracing (10), which can be used as alternative solutions.

The results of cyclic experiments on 24 struts of different steel shapes of sizes employed in practice are reported in this paper. The geometries of some of the specimens were so selected that they also simulate some frequently used sections of larger members. The reported hysteric loops provide a wide range of data on the inelastic behavior of struts under severe reversing loads. An approach for predicting analytically the deteriorating capacity of struts under extreme load reversals is suggested. Some practical implications resulting from this work are summarized at the end of the paper.

### SELECTION OF SPECIMENS

The individual specimens were selected from standard structural steel shapes primarily on the basis of two criteria: (1) That the slenderness ratios of the

<sup>1</sup>Prof., Dept. of Civ. Engrg., Univ. of California, Berkeley, Calif. 94720.

<sup>2</sup>Grad. Student, Dept. of Civ. Engrg., Univ. of California, Berkeley, Calif. 94720.

Note.—Discussion open until February 1, 1982. To extend the closing date one month, a written request must be filed with the Manager of Technical and Professional Publications, ASCE. Manuscript was submitted for review for possible publication on October 8, 1980. This paper is part of the Journal of the Structural Engineering Division, Proceedings of the American Society of Civil Engineers, ©ASCE, Vol. 107, No. ST9, September, 1981. ISSN 0044-8001/81/0009-1857/\$01.00.

test specimens be appropriate to those used in practice; and (2) that the member shapes and proportions be such as to represent typical brace and strut members in current use. The maximum size of the members was set by the capacity of the available double-acting hydraulic cylinder.

Since the effective slenderness ratio of a compression member has been shown to be the single most important parameter in determining its hysteretic behavior (1,8,9,16), care was taken that the chosen  $K\ell/rs$  allow the specimens to be compared with one another, as well as with members used in practice. A common slenderness ratio of 80 was used for specimens within each structural group to allow for comparison of results due to variation in cross-sectional shape. In addition, slenderness ratios of 40, very close to the range of plastic action,

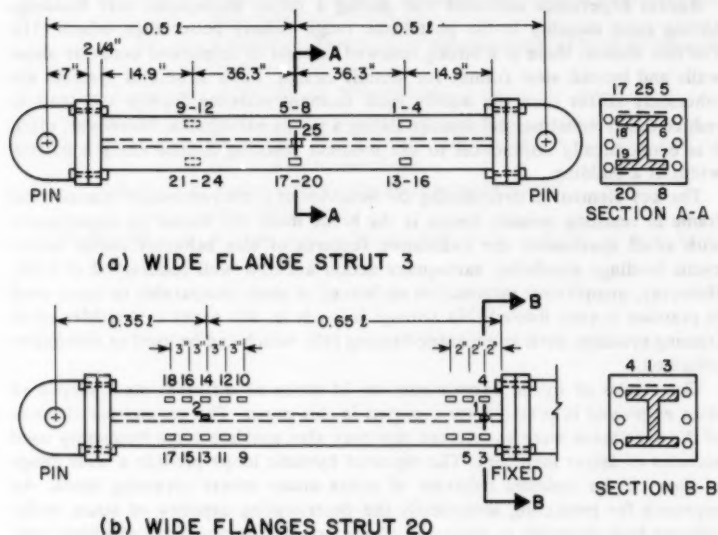


FIG. 1.—Typical Details of Specimens: (a) Pin-Ended; and (b) Pin-Fixed Ended (1 in. = 25.4 mm)

and of 120, very near the elastic buckling range, were assigned to several specimens.

To assess the effect of end restraint on brace behavior, two bounds on the possible end conditions were considered; both ends pinned, and one end pinned and the other end fixed. It should be recognized that in actual structures, something other than these idealized end restraints would be expected, depending on the frame configuration and loading, member slenderness, initial camber, and joint flexibility.

Included within the 24 selected specimens were six different cross-sectional shapes: wide flanges, thin and thick-walled square tubes, thin and thick-walled round pipes, structural tees, and fabricated double angles, and double channels.

TABLE 1.—List of Test Specimens

Strut number (1)	Shape (2)	$K/r$ (3)	Length, in feet (meters) (4)
(a) Struts Pinned at Both Ends			
1	W 8 × 20	120	12.50 (3.81)
2	W 6 × 25	40	5.10 (1.55)
3	W 6 × 20	80	10.07 (3.07)
4	W 6 × 20	80	10.07 (3.07)
5	W 6 × 20	80	10.07 (3.07)
6	W 6 × 16	120	9.67 (2.95)
7	W 6 × 15.5	40	4.87 (1.48)
8	2-L 6 × 3 1/2 × 3/8 <sup>a</sup>	80	9.27 (2.83)
9	2-L 5 × 3 1/2 × 3/8 <sup>a</sup>	40	4.87 (1.48)
10	2-L 4 × 3 1/2 × 3/8 <sup>a</sup>	120	12.50 (3.81)
11	2-C 8 × 11.5 <sup>a</sup>	120	9.83 (3.00)
12	WT 5 × 22.5	80	8.33 (2.54)
13	WT 8 × 22.5	80	10.47 (3.19)
14	Pipe 4 Std.	80	10.07 (3.07)
15	Pipe 4 Std.	80	10.07 (3.07)
16	Pipe 4 X-Strong	80	9.87 (3.01)
17	TS 4 × 4 × 0.250	80	10.00 (3.05)
18	TS 4 × 4 × 0.500	80	9.07 (2.76)
(b) Struts Pinned at One End and Fixed at Other End			
19	W 6 × 20	40	7.19 (2.19)
20	2-L 6 × 3 1/2 × 3/8 <sup>a</sup>	80	13.24 (4.04)
21	Pipe 4 X-Strong	40	7.19 (2.19)
22	TS 4 × 4 × 0.500	80	12.95 (3.95)

TABLE 1.—Continued

(1)	(2)	(3)	(4)
23	W 5 × 16	80	12.00 (3.66)
24	Pipe 3 1/2 Std.	80	12.76 (3.89)

<sup>a</sup>3/8 in. (9.5 mm) back to back of angles and channels; for double angles the shorter legs are turned out.

The built-up specimens were of special interest to see if the two elements would effectively act as a single member during extreme inelastic cyclic loading.

Typical details of specimens are shown in Fig. 1. In all cases, the test struts were welded to 1 3/4 in.-2 1/4 in. (44 mm-57 mm) thick end plates with full penetration welds. The specimens so prepared were attached to end fixtures with large high-strength bolts. The specimen length from pin to pin, or from the fixed end to the pin, included heavy end support clevises containing roller bearings and attachment flanges. Calculations showed that these end details would not significantly affect the buckling behavior of a specimen.

As finally selected, the program consisted of testing 24 specimens made of commercially available sections of sizes and shapes similar to those typically used in brace applications. The specimens were tested with different combinations of end conditions,  $K/r$  ratios, and cross-sectional shapes as previously mentioned. A complete list of the test specimens with pertinent information is given in Table 1.

#### TEST SET-UP

The experimental apparatus used to perform the strut tests is shown in Fig. 2. Depending on the desired end conditions, the right-hand end shown in Fig. 2 was either pinned [Fig. 1(a)], or rigidly attached to a foot frame or to a steel beam prestressed to a concrete reaction block [Figs. 1(b) and 2]. The other end of the strut was attached to a double-acting hydraulic jack that was pin-connected to another concrete reaction block. The jack-specimen connection was made via a headpin assembly that was restrained horizontally by a side arm and vertically by bolts in slotted holes. This arrangement allowed the primary buckling of the specimens to take place in a horizontal plane with negligibly small lateral movement of the headpin.

A load cell was inserted between the specimen and hydraulic jack to monitor the applied axial load (Fig. 2). A linearly variable displacement transducer (LVDT) was used to measure the axial displacement between the ends of a specimen, and linear potentiometers were used to determine the maximum horizontal and vertical displacements. The deflected shape of the specimens and the displacement of the head unit at selected points were recorded using photogrammetric techniques. Strain gages were placed at various locations along the specimens to monitor material yield histories (Fig. 1).

All specimens were subjected to quasistatically applied cycles of reversed axial displacements. These cycles generally resulted in compressive loads causing



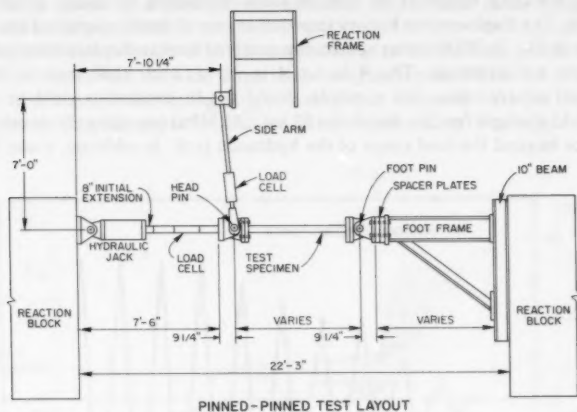


FIG. 2.—Experimental Set-Up (1 ft = 0.305 m; 1 in. = 25.4 mm)

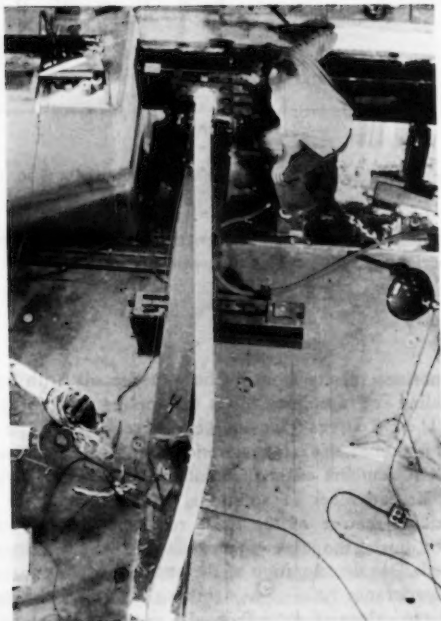


FIG. 3.—Strut 22 in Test Bay

inelastic buckling followed by tensile loads sufficient to cause yield in the specimen. The displacement history imposed on one of the fixed-pinned specimens is shown in Fig. 3. While other specimens received similar displacement patterns, they were not identical. The 4 in.  $\times$  4 in.  $\times$  1/2 in. (100 mm  $\times$  100 mm  $\times$  13 mm) square tubes, for example, could not be caused to yield in tension as the yield strength for this shape was 82 ksi (565 MPa) requiring the development of a force beyond the load range of the hydraulic jack. In addition, since loading

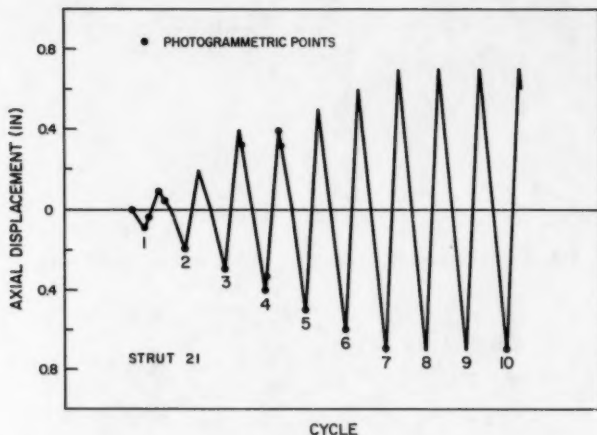


FIG. 4.—Typical Sequence of Applied Axial Displacements (1 in. = 25.4 mm)

cycles were continued until the axial strength of the specimen was exhausted, some struts experienced more cycles than others (Fig. 4).

#### EXPERIMENTAL RESULTS

The most important results from cyclic experiments with struts subjected to repeated buckling and stretching relate the applied axial force  $P$  to the axial displacement  $\delta$ . The  $P$ - $\delta$  curves trace out the hysteretic loops. The areas enclosed by such curves is a measure of hysteretic damping. Examples of hysteretic curves for several members with different cross sections are given in Figs. 5, 6, and 7. A large number of additional examples may be found in Ref. 2. The most striking feature of these results is the indication that once a strut had buckled, during the subsequent cycles the same capacity in compression cannot be reached. This deterioration of the critical buckling force  $P_{cr}$  is closely related to the slenderness ratio of a member. Typically, the hysteretic loops for struts with large values of  $K/r$  showed a more rapid deterioration in their compressive strengths than those with small values of  $K/r$  [compare Figs. 5(a) and 5(b)]. The ratio of a member's initial capacity in compression to that

in tension is similarly a function of the struts slenderness ratio, being larger for the more stocky struts.

While the  $P-\delta$  curves are of prime importance for the inelastic planar analysis of frames, one should note the large lateral displacements which are associated with a strut's axial shortening, e.g., from Figs. 6(a) and 6(b) for Strut 4 it can be seen that corresponding to an axial displacement  $\delta$  of approximately

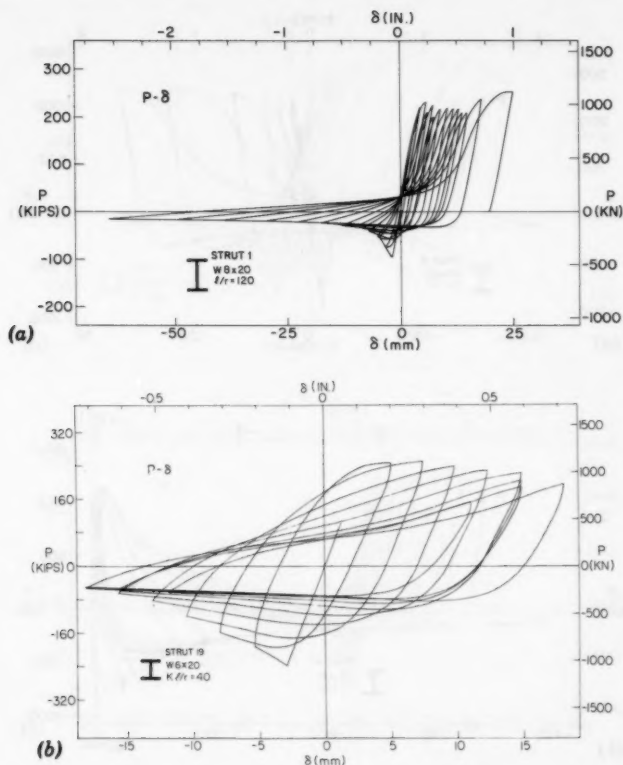


FIG. 5.—Hysteretic Diagrams of Axial Force Versus Axial Displacement for Struts 1 and 19

3/4 in. (19 mm), the midspan lateral displacement  $\Delta$  is nearly 9 in. (230 mm). Another important observation which can be made from the  $P-\Delta$  curves is the fact that an initially buckled strut even after a tensile cycle which caused yielding retains some midspan deflection. For the same example, note that at zero axial load following yielding in tension at the initiation of cycle 6 the residual deflection at midspan is approximately 1/4 in. (6 mm). Thus, this specimen begins the

next compressive cycle as already a slightly curved member which can considerably reduce its buckling capacity.

In order to explain the behavior of a strut subjected to inelastic cyclic loading, experimental data on the history dependence of the mechanical properties of a material are also required. This information is provided by the hysteretic curves for a material. A set of such curves for the W 6  $\times$  20 specimens is

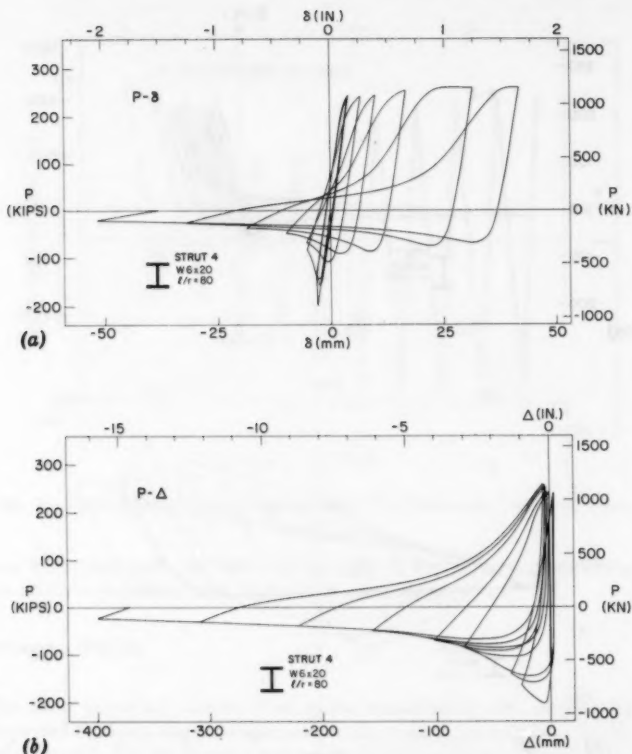


FIG. 6.—(a) Axial Force Versus Axial Displacement; and (b) Axial Force Versus Lateral Displacement for Strut 4

shown in Fig. 8. Here, it is important to note that upon load reversals the tangent modulus  $E_t$  is considerably lower than the initial elastic modulus  $E$ . While the number of cycles plays some role in this phenomenon, the major factor appears to be the amount of cumulative inelastic straining experienced by the material before the beginning of a new cycle. The amount of the cumulative strain  $\Sigma\epsilon_p$  is the absolute sum of the inelastic strain up to the beginning of

a cycle in question, e.g., for the second compressive cycle this quantity is equal to the strain from *a* to *b* plus the strain from *b* to *c*. In using this parameter, for the same level of stress the tangent moduli significantly decrease with an increase in the amount of cumulative strain, e.g., the corresponding tangent moduli in compressive cycle 6 for which  $\Sigma \epsilon_p \approx 0.054$ , are smaller than those for compressive cycle 3 where  $\Sigma \epsilon_p \approx 0.009$ . This is the result of the Bauschinger

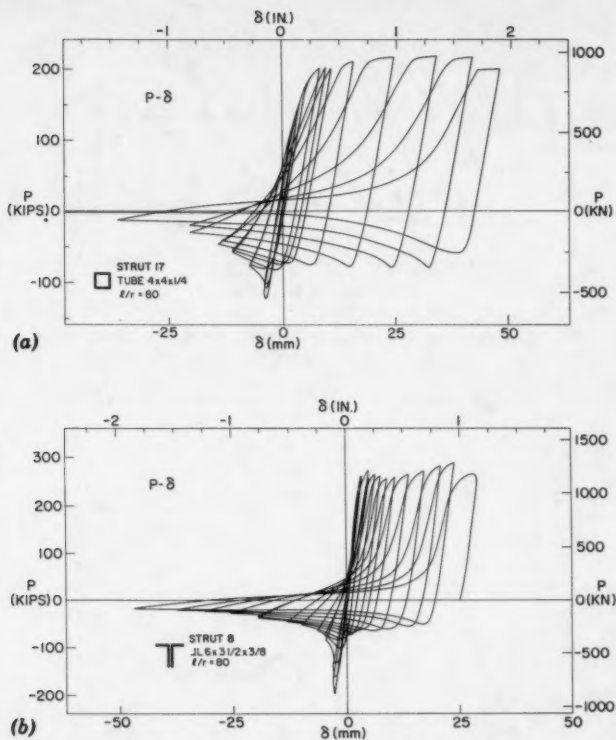


FIG. 7.—Hysteretic Diagrams of Axial Force Versus Axial Displacement for Struts 17 and 18

effect which has important implications on the cyclic buckling capacity of columns, and includes cases when a strut is initially caused to yield in tension.

The hysteretic loops shown in Fig. 8 are for a material which initially exhibited a well defined yield point. This was typical for the steels in wide flanges, double-angles, and double-channel specimens for which the yield strengths varied from 40 ksi–50 ksi (275 MPa–345 MPa). Most of the steels for tubes, however, showed no discernible yield point and this quantity was defined either by the

0.2% strain offset method, or by noting the attained yield plateau of a strut during the tensile phase of a cyclic test. On these bases, the tube yield strengths varied from a low of 24 ksi (165 MPa) for Strut 21 to a high of 82 ksi (565 MPa) for Struts 18 and 22. A typical stress-strain diagram from a coupon test

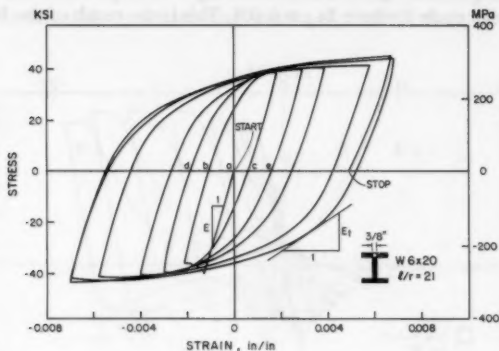


FIG. 8.—Hysteretic Stress-Strain Diagram for W 6 x 20 Material

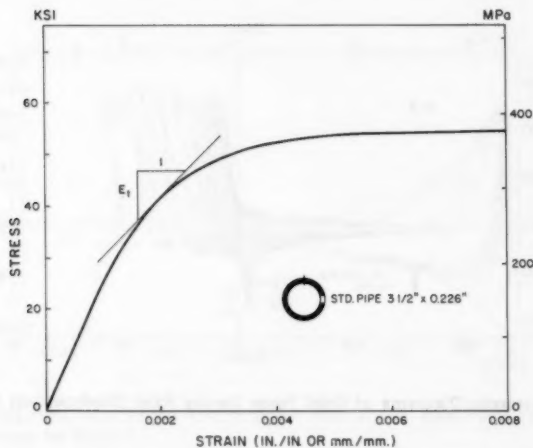


FIG. 9.—Monotonic Stress-Strain Diagram for 3 1/2 in. (89 mm) Pipe Coupon

for one of the tubes is shown in Fig. 9. As will be pointed out later, for struts made of such a material, in common with all steel struts with a previous inelastic cyclic loading history, either the tangent or the reduced modulus concepts can be successfully applied for determining buckling loads.

The experimental initial yield strengths determined on the aforementioned bases are given in Table 2 for all specimens. The experimental first buckling loads for the struts are also recorded in the table. Some representative examples

TABLE 2.—Comparison of Experimental and Predicted Initial Buckling Loads

Strut number (1)	Experimental $\sigma_y$ , in kips per square inch (2)	$P_{cr}^{exp}$ , in kips (3)	$P_{cr}^{exp} / P_{cr}^{calc}$ <sup>a</sup>		
			Based on $\sigma_y = 36$ ksi (4)	Based on experimental $\sigma_y$ (5)	Refined estimate (6)
1	40.4 <sup>b</sup>	95	0.81	0.81	0.98 <sup>e</sup>
2	42.2 <sup>c</sup>	263	1.05	0.90	1.07 <sup>f</sup>
3	40.2 <sup>c</sup>	202	1.19	1.09	—
4	40.2 <sup>c</sup>	201	1.19	1.09	—
5	40.2 <sup>c</sup>	152	0.90	0.83	0.96 <sup>g</sup>
6	44.7 <sup>c</sup>	112	1.19	1.21	—
7	50.0 <sup>d</sup>	201	1.28	0.95	—
8	40.8 <sup>c</sup>	197	1.08	0.98	—
9	43.6 <sup>c</sup>	292	1.43	1.17	—
10	41.6 <sup>d</sup>	97	0.92	0.92	1.06 <sup>h</sup>
11	35.5 <sup>d</sup>	105	0.79	0.79	1.05 <sup>i</sup>
12	39.5 <sup>c</sup>	186	0.98	0.91	—
13	41.8 <sup>b</sup>	196	1.11	0.99	—
14	47.5 <sup>d</sup>	114	1.25	1.03	—
15	47.5 <sup>d</sup>	110	1.21	0.99	—
16	24.0 <sup>d</sup>	87	0.69	0.95	—
17	59.0 <sup>d</sup>	123	1.21	0.88	0.98 <sup>g</sup>
18	82.0 <sup>c</sup>	272	1.54	1.00	—
19	40.2 <sup>c</sup>	240	1.19	1.07	—
20	40.8 <sup>c</sup>	180	0.98	0.89	—
21	24.0 <sup>d</sup>	107	0.99	1.05	—
22	82.0 <sup>c</sup>	239	1.35	0.88	—
23	35.7 <sup>d</sup>	165	1.22	1.23	—
24	46.3 <sup>d</sup>	85	1.10	0.92	1.05 <sup>g</sup>

<sup>a</sup>  $P_{cr}^{calc} = Q_s [1 - (K/r)^2 / (2C_c^2)] \sigma_y A$ .

<sup>b</sup> 0.2% offset in coupon test.

<sup>c</sup> Average yield from coupon tests.

<sup>d</sup> First yield in strut test.

<sup>e</sup> Initial max  $\Delta = 0.094$  in.

<sup>f</sup> Initial max  $\Delta = 0.16$  in.

<sup>g</sup> Tangent Modulus theory.

<sup>h</sup> Initial max  $\Delta = 0.05$  in.

<sup>i</sup> Initial max  $\Delta = 0.10$  in.

Note: 1 ksi = 6.89 MPa; 1 kip = 4.45 kN; and 1 in. 25.4 mm.

of struts at the end of tests are shown in Fig. 10. Fig. 11 shows two examples of local buckling occurring in double-angle struts. This buckling develops in the region of a plastic hinge at a stitch fastener in Strut 8, and between two

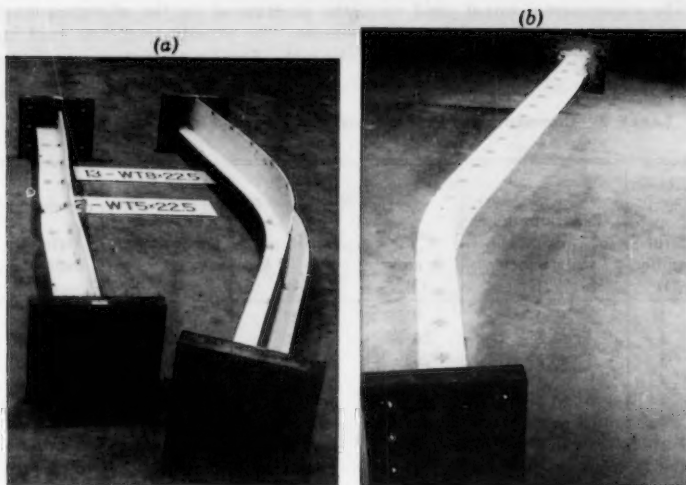


FIG. 10.—Representative Examples of Struts After Tests: Struts 12, 13, and 23

such fasteners in Strut 9. In another instance (not shown), during some severe cyclic excursions complete separation at one of the stitches of Strut 20 had occurred.

#### INITIAL AND CYCLIC BEHAVIOR OF STRUTS

**Initial Buckling Loads.**—In relating experimental results with design, a comparison of the carrying capacity of a strut to existing codes is particularly important. For the range of the slenderness ratios used in these experiments, the initial buckling capacity of a strut based on Eq. 1.5-1 of the AISC Specifications (7) without the factor of safety is appropriate. Using this approach, comparisons with the experimental results are given in Table 2. Since in practice the yield strength for the steels used in these experiments would usually be assumed to be 36 ksi (250 MPa), a comparison based on this value of the stress is included in the table. The strut buckling capacities based on the AISC formula using the experimentally determined yield strengths is also given.

In general, the experimentally determined initial buckling loads for the struts are in reasonably good agreement with the predicted ones based either on  $\sigma_y = 36$  ksi, or on the values of  $\sigma_y$  found from tests. However, improved correlations between theory and experiments can be found by recognizing the nonlinearity of the stress-strain relations for some steels, or by taking into account the initial curvature (imperfection) of a strut. The use of the tangent modulus theory is appropriate for resolving the first problem, and a well established procedure (15) for determining the capacity of eccentrically loaded elasto-plastic columns can be used to advantage for the second problem. As can be seen from the



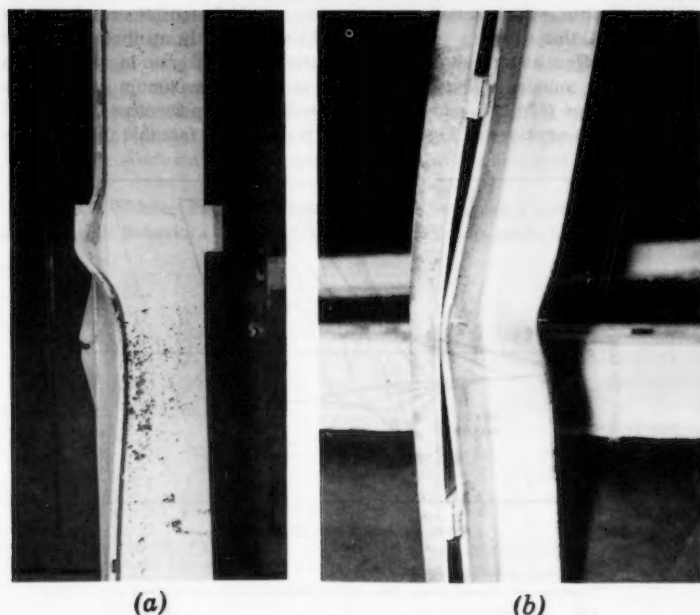


FIG. 11.—Local Buckling of Double-Angle Struts 8 and 9 in Plastic Hinge Regions

values given in the last column of Table 2, consistently better estimates of buckling loads can be found using these theoretically based refinements. The method of applying them is more fully considered in the section on Analytical Predictions of Cyclic Buckling Loads.

**Normalized Hysteretic Curves and Envelopes.**—By dividing the axial force  $P$  in a hysteretic  $P$ - $\delta$  diagram for a strut by its capacity  $P_y$  in tensile yield, and the axial displacement  $\delta$  by the displacement  $\delta_y$  at yield, one obtains a normalized hysteretic diagram. Such diagrams exhibit the experimental results in a meaningful manner by eliminating the effects of variations in material property, cross-sectional area, and specimen length. Further, because of an infinite variety of cyclic patterns that may be applied to a strut, it is convenient to make use of envelopes for a family of normalized hysteretic loops. In this analysis several comparisons of cyclic behavior among struts is made using such envelopes.

As an example, consider the envelope for the normalized hysteretic loops for two identical Struts 3 and 4 shown in Fig. 12(a). As can be seen, the shape of the envelope is essentially the same for the two struts which had different loading histories—a fact of considerable importance in studying random loadings occurring during severe earthquakes. This is true, however, only because the specimens experienced similar loading patterns. Both specimens were initially compressed, and each initially attained its maximum buckling load. By contrast,

an identical strut, which initially was caused to yield in tension, reached only about 75% of this capacity [Fig. 12(b)]. This is directly attributable to the Bauschinger effect as a result of which the stress-strain diagram in compression is significantly rounded, reducing the elastic range. The maximum compressive load of 152 kips (676 kN) with the associated axial displacement for Strut 5 falls outside the envelope of Fig. 12(a). This is due to the fact that the envelope

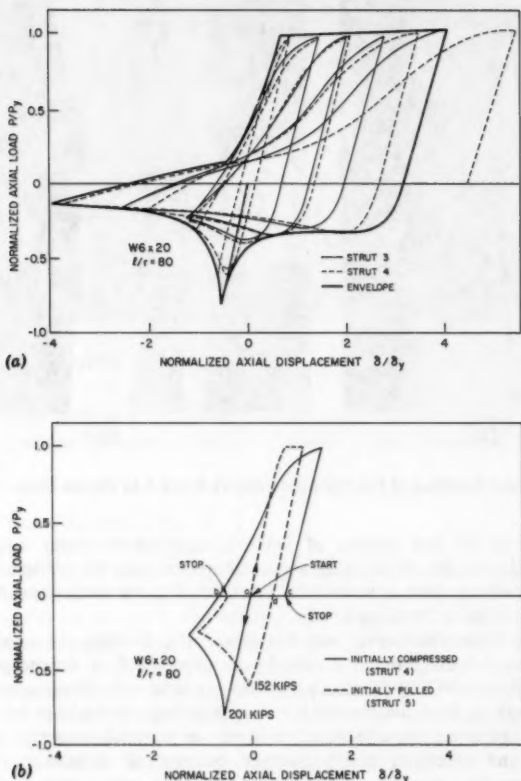


FIG. 12.—(a) Normalized Hysteretic Envelope for Struts 3 and 4; and (b) Hysteretic Curves for Two Identical Struts 4 and 5

drawn there was established from the tests which began with the application of a compressive cycle. At the beginning of a second hysteresis loop [such as at point *c* in Fig. 12(b)], the specimen's cumulative plastic strain was equal to the distances *ab* plus *bc* along the abscissa. By contrast, at point *d*, the beginning of the first compressive cycle for Specimen 5, the cumulative plastic

strain is given by the much smaller distance  $ad$ . If these differences in the history of loading are taken into account, the maximum first cycle compression load for Strut 5 can be made to lie on the envelope for Struts 3 and 4. The deterioration of the buckling capacity of a strut due to previous plastic working of the material is directly tied in with the Bauschinger effect. An approximate procedure for predicting the buckling capacity of struts subjected to random loadings is considered in the section on Analytical Prediction of Cyclic Buckling Loads.

**Effects of Slenderness Ratio, Boundary Conditions, and Cross-Sectional Shapes on Hysteretic Behavior.**—The effect of these parameters on the hysteretic behavior

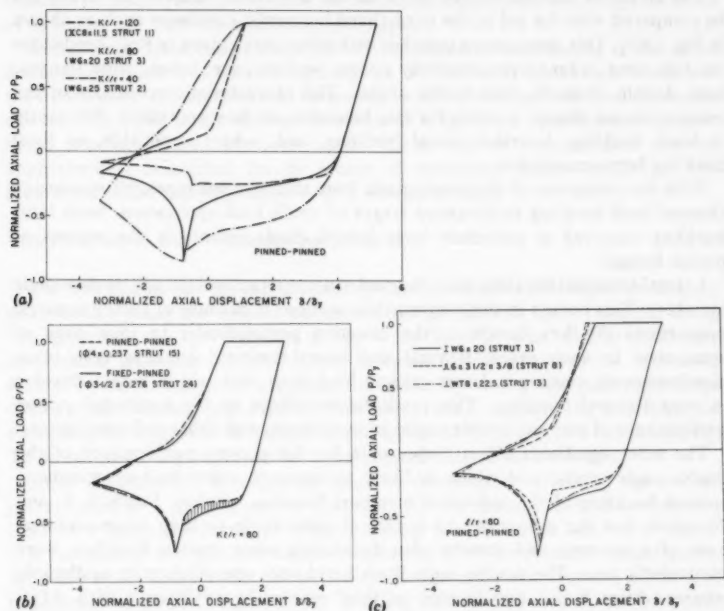


FIG. 13.—Comparisons of Normalized Hysteretic Envelopes for: (a) Struts with Different Slenderness Ratios; (b) Struts with Different Boundary Conditions; and (c) Struts with Different Cross-Sectional Shapes

of struts can be conveniently examined using the hysteretic envelopes displayed in Fig. 13. The dominant influence of the slenderness ratio on the hysteretic behavior of struts is clearly brought out in Fig. 13(a). For the slender Strut 11 the diagram is strongly biased, and the ratio between the capacity of the strut in compression to that in tension is significantly smaller than it is for the stockier struts. The initial buckling capacities of Struts 2 and 3 were nearly alike, however, upon repeated load reversals the maximum compressive loads for the more slender Strut 3 rapidly deteriorated. In the limit, for a strut with

a small value of  $K/r$  a hysteretic envelope tends to resemble a skew-symmetric shape for the material itself.

In Fig. 13(b), the normalized hysteretic envelope for a pin-ended specimen is compared with that for a specimen with fixed-pinned end conditions. Since the two envelopes essentially coincide, it appears reasonable to adhere to the effective length concept in the inelastic range of material behavior for cyclically loaded struts. Photogrammetric studies reported in Ref. 2 indicate that during inelastic buckling the curvature tends to concentrate in the regions of plastic hinges, but points of inflection do not migrate from their locations during the elastic regime.

The effect of cross-sectional shape on the hysteretic behavior of struts can be compared with the aid of the normalized hysteretic envelopes such as shown in Fig. 13(c). This comparison together with other cases given in Ref. 2 indicates the following order in progressively poorer performance: tubes, wide flanges, tees, double channels, and double angles. The characteristic properties of the cross-sectional shapes account for this behavior, as they contribute differently to local buckling, lateral-torsional buckling, and, where applicable, to local buckling between stitches.

With the exception of the struts made from thick-walled pipes, all specimens showed local buckling in advanced stages of cyclic load application. Such local buckling occurred at extremely large lateral displacements in the regions of plastic hinges.

Lateral-torsional buckling was observed in some structural tee and double-angle members. This occurs in singly symmetric sections if because of their geometric proportions (3) they buckle in the direction perpendicular to their axes of symmetry. In such cases, flexural and lateral-torsional buckling take place simultaneously causing a lower critical load than that which would develop in pure flexural buckling. This tends to contribute to the somewhat poorer performance of tees and double angles in comparison with tubes and wide flanges.

The most significant effect responsible for the poorest performance of the double-angle struts, and which is likely to apply to other built-up members, is local buckling of the individual members between stitches. Struts 8, 9, and 20 which had the propensity to buckle at right angle to their cross-sectional axes of symmetry, and thereby also developing some torsion buckling, were particularly poor. The double angle Strut 8 had only one stitch at its midlength; whereas Strut 9 had two located at third points. In conformity with AISC requirements, the slenderness ratio of the individual angles between the fillers did not exceed the governing slenderness ratio of the built-up member. During the initial application of the compressive load, both of these struts behaved well and their buckling capacities at first buckling load were good (see Table 2). However, as severe cyclic load excursions were applied, the angles tended to buckle locally in the region of plastic hinges. An example of this behavior in advanced stages of loading for Strut 8 is shown in Fig. 11(a), and for Strut 9 in Fig. 11(b). From these figures, it is apparent that as cyclic load applications proceeded, the flexural straining was concentrated in the middle of a specimen, and the webs tended to approach each other. This behavior was particularly pronounced in Strut 9. Cyclic plastic working of a strut in a hinge region softens the material due to the Bauschinger effect contributing further to its deterioration.

A complete failure of a stitch occurred in Strut 20. The spacers for this

strut were located at third points along the length and were 2 1/2 in. (64 mm) wide attached with four 5/16 in. (8 mm) fillet welds 2 1/2 in. (64 mm) long.

#### ANALYTICAL PREDICTIONS OF CYCLIC BUCKLING LOADS

In the analysis of diagonally braced frames for seismic excitations, the inelastic buckling behavior of struts must be mathematically modeled. A number of proposals for accomplishing this have been made (1,5,6,9,14), and the subject continues to be an active field of current research. Here, the experimental evidence on the behavior of struts subjected to inelastic cyclic buckling is examined and analytical procedures for predicting approximate buckling capacities of struts for the first few cycles are developed.

As has been noted earlier, there are two main causes contributing to the often dramatic decrease in a column capacity for inelastic cyclic loadings. These are the Bauschinger effect, exhibited by the steel subjected to inelastic load reversals, and the effect due to the residual curvature of a specimen resulting from plastic hinge rotations during previous cycles. Each one of these effects can be approximately accounted for by means of reduction factors applied to the theoretical initial carrying capacity of a straight column.

#### REDUCTION FACTOR DUE TO BAUSCHINGER EFFECT

It is well known that the initial buckling load of a strut can be rather accurately estimated by using the tangent modulus in the generalized Euler formula. Using this approach, the curve shown in Fig. 9 for Strut 24 was used to determine its buckling load (see the last column in Table 2) with good results. The same kind of stress-strain curves are clearly exhibited by steel in the post-yield range during cyclic loading (see Fig. 8). This observation suggests the possibility of extending the tangent or the reduced (double) modulus approach to cyclic loading. To do so, however, requires that some approximations be introduced.

Since the behavior at a plastic hinge is dominant in affecting the overall performance of a strut, it can be assumed (16) that the strains at the centroidal fiber of a hinge are decisive on the buckling behavior of a strut as a whole. It is recognized that this is a drastic simplification of the problem. Significantly different strain histories do occur elsewhere. Nevertheless, because of the key importance of plastic hinges on the buckling behavior of a strut, the proposed simplifying assumption seems reasonable. Next, each curve in a stress-strain diagram of a cyclic coupon test can be considered to represent a monotonic test on a material with a previous inelastic history. This history dependence can be conveniently approximated and defined by the absolute cumulative plastic strain at the beginning of a loading cycle, e.g., consider the tensile loading curve for cycle 2 from a coupon test for the W 6  $\times$  20 section shown in Fig. 8 reproduced in Fig. 14. At the beginning of this loading cycle, the absolute cumulative plastic strain  $\Sigma \epsilon_p$  at zero stress is 0.0055 in./in. (meter/meter). This is the sum of strains along the abscissa in Fig. 8 from *a* to *b* to *c* and then to *d*. Similar curves can be isolated and identified with different amounts of cumulative plastic strain for the other loading branches of the coupon test.

After establishing a stress-strain curve identified with a particular absolute cumulative plastic strain, as has been done in Fig. 14, the tangent moduli related

to the corresponding stresses can be determined. With this information, one can make use of the generalized Euler formula to calculate the buckling slenderness ratios  $Kl/r$ . The Euler formula in the appropriate form for this purpose reads

$$Kl/r = \sqrt{\pi^2 E_t / \sigma_{cr}} \quad (1)$$

in which  $E_t$  and  $\sigma_{cr}$  = the matching values of these quantities found from a stress-strain diagram such as Fig. 14. The calculated slenderness ratios  $Kl/r$  can then be plotted versus the critical buckling stress  $\sigma_{cr}$ . One of the resulting curves obtained in this manner corresponding to the data given in Fig. 14 for  $\Sigma \epsilon_p = 0.0055$  is shown in Fig. 15.

The family of curves in Fig. 15 identified with different amounts of cumulative plastic strain has been generated in the aforementioned manner. However, in this diagram, the curve corresponding to  $\Sigma \epsilon_p = 0$  was found using the AISI

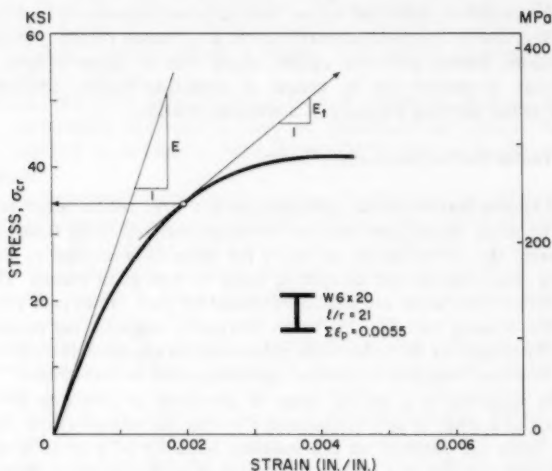


FIG. 14.—Tensile Loading Branch for Cycle 2 of Coupon Test of Fig. 8

column formulas with no factor of safety. The corresponding theoretical curve based on the simplifying assumption of ideal elastic-plastic behavior is known to be inaccurate in the relevant range (13), and the two available experimental points were considered to be insufficient to define the required curve. With this data, for a selected slenderness ratio of a strut, its capacity for a given cumulative plastic strain  $\Sigma \epsilon_p \neq 0$  divided by the capacity at  $\Sigma \epsilon_p = 0$  gives the reduction factor  $R_p$  accounting for the Bauschinger effect.

Since the struts in this series of experiments tended to develop a residual camber because of a residual curvature at the plastic hinges, it appears more appropriate to apply the reduced modulus theory rather than the aforementioned tangent modulus theory for determining the cyclic buckling loads. The rationale for this contention rests in the belief that in a slightly curved member the

unloading process of the fibers on the convex side of a strut is likely to occur earlier than it does in an initially straight member.

By limiting the application of the reduced modulus approach to the wide flange sections used in these experiments, the procedure is very direct. Since all of these members buckled around their  $X$ -axes, on neglecting the contribution of the web, the reduced modulus  $E_r$  can be taken as one for a rectangular section given by (13)

$$E_r = \frac{4 E E_t}{(\sqrt{E} + \sqrt{E_t})^2} \dots \dots \dots (2)$$

Where on exchanging  $E_t$  by  $E_r$  in Eq. 1, the procedure for establishing the column buckling curves as has been done in Fig. 15 can be repeated, and the reduction factors based on the reduced modulus approach can be determined.

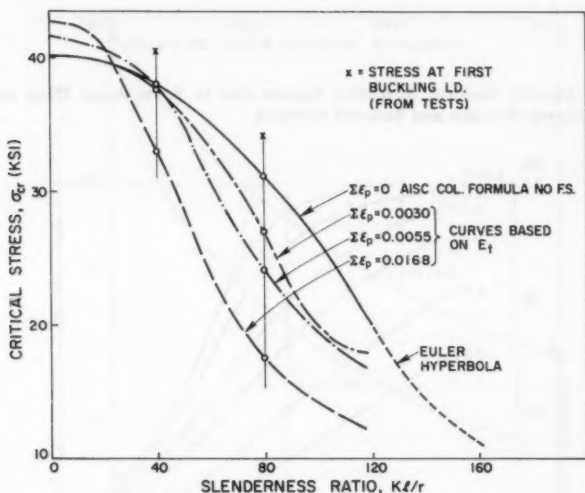


FIG. 15.—Column Buckling Curves Based on Tangent Modulus: W 6 × 20 Material

Curves giving the reduction factors arrived at on the aforementioned two bases to account for the Bauschinger effect as a function of the cumulative plastic strain are shown in Fig. 16. As to be expected, the tangent modulus approach indicates a larger reduction in the capacity of a strut than that predicted by the reduced modulus theory.

**Reduction Factor Due to Specimen Curvature.**—The second major cause for the decrease in column capacity during cyclic loading is that after an initial inelastic buckling cycle a specimen develops a residual curvature which generally is not removed by the subsequent tensile yielding. Therefore, an inelastically cycled member must be treated in the analysis as having an initial curvature or a camber. This effect can be approximated by classical solutions available

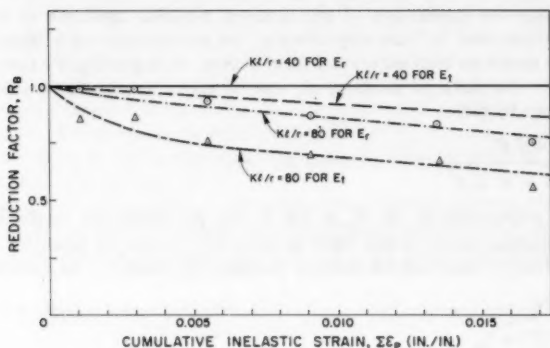


FIG. 16.—Column Buckling Reduction Factors Due to Bauschinger Effect on Two Bases: Tangent Modulus and Reduced Modulus

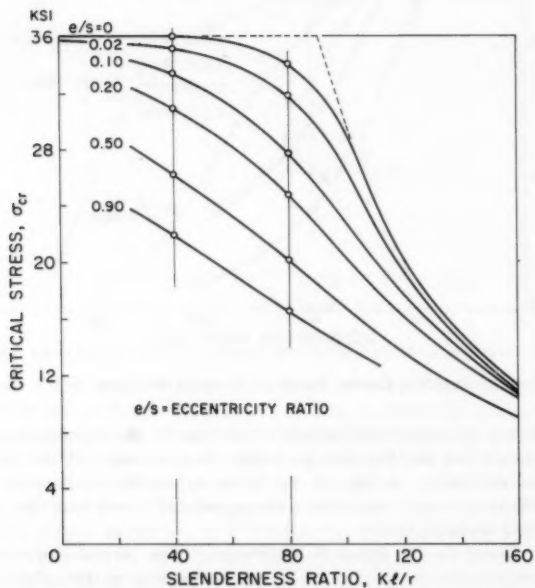


FIG. 17.—Column Buckling Curves for Eccentric Loadings (15)



in the literature (13,15) for eccentrically loaded elasto-plastic columns. Here, the solutions obtained by Westergaard and Osgod based on von Karman's concept for inelastic buckling of eccentrically loaded columns are utilized. Some of the column buckling curves obtained by them for eccentrically loaded struts (15) are reproduced in Fig. 17. In this figure,  $e$  denotes an eccentricity of the coaxial forces with respect to a column's centroidal axis, and  $s$  is the ratio of a cross-section's section modulus to its cross-sectional area (core radius). The ratio of  $e$  to  $s$  defines the eccentricity ratio.

As an approximation to the problem being considered here, the experimentally determined maximum effective lateral deflection  $\Delta$  of a strut at the beginning

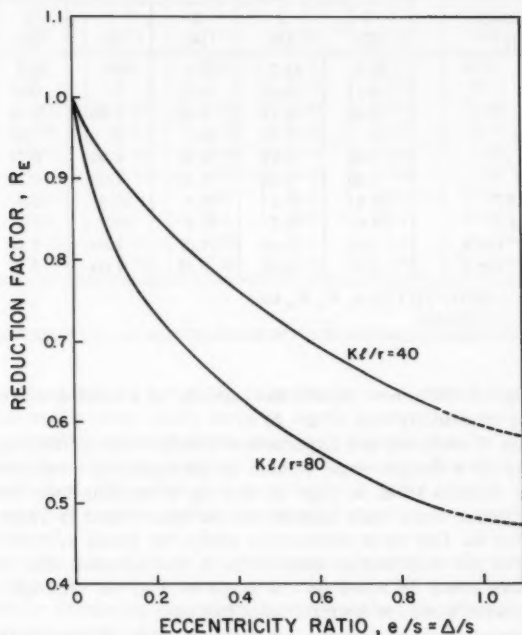


FIG. 18.—Column Buckling Reduction Factor Due to Eccentricity Effect

of a compression cycle can be taken as  $e$ . Adopting this approximation, the curves of Fig. 17 provide the necessary information for obtaining graphs for the reduction factor  $R_E$  as a function of the eccentricity ratio  $e/s \cong \Delta/s$ . Such graphs can be constructed in the following manner. For a selected slenderness ratio such as 80, the critical values of the stresses on the  $e/s$  curves in Fig. 17 are normalized using the capacity of a straight column ( $e/s = 0$ ). A continuous curve connecting these points gives an  $R_E$  plot for the selected column slenderness ratio as a function of the eccentricity ratio. Two graphs of this kind are

TABLE 3.—Experimental and Predicted Stresses

Variable (1)	Strut Number					
	2			3		
	SHAPE					
	W 6 × 25			W 6 × 20		
	$K/r$					
	40			80		
	Cycle Number					
	1 (2)	2 (3)	3 (4)	1 (5)	2 (6)	3 (7)
$\sigma_{cr}^{exp}$ ksi	36.0	32.7	31.5	34.1	16.3	13.8
$\Delta/s$	0.21	0.10	0.21	0	0.67	1.11
$R_E$	0.85	0.91	0.85	1.00	0.54	0.48
$\Sigma \epsilon_p \times 10^{-3}$	0	8.70	16.7	0	7.67	14.8
$R_B$ for $E_r$	1.00	0.92	0.87	1.00	0.71	0.65
$R_B$ for $E_r^a$	1.00	1.00	1.00	1.00	0.88	0.80
$\sigma_{cr}^{calc}$ for $E_r^a$	33.8	33.3	29.4	31.2	12.0	9.73
$\sigma_{cr}^{calc}$ for $E_r^a$	33.8	36.2	33.8	31.2	14.8	12.0
$\sigma_{cr}^{exp}/\sigma_{cr}^{calc}$ for $E_r$	1.07	0.98	1.07	1.09	1.36	1.42
$\sigma_{cr}^{exp}/\sigma_{cr}^{calc}$ for $E_r^a$	1.07	0.90	0.93	1.09	1.10	1.15

<sup>a</sup> $\sigma_{cr}^{calc} = [1 - (K/r)^2 / (2 C_c)] \sigma_y R_E R_B$  ksi.

Note: 1 ksi = 6.89 MPa.

shown in Fig. 18. Note how rapidly the capacity of a column decreases with an increasing eccentricity ratio  $e/s \approx \Delta/s$ .

**Comparison of Analytical and Experimental Results.**—By multiplying an initial buckling load for a straight virgin column by the appropriate reduction factors  $R_B$  and  $R_E$ , such as given in Figs. 16 and 18, a buckling load for the new condition is found. Some such calculations are summarized in Table 3, where the results for the first three consecutive cycles for Struts 2, 3, 4, 5, and 19 are given. For the purposes of illustration, it was assumed that for Strut 2 the  $R_B$  factors could be based on the graph of Fig. 16, although no cyclic coupon tests were made for the material of this strut.

The calculated buckling stresses for the first cycle of the struts listed in Table 3 were determined using an AISC formula (7) without the corresponding factor of safety and using experimentally determined yield strengths. However, since Strut 2 had an initial bow in excess of that permitted by the specifications, a reduction factor  $R_E$  was applied. Further, since Strut 5 was initially subjected to a tensile force causing the member to yield, a reduction factor  $R_B$  was employed. In these two cases as well as in all others, the experimental data were used to find  $\Delta$  and  $\Sigma \epsilon_p$ . By applying in a similar manner the required reduction factors to the second and third cycles, the corresponding estimates of the buckling stresses were found. As can be seen from the table, with the use of these factors the estimated buckling loads are in reasonably good agreement with the experimental results.

## at First Three Consecutive Buckling Cycles

4			5			19	
W 6 × 20			W 6 × 20			W 6 × 20	
80			80			40	
1 (8)	2 (9)	3 (10)	1 (11)	2 (12)	3 (13)	1 (14)	2 (15)
34.1	26.8	24.6	25.8	12.7	13.5	40.8	33.3
0	0	0	0	1.33	0.80	0	0.20
1.00	1.00	1.00	1.00	0.46	0.51	1.00	0.86
0	6.46	14.8	1.10	4.48	11.0	0	10.9
1.00	0.74	0.65	0.86	0.78	0.68	1.00	0.91
1.00	0.91	0.80	0.97	0.92	0.84	1.00	1.00
31.2	23.1	20.3	26.8	11.2	10.8	37.9	29.7
31.2	28.4	25.0	30.3	13.2	13.4	37.9	32.6
1.09	1.16	1.21	0.96	1.13	1.25	1.07	1.12
1.09	0.94	0.98	0.85	0.96	1.01	1.07	1.02

It would appear that the use of the reduction factor  $R_b$  based on the reduced modulus concept in most cases leads to better results than those based on the tangent modulus approach. However, it is noteworthy that for Strut 5 better results for the first buckling load are obtained by using  $R_b$  based on the tangent modulus procedure. This result can be anticipated, since Strut 5 initially was caused to yield in tension, and it was straight prior to the application of a compressive load.

Considering the complexity of the problem, the predictions for buckling loads using the aforementioned approach may be said to be satisfactory and may prove useful in developing algorithms for determining the deterioration of the cyclic buckling capacity of struts.

#### CONCLUSIONS AND RECOMMENDATIONS

Based on this investigation of inelastic cyclic buckling of struts of practical sizes of various cross-sectional shapes, several conclusions may be reached which have important design implications.

1. The conventional definition of an effective slenderness ratio  $K/r$  deduced on an elastic basis carries over into the inelastic range. The points of inflection on a deflected curve remain relatively fixed.
2. The effective slenderness ratio of a member appears to be the single most

important parameter in determining the hysteretic behavior. The stockier members generate fuller loops than the more slender ones. The use of normalized hysteretic curves in comparisons is particularly advantageous because a number of variables are removed from consideration by this process.

3. Hysteretic envelopes provide a convenient means for comparing specimens with different loading histories. They can be very useful in considering random loading effects on a brace during a severe earthquake. The use of normalized hysteretic envelopes is convenient for general formulations and studies.

4. The hysteretic performance of a member is somewhat influenced by its cross-sectional shape. The major determining factor appear to be related to a member's susceptibility toward lateral-torsional buckling, local buckling of outstanding legs, and web buckling between stitches in built-up members.

5. Stitching of built-up critical compression members for service under severe load reversals as currently specified in standard codes (7) is unconservative. In the regions of plastic hinges, the individual parts of a member, due to softening of the material, have a greater tendency to buckle than envisioned by the codes. Requiring the slenderness ratio  $\ell/r$  for the individual parts of members between stitches to be less than that of the member as a whole and specifying minimum fastener strengths would help in the problem. Just this kind of a provision was contained in the 1959 AISC Specifications (12) and can also be found in the current German ones (4). However, it would appear that for important applications in seismic design, where severe cyclic loading of a compression member can be anticipated, in the regions of potential plastic hinges built-up members should be either avoided or very thoroughly stitched together.

6. Significant reduction in buckling loads occurs during inelastic cyclic loadings. The hysteretic loops displayed in this paper can serve as an aid for developing and verifying computer models of strut behavior. The use of the reduction factors mentioned in the text may prove useful in such formulations. One of these reduction factors accounts for the material property changes associated with the Bauschinger effect that occurs in the plastic hinge regions of a member. The second factor accounts for the residual curvature that remains in a member following previous inelastic compressive cycles.

7. Designers should be aware of the variability in the mechanical properties of commercially available steel used in building construction. The yield strengths for rolled sections used in these experiments made of A36 steel varied over a relatively narrow range from about 36 ksi (250 MPa) to 50 ksi (340 MPa). Whereas for pipes and tubes made of A53 Grade B steel and A501 steel, respectively, the *nominal* yield strengths varied from 24 ksi (165 MPa)–82 ksi (565 MPa).

#### ACKNOWLEDGMENT

The writers gratefully acknowledge the National Science Foundation (NSF) support under Grants ENV 7604263 and PFR 7908984 with some support from AISI which made this work possible. Any opinions, findings, and conclusions or recommendations expressed in this paper are those of the writers and do not necessarily reflect the views of the sponsors. A number of graduate students and members of the laboratory staff participated in the project. Among these

the following were particularly helpful: W. Wenger, P. Shing, W. Yau, V. Zayas, B. Fong, P. Chin, K. Hjelmstad, and B. Lotz.

#### APPENDIX.—REFERENCES

1. Ashok, K. J., Goel, S. C., Hanson, R. D., "Hysteresis Behavior of Bracing Members and Seismic Response of Braced Frames with Different Proportions," *University of Michigan Research Report, UMEE '78*, University of Michigan, Ann Arbor, Mich., 1978.
2. Black, R. G., Wenger, W. A., and Popov, E. P., "Inelastic Buckling of Steel Struts Under Cyclic Load Reversals," *Report No. UCB/EERC-80/00*, Earthquake Engineering Research Center, University of California, Berkeley, Calif., Sept., 1980.
3. Chajes, A., and Winter G., "Torsional-Flexural Buckling of Thin-Walled Members," *Journal of the Structural Division, ASCE*, Vol. 91, No. ST4, Proc. Paper 4442, Aug., 1965, p. 103.
4. Stabilitätsfalle, *Stahlbau-Handbuch, DIN 4114* (German Industrial Standards), Industrie und Handelsverlag, Water Dorn GMBH, 1952, pp. 572-657.
5. Kahn, L. F. and Hanson, R. D., "Inelastic Cycles of Axially Loaded Steel Members," *Journal of the Structural Division, ASCE*, Vol. 102, No. ST5, Proc. Paper 12111, May, 1976, pp. 947-959.
6. Maison, B. F. and Popov, E. P., "Cyclic Response Prediction for Braced Steel Frames," *Journal of the Structural Division, ASCE*, Vol. 106, No. ST7, Proc. Paper 15534, July, 1980, pp. 1401-1416.
7. *Manual of Steel Construction*, 8th ed., American Institute of Steel Construction, Chicago, Ill., 1980.
8. Popov, E. P., "Inelastic Behavior of Steel Braces Under Cyclic Loading," *Proceedings, Second U.S. National Conference on Earthquake Engineering Research Institute*, Stanford University, Stanford, Calif., Aug., 22-24, 1979, pp. 923-932.
9. Popov, E. P., Takanashi, K., and Roeder, C. W., "Structural Steel Bracing Systems: Behavior Under Cyclic Loading," *Earthquake Engineering Research Center*, Report No. EERC 76-17, University of California, Berkeley, Calif., June, 1976.
10. Roeder, C. W. and Popov, E. P., "Eccentrically Braced Steel Frames for Earthquakes," *Journal of the Structural Division, ASCE*, Vol. 104, No. ST3, Proc. Paper 13619, Mar., 1978, pp. 391-412.
11. Sozen, M. A. and Roesset, J., "Structural Damage Caused by the 1976 Guatemala Earthquake," *Structural Research Series No. 426*, University of Illinois, Urbana/Champaign, Ill., Mar., 1976.
12. *Steel Construction Manual*, 5th ed., American Institute of Steel Construction, New York, N.Y., 1959, p. 293.
13. Timoshenko, S. P. and Gere, J. M., *Theory of Elastic Stability*, 2nd ed., McGraw-Hill Book Co., Inc., New York, N.Y., 1961, p. 200.
14. Wakabayashi, M., Nonaka, T., Nakamura, T., Morino, S., and Yoshida, N., "Experimental Studies on the Behavior of Steel Bars Under Repeated Axial Loading," *Disaster Prevention Research Institute Annals*, Kyoto University, Kyoto, Japan, No. 16B, 1973, pp. 113-125.
15. Westergaard, H. M. and Osgood, W. R., "Strength of Steel Columns," *Transactions, American Society of Mechanical Engineers*, APM-50-9, 1927-28.
16. Zayas, V. A., Popov, E. P., and Mahin, S. A., "Cyclic Inelastic Buckling of Tubular Steel Braces," *Report No. UCB/EERC-80/16*, Earthquake Engineering Research Center, University of California, Berkeley, Calif., June, 1980.



## DISCUSSION

Note.—This paper is part of the Journal of the Structural Division, Proceedings of the American Society of Civil Engineers, ©ASCE, Vol. 107, No. ST9, September, 1981. ISSN 0044-8001/81/0009-1885/\$01.00.

## DISCUSSIONS

Discussions may be submitted on any Proceedings paper or technical note published in any *Journal* or on any paper presented at any Specialty Conference or other meeting, the *Proceedings* of which have been published by ASCE. Discussion of a paper/technical note is open to anyone who has significant comments or questions regarding the content of the paper/technical note. Discussions are accepted for a period of 4 months following the date of publication of a paper/technical note and they should be sent to the Manager of Technical and Professional Publications, ASCE, 345 East 47th Street, New York, N.Y. 10017. The discussion period may be extended by a written request from a discussor.

The original and three copies of the Discussion should be submitted on 8-1/2-in. (220-mm) by 11-in. (280-mm) white bond paper, typed double-spaced with wide margins. The length of a Discussion is restricted to two *Journal* pages (about four typewritten double-spaced pages of manuscript including figures and tables); the editors will delete matter extraneous to the subject under discussion. If a Discussion is over two pages long it will be returned for shortening. All Discussions will be reviewed by the editors and the Division's or Council's Publications Committees. In some cases, Discussions will be returned to discussors for rewriting, or they may be encouraged to submit a paper or technical note rather than a Discussion.

Standards for Discussions are the same as those for Proceedings Papers. A Discussion is subject to rejection if it contains matter readily found elsewhere, advocates special interests, is carelessly prepared, controverts established fact, is purely speculative, introduces personalities, or is foreign to the purposes of the Society. All Discussions should be written in the third person, and the discussor should use the term "the writer" when referring to himself. The author of the original paper/technical note is referred to as "the author."

Discussions have a specific format. The title of the original paper/technical note appears at the top of the first page with a superscript that corresponds to a footnote indicating the month, year, author(s), and number of the original paper/technical note. The discussor's full name should be indicated below the title (see Discussions herein as an example) together with his ASCE membership grade (if applicable).

The discussor's title, company affiliation, and business address should appear on the first page of the manuscript, along with the *Proceedings* paper number of the original paper/technical note, the date and name of the *Journal* in which it appeared, and the original author's name.

Note that the discussor's identification footnote should follow consecutively from the original paper/technical note. If the paper/technical note under discussion contained footnote numbers 1 and 2, the first Discussion would begin with footnote 3, and subsequent Discussions would continue in sequence.

Figures supplied by the discussor should be designated by letters, starting with A. This also applies separately to tables and references. In referring to a figure, table, or reference that appeared in the original paper/technical note use the same number used in the original.

It is suggested that potential discussors request a copy of the *ASCE Authors' Guide to the Publications of ASCE* for more detailed information on preparation and submission of manuscripts.



## STABILITY OF FLEXIBLY CONNECTED PLATE SYSTEMS<sup>a</sup>

### Errata

The following corrections should be made to the original paper:

- Page 2077, paper title: Should read "Flexibly" instead of "Flexibility"  
Page 2077, paragraph 1, line 4: Should read "factor is a function" instead of "factor = a function"  
Page 2077, paragraph 2, line 6: Should read "welding and/or when" instead of "welding when"  
Page 2077, paragraph 3, line 3: Should read "rigid" instead of "ridid"  
Page 2078, paragraph 1, line 2: Should read "general" instead of "generally"  
Page 2084, paragraph 2, line 1: Should read " $k_7$  .... For  $m$  even only  $k_2$ " instead of " $k_7$  ..., for  $m$  when only  $k_2$ "  
Page 2085, paragraph 3, line 5: Should read "When" instead of "when"  
Page 2085, paragraph 4, line 1: Should read "local" instead of "total"  
Page 2087, Table 1 Note: Should read " $k$  are for a continuous (100%) 6.3 mm" instead of " $k$  are continuous (100%) for a 6.3 mm"  
Page 2096, line 12: Should read " $\alpha_n, \beta_n$ " instead of " $\alpha_n = \beta_n$ "  
Page 2096, line 13: Should read " $\alpha_n b_n, \beta_n b_n$ " instead of " $\alpha_n b_n = \beta_n b_n$ "

---

## RESEARCH NEEDS IN STABILITY OF METAL STRUCTURES<sup>b</sup>

Discussion by Charles E. Massonnet<sup>2</sup> and René J. Maquoi<sup>3</sup>

The writers wish to congratulate Bjorhovde for the excellent state-of-the-art report on the research needed in the field of stability of metal structures. As the paper reflects, mainly, the viewpoint of the Structural Stability Research Council (SSRC), the writers believe that their respective positions in Technical Committee TC8 of the European Convention for Constructional Steelwork (ECCS)

<sup>a</sup>October, 1980, by Milija Pavlović, Donald S. Mansell, and Leonard K. Stevens (Proc. Paper 15766).

<sup>b</sup>December, 1980, by Reidar Bjorhovde (Proc. Paper 15926).

<sup>2</sup>Prof., Univ. of Liège, Liège, Belgium.

<sup>3</sup>Asst. Prof., Univ. of Liège, Liège, Belgium.

and the fact that the senior writer has for many years, been a corresponding member of the SSRC, allow them to comment, somewhat, and eventually to complete the valuable information brought by their overseas colleague. This is done as representatives of TC8.

**Centrally Loaded Columns.**—Indeed, the scientific study of the occurrence of residual stresses during the manufacturing process is needed in order to better know the connection between the structural properties and imperfections and the fabrication conditions. In this field, research on the effects of rotorizing on buckling is under way in Liège.

Simple methods of residual stress prediction should be welcome, more especially, for welded built-up sections. A step forward has been made recently in this field (42). The asymmetric shape of the cross section is not clearly known and a limited number of tests on asymmetric  $H$  shapes will be performed in Liège in the near future.

The problem of an out-of-straightness larger than  $L/1,000$  is encountered. Assuming that the residual stresses are the same as in regular shapes, a simple method has been suggested (43) to evaluate the ultimate load of such columns.

TC8 is of the opinion that, as the new European buckling curves are more favorable than the older regulations, and as the SSRC curves evolve in the same way, one must be cautious when defining the effective length, which, despite its criticism, remains a useful design tool. More importantly, the effective length of compressed chords of trusses for buckling in the plane of the truss, should be raised from  $0.8 l$  to  $0.9 l$ , as clearly shown by numerical simulation, taking into account elastoplastic behavior and large displacements. This has already been done in some national standards (SIA 161: Swiss Standard on Steel Construction, 1979, and NBN B51-001: Belgian Standard on Steel Construction, 1977).

The author is right in believing that the effect of imperfections on the buckling of a column belonging to a reticulated structure—the column being connected to other beams and columns at its joints—could be somewhat reduced compared to the behavior of a centrally loaded column. The writers also believe that many structural columns should be designed as beam-columns, and that valuable simplifications could be achieved by the definition of fewer column curves in these cases. Unfortunately, such thinking is not yet sufficiently supported by tests to be completely and accurately reflected in design rules.

**Biaxially Loaded Columns.**—Design rules for biaxially loaded columns that are extrapolations of rules for uniaxially loaded columns have been tested recently (44). It appears from the results that both the Belgo-American and ECCS interaction formulas behave satisfactorily. The Belgo-American approach formula is approximately 3% more conservative than the ECCS formula; the Chen-Atsuta approach is generally on the safe side, but with a greater proportion of unsafe results than the aforementioned formula. It is shown, in addition, that most current equivalent moment formulas lead to a very marginal difference, with a slight advantage to the AISC/ECCS formula.

The simulation tool first available for buckling of centrally loaded columns is no longer valid for biaxially loaded columns, due to torsional effects. Therefore, a new type of finite element is needed to achieve this goal. Such a work is in progress in Liège.

**Tubular Columns.**—Although interesting progress has been made in this field,

this topic will not be reviewed here because a separate discussion devoted to it is presented by J. Rondal.

**Laterally Unsupported Beams.**—Indeed, many tests are available on the lateral buckling of beams, and it has been clearly shown (45) that the behaviors of hot-rolled sections and welded built-up sections are significantly different. It is obvious that residual stresses, initial out-of-straightness, and cross-sectional distortions have a substantial influence on the ultimate strength by lateral buckling. However, in the writers' opinion, lateral buckling depends more on the more or less precise manner in which the actual conditions of support and load transmission are taken into account. Therefore, the writers feel that it is more useful to analyze lateral buckling with realistic conditions than to refine certain effects while the support conditions remain rather too ideal.

The author states that the danger of lateral buckling is greater during erection of the structure, when it is not yet braced, than in service conditions, which benefit from stabilizing secondary elements. There is, in addition, a range of problems that requires attention regarding the level of applied loads—problems dealing with handling operations during which the girders are often suspended at attachments located on the compressed members.

**Stability of Frames.**—The writers wish to emphasize the fact that, in spite of valuable information drawn from past research, the designer needs a tool that will eliminate the need for sophisticated calculations, taking into account second order effects, if the expected increase of accuracy is not worthwhile. In other words, it is imperative to distinguish between braced and unbraced frames, with respect to the requirement of a second order theory, and to provide simplified second order methods of design. In Europe, the trend is to simplify on the basis of two classes of values for the sway angle  $\psi$  at each floor and two classes of values of coefficient  $\epsilon = \pi \sqrt{N/N_{cr}}$ , resulting in four approaches of increasing complexity, from the first order theory with no  $P-\Delta$  and no  $\epsilon$  effects to the full second-order theory with full account of both  $P-\Delta$  and  $\epsilon$  effects. Such a proposal, already partially introduced in German specifications (50), should be published in the first edition of Eurocode 3.

A practical method of second order design for sway frames has been suggested by Vandepitte. It results from a modification of the horizontal equilibrium equations used in the regular slope deflection method. Such a procedure leads to a noniterative system of linear equations and can be generalized for the occurrence of plastic hinges.

**Plate and Box Girders.**—Plate and box girders are two fields in which significant progress has been made during the past decade. In determining the ultimate strength of transversally stiffened plate girders, mathematical models are now available which provide accuracy. Unfortunately, when the web is stiffened, the design of longitudinal stiffeners is not sufficiently solved to allow the use of these ultimate models for designing longitudinally stiffened webs. The writers feel that stiffeners designed according to the linear theory of buckling (by multiplying their relative rigidity  $\gamma$  by a factor of the order of 4 to insure that they remain rigid up to collapse) provide a check for the buckling of web plate subpanels and that, in this case, the postcritical strength reserve can be appraised on the basis of a theoretical and numerical investigation performed at Imperial College (46).

Technical Working Group TC 8/3 (Plate buckling) of ECCS is preparing a

book about the behavior and design of steel plated structures, which is a compilation of knowledge in the area of stability problems dealing with plated construction. Three other books in initial stages of development deal respectively with:

1. Stability behavior of components.
2. Stability behavior of systems.
3. Stability of shells.

Regarding fabrication tolerances and their effect on ultimate strength, a S.o.A. report prepared by the senior writer for an IABSE ad hoc Committee is worth mentioning (Tolerances in Steel Plated Structures. IABSE Surveys, S-14/80.)

**Composite Columns.**—A model code has been prepared by an international joint Committee (IABSE-FIP-CEB-ECCS) (47). It deals with the design and construction of composite structures and structural parts, and was designed for use as a common basis or reference for national and international codes or specifications. The design method for composite columns presented in this model code is based on an ultimate load design philosophy. It is very broad in scope and covers encased columns and concrete filled circular and rectangular steel tubes, which are loaded with any combination of end loads and moments.

The code's basic assumptions are that there is full interaction between concrete and steel up to the point of collapse, that proper account must be taken of the steel and concrete stress-strain curves as given in the ECCS and CEB Recommendations dealing with steel and concrete respectively, and that allowance must be made for imperfections which are consistent with those adopted for assessing the strength of axially loaded base steel columns. On the basis of this last assumption a new concept of column slenderness is introduced which leads to the same expression as that used in the European buckling curves and enables these curves to be used as the basic design curves for composite columns.

The method has been compared with a large number of known experimental results on several types of composite columns and agreement is shown to be excellent (48,49).

**Shells.**—The influence of the amplitude and distribution of imperfections on the ultimate strength capacity of shells is well known. Studies dealing with the connection between imperfections and ultimate loads would be welcome. Longitudinally stiffened cylinders axially or eccentrically compressed is an area of practical interest in this field. The least investigated field concerns cylinders with few stringers.

#### APPENDIX.—REFERENCES

42. Plumier, A., "Relation between the Welding Parameters and the Ultimate Buckling Load of Columns," thesis presented to the University of Liège, Belgium, in 1979, in partial fulfillment of the requirements for the degree of Doctor of Philosophy.
43. Rondal, J., and Maquoi, R., "The Buckling of Steel Columns," *Chambre Syndicale des Fabricants de Tubes d'Acier*, Paris, Notice 1091, 1980.
44. Ansljñ, R., and Massonnet, Ch., "New Tests on Steel I Beam-columns in Mild Steel Subjected to Thrust and Biaxial Bending," *Festschrift Otto Jungbluth—60 Jahre*, Prof. Keller, ed., Technische Hochschule, Darmstadt, Germany, 1978.

45. Fukumoto, Y., and Kubo, M., "An Experimental Review of Lateral Buckling of Beams and Girders," Presented at the May 17-19, 1977, International Colloquium on Stability Structures under Static and Dynamic Loads, Washington, D.C.
46. Harding, J. E., and Dowling, P. J., "The Basis of the Proposed New Design Rules for the Strength of Web Plates and Other Panels Subject to Complex Edge Loading," *Stability Problems in Engineering Structures and Components*, Appl. Science Publish. Ltd., Barking, England, 1979, pp. 355-376.
47. "Draft Model Code for Composite Structures," Recommendations of the CEB-ECCS-FIP-IABSE Joint Committee on Composite Structures, The Construction Press, London and New York.
48. "The Design of Composite Steel Concrete Structures," Second International Colloquium on Stability," Introductory Report, Liège, Belgium, April, 1977.
49. "Mixed Construction," *Structural Design of Tall Steel Buildings*, Volume SB, Chapter SB-9, ASCE, 1979.
50. Vogel, U., and Lindner, J., "Commentary on DIN 18800, Teil 2 (Gelbdruck)—Stabilitätsfälle im Stahlbau," *Knicken von Stäben und Stabwerken*, in German, DAST Berichte aus Forschung und Entwicklung, Nov., 1981.

#### Discussion by Roman Wolchuk,<sup>4</sup> F. ASCE

With reference to problems related to box girders, listed as being in need of clarification, the writer wishes to call attention to considerable work done in this field, the results of which were published after the author's most comprehensive survey of research needs was first presented in April, 1979.

This work was done under a two-year research contract sponsored by the Federal Highway Administration. The results, based on the latest advances of engineering knowledge in this field, in the United States and Europe, are presented in the final report on the "Proposed Design Specifications for Steel Box Girder Bridges" (51).

The report contains a detailed discussion and proposed tentative engineering solutions to the questions listed by the author (box girder webs, diaphragms, shear lag, fabrication tolerances) and other problems, such as the strength of compression flanges, interaction between the webs and the flanges in the cases where webs are designed with utilization of the ultimate (tension field) strength, design of the transverse, and the multiple horizontal web stiffeners with consideration for the ultimate behavior of the web under simultaneous flexure and shear.

Criteria proposed for evaluation of the strength of stiffened compression flanges are based on the "column approach," with consideration for the effects of out-of-straightness and residual stresses.

Of all components of a box girder the design of the webs presents the most difficult problems. Design recommendations given (51) are based on maximum utilization of the elastic beam strength of the web subpanels (requiring rigid stiffeners) and partial utilization of the tension field strength (corresponding to "true Basler" solution). The solutions developed for the box girder webs are also applicable, with some necessary modifications, to the webs of plate girders.

The proposed rules are necessarily conservative. Their liberalization and improvement should be undertaken as the questions not yet sufficiently clarified

<sup>4</sup>Partner, Wolchuk, and Mayrbaur, Cons. Engrs., New York, N.Y.

and more fully answered by continuing research.

Suggestions for future research on box girders are given in report (42) pp. 5-16 where they have been summarized as follows:

a) Parametric studies of applications of the proposed design rules for webs, web stiffeners, unstiffened and stiffened flanges in compression are very desirable. Such studies will permit evaluation of the range of plate and stiffener sizes, determine which of the various parameters are of principal importance in practical design, and may indicate ways to improve and simplify the proposed rules.

b) It is generally recognized that many questions pertaining to the design of stiffened webs and, particularly, the web stiffeners are still not definitively solved and remain to be answered by continuing research. Further theoretical and experimental work on these problems is much needed.

The report contains an extensive bibliography of the subject.

A general overview of the proposed design criteria for box girders is given in (52), and theoretical background of the proposed solutions is discussed concisely in (53).

#### APPENDIX.—REFERENCES

51. "Proposed Design Specifications for Steel Box Girder Bridges," Report No. FHWA-TS-80-205, Wolchuk and Mayrbaur, Consulting Engineers, Federal Highway Administration, Washington, D.C., Jan., 1980.
52. Wolchuk, R., "Proposed Specifications for Steel Box Girder Bridges," *Journal of the Structural Division*, ASCE, Vol. 106, No. ST12, Proc. Paper 15946, Dec., 1980, pp. 2463-2474.
53. Wolchuk, R., "Design Rules for Steel Box Girder Bridges," IABSE Proceedings, P-41/81, Zurich, Switzerland, May, 1981.

---

## MEMBRANE REINFORCEMENT IN SHELLS<sup>a</sup>

Discussion by Morris N. Fialkow,<sup>2</sup> F. ASCE

The author investigates the capacity of shells to resist membrane forces and proposes procedures for the design of the associated membrane reinforcement. However, as this discussion will indicate, the writer believes that the capacity determination and design procedures of the paper are not in accord with the strength criteria and the strength design method of the ACI 318-77 Code (2).

The strength design method is summarized in section 9.1.1 of ACI 318-77

---

<sup>a</sup>January, 1981, by Ajaya K. Gupta (Proc. Paper 15975).

<sup>2</sup>Civ. Engrg., Specialist, Burns and Roe, Woodbury, N.Y.

as follows: "Structures and structural members shall be designed to have design strengths at all sections at least equal to the required strengths calculated for factored loads and forces. . . ." The strength design method is based on satisfaction of equilibrium and strength (yield) requirements and thereby complies with the lower bound theorem of Limit Analysis (16). It then follows from Limit Analysis that the structure has sufficient capacity to sustain the applied factored loads. Determination of the critical failure mode or cracking pattern which is taken up in the paper is not involved in the strength design method or in the lower bound theorem.

The strength criteria of ACI 318-77 relative to the combined action of tension and shear, as indicated in sections 11.3 and 11.7 of the Code provide that the reinforcement required for each type of stress be determined explicitly. The shear strength provided by shear reinforcement is stated in section 11.5.6.2 when shear strength is governed by diagonal tension and in section 11.7.3 when shear friction governs.

Using the terminology of ACI 318-77 and notation in line with the paper,  $N_x^*$ ,  $N_y^*$ ,  $N_{xy}^*$ , and  $N_{yx}^*$  are the design strengths of the shell relative to membrane forces and  $N_x$ ,  $N_y$ , and  $N_{xy}$  (equal to  $N_{yx}$ ) are the required strengths or internal forces which are in equilibrium with the applied factored loads. By strength design, the design equations are

$$N_x^* \geq N_x; \quad N_y^* \geq N_y; \quad N_{xy}^* \geq N_{xy}; \quad N_{yx}^* \geq N_{yx} \quad \dots \quad (46)$$

The design equations for the orthogonal reinforcement are then obtained by using the provisions of the Code for tensile strength and shear strength. After setting  $N_{xy}^* = N_{yx}^*$  and summing the reinforcement requirements in each direction for tension and shear, the following sets of equations are obtained for the total reinforcement in each direction. Case 1: Shear strength controlled by shear friction

$$A_{sx} \geq \frac{N_x}{\phi f_y} + \frac{N_{xy}}{\mu \phi f_y}; \quad A_{sy} \geq \frac{N_y}{\phi f_y} + \frac{N_{xy}}{\mu \phi f_y} \quad \dots \quad (47)$$

Case 2: Shear strength controlled by diagonal tension.

If  $N_{xy} \leq \phi V_c$  (per unit width)

$$A_{sx} \geq \frac{N_x}{\phi f_y}; \quad A_{sy} \geq \frac{N_y}{\phi f_y} \quad \dots \quad (48)$$

If  $N_{xy} > \phi V_c$  (per unit width)

$$A_{sx} \geq \frac{N_x}{\phi f_y} + \frac{N_{xy}}{\phi f_y}; \quad A_{sy} \geq \frac{N_y}{\phi f_y} + \frac{N_{xy}}{\phi f_y} \quad \dots \quad (49)$$

The application of the strength design method as described above can be accomplished in any selected coordinate system with respect to the equilibrium analysis and the provision of design strength by orthogonal reinforcement. Investigation of the adequacy of the design relative to other coordinate systems which, the author indicates, is a necessary part of the design process is not required. This follows from the lower bound limit theorem which, in alternate form (17), states that if an equilibrium distribution of stress can be found which



balances the applied load and is everywhere less than or equal to the design strength (yield stress), the structure will not fail. Physically, it follows because the membrane element cannot fail if the design strength relative to two orthogonal directions exceeds the required strength.

Comments on the development of procedures in the paper are furnished below taking into account the preceding discussion of Code methods and criteria.

a. The principle of minimum resistance, which is utilized by the author, can be applied, as in references (6) and (18), to determine the critical failure mode (i.e.,  $\Theta_c$ , the direction of the yield line) and the magnitude of the collapse load for a given concrete slab. Its application requires that the design strength ( $N_x^*$ ,  $N_y^*$ ) and the internal forces due to a loading pattern ( $N_x$ ,  $N_y$ ,  $N_{xy}$ ) be known. The internal forces due to the collapse load are represented in terms of a load parameter  $k$  by  $kN_x$ ,  $kN_y$ , and  $kN_{xy}$ . The parameters to be evaluated by the principle are  $\Theta$  and  $k$ . Accordingly, it is apparent that the principle of minimum resistance has no direct application to the design problem of determining the amount of orthogonal reinforcement required to sustain a given factored load and that the principle is not pertinent to the Strength Design Method.

b. The author states that the development of the design equations 5a and 5b and the associated yield criterion 6 are based on the principle of minimum resistance. However, Eqs. 5a and 5b (of the original article) are obtained directly from Eqs. 2, 3, and 4 and do not utilize the minimum principle Eq. 1 at all. In fact, it can be readily shown that the critical value of  $\Theta$  obtained by using the principle via Eqs. 1, 3, and 4 bears no relationship to the values of  $\Theta$  defined by Eqs. 5a and 5b.

c. In view of the preceding it appears that Eqs. 5a and 5b have been adopted as "the design equations for any assumed value of  $\Theta$ " on the basis of satisfying Eqs. 2, 3, and 4. In this formulation the strength criterion is represented by Eq. 4. Review of this equation shows that, in contrast with aforementioned ACI Code provisions, no explicit strength contribution due to the shear strength of reinforced concrete is included in the strength criterion. The resulting deficiency in the paper's strength criterion is apparent when the design Eqs. 5a and 5b are applied for values of  $\Theta = 90^\circ$  and  $\Theta = 0^\circ$ . The design equations would then require infinite  $N_x^*$  and infinite  $N_y^*$  respectively and cannot be satisfied.

d. The statement by the author, leading to Eq. 7, that a compressive force parallel to the crack is necessary in order to maintain internal equilibrium, is not concurred with. The internal forces acting on the shell membrane elements which have been determined by prior analysis to be in equilibrium with each other and with the applied factored loads are generically the forces  $N_x$ ,  $N_y$ , and  $N_{xy}$ . The actual internal state of stress relative to any direction follows from the values of  $N_x$ ,  $N_y$ , and  $N_{xy}$  and can be pictured via the associated Mohr circle of stress. The case of  $N_x$  and  $N_y$  both positive, has been pictured in Fig. 11. For the relative magnitudes used, it is apparent that no compression in any direction exists. The author considers the case in which the orthogonal reinforcement is at the design strength levels,  $N_x^*$  and  $N_y^*$ . However, the associated stress state is, by definition,  $N_x$ ,  $N_y$ , and  $N_{xy}$  so that the absence of compression still applies.

e. The state of strain is investigated by the author assuming continuity of material. Several basic deficiencies in the investigation lead to incorrect conclu-



sions relative to the state of strain. The author improperly omits any consideration of the shear strain  $\gamma_{xy}$  and uses only  $\epsilon_x$  and  $\epsilon_y$  to define the state of strain. In this regard, the additional Eq. 50 below must be included, besides Eqs. 12 and 13, to define the relationship between  $\epsilon_x$ ,  $\epsilon_y$ , and  $\gamma_{xy}$  and  $\epsilon_1$ ,  $\epsilon_2$ , and  $\Theta$ .

$$\tan 2\Theta = \frac{\gamma_{xy}}{\epsilon_x - \epsilon_y} \dots \dots \dots (50)$$

Also, for the case of  $N_x$  and  $N_y$  at capacity tensile stress, the paper incorrectly postulates that  $\epsilon_2$  must be compressive. The invalidity of this assumption has been discussed in preceding paragraph d. In addition, inconsistency in the meaning of the angle  $\Theta$  occurs in the paper. By definition, via Eqs. 12, 13, and 50,  $\Theta$  is the angle between the direction of the largest principal strain and the

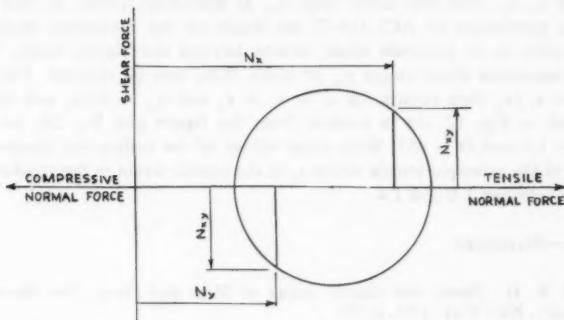


FIG. 11.—Mohr Circle of Membrane Forces:  $N_x$ ,  $N_y$ ,  $N_{xy}$  Given

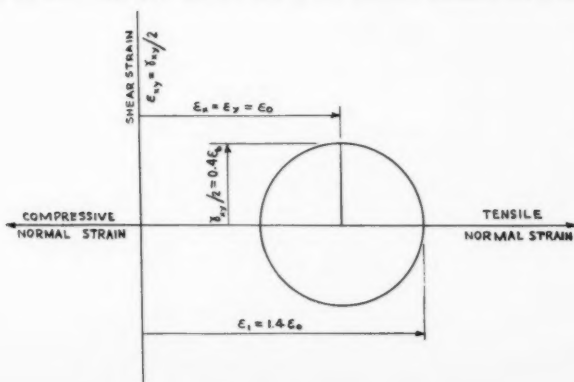


FIG. 12.—Mohr Circle of Strain for Maximum  $\epsilon_1/\epsilon_x$

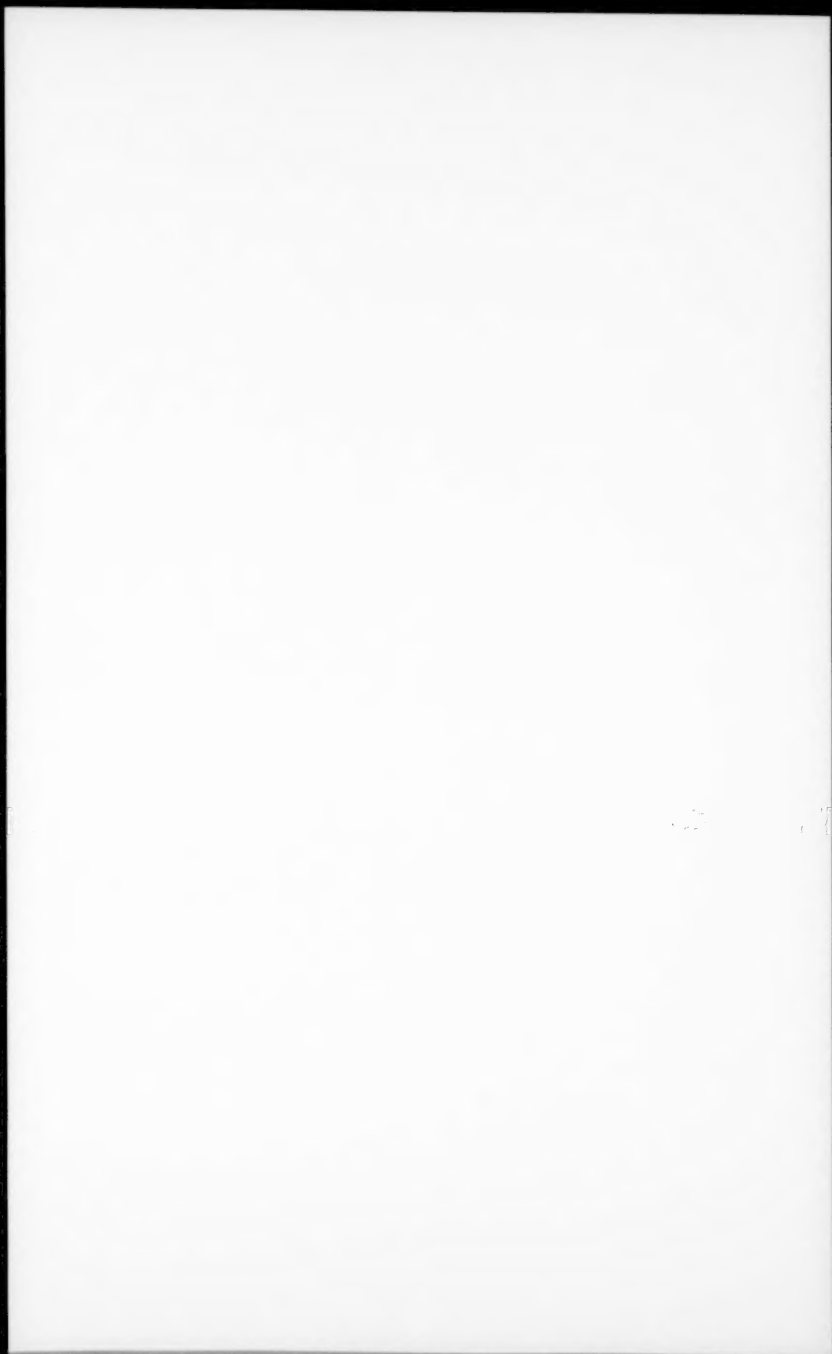
x-direction. However, although it is stated that the minimum size cracks (or strain) occur when the reinforcement and the principal strain are in the same direction, i.e., with  $\Theta = 0^\circ$ , Fig. 2 shows minimum strain when  $\Theta = 45^\circ$ .

The unrealistic results which are obtained with the author's methods are apparent from Fig. 2 which pictures Eqs. 14 and 15. For the case of  $\Theta = \text{zero}$ , the orthogonal reinforcement lies in the principal directions so that  $\epsilon_1 = \epsilon_x$  and  $\epsilon_2 = \epsilon_y$ , as is evident from the standard strain Eqs. 12 and 13. This contrasts with the value of  $\epsilon_1$  from Fig. 2 and Eq. 14 which indicate infinite strain for  $\Theta = \text{zero}$ .

The author reaches the conclusion that rapidly increasing strains result as the angle  $\Theta$  between the reinforcement and the principal strain direction increases from  $0^\circ$  to  $45^\circ$ . The validity of this conclusion is now considered using the Mohr circle of strain as in Fig. 12. Towards this end, we seek the largest ratio,  $R = \epsilon_1 / \epsilon_x$  with  $\epsilon_x \geq \epsilon_o$  where  $\epsilon_o$  is the tensile strain at yield. For any values of  $\epsilon_x, \epsilon_y$ , this will occur with  $\gamma_{xy}$  at maximum value. In this regard, the shear provisions of ACI 318-77 set limits on the maximum shear stress and are such as to preclude shear strains beyond the elastic range. On this basis, a maximum shear strain  $\gamma_{xy}$  of about  $0.8\epsilon_o$  can be derived. The largest ratio  $R = \epsilon_1 / \epsilon_x$  then occurs for  $\epsilon_x = \epsilon_y = \epsilon_o$  and  $\gamma_{xy} = 0.8\epsilon_o$  and this case is pictured in Fig. 12. As is evident from the figure and Eq. 50, the largest ratio  $R = 1.4$  and  $\Theta = 45^\circ$ . With other values of the orthogonal strains  $\epsilon_x, \epsilon_y$ , the ratio of the principal tensile strain  $\epsilon_1$  to the tensile strain in the reinforcement  $\epsilon_x$  will be between 1.0 and 1.4.

#### APPENDIX.—REFERENCES

16. Wood, R. H., *Plastic and Elastic Design of Slabs and Plates*, The Ronald Press Company, New York, 1961, p. 15.
17. *Plastic Design in Steel, Manual No. 41*, 2nd ed., by a Joint Committee of the Welding Research Council and the American Society of Civil Engineers, ASCE, 1971, p. 10.
18. Jain, S. C., and Kennedy, J. B., "Yield Criterion for Reinforced Concrete Slabs," *Journal of the Structural Division*, ASCE, Vol. 100, No. ST3, Mar., 1974, pp. 631-644.



...the ... ..

...the ... ..

...the ... ..

...the ... ..

...the ... ..

...the ... ..

...the ... ..

...the ... ..

...the ... ..

...the ... ..

...the ... ..

...the ... ..

...the ... ..

...the ... ..

...the ... ..

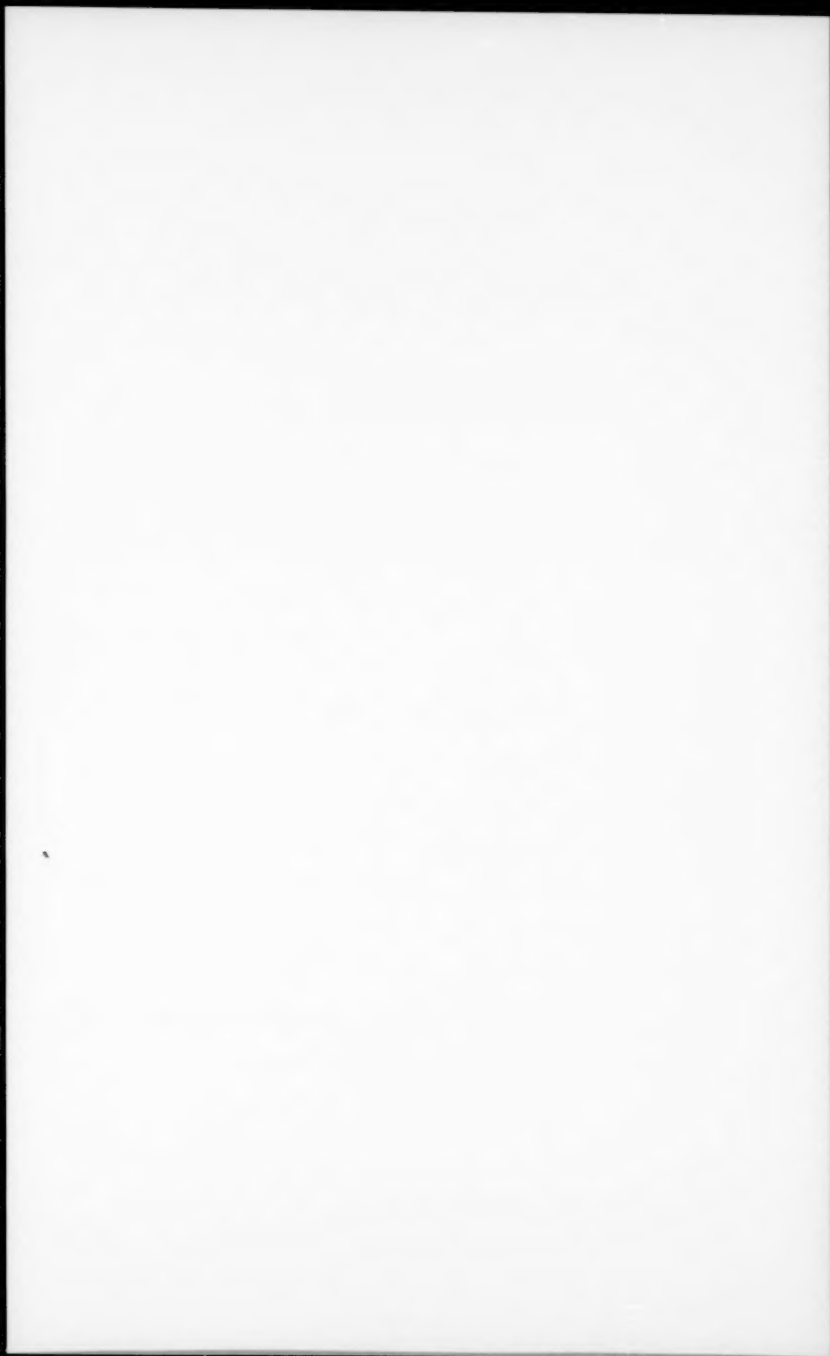
...the ... ..

...the ... ..

...the ... ..

...the ... ..

...the ... ..



1. The first part of the paper is devoted to a general discussion of the problem of the existence of solutions of the system of equations



## TECHNICAL PAPERS

Original papers should be submitted in triplicate to the Manager of Technical and Professional Publications, ASCE, 345 East 47th Street, New York, N.Y. 10017. Authors must indicate the Technical Division or Council, Technical Committee, Subcommittee, and Task Committee (if any) to which the paper should be referred. Those who are planning to submit material will expedite the review and publication procedures by complying with the following basic requirements:

1. Titles must have a length not exceeding 50 characters and spaces.
2. The manuscript (an original ribbon copy and two duplicate copies) should be double-spaced on one side of 8-1/2-in. (220-mm) by 11-in. (280-mm) paper. Three copies of all figures and tables must be included.
3. Generally, the maximum length of a paper is 10,000 word-equivalents. As an *approximation*, each full manuscript page of text, tables or figures is the equivalent of 300 words. If a particular subject cannot be adequately presented within the 10,000-word limit, the paper should be accompanied by a rationale for the overlength. This will permit rapid review and approval by the Division or Council Publications and Executive Committees and the Society's Committee on Publications. Valuable contributions to the Society's publications are not intended to be discouraged by this procedure.
4. The author's full name, Society membership grade, and a footnote stating present employment must appear on the first page of the paper. Authors need not be Society members.
5. All mathematics must be typewritten and special symbols must be identified properly. The letter symbols used should be defined where they first appear, in figures, tables, or text, and arranged alphabetically in an appendix at the end of the paper titled Appendix.—Notation.
6. Standard definitions and symbols should be used. Reference should be made to the lists published by the American National Standards Institute and to the *Authors' Guide to the Publications of ASCE*.
7. Figures should be drawn in black ink, at a size that, with a 50% reduction, would have a published width in the *Journals* of from 3 in. (76 mm) to 4-1/2 in. (110 mm). The lettering must be legible at the reduced size. Photographs should be submitted as glossy prints. Explanations and descriptions must be placed in text rather than within the figure.
8. Tables should be typed (an original ribbon copy and two duplicates) on one side of 8-1/2-in. (220-mm) by 11-in. (280-mm) paper. An explanation of each table must appear in the text.
9. References cited in text should be arranged in alphabetical order in an appendix at the end of the paper, or preceding the Appendix.—Notation, as an Appendix.—References.
10. A list of key words and an information retrieval abstract of 175 words should be provided with each paper.
11. A summary of approximately 40 words must accompany the paper.
12. A set of conclusions must end the paper.
13. Dual units, i.e., U.S. Customary followed by SI (International System) units in parentheses, should be used throughout the paper.
14. A practical applications section should be included also, if appropriate.







